UC San Diego
UC San Diego Electronic Theses and Dissertations

Title

Out-of-Plane Compressive Response of Honeycomb Cores Used in Sandwich Composites

Permalink

https://escholarship.org/uc/item/8v78s2cd

Author

Anagnostopoulos, Konstantinos

Publication Date

2019

Peer reviewed|Thesis/dissertation

UNIVERSITY OF CALIFORNIA SAN DIEGO

Out-of-Plane Compressive Response of Honeycomb Cores Used in Sandwich Composites

A dissertation submitted in partial satisfaction of the requirements for the degree
Doctor of Philosophy

in

Structural Engineering

by

Konstantinos Anagnostopoulos

Committee in charge:

Professor Hyonny Kim, Chair
Professor Yuri Bazilevs
Professor Nicholas S. Boechler
Professor John B. Kosmatka
Professor Francesco Lanza di Scalea

2019

The Dissertation of Konstantinos Anagnostopoulos is approved, and it is

acceptable in quality and form for publication on microfilm and electronically:

_____

_____

_____

_____

Chair

University of California San Diego

2019

DEDICATION

To my parents and sister.

TABLE OF CONTENTS

LIST OF FIGURES

xi

LIST OF TABLES

ACKNOWLEDGEMENTS

First and foremost, I would like to express my sincere appreciation towards my advisor, Prof. Hyonny Kim for the opportunity to work under his supervision. I feel grateful to him for introducing me to research paths that were initially unknown, yet intriguing to me, and constantly encouraging me throughout my graduate studies. Professor Kim's technical expertise, guidance and integrity truly stimulated me at both academic and personal levels. Without his support, this dissertation would not have been possible. I would also like to thank Prof. Kim for the opportunity he has given me to work with him as a postdoctoral scholar after the end of my Ph.D. studies.

I would further like to extend my gratitude to Prof. Michael W. Czabaj from the University of Utah for his major contributions regarding the X-ray computed tomography scans performed at Utah Composite Mechanics Lab. I highly appreciate his efforts, willingness to share his knowledge as well as the fruitful interactions we have had during the last two years of my studies.

I would also like to thank my committee members, Prof. Yuri Bazilevs, Prof. Nicholas S. Boechler, Prof. John B. Kosmatka, and Prof. Francesco Lanza di Scalea for their critical feedback on my research. I would also like to thank Prof. Chia-Ming Uang and Prof. Vitali Nesterenko for their useful suggestions during my advancement to Candidacy. I am additionally grateful to Prof. Kosmatka for the inspiring and valuable discussions we had together on course related topics.

I am thankful to Prof. Joel P. Conte for his support throughout my Master's degree. It is due to the joint efforts of Prof. Kim and Prof. Conte that I am standing here, writing these few acknowledgment lines and my dissertation.

I also wish to acknowledge Prof. Kenneth Loh and ARMOR lab for letting me make use

of their equipment. More particularly, I would like to thank Mr. Sumit Gupta and Mr. Gianmarco Vella from ARMOR lab for their great friendship and the endless number of hours we jointly spent for mechanical properties characterization.

I am also very thankful to Prof. Daniel Whisler and Dr. Zhi Chen for making me feel extremely comfortable when I first joined the research group of Prof. Kim. Furthermore, I would like to thank Dr. Andreas Koutras for his true friendship and helpful advice over the course of my studies. I wish to further thank my fellow research group colleagues, namely Mr. Javier Buenrostro, Mr. Andrew Ellison, Mr. Hyung Kim, Mr. Moonhee Nam, Dr. Mimi Ngo, Ms. Chaeane Wiggers de Souza, for the collaboration and their feedback.

I am grateful to all the friends in the US that contributed the most to this unforgettable experience as well as my friends all around Europe for their support. Most importantly, I would like to thank my parents, Vasilis and Evanthia, and my sister, Eirini, for their support on my choices, constant encouragement, guidance, and their love.

Parts of Chapter 2 are a reprint of the material that appears in the conference paper "Phenomenological Investigation of Nomex® Core Damage Mechanics in Honeycomb Sandwich Panels under Transverse Impact and Quasi-Static Loading", 2016, (with Anagnostopoulos K., Kim H.) which was submitted in the 31st Annual ASC Technical Conference in Virginia. The author of this dissertation was the primary investigator and author of this manuscript.

Chapter 3, in part is currently being prepared for publication of the material. Anagnostopoulos, K., Czabaj, M. W., Kim, H. The author of this dissertation is the primary investigator and author of this material.

VITA

2009   Diploma in Civil Engineering, University of Patras, Greece

2013   Master of Science in Structural Engineering, University of California San Diego

2019   Doctor of Philosophy in Structural Engineering, University of California San Diego

ABSRACT OF THE DISSERTATION

Out-of-Plane Compressive Response of Honeycomb Cores Used in Sandwich Composites

by

Konstantinos Anagnostopoulos

Doctor of Philosophy in Structural Engineering

University of California San Diego, 2019

Professor Hyonny Kim

Sandwich structural elements consist of two metallic or non-metallic laminated skins separated by a lightweight thicker core layer, maximizing in this manner weight efficiency and structural performance. From the available core configurations, phenolic resin impregnated Nomex® paper honeycomb cores are highly preferred in aerospace industry because of their lower density, excellent thermal resistance, and curved shape adaptability.

Despite the inherent benefits of Nomex® paper sandwich structures, their impact response is still questionable. Towards this direction, a series of simulated hail ice impact tests was performed on flat carbon fiber sandwich panels via gas gun test apparatus to assess Nomex® paper core damage. Impact test results revealed significant core crushing in the form of cell collapse without any externally visible signs of damage on the impacted skin surface.

Since high-velocity impact tests on sandwich panels are by nature highly complex, the out-of-plane response of over-expanded Nomex® cores was phenomenologically characterized through quasi-static flatwise compression tests on stabilized sandwich core coupons. Localized detachment and crushing of the phenolic resin accumulation regions between adjacent cell walls, were the main damage modes that triggered honeycomb collapse.

X-ray Computed Tomography (CT) scans were also employed to assess damage modes on the interior cells of tested sandwich core coupons. Given several sets of X-ray CT scan 3D data, an automated B-spline image-based reconstruction scheme was developed to numerically capture scanned honeycomb core geometries. Different applications of the proposed reconstruction scheme are going to be presented. Finally, the contribution of the phenolic resin accumulation regions on the out-of-plane response was investigated through numerical modeling of the reconstructed B-spline geometry. To this end, constituent material properties were determined through uniaxial tensile testing on in-situ phenolic resin impregnated paper coupons as well as bare aramid paper coupons. Numerical simulations on sandwich cores without the phenolic resin accumulations yielded significant reduction of the collapse limit, validating in this way the experimental observations.

CHAPTER 1: INTRODUCTION

1.1   BACKGROUND

Sandwich structures have been adopted in aerospace industry due to their high stiffness and strength to weight ratios respectively. Sandwich elements typically consist of two metallic or non-metallic skins separated by a lightweight and relatively thick core. The skins are primarily carrying the in-plane forces while any transverse shear forces are being taken by the core constituent. In this sense, sandwich plate is equivalent to I-beam configuration extended to 2D space. The efficiency of sandwich construction relative to monolithic composite or metallic structures is demonstrated in Table 1.1, assuming perfect bonding between the individual sandwich components [Bitzer, 1997]. The increase of bending stiffness allows for smaller deflections under loading, an important feature for high performance structures. The existence of core also increases the buckling resistance of the entire sandwich structure and the skin parts that are subjected to axial compressive loads.

In fuselage and wing designs, the need for stringers and hooped frames that are attached to the cylindrical thin skin is eliminated when sandwich construction is utilized. Schematics of two different fuselage configurations are shown in Figure 1.1. Sandwich construction reduces the analysis, manufacturing and maintenance time because of the overall geometric simplicity. The continuous and integrated stiffening of a sandwich structure permits a smaller number of parts and fasteners reducing in this manner labor cost and logistics during assembly [Herrmann et al., 2005]. Abrate reported that sandwich construction could lead up to 85% reduction in part numbers and 50% reduction in labor man-hours for the Boeing 360 helicopter, compared to a semi-monocoque stringer-based aluminum skin [Abrate, 1997]. Sandwich construction is also superior regarding

fatigue resistance. In monolithic design, the holes around rivets are regions of high stress concentration and initial cracks can propagate through repetitive cyclic loading. For all these reasons, sandwich construction is considered one of the most efficient options for weight and safety critical aerospace applications.

The main types of core configurations that can be utilized in sandwich structures are honeycomb, cross-banded, corrugated, waffle-type, foam and balsa wood cores [Composite Materials Handbook-17, 2013]. Of all these types, foam and honeycomb cores are the most commonly used. Honeycomb cores are industrial products and are basically consisted of an array of open cells joined together through adhesive nodes. The cell configurations presented in Figure 1.2 allow for different levels of shape morphing and mechanical response. For hexagonal core configuration, it has been reported that roughly 95% of the volume of a honeycomb core is occupied by the entrapped air [Rinker et al., 2013]. Foam cores have excellent energy absorption capabilities and are widely implemented in automotive industry. On the other hand, honeycomb cores are preferred in aerospace industry over foam cores because they exhibit higher specific stiffness and strength values. Towards this direction, we also need to mention that honeycomb cores and especially Flex-Core configuration can be easily morphed to curved shapes while foam cores need extensive machining.

Honeycombs are made of various thin sheet materials also known as ribbons such as Nomex® paper, aluminum, titanium, Kevlar® paper and Kraft paper. Hermann reported that the predominant base material for commercial aircraft applications is Nomex® paper. Nomex® paper is a flame-resistant meta-aramid material belonging to the same family with the most known Kevlar® paper. It is being produced from condensation reaction between the monomers m-phenylenediamine and isophthalic acid. The most common manufacturing method for honeycomb

cores involves two stages, namely the adhesive bonding and the expansion process. Adhesive lines at a predefined spacing are printed on the first sheet of base material. The same procedure is repeated at the next sheet which is then stacked on top of the first one. It is important to note that the adhesive lines of the second sheet are placed at the mid-span of the first sheet adhesive lines. This procedure is repeated for multiple layers and the end product is compacted and cured at elevated temperature. Then, the cured block of base material is cut to the desired thickness and finally expanded to form a nearly hexagonal array. The direction of continuous ribbon is called the L-direction. The direction at which the block of stacked sheets is expanded is called the W-direction. The direction normal to the open cell faces is named as the T-direction or core thickness direction. Honeycomb core makers only supply a wide range of core thicknesses. Finally, paper-based honeycomb cores are dipped into phenolic resin to increase system stability and then cured in an oven. In this case, the expanded block must be dipped multiple times to ensure that the nominal core density is met. In this sense, paper honeycomb cores essentially have a composite meso-structure. Figure 1.3 shows a schematic of the honeycomb core manufacturing processes as well as the set of principal directions [Wadley, 2005]. For high-density metallic cores, corrugation process is commonly used but further details on its aspects are beyond the scope of the presented work. A snapshot of Nomex® paper based over-expanded (OX) core sample of 3/16" cell size is shown in Figure 1.4.

A schematic of the individual components of a sandwich panel is shown in Figure 1.5. Manufacturing of honeycomb sandwich panels is slightly different compared to traditional composite laminates. Skins are bonded to the honeycomb core through an interfacial layer of film adhesive. Since the open cell surfaces are not continuous as in the case of foam cores, adhesive films need to be viscous enough during sandwich assembly so that meniscus-shaped fillets can be

formed to increase the total core bonded area. Figure 1.6 shows a scanning electron microscope snapshot of the film adhesive meniscus-type fillets [Heimbs et al., 2006]. When composite skin fabrication is employed, face sheets can either be co-cured and solidified with the adhesive film at the same time under heat and vacuum pressure or can be secondarily bonded to the honeycomb core after they have been cured separately. In general, co-curing method is preferred as all the constituents are conforming to the same shape without any residual stresses. Co-curing method may not be that advantageous when light-weight skins of 2-3 plies and relatively large cell size cores are combined. In such cases, the cured sandwich panel will exhibit dimples as the initially flexible non-cured plies tend to drape inside the honeycomb cells, thus reducing the effectiveness of vacuum pressure on void removal and ply consolidation. This phenomenon can be minimized by using a relatively thicker layer of adhesive film. A step-by-step procedure of flat sandwich panel co-curing method is shown in Figure 1.7. The assembly is always performed on top of a tooling metal plate.

Sandwich construction has been adopted in numerous applications at Airbus fleet [Hermann et al., 2005]. Examples are radomes, belly fairings, leading and trailing edge fairings, interior floors as well as control surfaces such as elevators, ailerons and rudders. Figure 1.8 gives a summary of sandwich applications in Airbus A380. Thévenin also showed sandwich construction sketches of Airbus A320 elevator and Airbus A310 rudder [Thévenin, 2007]. Nomex® paper honeycombs have been used as the core material for the floors, overhead bins and ceilings of Boeing B-747 [Bitzer, 1997]. Boeing's latest mid-size aircraft, B-787, incorporates sandwich parts for the main control surfaces and the engine fan cowl doors. Beechcraft Starship was the first business jet exclusively made of Nomex® honeycomb sandwich composites including the wings and the fuselage. The latest effort of Nomex® paper honeycomb-based fuselage was made by

Bombardier and the Learjet-85 development program. Despite the mockup of the prototype jet at Paris Air Show in 2009, mass production was cancelled in 2015. Finally, an experimental and computational study on a composite sandwich fuselage part at NASA revealed that frames spacing can be twice the frame spacing of semi-monocoque fuselages without violating safety factors and damage tolerance criteria [Rouse et al., 1997].

1.2   IMPACT RELATED DAMAGE ON AIRCRAFT STRUCTURES

Impact damage in aircrafts can be caused by a wide range of objects during operation and maintenance. Bird strikes, hail storms, tool drops and wide area collision with ground service equipment are the most common impact threats. A study has revealed that bird strikes on commercial aircrafts can cause losses of approximately 1.2 billion USD [Meguid, 2008]. Moreover, DeFrancisci reported that 50% of major damage in aircrafts is attributed to baggage vehicles collision [DeFrancisci, 2013]. A schematic of possible locations of damaged regions due to different types of objects and impact energy levels is shown in Figure 1.9 [Neidigk, 2017]. It is evident that bird strikes, hail storms and runway debris are on the high velocity and kinetic energy regimes while collision while ground service equipment and tool drops lie on the lower velocity bound.

In many cases, damage can be visually detectable as in Figure 1.10 and thus immediate repair needs to be scheduled. Depending on the aircraft damage severity and its visibility, Federal Aviation Administration (FAA) in the Advisory Circular has established five damage categories based on the load carrying capacity thresholds [U.S. Department of Transportation, Federal Aviation Administration, 2009]. The damage categories reported in Figure 1.11 are associated to specific thresholds regarding load carrying capacity. Of interest is Category 5 damage which is

defined as the damage not accounted for in the design criteria. While load resistance is decreased as damage detectability increases for the first four categories, Category 5 can cover the entire span of damage visibility ranging from barely visible impact damage up to catastrophic loss as in the case of Figure 1.12.

Impact-related damage categorization is more challenging for sandwich structures because by default their impact resistance is relatively low. When sandwich elements are subjected to localized transverse loading, honeycomb cores are most likely to fail first due to their low out-of-plane strength. This state of internal core damage may go undetected during regular inspection as the exposed composite skin may not exhibit visual signs of damage such as scratches, cracks and residual dents.

As a matter of fact, in March 2005, the Air Transat Airbus A310-308 (Flight no. 961) entered a Dutch roll at an altitude of 1,000 ft after departing Varadero airport in Cuba. The aircraft safely landed back to the same airport and only minor injuries were reported. Apparently, the rudder started fluttering immediately after take-off and a large portion got detached from the vertical tail plane leading to the Dutch roll instability. A side view photo of the vertical tail plane after the accident is shown in Figure 1.12. The rudder was consisted of Nomex® honeycomb core and a combination of carbon fiber and glass fiber skins. Post-inspection of the residual rudder revealed significant disbonding within the core layer which suggests that core crushing had already existed as shown in Figure 1.13 [Thévenin, 2007]. The most likely scenario is that disbonding kept growing over the years of operation, reaching a critical point at which the aerodynamic features of the designed rudder changed and thus flutter was triggered. Since the size of the residual rudder was relatively small, the investigation could not eliminate that the rudder may have experienced some impact event that could have resulted in significant core damage either on the ground or in

flight.

1.3   PROBLEM STATEMENT

From the available core configurations, honeycomb cores are widely used in aerospace industry because of their higher compression and transverse shear moduli as shown in Table 1.2. Compared to more conventional aluminum cores, phenolic resin impregnated Nomex® paper honeycomb cores have slightly lower density, better curved shape adaptability, excellent flame resistance, and comparable mechanical performance.

As a result of the phenolic resin dipping process, Nomex® paper honeycomb cores exhibit a complex meso-structure which is primarily consisted of composite cell wall cross-sections, and phenolic resin accumulation regions at the intersection between adjacent paper ribbons. Figure 1.14 shows a typical through-thickness cross-sectional view of an over-expanded Nomex® core configuration. Of special interest in Figure 1.14 are the dark-colored accumulations of phenolic resin also known as fillets at the junctions between single and double walls, and the composite nature of cell wall meso-structure.

The characterization of the out-of-plane response of honeycomb cores is important because core crushing is one of the prevailing failure modes of sandwich panels ultimately leading to facesheet/core or core/core disbonding [Wang, 2004]. For aluminum core configurations, honeycomb collapse under out-of-plane loads is attributed to plastic yielding due to excessive wall buckling [Wilbert et al., 2011]. On the other hand, the triggering damage mechanism on Nomex® paper cores related to cell wall collapse has not been investigated. The contribution of the phenolic resin fillets on the honeycomb core out-of-plane load carrying capabilities response needs to be established in order to further understand the macroscopic behavior of Nomex® cores under out-

of-plane loading.

At the same time, visualization of damage morphology is limited by the fully enclosed nature of honeycombs, thus 3D imaging techniques need to be employed to accurately assess damage features of tested honeycomb core coupons. To this end, X-ray computed tomography is an advanced imaging technique that can be used for detailed 3D description of limited size honeycomb core coupons. In terms of computational modeling, research efforts on the out-of-plane compressive behavior of Nomex® cores have been limited on idealized cell size geometry metrics provided by core manufacturers that do not reflect inherent cell irregularities [Aktay et al., 2008; Asprone et al., 2013; Fischer et al., 2009; Giglio et al., 2011; Heimbs, 2009; Liu et al., 2015; Seemann and Krause, 2017]. For Nomex® paper cores, the provided idealized cell metrics charts do not report any nominal size for the formed fillets. Under this context, X-ray computed tomography and image-based reconstruction of scanned geometries can bridge the gap between idealized and actual geometry description. Since explicit modeling of Nomex® core geometry features has been performed to obtain insight of the domineering failure mechanisms, the contribution of the resin accumulation regions on the load carrying capacity and system stability has been totally neglected.

Towards this direction, we propose a framework including coupon level experiments, imaging techniques and finite element modeling to identify governing failure mechanism and assess the role of each constituent to the mechanical response of the pre-impregnated Nomex® paper cores under compressive loading. In terms of computational modeling, the composite nature of the impregnated Nomex® paper cores along with the resin accumulation regions formed between adjacent paper ribbons are accounted for via X-ray computed tomography and optical microscopy. In this manner, an accurate numerical description of the Nomex® core geometry and

material distribution is attained.

1.4   OBJECTIVES AND APPROACH

The first objective of the presented work is to experimentally establish core crushing as one of the main damage modes associated to hail impact events. Towards this direction, governing parameter is the low external damage visibility. To simulate realistic impacts on control surfaces, hail ice projectiles were launched with a gas gun apparatus targeting sandwich panels at 10° oblique angle of attack.

The second major objective is to phenomenologically investigate the out-of-plane flatwise compression behavior and assess the key mechanisms by which damage initiates. The focus is on determining the geometric features that govern cell wall collapse. Damage modes of failed coupons were evaluated using photography and optical microscopy.

Since most part of the honeycomb structure is fully enclosed, and observations can only be performed on the outer edges, visual access to the interior cell geometry is needed to get a full view of damage morphology. Based on X-ray computed tomography, an image-based reconstruction scheme was established to numerically model the geometric features of scanned Nomex® honeycomb core samples. In this sense, the proposed automated scheme can be utilized as a non-destructive tool to obtain metrics of core irregularities. The sequence of failure phenomena was also captured by analyzing core samples at different damage states.

Finally, finite element models were run to supplement the phenomenological observations from flatwise compression tests. Parametric studies on the fillets demonstrate their effect on global response. X-ray computed tomography and optical microscopy along with the proposed image-

based reconstruction scheme were employed to recreate a virtual domain that reflects the in-situ geometric features of Nomex® paper honeycomb cores.

Aligned with the list of objectives, Chapter 2 covers the experimental work on Nomex® honeycomb cores, namely the simulated hail ice impact tests and the flatwise compression tests under quasi-static strain rates. Low external visibility along with representative in-flight hail speeds were the driving parameters for the simulated hail impact tests. In regards to the investigation of the crushing phenomena using flatwise compression, key damage mode was related to local detachment and kinking of the fillet component surrounding the intersection of two adjacent ribbons.

Chapter 3 presents an automated reconstruction scheme which is based on a stack of images obtained from X-ray computed tomography scans, and B-spline surface and volume fitting. The proposed scheme was utilized to assess the extent of damage on tested core coupons, and to create computational models that were later analyzed in commercial finite element software. MATLAB scripting software was employed for the development of the proposed scheme.

Chapter 4 covers the numerical simulation of a fully enclosed honeycomb cell subjected to flatwise compression as extracted from the X-ray CT reconstruction scheme. Base material mechanical properties were obtained from literature and uniaxial tensile tests on in-situ thin coupons extracted from honeycomb cells. Finally, Chapter 5 summarizes the key findings of this research work.
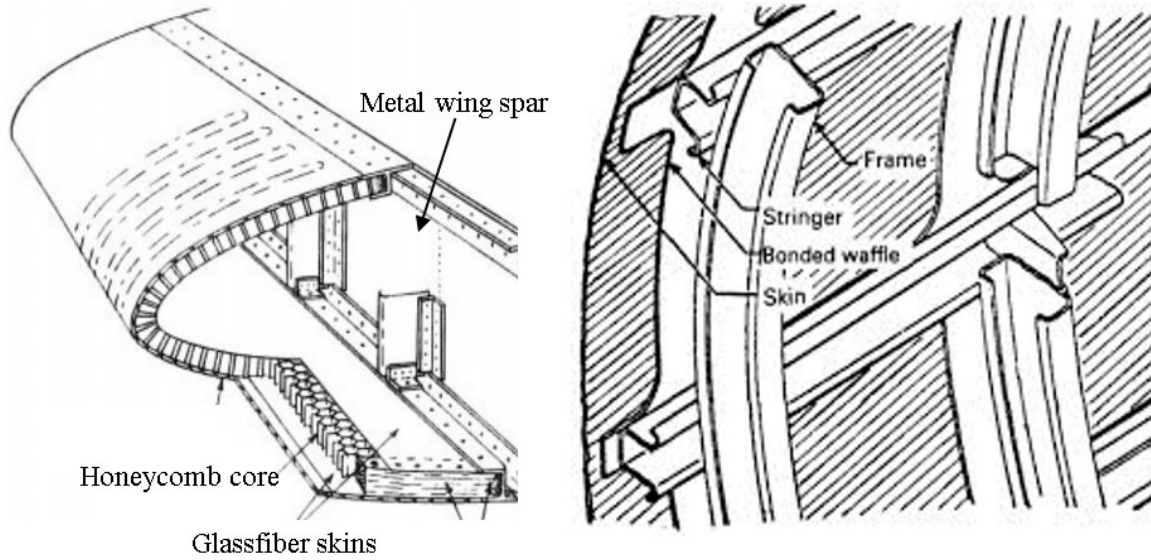
Figure 1.1. Schematics of: (a) Sandwich wing construction [Laxmi Narain Verma Memorial Society Group of Institutes, 2007]; (b) Semi-monocoque fuselage [Niu, 1997]
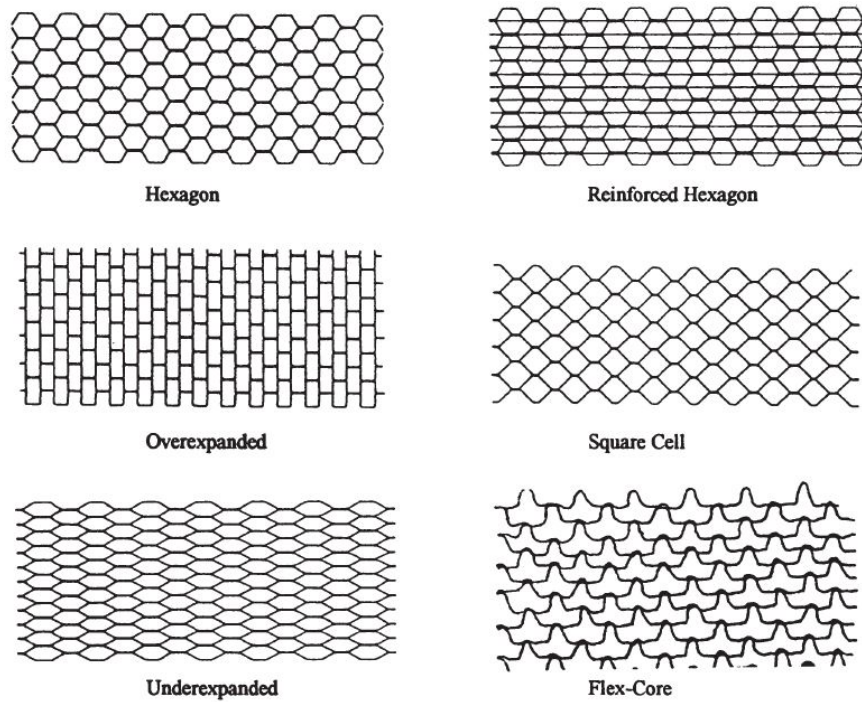
Figure 1.2. Honeycomb core configurations [Bitzer, 1997]
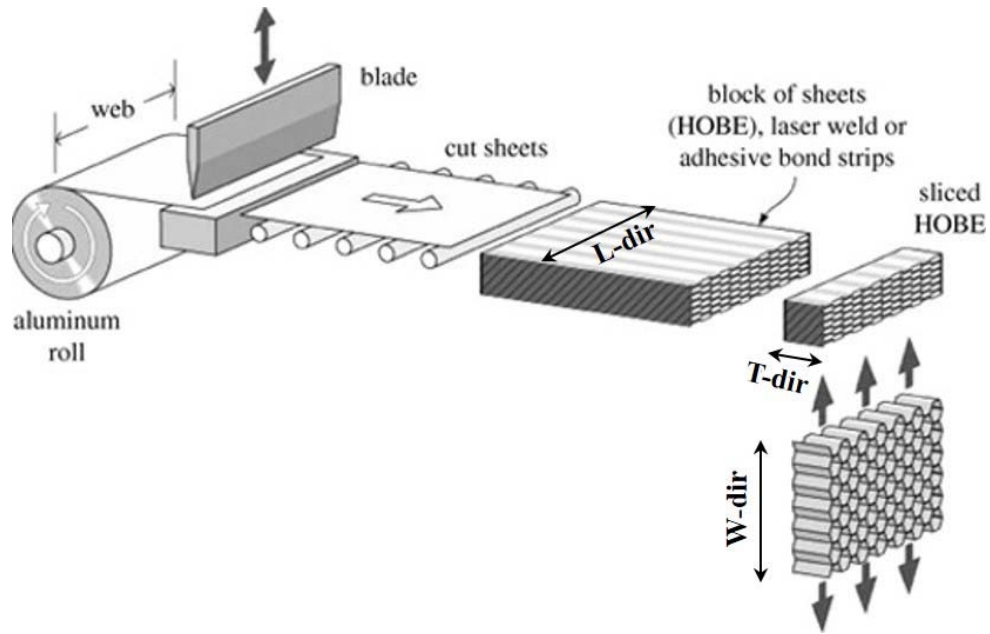
Figure 1.3. Schematic of adhesive bonding and expansion process [Wadley, 2005]
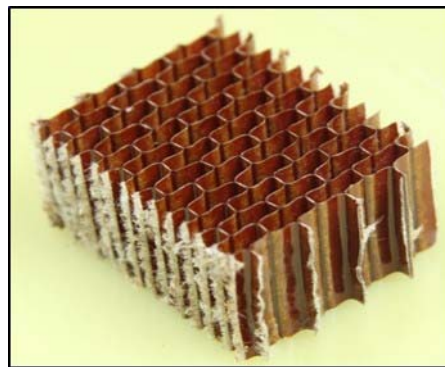
Figure 1.4. Snapshot of 25.4 mm thick Nomex® paper over-expanded honeycomb core sample
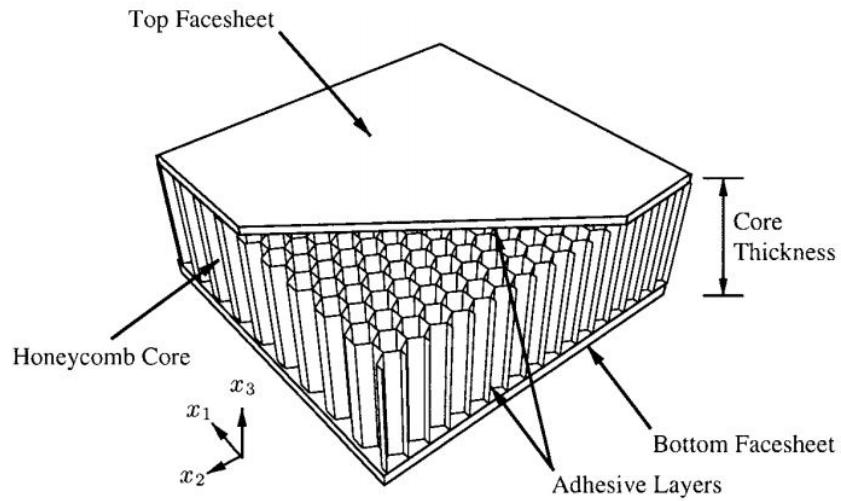
Figure 1.5. Individual components of sandwich honeycomb panels [Han et al. 2002]
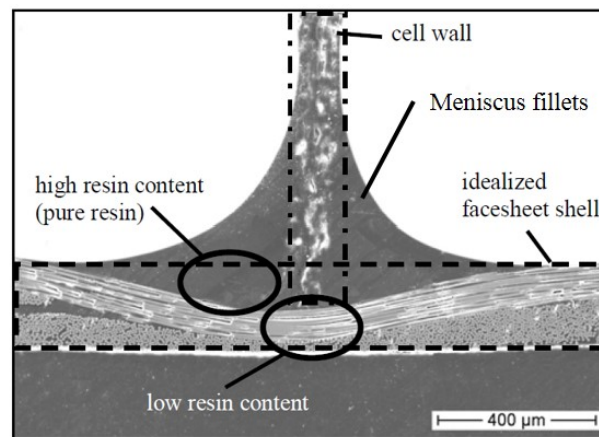
Figure 1.6. Scanning electron microscopy of bond between bottom skin and honeycomb cells

[Heimbs et al., 2006]

13

a) Tool

b) Raw materials used

Paper Backing on Film Adhesive

Film Adhesive

Bleeder/ Breather

Honeycomb

Porous Release Film

Peel Ply
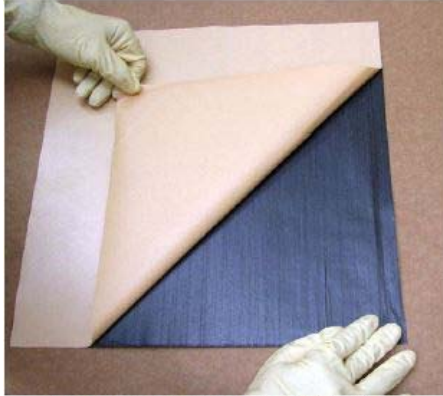
Prepreg

c) Laying up a face sheet from prepreg

d) Applying film adhesive

e) Inserting honeycomb core

f) Bagging assembly

Figure 1.7. Step-by-step co-curing manufacturing process [Composite Materials Handbook-17, 2013]
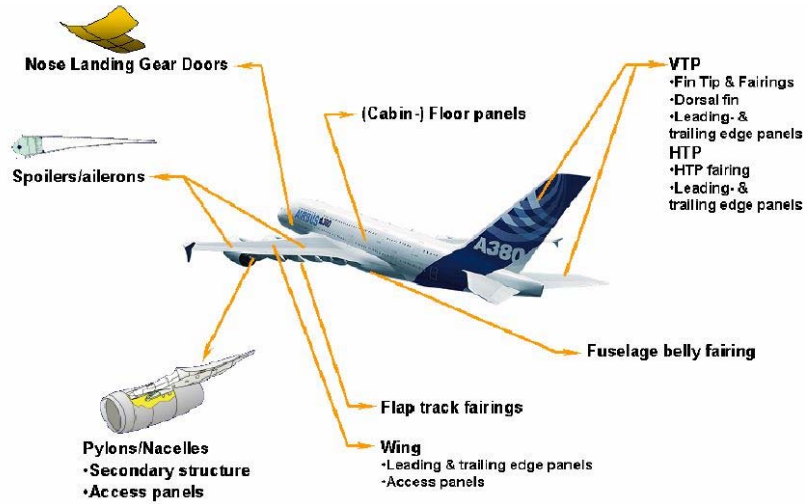
Figure 1.8. Sandwich applications at Airbus A380 [Herrmann et al., 2005]
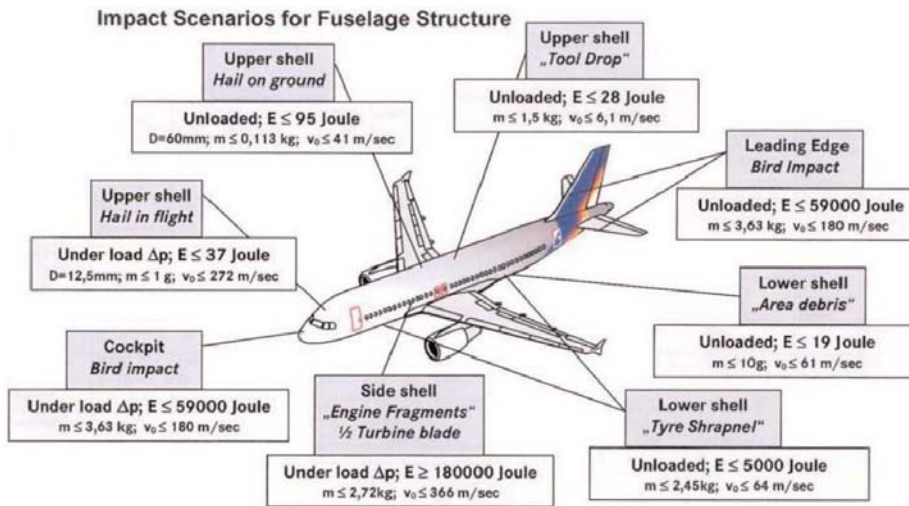
Figure 1.9. Possible impact threats on commercial aircrafts [Neidigk, 2017]
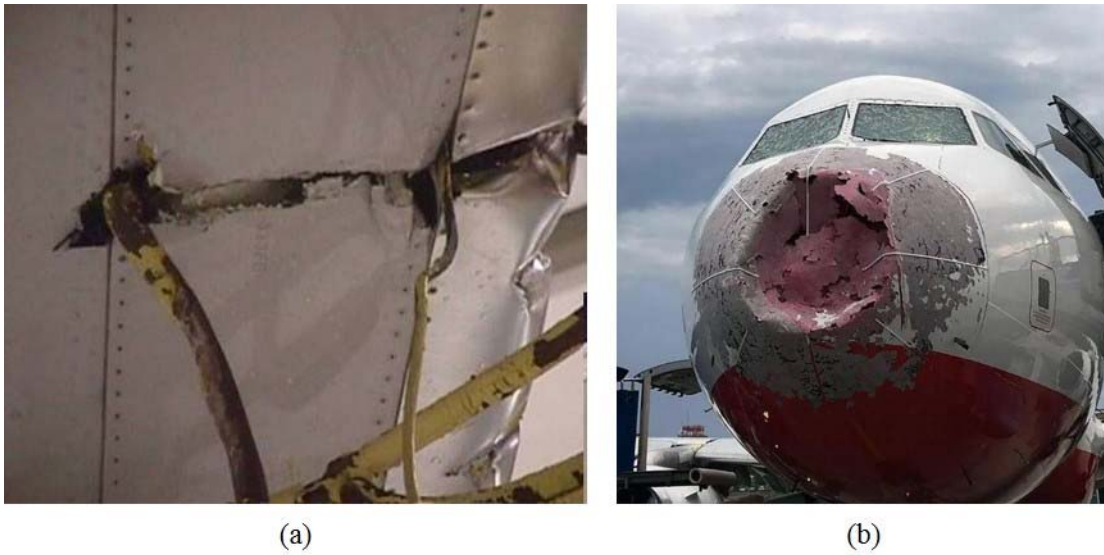
Figure 1.10. Examples of impact damage: (a) Wing skin and spar damage due to ground handling equipment [Fawcett and Oakes, 2007], (b) Hail strike on radome of Atlas Global Airbus A320 [Webb, 2017]
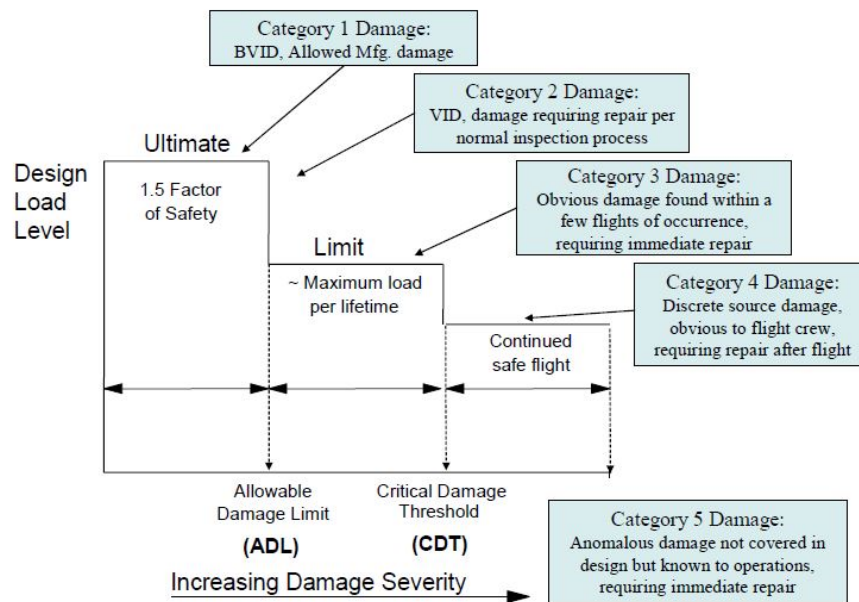
Figure 1.11. Schematic diagram of design load levels with respect to damage severity [U.S. Department of Transportation, Federal Aviation Administration, 2009]

Figure 1.12. Side view of vertical tail plane and residuals of rudder of Airbus A310-308 aircraft

after Air Transat Flight 961 [Transportation Safety Board of Canada, 2005]
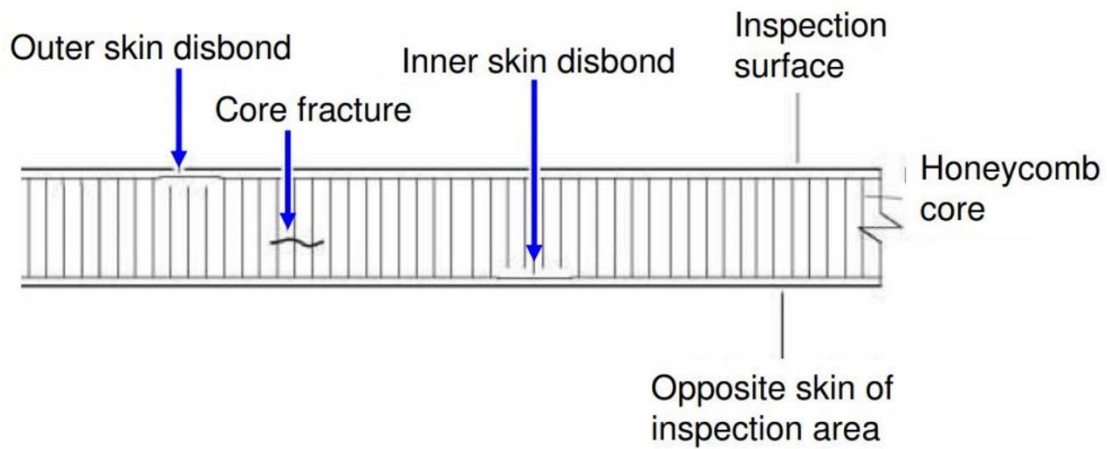
Figure 1.13. Schematic of pre-existing damage on Air Transat Flight 961 A310-308 aircraft

[Thévenin, 2007]
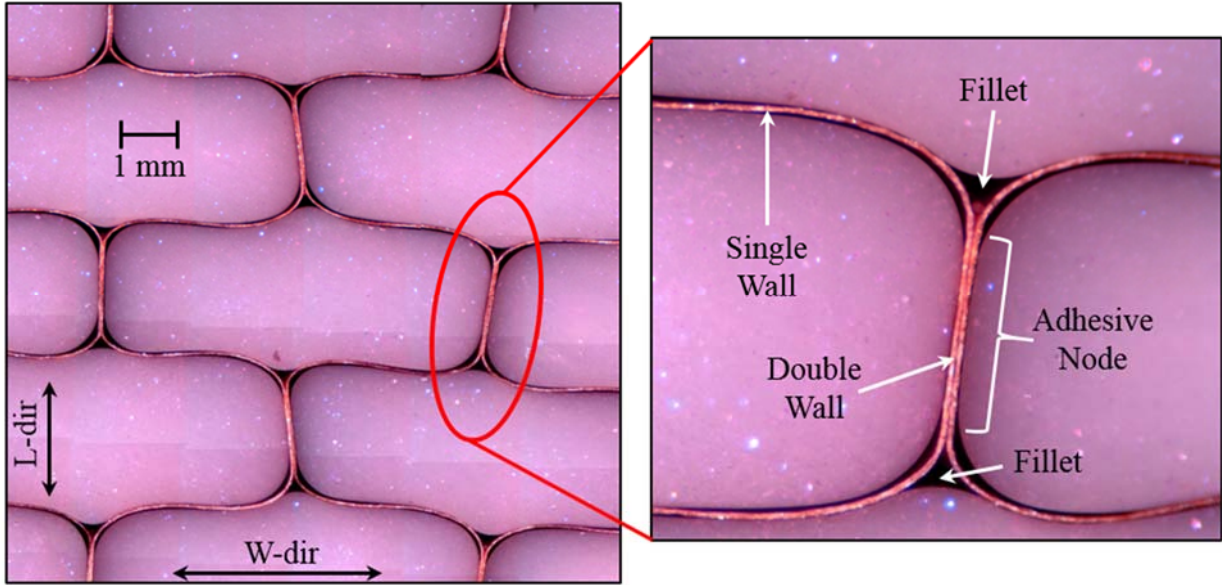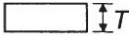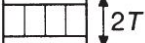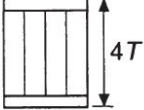
Figure 1.14. Microscopy on Nomex® over-expanded (OX) honeycomb core sample

Table 1.1. Sandwich construction efficiency [Bitzer, 1997]

	T	$2T$	$4T$
Relative stiffness	1	7	37
Deflection (in.)	1.000	0.140	0.027
Relative bending strength	1	3	7
Weight (psf)	0.910	0.978	0.994

Assumes 0.064 in. (1.626 mm) aluminum, 3.0 pcf (48 kg/m^3) core, 0.03 psf (1.4 N/m^2) adhesive.

Table 1.2. Comparison between honeycomb and foam cores [Bitzer, 1997]

Material	Density (pcf)	Compression		Shear	
		Strength (psi)	Modulus (ksi)	Strength (psi)	Modulus (ksi)
Aluminum honeycomb	3.1	300	75	210	45
Nomex honeycomb	3.0	325	20	175	6
Fiberglass honeycomb	3.0	410	23	195	19
Rohacell foam	3.1	128	10	114	3
Klegecell foam	3.0	69	2.7	51	1.1
Rigicell foam	3.0	80	2.5	70	2.5
Divinycell foam	3.1	100	10.2	73	2.5

1 ksi = 1000 psi.

CHAPTER 2: EXPERIMENTS

2.1 OVERVIEW

High energy simulated hail ice tests were conducted on flat sandwich panels consisted of carbon fiber epoxy skins and Nomex® paper over-expanded honeycomb core. The sandwich panels were tested at the gas gun facility located at Sho Funai Impact Research Facility at UC San Diego. The angle of attack defined as the angle between the hail projectile trajectory and the sandwich plane orientation was equal to 10° degrees. The chosen oblique angle of attack is representative of hail strikes on fuselage crowns and leading edges of airfoils during flight. Higher angles of attack accompanied by lower hail velocities are more common for ground hail impacts. The angle of attack is governed by the velocity of the aircraft and hail as well as the geometric angle of the targeted structural component.

The scope of this benchmark study is to address the issue of low external damage visibility after gas gun testing. Since hail ice tends to slide along the target at this low angle regime, the possibility of negligible exterior damage increases. After testing, residual dent profiles were measured and then the targets were sectioned close to the initial contact region to assess any core damage. Two gas gun tests at different energy levels were successfully conducted. Post-test sectioning revealed significant core crushing, and its extent was captured. Skin damage assessment was evaluated based upon existence of scratches, cracks, as well as residual dent profiles. Non-destructive evaluation techniques such as C-scan ultrasounds on impacted composite skins are commonly used to assess possible delaminations and matrix cracking. For this study, these techniques were not employed because the composite skins of the sandwich panels had already exhibited relatively large voids prior to testing.

Impact tests that involve the interaction of a brittle projectile with a composite laminated skin and a honeycomb sandwich core underneath are by nature complicated. Since the sandwich Nomex® honeycombs exhibited significant damage during the gas gun tests, the resistance of this type of cores under-out-of-plane loading conditions needs to be characterized. To this end, a phenomenological investigation of the crushing phenomena was established on Nomex® honeycomb core samples that were tested under out-of-plane flatwise compression. These tests were run at a quasi-static rate to visually capture the sequence of failure modes that ultimately led to core crushing. The planar dimensions of the sandwich core coupons varied to check if there are any free edge effects on the response. Finally, comparison between crushed and nearly-crushed specimens revealed the contribution of the resin-rich accumulation zones on cell wall collapse mechanism.

2.2   PREVIOUS WORK ON SANDWICH PANEL IMPACTS

Impacts on either monolithic or sandwich structures can be classified into two main categories, namely low and high-velocity impacts. Low-velocity impacts are mostly representative of impact events on aircrafts not in operation including tool drop or collisions with ground service equipment. Abrate provided a comprehensive review on the contact laws associated to a rigid indentor and identified five different failure modes in respect to low-velocity impacts [Abrate, 1997]. These failure modes are core buckling, delamination on the impacted face, core cracking, matrix cracking and fiber breakage. A more recently published review covered topics such as contact laws, sandwich plate response using analytical and finite element methods, impact influence parameters and finally different damage mechanisms [Chai and Zhu, 2011]. A detailed study on the transverse localized resistance of both monolithic and sandwich elements using both static indentation and low-velocity tests was performed [Lagace et al., 1993]. Impacts on sandwich

panels with different core configurations indicated that aramid paper cores exhibited higher impact resistance compared to aluminum cores [Dear et al., 2005]. The effect of impactor mass has been investigated and test results revealed that the impacted face damage size is more dependent on the kinetic energy rather the mass or velocity of the impactor itself [Robinson and Davies, 1992]. Flat Nomex® core sandwich panels representative of fan cowl door systems were impacted by a drop-weight tower at energy levels ranging from 5 to 20 J, but other than post-test C-scanning and residual dent depth measurements on the impacted skin, the core crushing extent was not investigated [Meo et al., 2005]. On a similar impact study, Nomex® sandwich panels were fabricated by directly co-curing the skins to the core without any adhesive film, a process that led to extra resin pooling down to the bottom skin resulting in uneven distribution of the meniscus-type of fillets [Anderson and Mandenci, 2000]. Thorough static and low-velocity indentation studies on Nomex® sandwich panels ranging from 4-ply up to 48-ply skins revealed that the load threshold at which major load drop occurs highly depends on the applied impact rate [Herup and Palazotto, 1998]. An empirical relationship between the input kinetic energy and the absorbed energy was established for different skin and Nomex® core configurations [Foo, 2013]. Core damage span and depth on lightweight sandwich panels as a function of input kinetic energy have been reported [Chan, 2014]. Similar impact studies have been performed on aluminum sandwich panels and core crushing failure takes the form of plastic folding [Hazizan and Cantwell, 2003, Zhou et al., 2006, Foo et al., 2008]. Low-velocity impact tests at glancing angles indicated that damaged area was decreasing for less normal to impacted face impacts [Iváñez et al., 2015].

High-velocity impact studies are not as extensive mainly due to the complexity of the required experimental apparatus. Ballistic impacts are associated to full penetration; thus, they do not generally fall under the high-velocity group. Even though literature on this topic is limited,

most of it focuses on hail-ice impacts. For simulated hail diameters ranging from 25.4 mm to 50.8 mm, Kim et al. identified five different damage modes on impacted monolithic panels, namely delamination, backside fiber failure, through-thickness cracks, extensive through-thickness cracks and clean hole penetration [Kim et al., 2003]. Ultrasonic C-scans were employed after impact testing to quantify failure threshold energies [Rhymer et al, 2012]. Similar impact studies were followed by compression after impact tests to assess residual strength of impacted panels [Appleby-Thomas et al., 2011].

Damage progression of hail spheres on rigid platen has been captured using high-speed cameras [Asp and Juntikka, 2009]. Simulated hail ice has been modelled using two approaches. Kim and Kedward employed an elastic-plastic with failure continuum-based material model [Kim et al., 2003]. Their model was calibrated based upon some experimentally measured ice impact force histories on titanium platen. On the other hand, ice balls have been modeled using smooth particle hydrodynamics to capture fragmentation process in a more realistic manner [Olsson et al., 2013]. Compression after impact virtual experiments on impacted sandwich panels was modelled using a modified cohesive crack surface formulation [Das et al., 2009].

Lastly, a thorough experimental study that involved high-velocity impacts on lightweight Nomex® sandwich panels used in control surfaces revealed significant core damage extent accompanied by low external visibility [Luong, 2014].

2.3   GAS GUN SIMULATED HAIL ICE TESTS

2.3.1   Gas Gun Test Apparatus

The test apparatus of the gas gun facility at UC San Diego consists of a 3.0 m barrel with

inner bore diameter of 79 mm and a breech that allows projectile launches as shown in Figure 2.1. The gas gun is operated by a pressurized tank filled with either nitrogen or helium gas. Installed pressure gauge track the line pressure. Once the tank pressure reached a certain level, a helium gas pressure-operated ball valve was triggered, and the contained gas was released to the launched projectile. The projectiles, in our case the hail spheres, were placed into a polyurethane sabot cylinder which precisely fits the inner diameter of the barrel. Details on the fabrication of the hail spheres and the sabots are given in the following section. At the end of the barrel, the gas gun is equipped with a steel stop plate with a circular hole to allow separation of the hail projectile from the sabot as shown in Figure 2.2.

The released hail projectiles traveled through a measuring velocity chamber consisted of two laser beams spaced at 127.5 mm distance and connected to two different photogate systems as shown in Figure 2.3. When each of the laser beams was interrupted by the hail projectile, a sharp step-wise voltage change on the photogate system occurred. Both photogate voltage signals were connected to a digital oscilloscope and the velocity of the projectile was finally obtained by calculating the time between the occurrence of abrupt signal rises in a way like Figure 2.4.

At the other end of the apparatus, a supporting fixture primarily made of 80/20® Inc. aluminum profiles, hosts the targeted specimens. This fixture can be pivoted so that impacts at glancing angles can be conducted, allowing for impacts at very low angles of attack as well as totally normal to plane of the target. Figure 2.5 demonstrates a schematic view of the supporting fixture and three different orientations [Luong, 2014]. Given the size of the barrel and the allowable maximum tank pressure, hailstone projectiles of 50.8 mm diameter can travel up to 200 m/s.

2.3.2 Preparation of Simulated Hail Ice

Hailstones are formed during strong updraft wings when irregular raindrops grow by accumulatively collecting droplets below freezing point. Typical metrics of hail diameter and corresponding falling speeds are shown in Figure 2.6. The falling speeds refer to terminal speeds in the ground and the boundaries of the gray shaded region represent the upper and lower limits of the analytical relationship among speed, size and drag coefficient. Figure 2.7 shows typical hailstones which are generally amorphous and have an onion-like shape as a result of the accumulation of frozen raindrops. In laboratory environment, it is hard to test real hailstones, thus an idealization of the shape and manufacturing method of simulated hail ice is needed. Aligned with this direction, ASTM F320-16 standard which is related to hail impact resistance of aerospace transparent enclosures, suggests the use of ice spheres with diameters 13, 25, 51 mm respectively for gas gun experimental studies [ASTM International, 2016].

Producing the hail ice projectiles for this study involves two steps, namely the fabrication of the split foam sabots and the spherical hailstones [Rhymer, 2012]. For the fabrication of split sabots, two-part FOAM-It™ polyurethane foam was poured into cylindrical steel molds with a 50.8 mm spherical cavity. After 2-hr curing cycles, the formed sabots were demolded and cut in half to improve its aerodynamic performance per ASTM F320-16 recommendation. It is important to highlight that the split sabot should not be very tough as impact of a relatively hard material on the stop plate creates secondary interactions with the hailstone inside and as result its trajectory deviates. So, a selection of polyurethane that can sustain its shape under the released pressure and easily crush upon impact with sabot stop plate as shown in Figure 2.8 is needed. After several trial impact tests on scrap pieces, FOAM-It™ 5 polyurethane foam with 80.1 kg/m^3 nominal density was selected.

Regarding the hail fabrication, a set of split molds with 50.4 mm diameter hemispherical cavities was utilized. The two halves were held together with a dowel and then C-clamped, after a light coating of petrolatum was applied on the inner flat surface to prevent any water leak as the cavities were filled with water. The top split mold had a small hole and water was filled through a syringe. The water was initially boiled to remove gas content. Once water overflowed the cavities, 6 g were finally removed from the cavities to account for volume increase as soon as the assembly is placed into the freezer for 8 hours. After 8 hours, the clamps and top split mold were carefully removed. The bottom split mold was placed into a basin of hot water until the hail sphere could freely detach from the hemispherical cavities. A visual inspection on the ice spheres was performed and those having a very smooth surface without any cracks were weighed and stored back into the freezer. The assembly of the simulated hail ice and the split polyurethane mold is shown in Figure 2.9.

2.3.3 Sandwich Panel Description

The tested sandwich panels were donated to UC San Diego and consisted of prepreg carbon fiber skins separated by a 25.4 mm thick over-expanded Nomex® honeycomb core. The design of these panels considered many parameters and loading conditions for sizing, among which impact damage resistance was one of the main aspects, leading to thicker laminate at the exposed surface. The chosen prepreg material system was 5320 T650-8HS, a system that allows curing of the resin under vacuum compaction. The core density was 64 kg/m^3, a value that is closer to heavyweight core classification for aerospace applications, and the cell size was 4.76 mm. Core wall geometry is similar to the one of Figure 1.14. For the gas gun tests, the sandwich panels were 1.0 m long in the impact direction and 0.3 m long in the transverse direction. The exterior skin was consisted of a thick laminate of 14 plies with a smooth layer of paint. The choice of a thicker exterior skin was

based upon impact resistance demands. Figure 2.10 shows the front view of a sandwich panel. The interior skin consisted of 4 plies. Both skins and the honeycomb core were co-cured together with the aid of adhesive films on the top and bottom. The interior skin was tapered down to the edge of the panel as illustrated in Figure 2.11, a common practice used in aerospace industry for bolting down sandwich elements into other structural parts. In Figure 2.11, the projectile direction coincides with the L-direction of the honeycomb core, or in other words the normal to the field of view.

2.3.4 Gas Gun Test Results

Even though the hail falling speed rarely exceeds 45 m/s, the resultant speed at which the hailstone impacts a structural component can be much higher when an aircraft is in flight. A combination of the falling speed and the relative aircraft speed along with the aircraft target geometric angle can provide an estimate of the total angle of attack. Hence, oblique angles of attack are representative of an in-flight impact in components such as the fuselage crown, the upper canopy, the upper part of the aircraft wing including the leading and trailing edges. Figure 2.12 shows the total angle of attack of the supporting fixture required to mimic a hail impact on a wing airfoil.

The angle of attack was chosen to be equal to 10° degrees. Figure 2.13 depicts the sandwich panel attached to the pivoting supporting fixture via C-clamps. Given the limited number of sandwich panels as well as the capacity of the gas gun, simulated hail ice was fired on the interior thinner side to make sure that core damage would be present. Two tests in total were conducted at nominal speeds of 85-90 m/s and 130-135 m/s respectively. The lower velocity regime illustrates the approach of a business or midsize range aircraft in the runaway, while the latter velocity regime

reflects speeds of descended aircrafts. Previous launches of 50.4 mm diameter hail stones at the gas gun have established a least square fitting curve relating tank pressure and recorded inbound projectile velocity. Tank pressures of 200 and 450 psi respectively were selected in order to meet the prescribed velocity regimes.

Few moments prior to testing, both the hail ice and the split sabot assembly were weighed. After testing, the input kinetic energy was measured based on the ice mass and the measured velocity. For the least severe test, the measured velocity and kinetic energies were equal to 93.9 m/s and 275 J respectively, while the higher tank pressure resulted in an inbound velocity of 136.3 m/s and 590 J kinetic energy. Each gas gun test was recorded by Phantom v7.3 highspeed camera. For the 275 J impact, a frame rate of 10,000 fps and exposure of 7 µs were applied to capture crisp still images. For the faster impact case, the frame rate was cranked up to 12,000 fps and the exposure was set to 4 µs. To meet those parameters, additional lighting in the form of halogen lamps was provided. The progression of 590 J impact test is shown in Figure 2.14. The panel was positioned in the supporting fixture such that the hail ice would first contact the "0 mm" marking. However, the projectile went slightly high and started cracking at about 10 mm forward from the origin as can be observed in the second snapshot of Figure 2.14. Based on the third snapshot, maximum dent was expected to occur between the "20 mm" and "40 mm" marking. After that footprint, the projectile got significantly fragmented, and it ended up sliding on the panel surface instead of denting as shown in the last snapshot of Figure 2.14.

Since scheduled inspection of an aircraft does not happen on a daily basis, residual dents were measured a week after the tests to account for material relaxation. For this purpose, a dent depth fixture equipped with an attached dial indicator was built and placed on a precision ground table as shown in Figure 2.15. Prior to testing, pristine surface measurements were taken at

intervals of 10 mm to create a baseline from which the post-test measurements were subtracted to calculate local dents. Measurements at a single location were repeated three times and the resulting dent profiles are summarized in Figure 2.16. We should note that the impacted skin corresponded to the vacuum bag side and not the tool plate side. Thus, the interior skin surface was rough as illustrated by the measured noise in Figure 2.16. For the 275 J impact, measurements did not reveal any damage on the impacted skin, while localized residual dent was measured at the span between "0 mm" and "50 mm" stations. That residual dent was not visually detectable either.

After dent measurements, the tested panels were destructively sectioned using a diamond blade tile saw to assess core damage extent. As illustrated in Figure 2.17, the ribbon direction coincided with the projectile direction. Core damage was accumulated on the side closer to the impacted face sheet and was consisted of excessive single and double wall kinking after phenolic resin coating locally fractured in a brittle way as shown in Figure 2.18. The core damage extent for 275 J impact was equal to 25 mm. In Figure 2.18c, cross-sectional cut along the expansion direction revealed that damage occurred in only one fillet column for the 275 J impact. The described damage mode was the same for both tests. However, wall kinking was more severe on the higher energy impact. Figure 2.19 shows that core damage spanned 80 mm along ribbon direction. On top of the significant core damage, delamination can also be visually observed in Figure 2.19c. The number of damaged cells along the transverse to impact direction also increased as seen in Figure 2.19d.

The benchmark impact studies presented herein revealed significant core damage with no external visibility and minor residual dent profile for the stronger impact test case. The complexity of those impact tests including the oblique angle of attack, the dynamic nature of the hail ice, the local indentation as well as the enclosure of the honeycomb core by the composite skins does not

allow for direct assessment of core damage mechanisms under out-of-plane loads. A phenomenological investigation of the out-of-plane failure phenomena taking place on Nomex® cores needs to be established as a first step towards characterization of damage formation. This investigation is a necessary procedure for newly developed material systems that are to be used for performance critical applications. To this end, flatwise compression tests on small coupons are utilized in the subsequent sections due to their overall simplicity and the number of influencing parameters.

2.4   PREVIOUS WORK ON OUT-OF-PLANE FLATWISE COMPRESSION TESTS ON NON-METALLIC HONEYCOMB CORES

Since the primary function of honeycomb cores are to carry shear and normal forces, flatwise compression tests are used to characterize their out-of-plane structural behavior. Honeycomb core manufacturers provide effective modulus and strength data for cores with specific geometric features, but statistical variability is a major concern [Daggett and Fuller, 2016]. Zhang and Ashby examined the out-of-plane behavior of non-metallic honeycomb cores and reported that it is elastic until fracture suddenly occurs in the honeycomb cell walls leading to loss of load carrying capacity [Zhang and Ashby, 1992]. After loss of load carrying capacity, the core enters a crushing plateau in which the walls exhibit successive folding at a constant effective stress level. This crushing plateau is followed by the densification zone as soon as fractured walls start interacting with neighboring walls as a result of volume change. A schematic view of the overall out-of-plane response is shown in Figure 2.20.

In regard to the buckling and post-buckling behavior of cellular structure, an analogy between the vertices of a honeycomb cell and a stiffened flat panel was first drawn [Castanié et

al., 2008]. To further understand the collapse mechanisms of cellular structures, Aminanda et al. manufactured larger size cells made of drawing paper and demonstrated the failure deformation which was dominated by successive core wall angle folding after the initial elastic buckling of the walls [Aminanda et al., 2005].

Crushing tests on bare Nomex® cores and cores bonded to composite skins revealed a substantial increase in compressive effective strength and modulus for stabilized coupons due to the constraints imposed by the bonded skins [Othman and Barton, 2008]. Numerical and similar experimental studies on sandwich panels were conducted and then modeled using idealized cell wall geometry [Giglio et al., 2012]. Out-of-plane core crushing tests at different size Nomex® core coupons showed a reduction of effective modulus as the number of cells increased [Foo et al., 2007]. The cyclic response of Nomex® cores within the compression regime showed significant hysteresis loop when unloading occurred at the crushing plateau as a result of excessive local fracture and wall folding [Liu et al., 2015]. Finally, Heimbs et al. posed the question of possible reinforcement effects of the meniscus-shaped resin fillets created during curing process of the skin prepregs but the out-of-plane stiffness of the Nomex® core was not significantly altered [Heimbs 2006].

On a dynamic characterization study, Heimbs reported a 15% increase on the effective strength of over-expanded phenolic-impregnated aramid paper cores tested at 300 s^{-1} strain rate levels [Heimbs et al., 2007]. Similarly, Zinno et al. determined a 1.2 increase factor for 200 s^{-1} strain rates [Zinno et al., 2011].

Most of the experimental studies summarized herein, have characterized the out-of-plane behavior of non-metallic cores all the way up to densification, in which the cellular structure has

already been completely distorted. In reality, the core should be considered damaged by the time the core falls into the crushing plateau. In this sense, the area of interest should be geared towards the peak response and the crushing onset instead. The experimental studies presented in the next section aim to provide a more detailed description of the behavior of Nomex® cores within the aforementioned range and also highlight the possible effects of the phenolic resin accumulation at the cell wall junctions.

2.5   FLATWISE COMPRESSION TESTS ON NOMEX® PAPER HONEYCOMB CORES

2.5.1   Experimental Setup and Specimen Preparation for Flatwise Compression Tests

Quasi-static tests provide the capability to directly observe damage initiation and progression in a controllable manner. Sandwich coupons used for this experimental activity were cut out from the same batch of prefabricated development aircraft skin sandwich panels used for the gas gun tests. To prevent premature core failure and localized crushing at the free edges, the composite skins were not removed. The core configuration leaned towards the heavy-weight side as the nominal mass density of the core was 64 kg/m^3. The nominal thickness of Nomex® paper sheets was equal to 0.05 mm. To increase cell stability, paper walls are impregnated with phenolic resin giving a brownish-red color to the final product. Since the core had over-expanded pattern, the spacing of the cells is different on the L and W directions. Over-expanded configuration is typically preferred over hexagonal pattern for curved structural elements because of the significantly reduced anticlastic response when flexed. The cellular geometry of a typical core coupon used for the flatwise quasi-static tests is shown in Figure 2.21. In this figure, the resin-rich vertical accumulations of resin exhibit a dark brown color. In general, the darker the color of the

honeycomb cell, the larger the amount of phenolic resin coating locally is. Figure 2.22 identifies the key elements of the honeycomb core meso-structure as a result of the expansion and dipping process explained in Chapter 1. The phenolic resin dipping process is repeated as many times until a global nominal density is met. However, it will be shown that despite this criterion, resin distribution may significantly vary among the sandwich panels with the same nominal core density. Double walls are effectively formed when two adjacent paper sheets are glued together with adhesive nodes. Due to resin impregnation, the honeycomb walls basically become thin composite plates subjected to membrane loads.

The core coupons were cut out using a tile saw with diamond blade and polished with diamond polishing pads to remove fuzzy edges. The free edge walls were slightly distorted because of the saw cut but ultimately did not affect interior cell wall behavior. For some core coupons, Accutom-5 cutoff machine with 0.4 mm thick diamond blade shown in Figure 2.23 was utilized for high precision sizing.

The quasi-static tests were performed using servo-hydraulic testing system MTS 810. The system is equipped with 100 kN load cell. Two supporting fixture configurations were utilized. In the first configuration, two compression platens were machined and held by the wedge grips of the load frame. The bottom compression platen of Figure 2.24 is attached to the load frame actuator. Any source of misalignment arising from load frame or the tested core coupon was not accommodated with this configuration. Misalignment issues were assessed based upon initial transition slope on the load-displacement curves of tested core coupons, and the affected ones were not further post-processed. A self-aligning fixture was later developed to minimize those effects. Two hemispherical caps separated fitted into a stainless-steel sphere were assembled on the lower compression platen to allow adjustment of the bottom loading face and facilitate uniform core

crushing in case of minor initial misalignment. Once the position of the rotating top cap was set, lock screws touching the bottom cap ensured the same orientation of the loading face during testing. This self-aligning feature was necessary for testing of larger size core coupons, where the chances of minor misalignments are generally greater. Both fixture configurations are shown in Figure 2.24.

The out-of-plane tests were run in displacement control at 0.50 mm/min displacement rate. During early stages of test plan, displacement rates up to 5 mm/min were chosen, but the sequence of failure phenomena was not properly captured given the frame rate of the digital camcorder. However, force-displacement data were consistent and for this reason they are included herein. Most of the tests were run monotonically until the onset of the crushing plateau, but some of them were loaded and unloaded at earlier stages in order to visually assess different damage features after testing. The total number of tests conducted for this experimental study was equal to 58 after eliminating the vastly inconsistent ones. Once again, the primary focus on this study is to investigate the key governing parameters of failure initiation.

2.5.2 Features of Nomex® Sandwich Core Coupons

The sandwich core coupons used for flatwise compression were extracted from four different prefabricated aircraft design sandwich panels with the same type of Nomex® core. Testing core coupons from four different panels allowed further examination of possible discrepancies in their mechanical response. Different size core coupons were cut and tested to assess the effect of number of cells on the overall response. Table 2.1 summarizes the nominal dimensions of the core samples and the number of cells along each direction. Table 2.2 displays the number and sizing of core coupons per each prefabricated sandwich panel.

34

Since the precise honeycomb cell geometry was initially unknown, a representative sandwich coupon was sectioned through the core. Buehler SamplKwick acrylic resin system was casted in the open-faced core to avoid any fuzzy edges attributed to the fibrous nature of Nomex® paper. After resin cure, samples were sectioned in high-precision cutoff machine to create a sharp and clean cross-section that was later taken into optical microscope as shown in Figure 2.25. This image was a tile-up of multiple images taken after the casted sample was placed on XY microscope stage. This figure illustrates that the phenolic resin coating is not saturated with the Nomex® paper surface, but two distinct layers are formed with a small joint interface instead. Since that is the case, volume fractions of each constituent relative to the net core area were obtained through basic image processing within MATLAB environment.

The first step on segmenting the microscopy image was to apply a K-means clustering scheme commercially available in MATLAB to effectively create three clusters of pixel data corresponding to the different elements of the meso-structure, namely the voids, paper and phenolic resin. The K-means clustering is an iterative procedure that allows image segmentation in predefined number of clusters based on a least square minimization of the continuously updated mean intensity of each cluster and the color intensity of each pixel within each loop. Figure 2.26 shows the segmentation of the pristine image after the K-means algorithm was applied. For this particular microscopy image, the paper walls occupied 2.5% of the total planar area while the phenolic portion came out to be 3.0% in total from which 0.5% was occupied by the fillets. To quantify paper thickness which was nominally equal to 0.05 mm, a flood-fill algorithm was applied on the segmented image to calculate the double wall thickness. The double wall thickness came out equal to 90 μm and as a result the single wall thickness was equal to 45 μm. Finally, the cells spanned roughly 7 and 3 mm in the expansion and ribbon directions respectively.

2.5.3 Phenomenological Investigation of Damage Modes on Nomex® Paper Core Coupons Subjected to Flatwise Compression

In this section, the sequence of failure mechanisms of Nomex® core under uniform compression is presented in detail. For most tests, the applied displacement rate was 0.5 mm/min for observation of the damage progression. The force recording was divided by the total planar area of the sandwich specimen to obtain an effective stress. The crosshead displacement sensor encapsulated within the moving actuator was used to measure its position during the test. In order to make sure that the displacement readings from this sensor were accurate, a direct comparison with a non-contact laser extensometer locally measuring the distance between the two compression platens was performed as shown in Figure 2.27. From this figure, both displacement channels have similar history, and we ultimately relied on the crosshead sensor because the signal was less noisy. Effective out-of-plane strain was determined after normalizing the displacement history by the nominal core thickness of 25.4 mm. This normalization may not be very accurate since the adhesive film slightly reduces the free gage thickness. A gap between the surface of the sandwich core coupon and top compression platen was present at the start of each test in order to capture the initial toe region. For consistency, each plot was then shifted along the effective strain axis based upon linear regression of the elastic portion of the curve as shown in Figure 2.28. The effective normal stress versus effective strain plots are shown in Figure 2.29 for specimens of sizing category V extracted from the four different panels.

A more detailed description of the sequence of failure events of an entire loading-unloading cycle is depicted in Figure 2.30 in conjunction with Figure 2.31. The camera video and data acquisition files were synchronized through a LED screen in the background that displayed the load cell reading straight out of the load frame controller. The snapshots shown in Figure 2.31

coincide with the distinct points of the loading/unloading plotted line of Figure 2.30. The sequence of phenomenological observations on the tested coupon CCB-023 is summarized below:

i. <u>Undeformed configuration</u>: Cell walls exhibited manufacturing imperfections and possible perturbations due to co-curing process.

ii. <u>Initial axially dominated behavior</u>: Due to initial gap between the compression platen and the top face, there is initially a transition toe zone until full contact is established. Beyond this transition, the cell walls acted as membrane members subjected to axial displacements.

iii. <u>Initial single cell wall buckling</u>: The geometric imperfections triggered buckling and post-buckling of single cell walls which were the weakest links in this complex geometry (point A of Figure 2.30 and Figure 2.31a). Core structure was still in the linear elastic region possibly because not all the single walls started buckling at the same time. The post-buckling behavior was detectable by the different reflections of light in Figure 2.31b. For this particular case, concentrated light contours could be observed at ~20% of peak load.

iv. <u>Extension of cell wall buckling</u>: Cell wall buckling proceeded to multiple single walls. Nonlinear relationship between load and displacement started to be present at around 2.20 MPa, as shown by decreasing stiffness beyond point A in Figure 2.30. For smaller coupons falling into categories I and II, the deviation from linear behavior occurred when the outer walls with the free edges exhibited buckling.

v. <u>Edge wall fracture</u>: At about 2.40 MPa, a pop sound on the camera video revealed onset of brittle fracture of the phenolic resin coating of the outer double walls due to the

37

unsupported edges.

vi. <u>Buckling of double cell walls</u>: On the nonlinear regime and before peak response, double walls experienced buckling and post-buckling behavior as observed at a different test in which the video camcorder was shifted towards the L-direction of the core coupon. Figure 2.32 supplements this argument by comparing light reflections on the L-direction face at two different time instances, namely the start of the test and about 90% of the peak load resistance. The response acted more nonlinear, but residual deformed core shape was almost recoverable upon unloading. By the time of visual double wall buckling, some light pop sounds indicate that inner single walls had locally fractured under tension due to post-buckling induced moments.

vii. <u>Detachment of resin fillets from single walls</u>: After visual post-buckling of double walls and approaching point B of the curve in Figure 2.30, resin fillet columns started local detachment from the single wall region possibly as a result of mode-I and mode-II loading at the interface. Immediately after the local detachment, the resin fillets fractured at the disbonded region due to the free unsupported span. This rupture triggers kinking on the surrounding double wall region as well. At peak recorded load (point B of Figure 2.30 and Figure 2.31b), local failure of fillets and double walls had propagated to multiple cells. The sequence of events described in this stage last about 1 s for the 0.5 mm/min loading rate.

viii. <u>Propagation of crushing phenomena:</u> Beyond point B, damage had expanded to a critical number of cells, and progressive collapse of the honeycomb structure eventually occurred. Referring to point C of Figure 2.30, further opening cracks between the fillet and the single walls can be observed in light yellow color in Figure

38

2.31c. Cell wall folding in the form of kinks was also evident in Figure 2.31c.

ix. <u>Residual damage</u>: Damage was accumulated on the fractured points highlighted in Figure 2.31d. The crushed core recovered most of its pristine shape at the undamaged regions. Buckled walls during maximum applied displacement became nearly straight (point D in Figure 2.30 and image in Figure 2.31d). However, detailed metrics of the residual deformation of the cell walls should be established to assess the condition of the core coupon after testing. The ribbon and expansion faces of the damaged core in Figure 2.33 revealed permanent detachment of the fillets from the surrounding structure as well as post-buckling induced fracture at the single and double walls.

To further understand the triggering collapse mechanism, we directly compared the monotonic response described above with a special case of cyclic test in which loading and unloading occurred before the peak threshold value. In total, 6 different cyclic tests were conducted. The two plots are very similar during the up-loading stage, with small discrepancies attributed to geometric irregularities. Specimen CCB-23 was loaded monotonically significantly beyond core failure before unloading. Having the full crushing load-displacement curve of specimen CCB-23, specimen CCB-24 was loaded and unloaded just prior to peak (black line in Figure 2.34). Two cycles were applied in this manner, and the residual deformation was negligible indicating no accumulated damage as observed in Figure 2.34. After testing, microscopy photos were taken from both specimens. Phenolic resin fillet detachment and fracture were clearly observable in the damaged specimen as shown in the left snapshot of Figure 2.35. On the contrary, an initial longitudinal crack at the interface between the fillet and the single wall was visible indicating the onset of detachment in Figure 2.35b. At this stage, the core barely reached its load carrying capacity illustrating in this way that local fillet fracture extended to a few cells is the key

collapse mechanism.

For a test case of sizing category V, the damaged core that was compressed until the onset of crushing stage, was casted into a pool of acrylic resin and was then sectioned into high precision saw to assess damage modes. Figure 2.36 shows a comparison between a non-damaged and damaged junction. We can observe major cracking in the phenolic resin coating along the major axis of the single wall plate. In addition to that, there is clear indication of fillet detachment from the single walls shown in light blue circle, a fact that validates the assumptions drawn during testing.

A summary of all 58 flatwise compression tests is given in Table 2.3. In this table, only the coupons that exhibited damage on all 4 edges are included. Aside from the geometric features of each core coupon, the effective out-of-plane modulus and peak effective strength are also reported. Regarding the homogenized modulus, a linear regression on the elastic portion was performed on each set of data. The selected limits of the linear portion of the curve were the limits at which the first derivative of the force displacement was smooth and nearly constant after a low pass-filter was applied. The peak effective strength reflects the limit peak load normalized by the planar area. Figure 2.37 shows that the effective homogenized modulus decreases as the core coupon size increases for coupons extracted from the same sandwich panel. This trend can be attributed to possible non-uniform compression of the entire surface at the beginning of testing despite the existence of the self-aligning fixture. As a result, not all the cell walls were exhibiting the same amount of straining. Regarding the homogenized modulus among different panels, the average of the homogenized core moduli all differed from panel to panel. More specifically, the average modulus of panel -061 is 18% higher than the average modulus of panel -035.

In a similar manner, Figure 2.38 demonstrates the corresponding variation of peak effective strength which is not dependent on the sandwich core size as a result of load redistribution after initial kinking of single walls. The number of fractured cells that would lead to ultimate collapse increases for increasing sizing category, thus peak effective strength remains at the same levels. Regarding variation among different panels, the average strength on panel -061 came out to be 17% larger compared to the -056 sandwich panel coupons. As a final remark, Figure 2.39 depicts four different sandwich coupons from the four sandwich panels. The discrepancies among different panels could be a result of different distribution of phenolic resin coating.

In conclusion, since single cell wall buckling was initiated well before peak load, resin rich parts along with the neighboring double walls significantly contributed to the stability of the whole system. Unlike aluminum cores where plastic folding is the dominant failure mode, Nomex® cores behaved in more brittle manner during the crushing stage. Based on this experimental investigation, it can be concluded that the intersection of the double and single walls, where resin fillets are formed, behaves like a stiffened region. In terms of core damage assessment, the observed fillet detachment and rupture is a sufficient condition for the establishment of a local qualitative failure threshold metric.

Since efforts have been made to simulate damage in phenolic resin impregnated Nomex® cores using detailed numerical models, these stiffened regions should be accounted for as they affect the peak load, damage onset and evolution. Further studies on the effect of phenolic resin fillets on the out-of-plane response will be presented in the finite element simulation chapter.

Parts of Chapter 2 are a reprint of the material that appears in the conference paper "Phenomenological Investigation of Nomex® Core Damage Mechanics in Honeycomb Sandwich

Panels under Transverse Impact and Quasi-Static Loading", 2016, (with H. Kim) which was submitted in the 31st Annual ASC Technical Conference in Virginia. The author of this dissertation was the primary investigator and author of this manuscript.
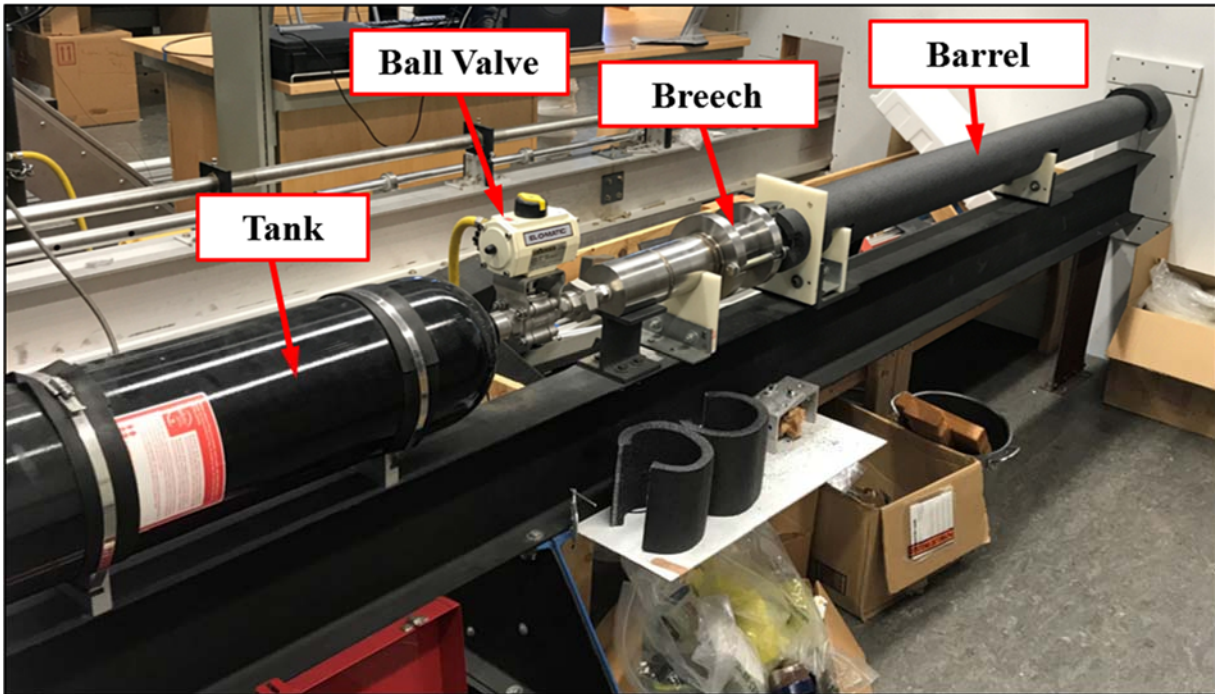
Figure 2.1. Snapshot of gas gun apparatus at UC San Diego
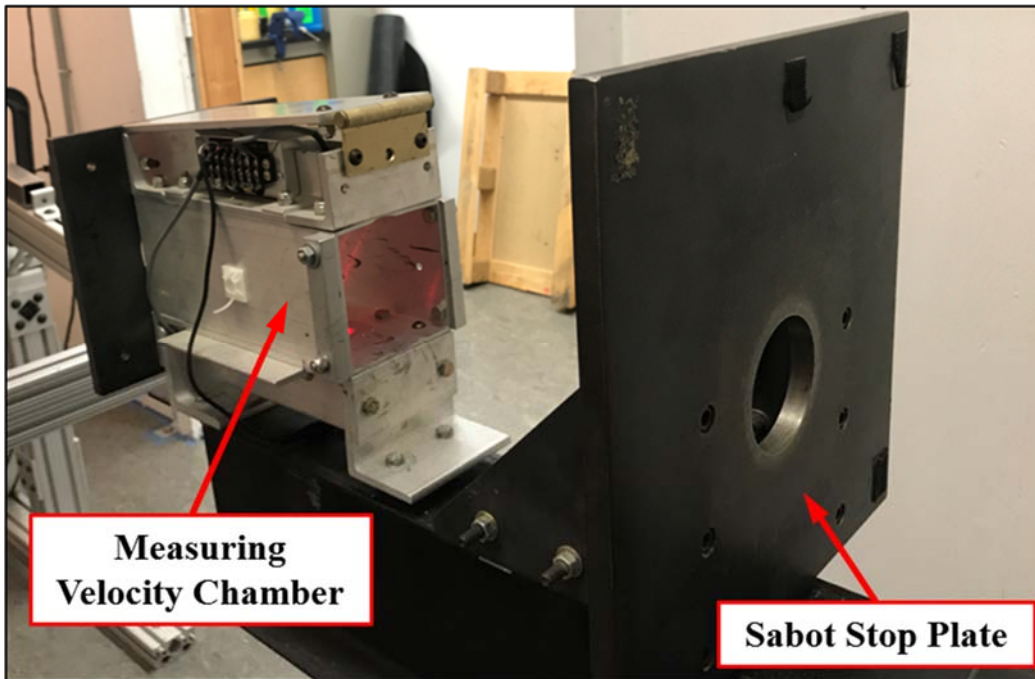
Figure 2.2. Sabot stop plate and measuring velocity chamber after projectile exits barrel
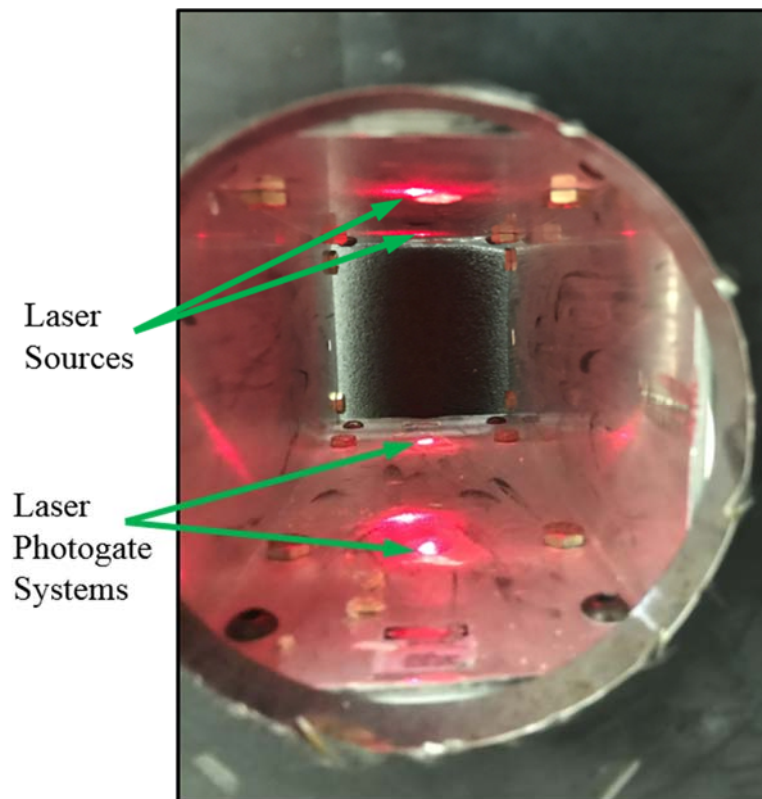
Figure 2.3. Sequence of laser photogate systems for inbound velocity calculations
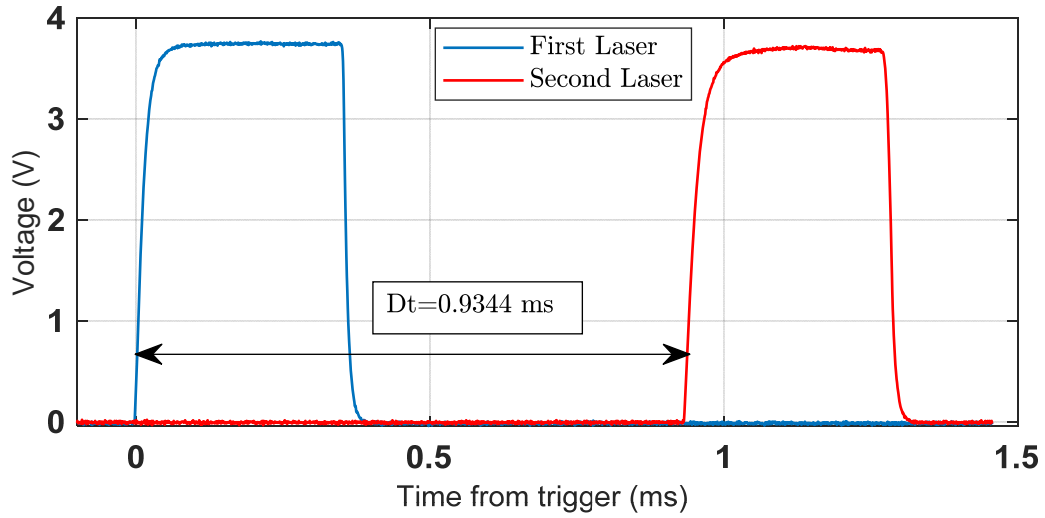
Figure 2.4. Signals of laser photogate systems during projectile interference
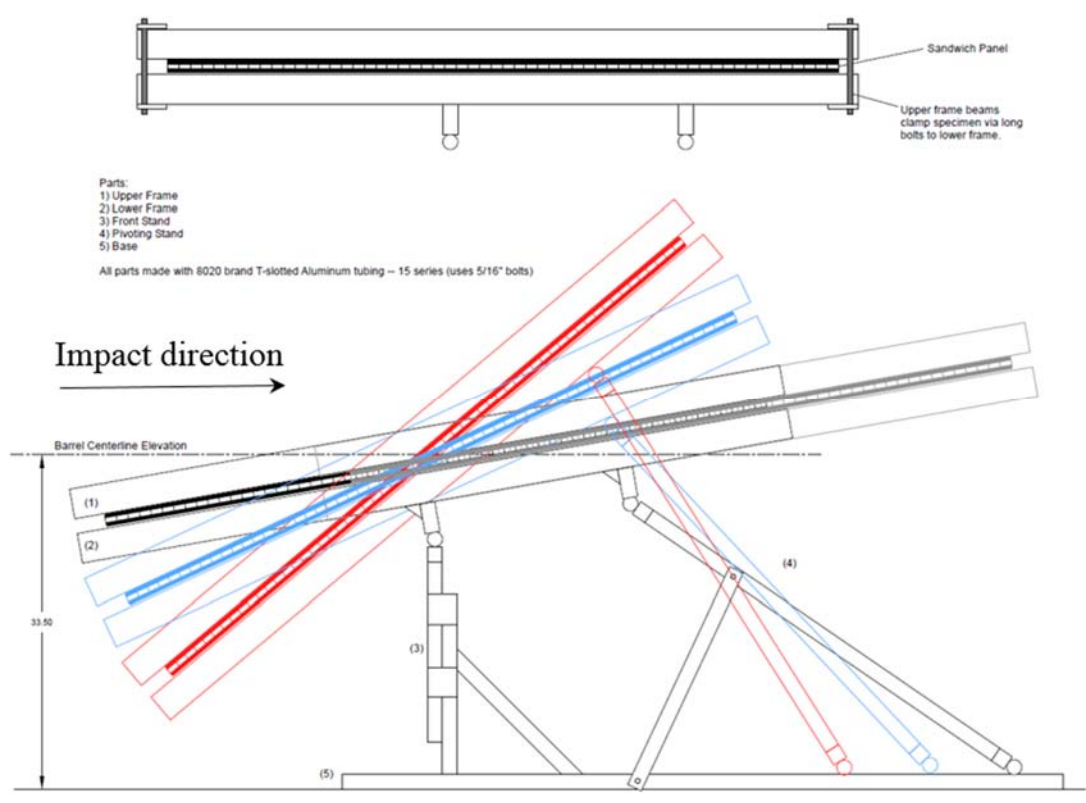
Figure 2.5. Schematic of gas gun supporting fixture [Luong, 2014]
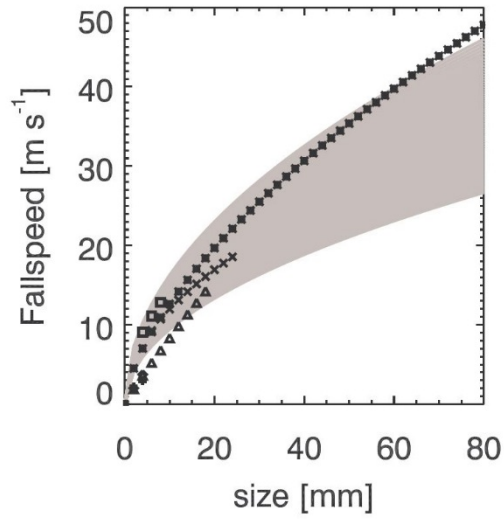
Figure 2.6. Hail falling speed as a function of its diameter [European Aviation Safety Agency, 2009]

Figure 2.7. Reported hailstones in amorphous shape [Olsson et al., 2012]
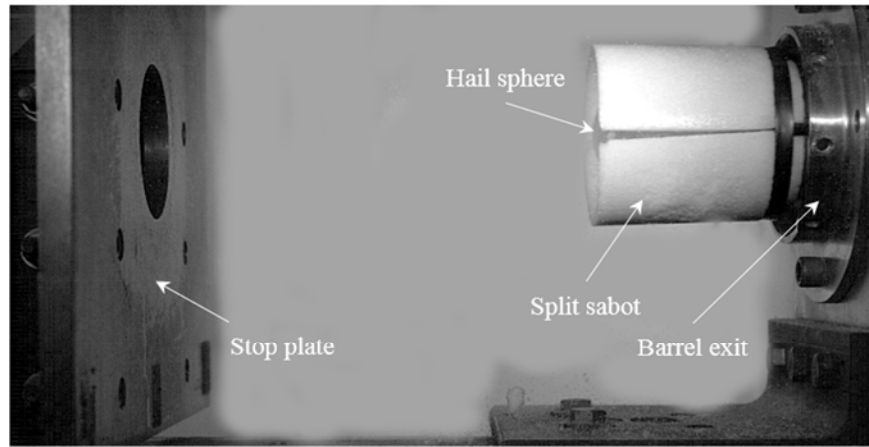
Figure 2.8. Split sabot: (a) After barrel exit; (b) During impact with stop plate
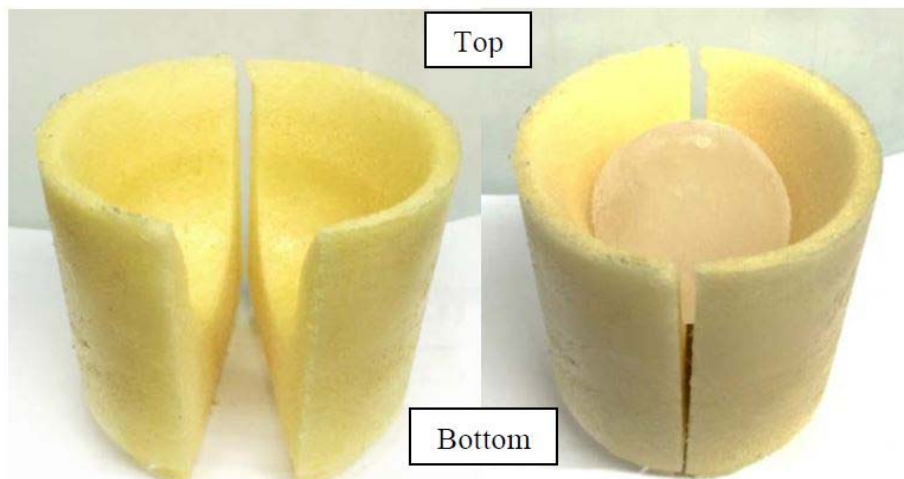
Figure 2.9. Split sabot and hail projectile [Luong, 2014]
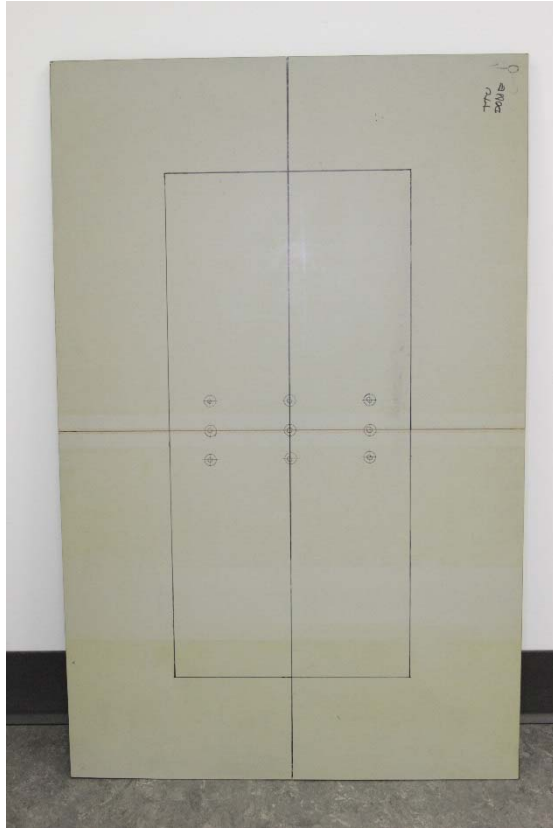
Figure 2.10. Exterior skin of flat sandwich panel
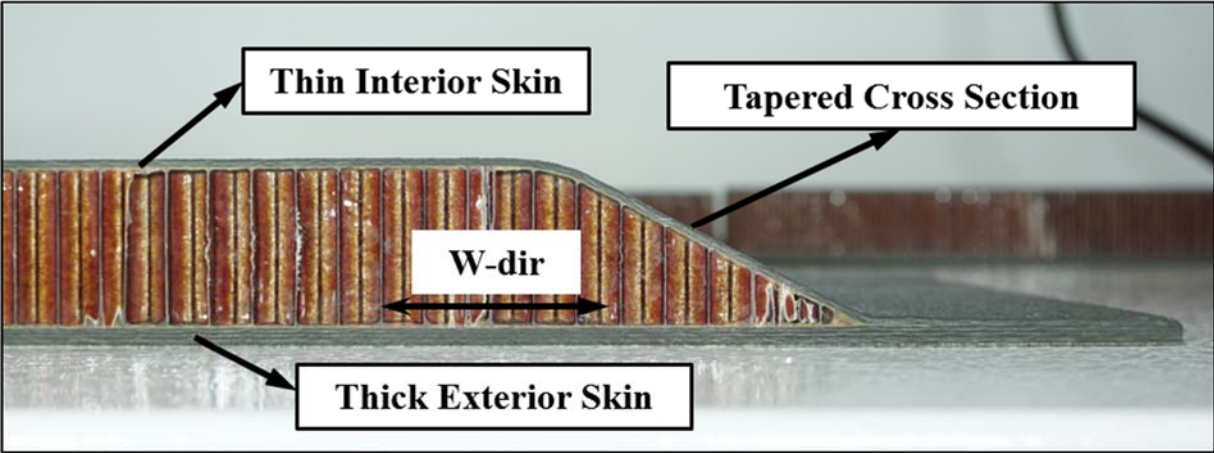
Figure 2.11. Cross-sectional view of sandwich panel (impact direction coincides with L-direction)
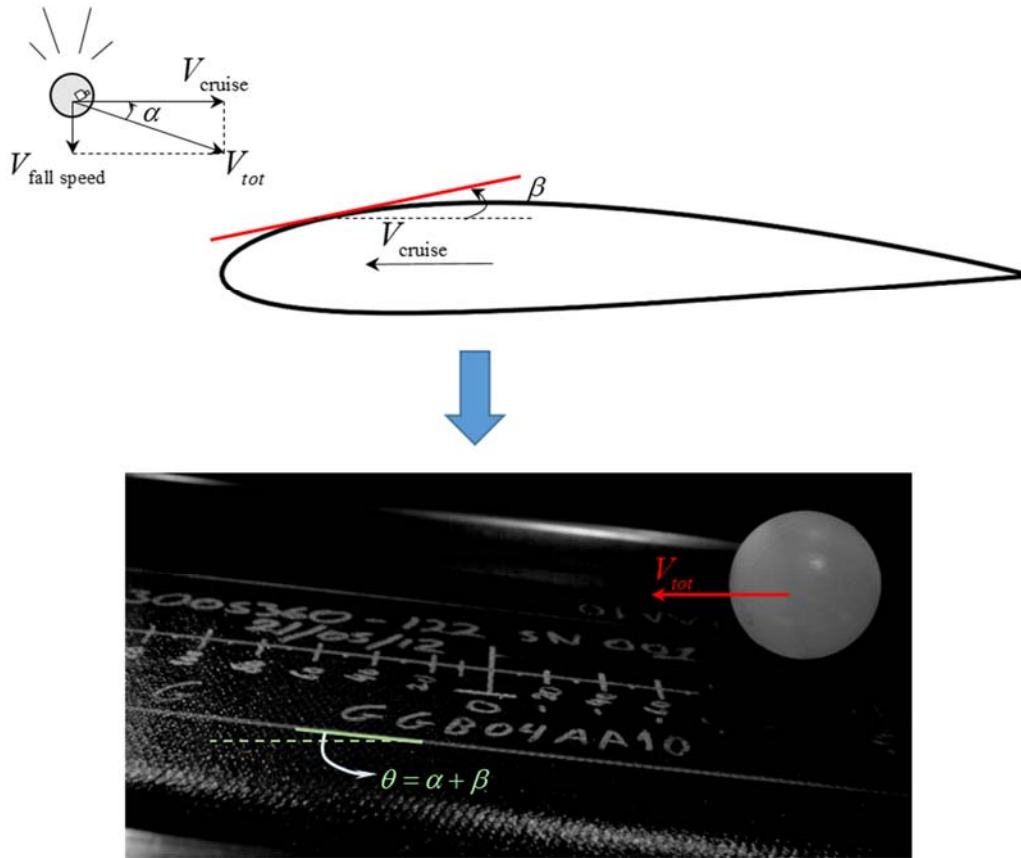
Figure 2.12. Schematic of hail projectile angle of attack and gas gun supporting fixture orientation
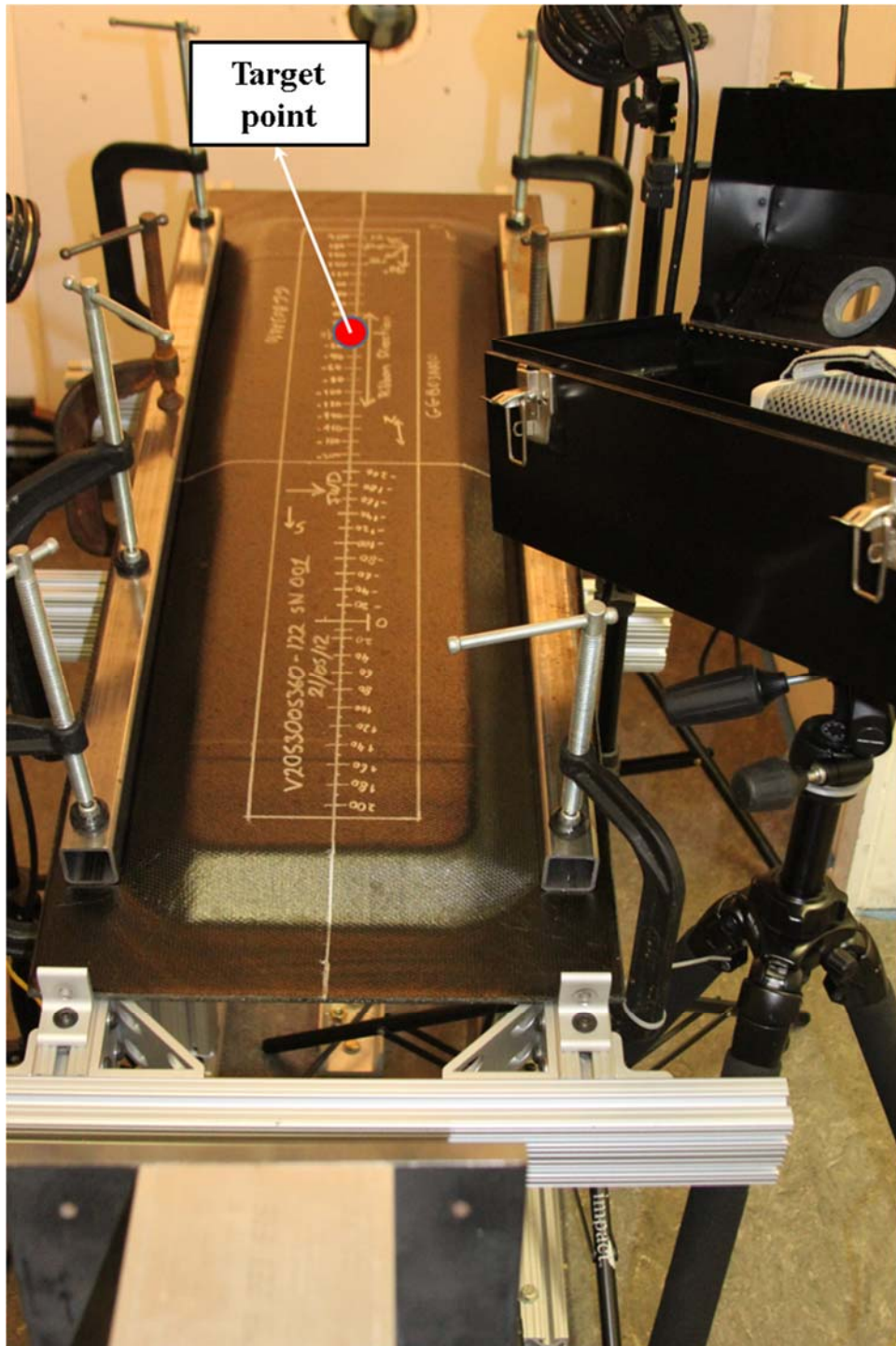
Figure 2.13. Hail impact test setup
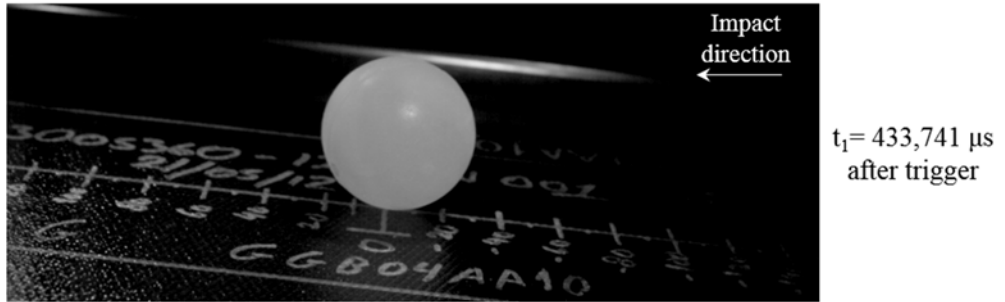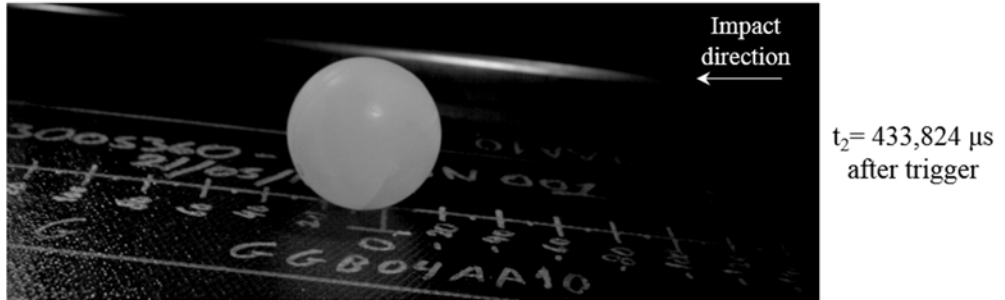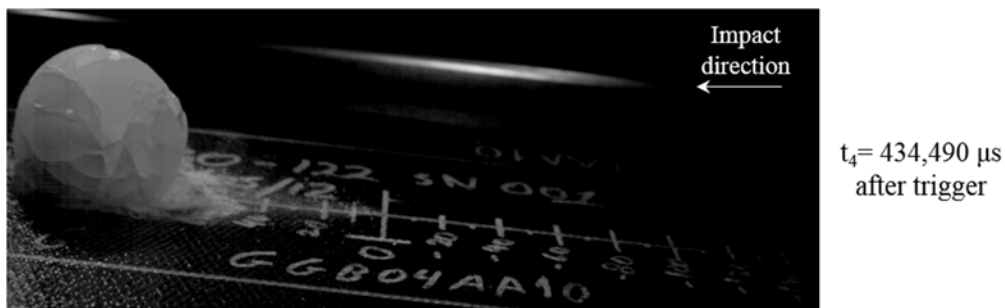
Figure 2.14. Progression of 590 J impact; (a) Intact hail ice (b) Initial contact with skin and first major crack on projectile; (c) Time instance of maximum dent location accompanied by hail fragmentation onset; (d) Sliding of hail along panel surface
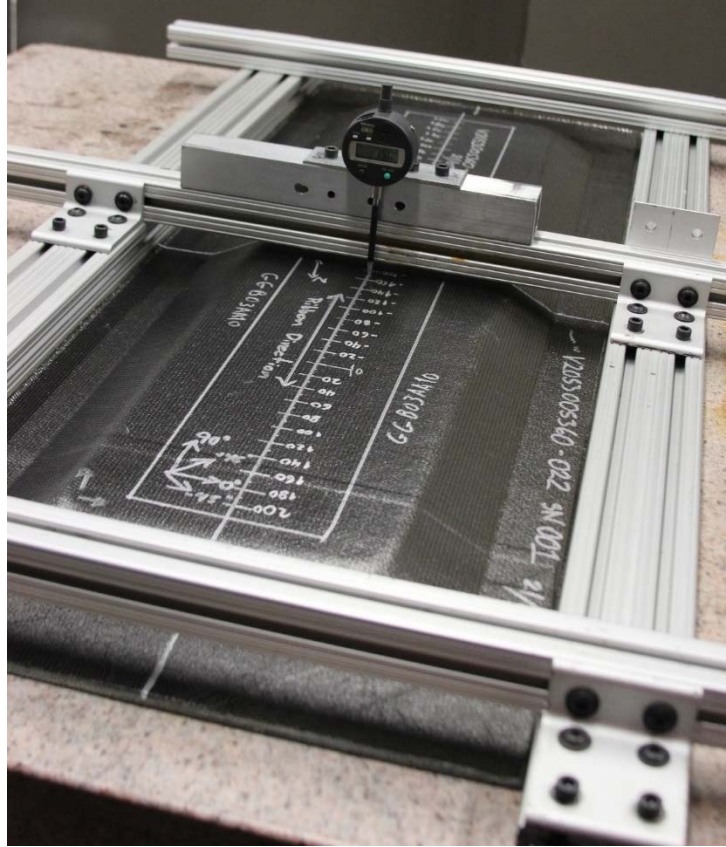
Figure 2.15. Dent depth fixture and dial indicator scans along main impact line
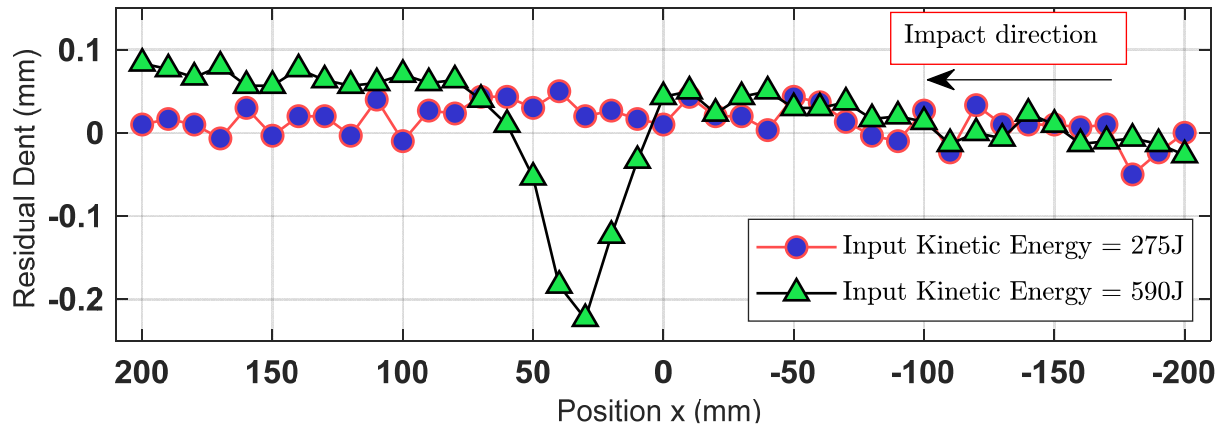
Figure 2.16. Residual dent profiles along impact direction
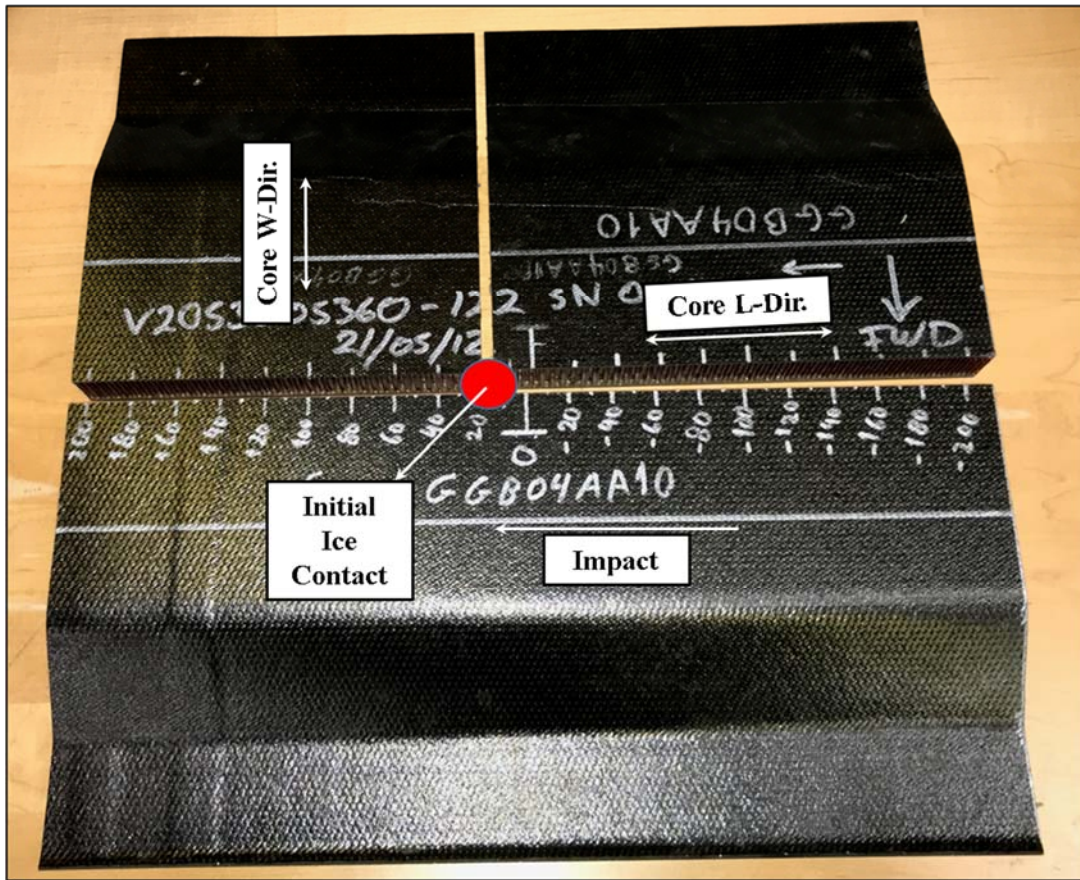
Figure 2.17. Tile saw cutting pattern on tested sandwich panel
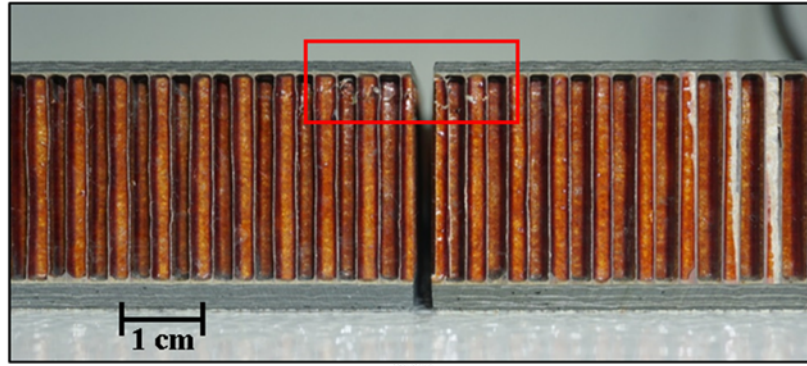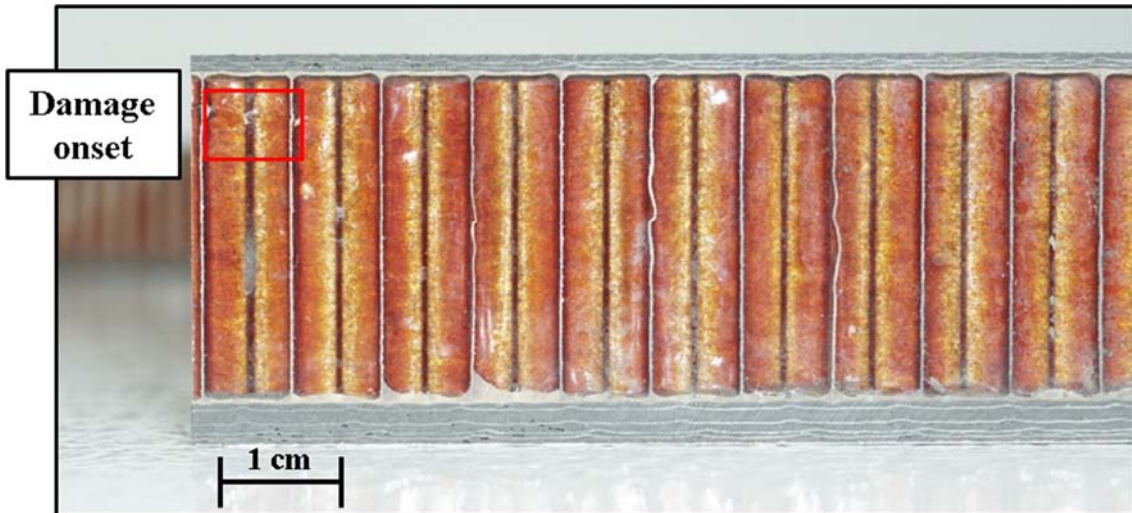
Figure 2.18. Core damage on 275 J impacted panel; (a) Core damage extent along projectile direction; (b) Closeup view of damaged double walls; (c) Damage onset along the transverse to impact direction
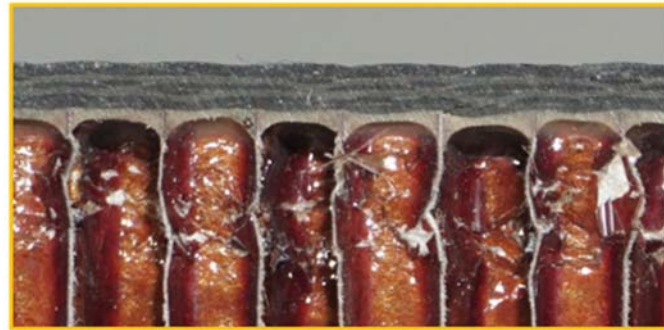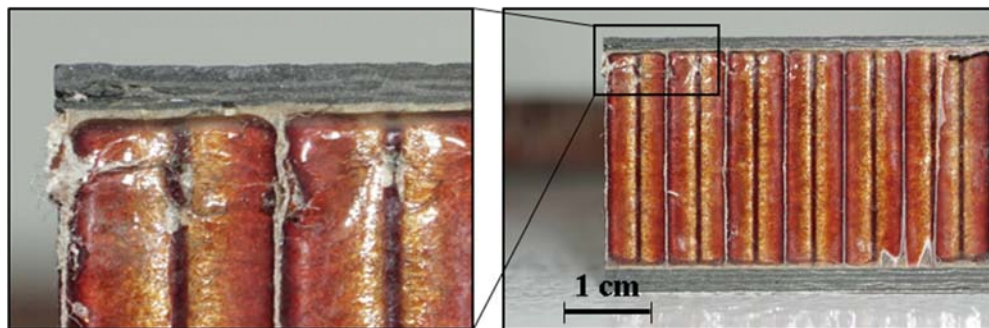
Figure 2.19. Core damage on 590 J impacted panel; (a) Core damage extent along projectile direction; (b) Closeup view of damaged double walls; (c) Ply delamination on impacted skin; (d) Damage span along the transverse to impact direction
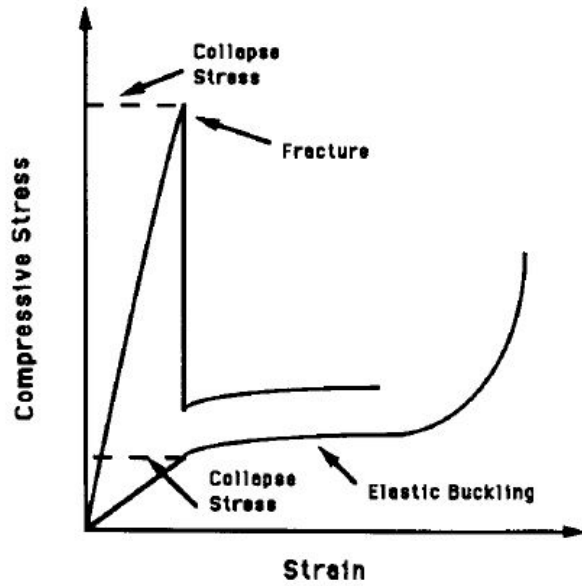
Figure 2.20. Typical effective stress-strain curve for Nomex® honeycombs [Zhang and Ashby, 1992]
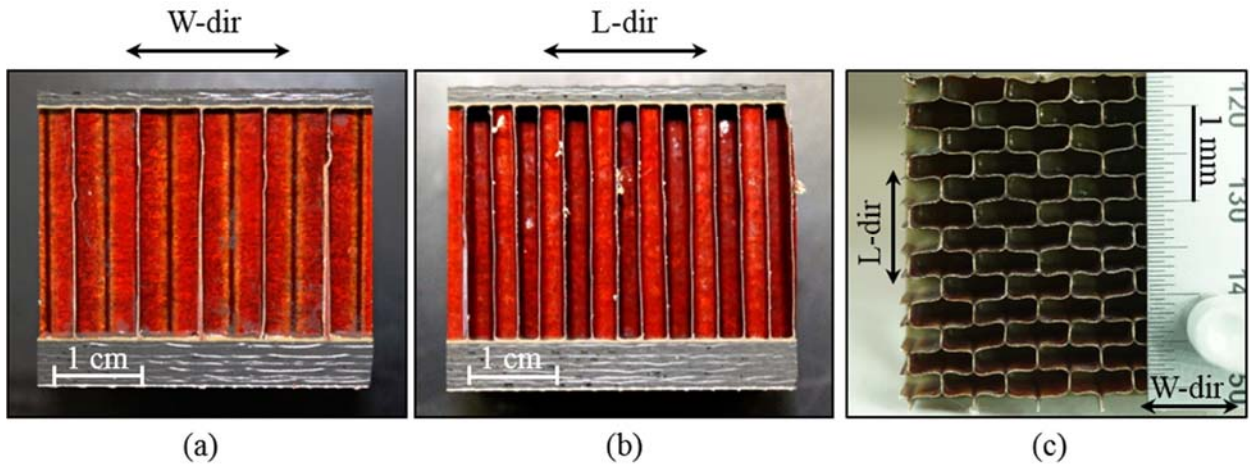
Figure 2.21. Over-expanded Nomex® core geometry
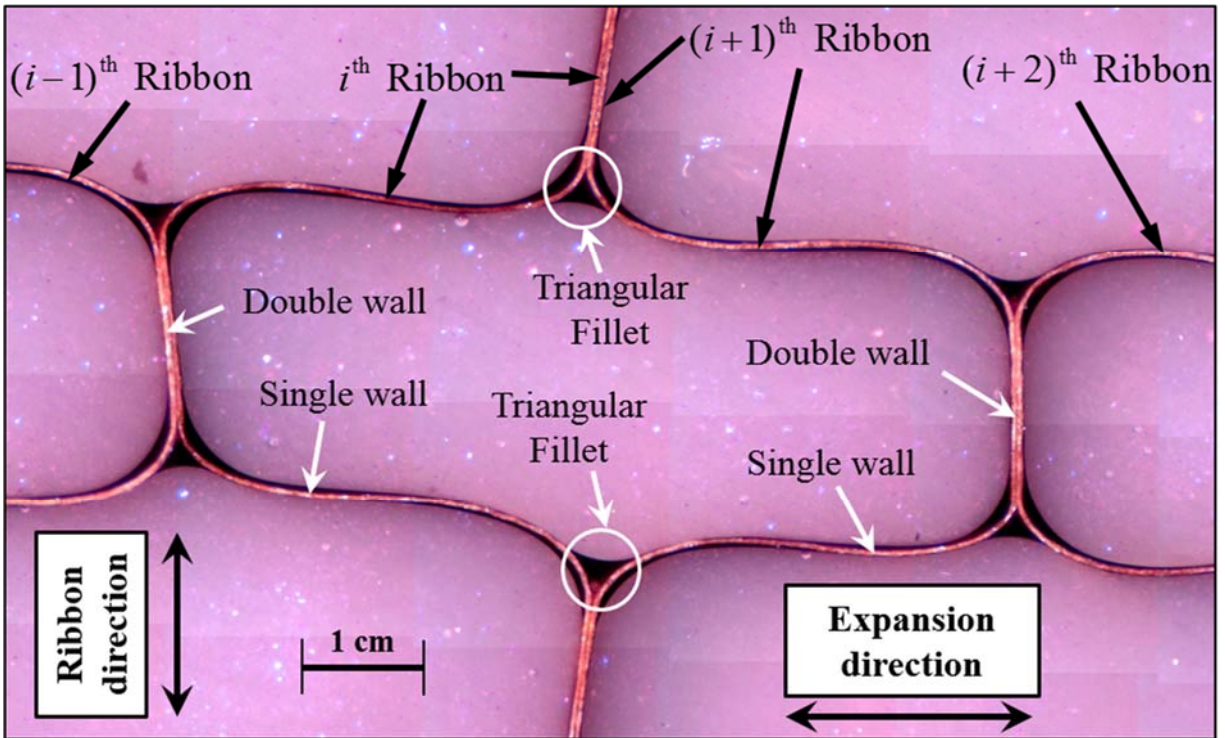
Figure 2.22. Key elements of honeycomb meso-structure

Figure 2.23. High precision cutoff machine
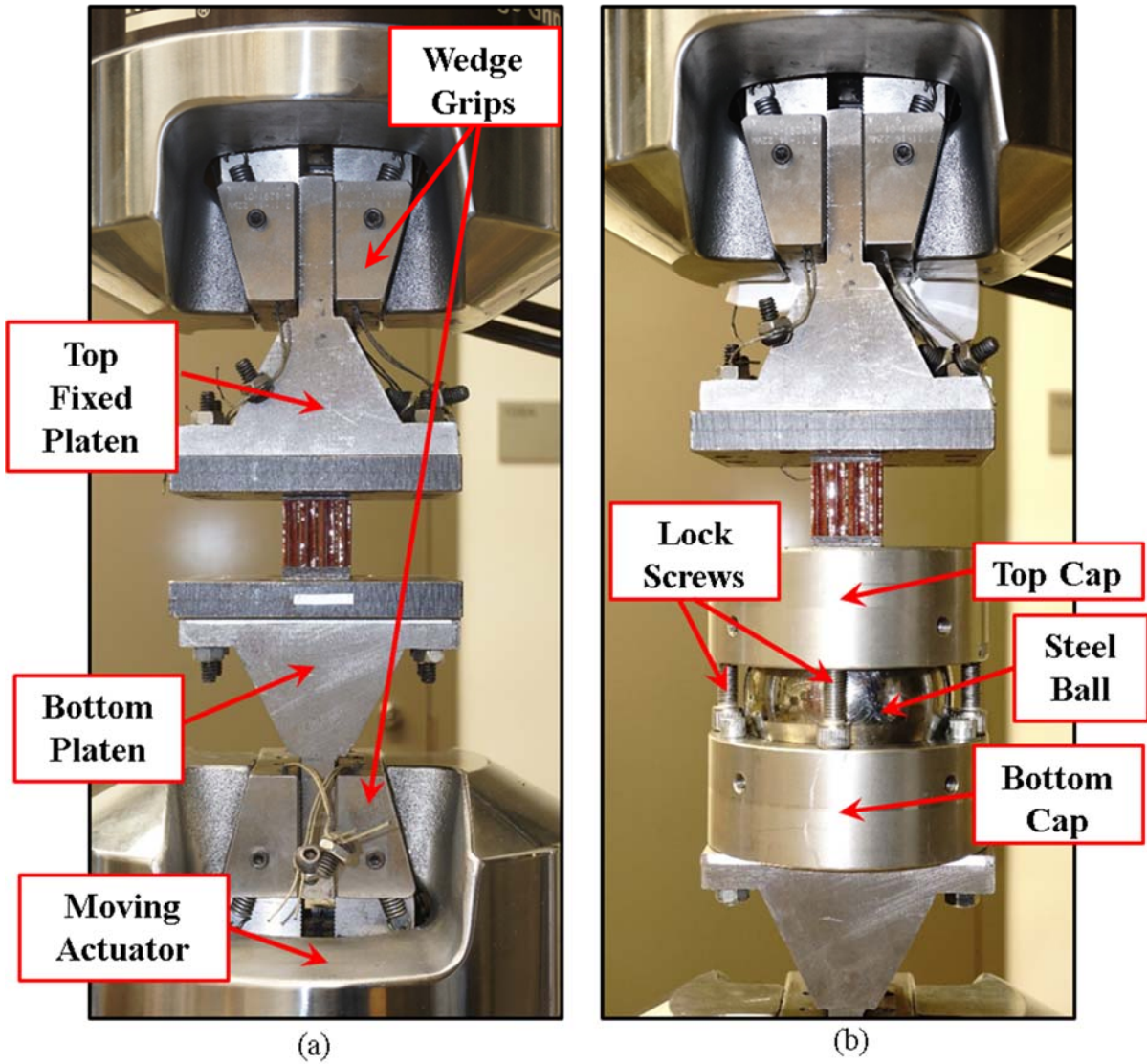
Figure 2.24. Quasi-static load frame apparatus: (a) Fixed compression platens; (b) Self-aligning bottom platen
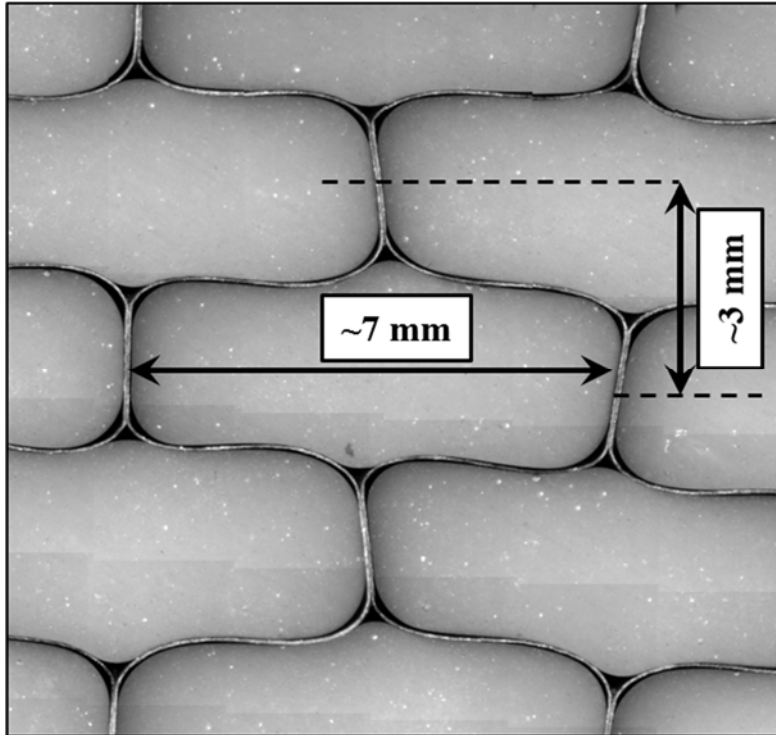
Figure 2.25. Cellular geometry under optical microscope
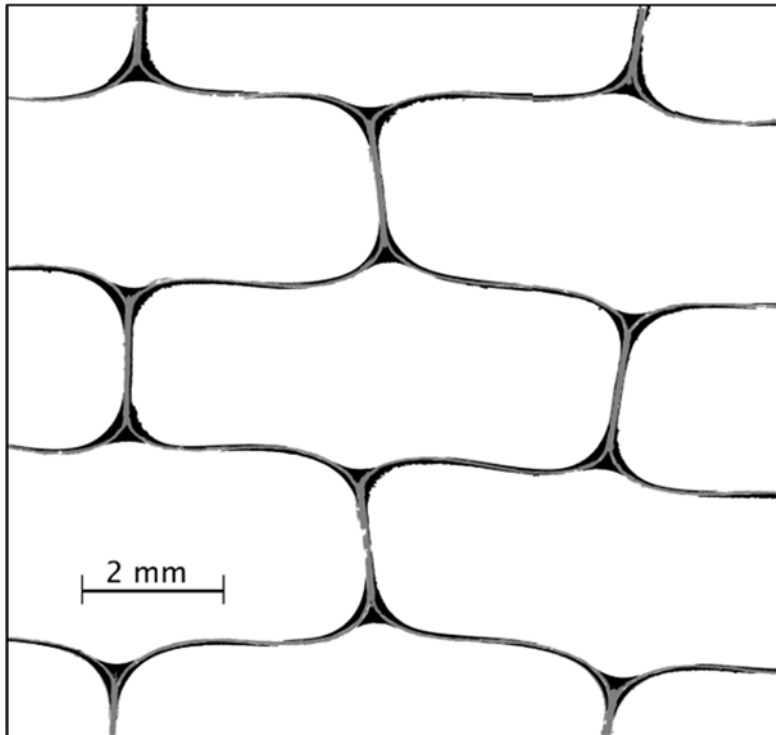
Figure 2.26. Segmentation of cellular geometry based upon K-means clustering algorithm
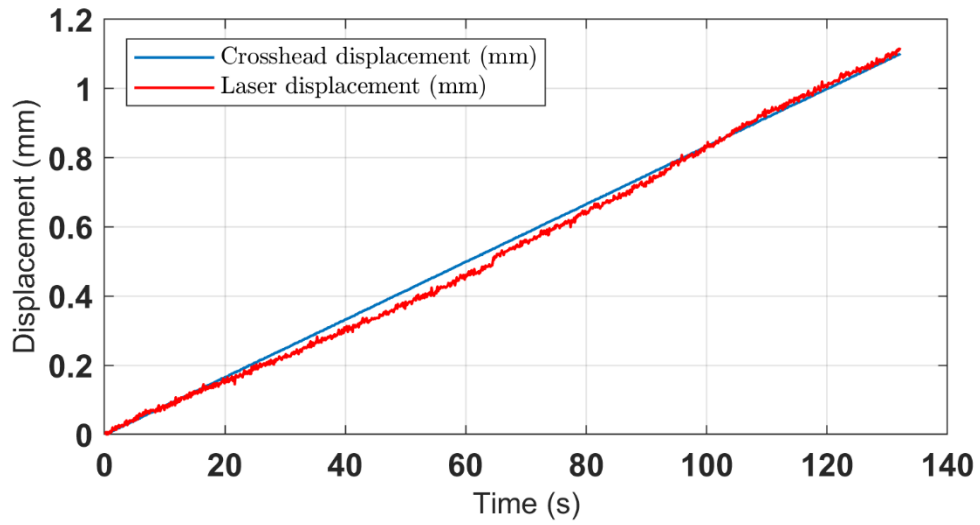
Figure 2.27. Laser vs. crosshead displacement history
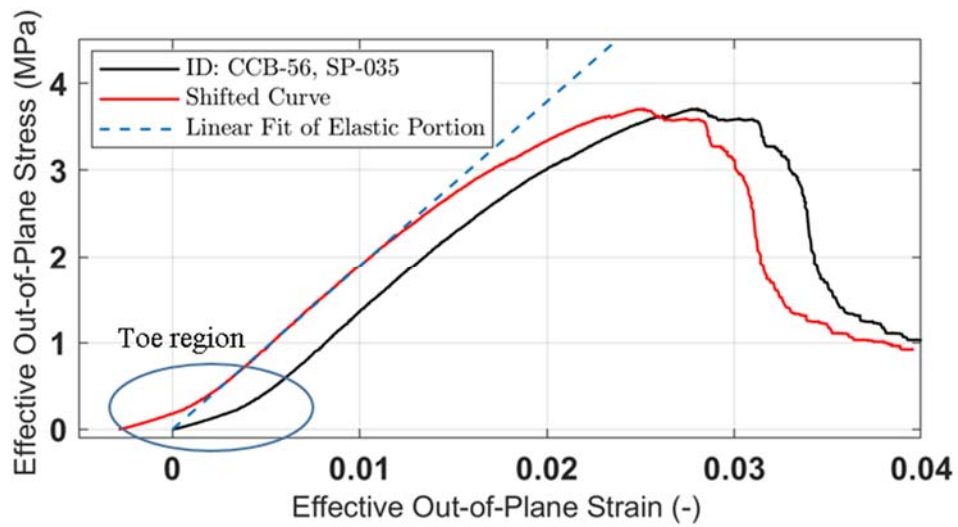
Figure 2.28. Offsetting effective stress-strain data based on linear regression
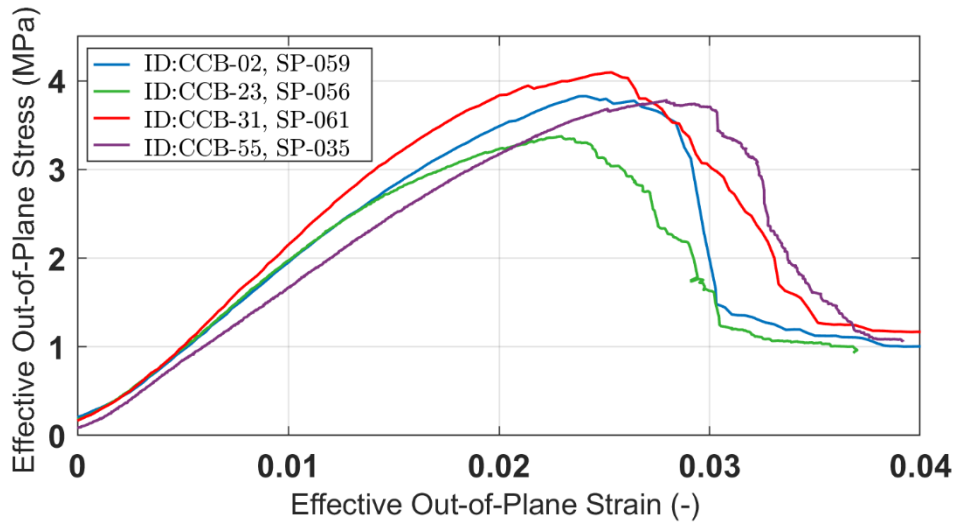
Figure 2.29. Typical effective stress-strain plot for four different coupons
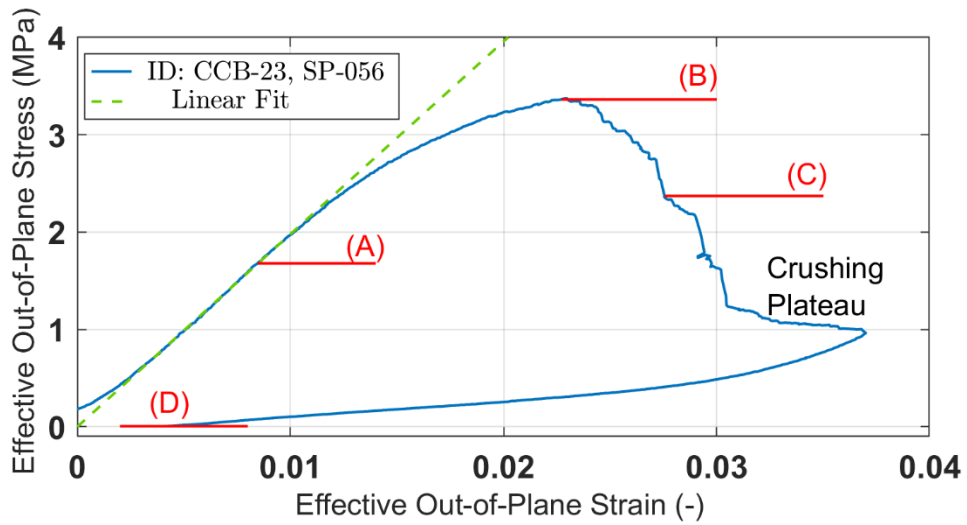
Figure 2.30. Effective stress vs. strain for a full loading/unloading cycle
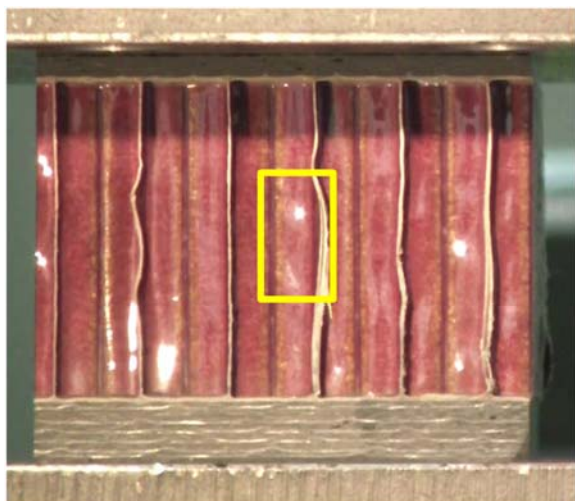
(a) Cell wall elastic buckling
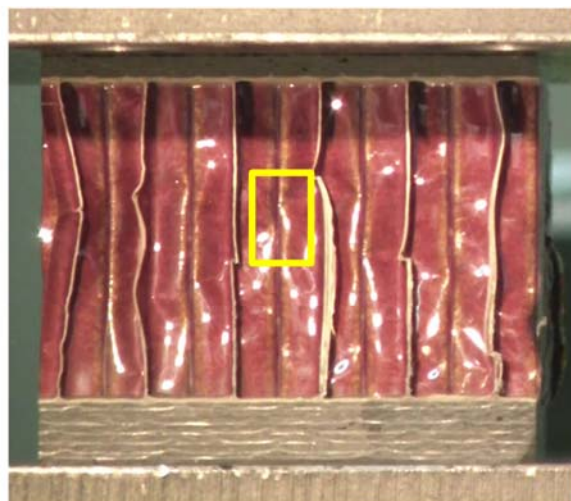
(b) Fracture initiation on resin columns
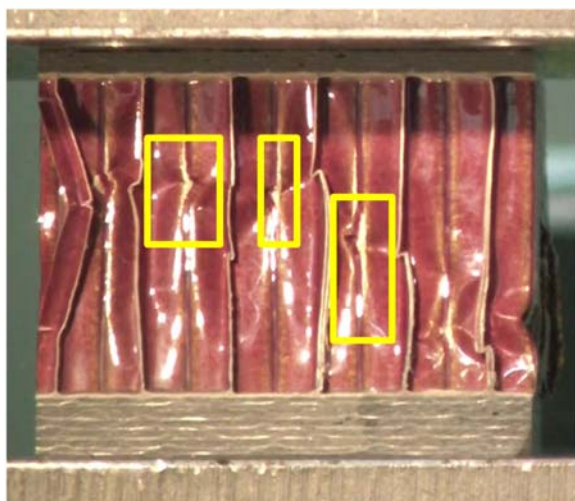
(c) Angled kinking of failed walls
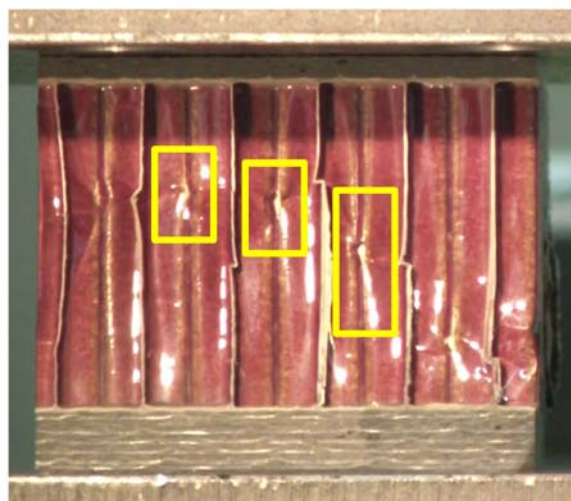
(d) Residual profile (permanent detachment of cell walls)

Figure 2.31. Sequence of Nomex® core failure mechanisms developed on the W-direction of core CCB-023 coupon
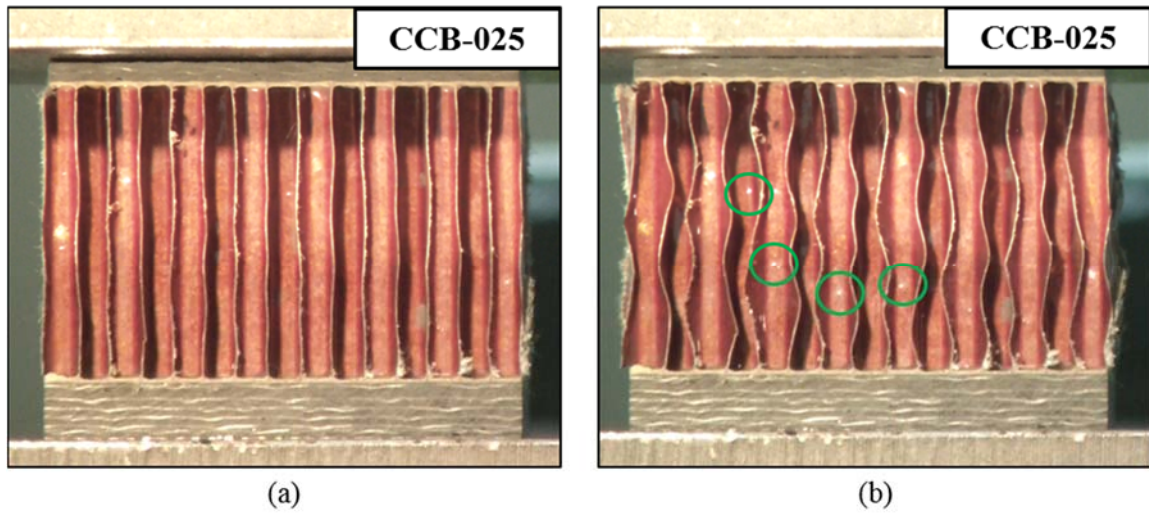
Figure 2.32. View of ribbon direction at test coupon CCB-025; (a) Before test; (b) Onset of double wall buckling at 90% of peak load
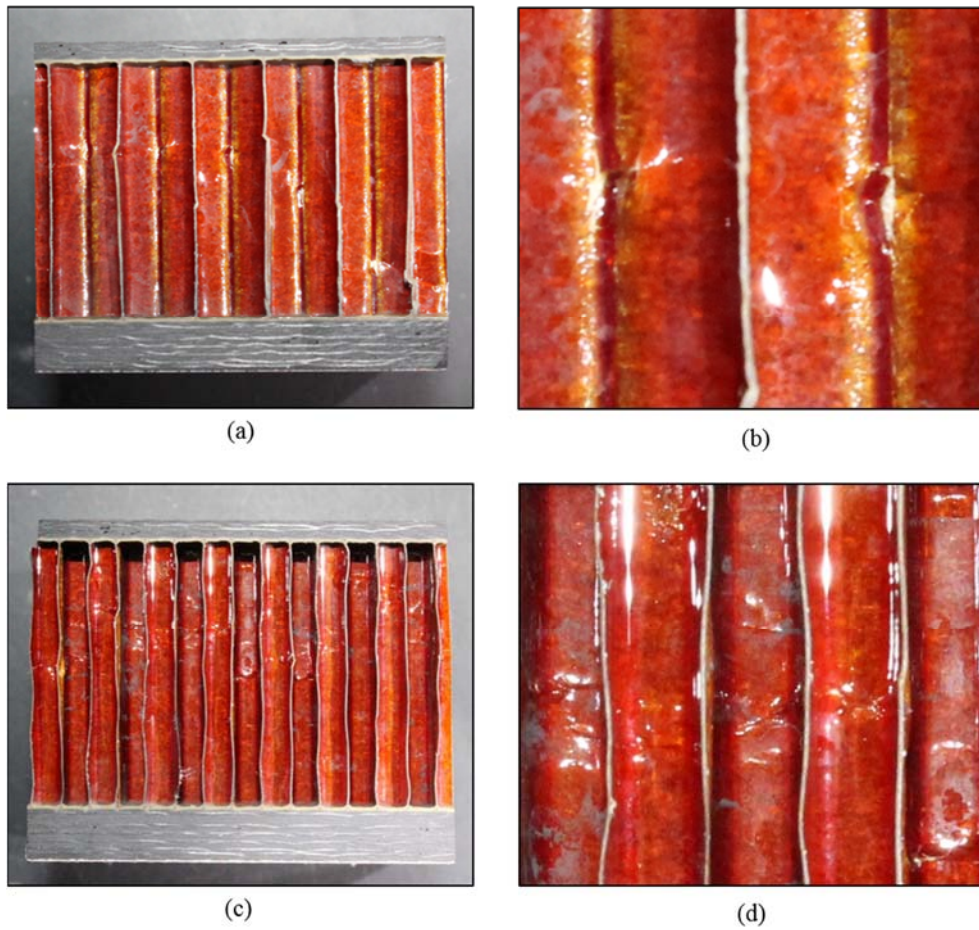
Figure 2.33. Snapshots of damage state on CCB-023 coupon
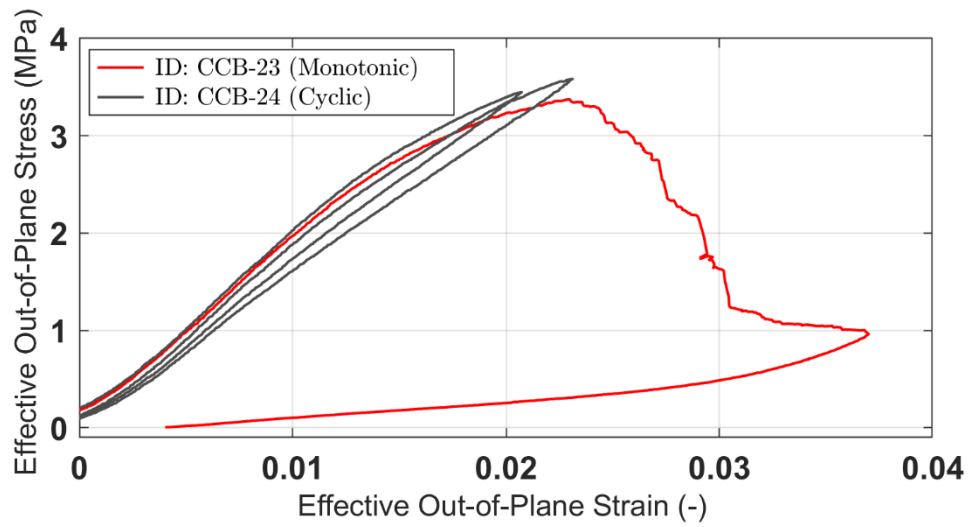
Figure 2.34. Monotonic vs. cyclic flatwise compression response
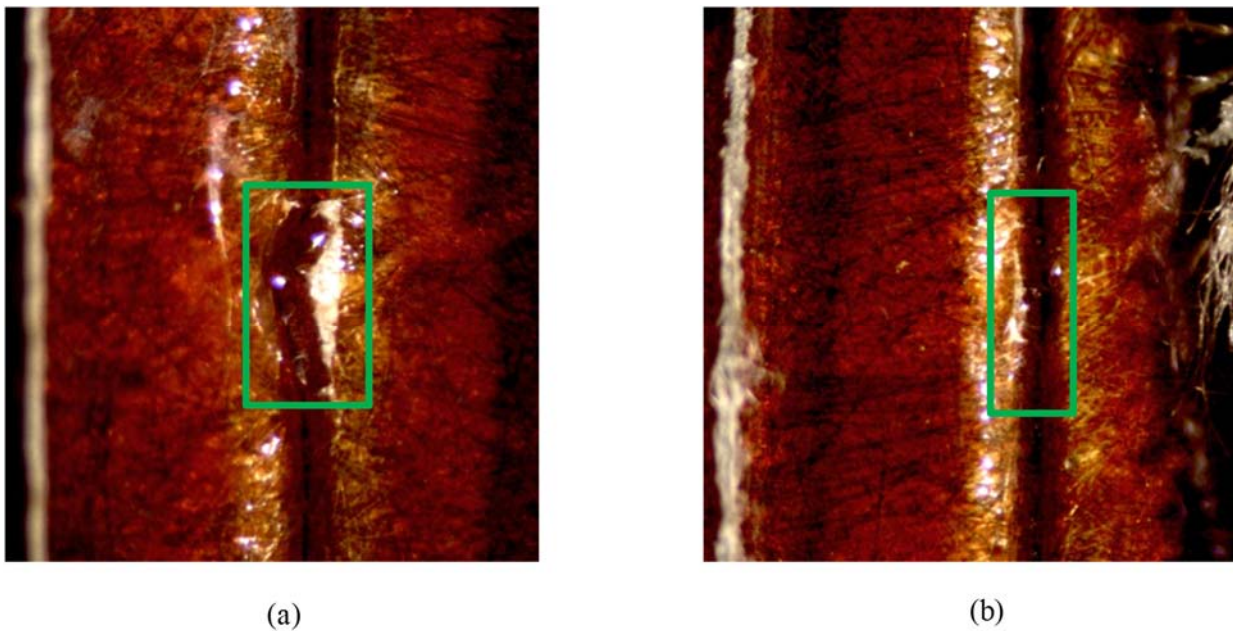
Figure 2.35. View of resin fillet columns after testing for: (a) Tested core with strain reversal upon onset of crushing plateau; (b) Tested core with strain reversal upon peak load resistance
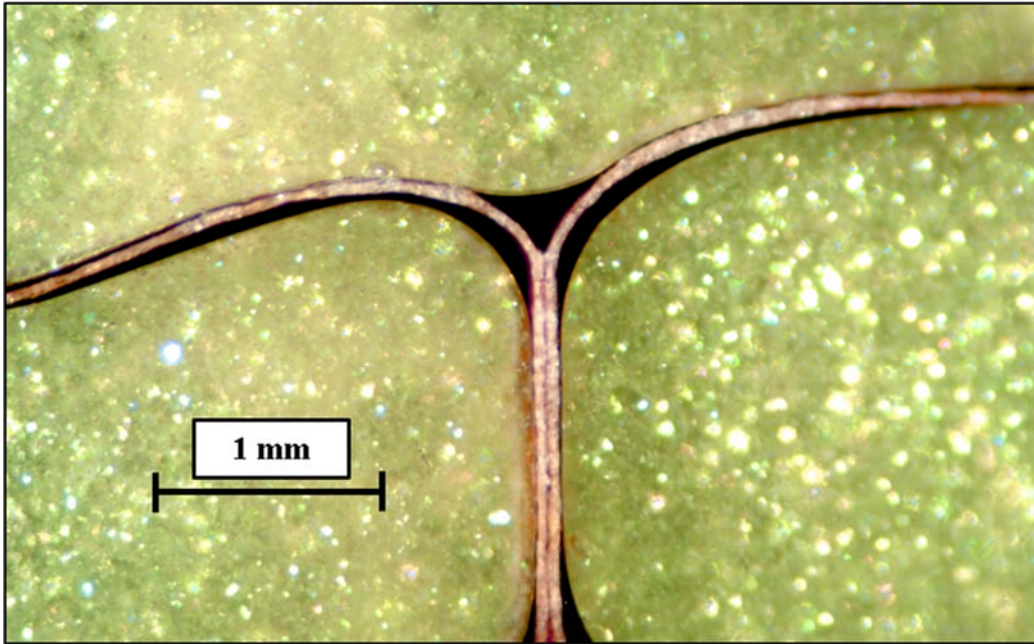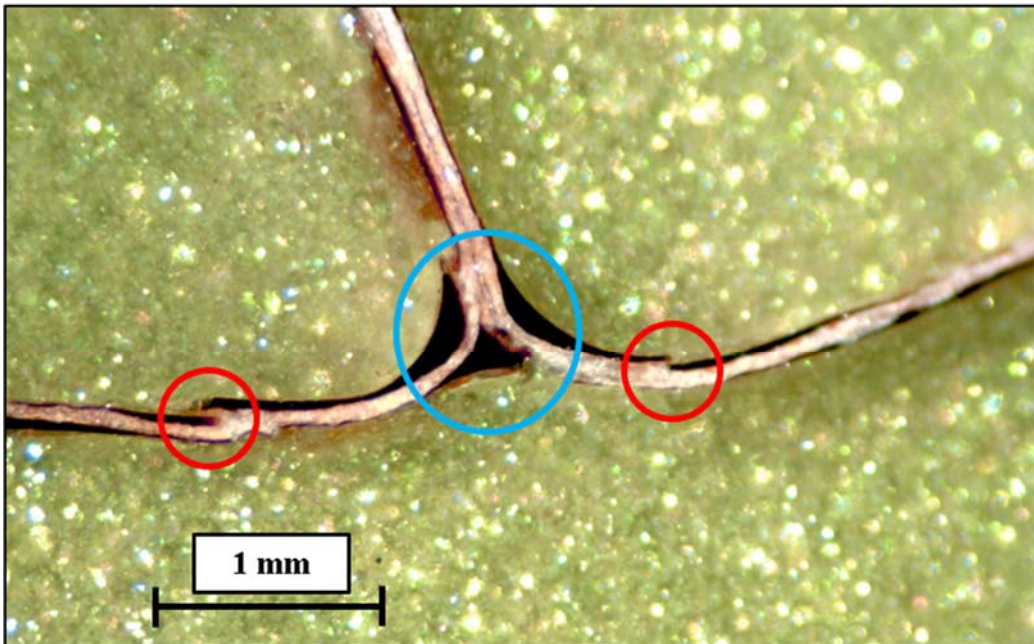
Figure 2.36. Post-test damage evaluation: (a) Undamaged region; (b) Damage in the form phenolic resin cracking and fillet detachment
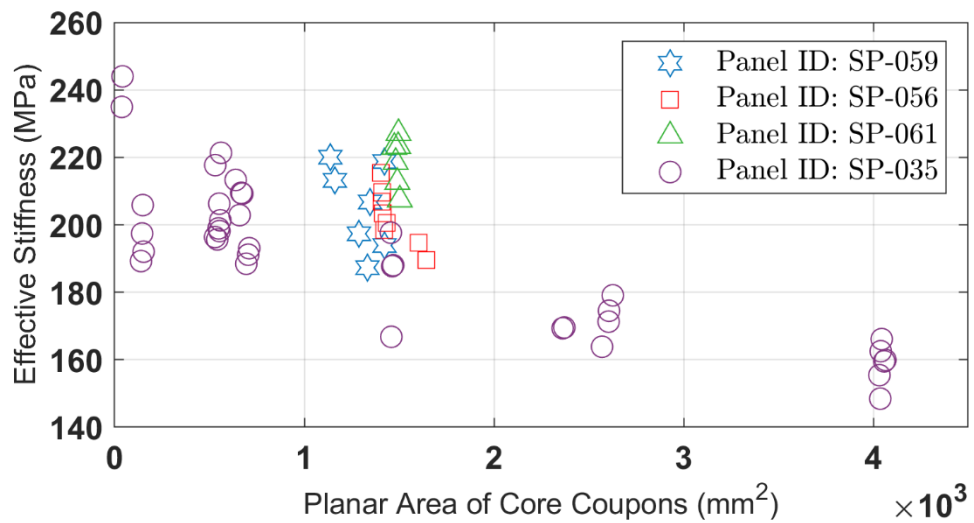
Figure 2.37. Homogenized out-of-plane modulus values for different sandwich core sizes
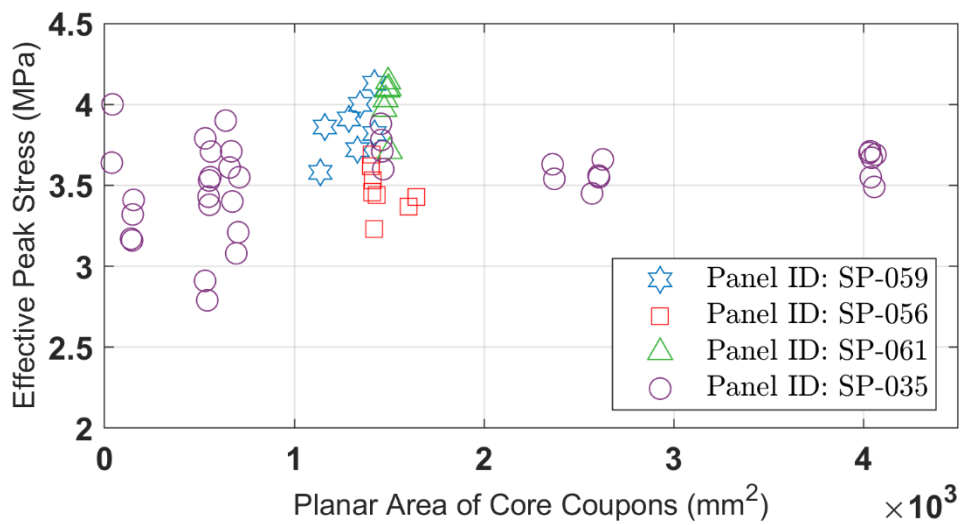
Figure 2.38. Effective out-of-plane strength values for different sandwich core sizes
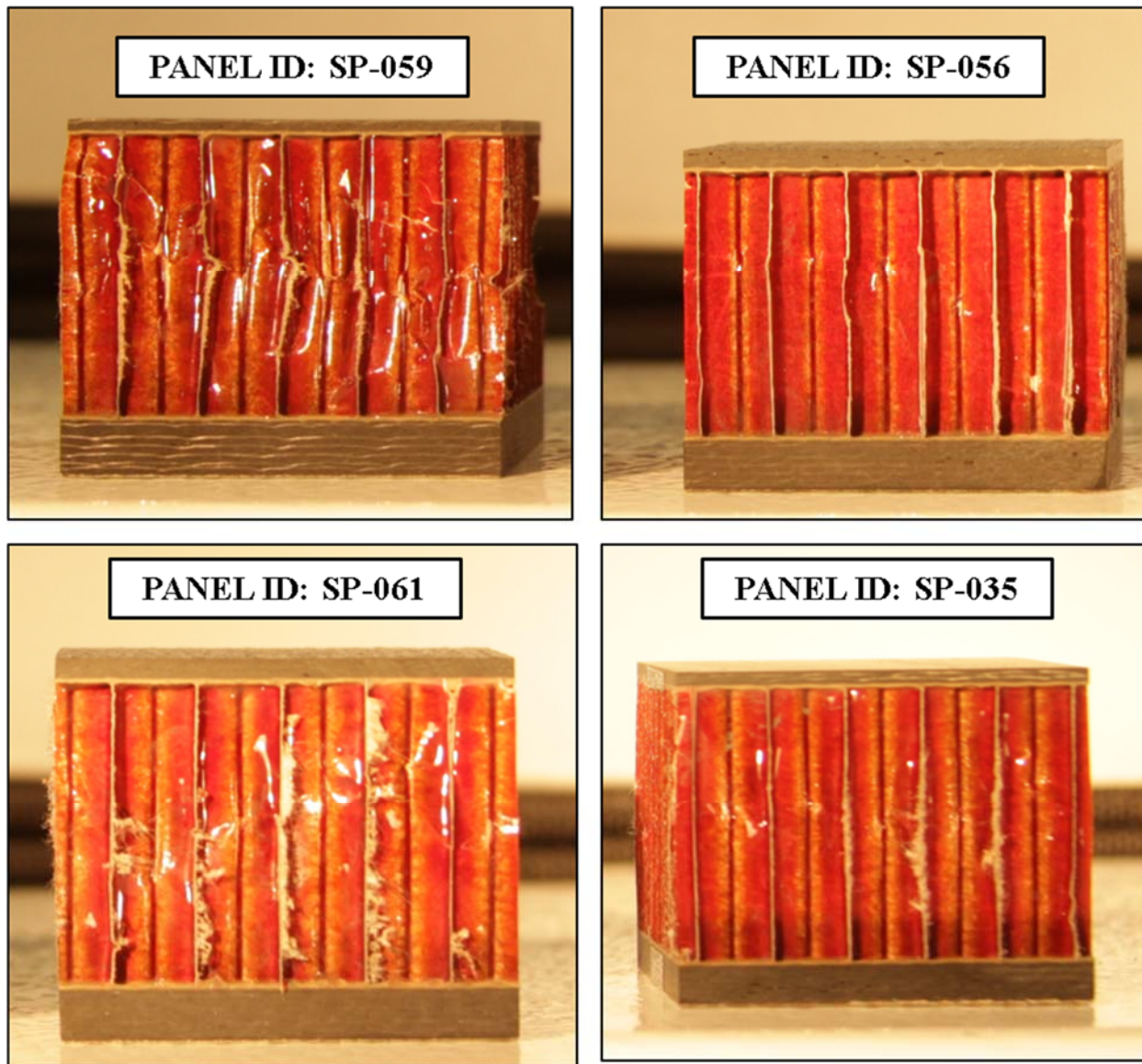
Figure 2.39. Tested specimens extracted from 4 different sandwich panels

Table 2.1. Sizing of core coupons

Sizing Category	Nominal length in ribbon direction (mm)	Nominal length in expansion direction (mm)	Number of cells in ribbon direction	Number of cells in expansion direction
I	5.0	8.0	1	1
II	9.5	15.5	3	2
III	23.0	23.0	8	3
IV	26.0	26.0	10	3
V	37.5	37.5	12	5
VI	40.0	37.5	14	5
VII	50.0	50.0	19	7
VIII	63.5	63.5	23	8

Table 2.2. Test matrix for flatwise compression tests

Panel ID	Core density (kg/m^3)	Number of coupons tested	Core coupon sizing category
SP-059	64	7	V
SP-056	64	8	V, VI
SP-061	64	6	VI
SP-035	64	37	I, II, III, IV, VI, VII, VIII

Table 2.3. Summary of flatwise test results

Coupon ID	Panel ID	Sizing Category	Applied rate (mm/min)	W-dir. (mm)	L-dir. (mm)	Effective Modulus (MPa)	Effective Peak (MPa)
CCB-01	059	V	5.0	38.70	34.44	187	3.72
CCB-02	059	V	2.5	38.25	37.20	194	3.82
CCB-03	059	V	5.0	37.88	35.55	207	4.00
CCB-04	059	V	10.0	37.90	33.98	197	3.91
CCB-05	059	V	2.5	37.66	37.77	219	4.13
CCB-07	059	V	4.0	37.71	37.16	220	3.58
CCB-08	059	V	4.0	37.65	37.84	213	3.86
CCB-09	056	V	0.5	37.80	37.43	203	3.53
CCB-10	056	V	0.5	37.82	37.52	199	3.23
CCB-11	056	V	0.5	37.89	37.88	200	3.44
CCB-12	056	V	0.5	37.26	37.81	210	3.46
CCB-13	056	V	0.5	37.59	37.40	207	3.69
CCB-14	056	V	0.5	37.36	37.57	215	3.62
CCB-23	056	VI	0.5	37.97	40.14	195	3.37
CCB-25	056	VI	0.5	37.60	40.50	189	3.43
CCB-27	061	VI	0.5	37.64	39.17	223	3.97
CCB-28	061	VI	0.5	37.83	39.56	227	4.10
CCB-29	061	VI	2.0	37.69	39.31	219	4.03
CCB-31	061	VI	2.0	38.02	39.20	213	4.09
CCB-32	061	VI	5.0	37.92	39.42	223	4.14
CCB-45	061	VI	0.5	38.68	38.87	207	3.71
CCB-50	035	VI	0.5	38.13	38.52	188	3.60
CCB-51	035	VI	0.5	38.05	38.27	197	3.88
CCB-52	035	VII	0.5	51.06	51.44	179	3.66
CCB-53	035	VIII	0.5	63.84	63.66	160	3.69
CCB-54	035	VIII	0.5	63.43	63.68	163	3.55
CCB-55	035	VI	0.5	38.19	38.20	167	3.78
CCB-56	035	VI	0.5	38.57	37.95	188	3.71
CCB-57	035	VII	0.5	50.94	51.13	171	3.56
CCB-58	035	VII	0.5	51.27	50.84	175	3.55
CCB-59	035	VIII	0.5	63.57	63.62	166	3.67
CCB-60	035	VII	0.5	48.63	48.57	169	3.63
CCB-61	035	VII	0.5	49.16	48.23	170	3.54
CCB-62	035	VII	0.5	52.18	49.25	164	3.45
CCB-63	035	VIII	0.5	63.46	63.54	155	3.70
CCB-64	035	VIII	0.5	63.60	63.47	148	3.71
CCB-65	035	VIII	0.5	63.87	63.53	160	3.49
CCB-71	035	III	0.5	23.91	23.30	201	3.55
CCB-72	035	III	0.5	24.07	22.76	199	3.43

Table 2.3. Summary of flatwise test results (cont'd)

Coupon ID	Panel ID	Sizing Category	Applied rate (mm/min)	W-dir. (mm)	L-dir. (mm)	Effective Modulus (MPa)	Effective Peak (MPa)
CCB-73	035	III	0.5	23.27	22.80	218	3.79
CCB-74	035	III	0.5	23.58	23.45	198	3.38
CCB-75	035	III	0.5	24.11	22.87	206	3.53
CCB-76	035	III	0.5	23.81	23.54	221	3.71
CCB-77	035	III	0.5	24.83	21.32	196	2.91
CCB-78	035	III	0.5	25.43	21.28	196	2.79
CCB-79	035	IV	0.5	26.84	25.85	188	3.08
CCB-80	035	IV	0.5	26.97	24.96	209	3.40
CCB-81	035	IV	0.5	26.13	25.55	209	3.71
CCB-82	035	IV	0.5	27.60	25.71	193	3.55
CCB-83	035	IV	0.5	25.89	25.44	203	3.61
CCB-84	035	IV	0.5	26.78	26.30	191	3.21
CCB-85	035	IV	0.5	25.65	24.88	213	3.90
CCB-88	035	II	0.5	15.26	9.49	197	3.16
CCB-89	035	II	0.5	15.83	9.64	192	3.41
CCB-91	035	II	0.5	14.97	9.29	189	3.17
CCB-93	035	II	0.5	15.84	9.35	205	3.32
CCB-99	035	I	0.5	8.32	4.98	244	4.00
CCB-100	035	I	0.5	8.42	4.48	235	3.64

CHAPTER 3: IMAGE-BASED HONEYCOMB CORE RECONSTRUCTION

3.1   OVERVIEW

X-ray computed tomography (CT) which is a non-destructive 3D imaging technique, has been implemented for damage detection at coupon and element level composite parts. This chapter initially details the application of this technique into honeycomb cores to visually assess the 3D damage state and the governing damage mode when tested under flatwise compression. Despite its qualitative nature, this approach provides further insight along the direction of the phenomenological failure observations presented in the previous chapter. Furthermore, with the available X-ray CT-scan data, we propose an image-based reconstruction method to mathematically represent the actual honeycomb core shape with B-spline surfaces and volumes. Since flatwise compression on honeycombs involves buckling and post-buckling phenomena, determination of initial imperfections is the first step towards computational model generation. Through the proposed scheme, metrics of the wall imperfections and cellular shape distortions on undamaged coupons as well as residual displacements on tested coupons are established. Finally, image-based reconstruction of the buckling evolution on progressively compressed coupon that was in-situ CT-scanned at specified intervals is also presented. The latter approach is probably one of the most comprehensive strategies towards understanding core compression response at the meso-scale level.

3.2   PREVIOUS WORK ON X-RAY COMPUTED TOMOGRAPHY IN SANDWICH COMPOSITES

Computed tomography of 3D objects utilizes X-ray beam radiation combined with an electronic detector for the recording of the attenuated signals [Caldemeyer, 1999]. Multiple scans

are performed when the X-ray beam as well as the detector rotate around the targeted object leading to different planar projections each time from which the full 3D geometry can be reconstructed. The results of such a representation is a 3D array of voxels, short for volumetric pixels, which is essentially a 3-dimensional matrix with different color intensity entries. This array can be post-processed such that cross-sectional cuts also known as CT slices are obtained along the three Cartesian coordinate axes.

The application of CT scans in honeycomb composites is not as extensive as in monolithic composites. Ultrasonic, computed tomography, and infrared inspections were employed to assess artificial flaws on Nomex® sandwich panels in the form of disbonds at the film adhesive, inter-ply skin delaminations, and honeycomb core regions locally potted with foam [Moore, 2012]. Based on the results, computed tomography was the most accurate technique to assess through-thickness flaws within the skin and core. In another study, flash thermography and X-ray CT yielded similar results in terms of skin delaminated regions of impacted sandwich panels, but CT scans were still superior at capturing the crushed core with high resolution images [Zalameda and Parker, 2014]. X-ray CT scans on impacted sandwich panels with aluminum core were also used as a baseline for comparison with an in-house non-contact laser-based system [Girolamo et al., 2018]. On a curved sandwich panel, the angle between the impacted region of interest and the reconstruction volume was optimized to obtain CT scan slices that directly depicted through-thickness damage [Liu and Malcolm, 2010]. Significant cell wall buckling was documented on hybrid fiber paper core as a result of the curing cycle [Song et al., 2010]. The collapse mode of aluminum honeycomb core sandwich panels subjected to impact and three-point loading was assessed through CT scanning for various size cells [Crupi et al. 2011, 2013, 2016]. In a different study, commercial CT visualization software VGStudio MAX 2.0 was utilized to import voxel

data of aluminum core sandwich panel into ABAQUS finite element software and low-velocity impact response was investigated [Crupi et al., 2014].

Based on literature, quantitative interpretation of X-ray CT data on sandwich honeycomb cores has not been applied yet. Since honeycombs are enclosed structures, X-ray CT scans are employed to visually investigate 3D damage state on a tested core sample without any destructive interference. Furthermore, the scope in the remainder of this chapter is to numerically reconstruct scanned samples and ultimately obtain metrics of initial imperfections and detect post-buckling evolution. The proposed automated image-based reconstruction scheme is going to be the basis for generation of computational models presented in the following chapter.

3.3   DAMAGE ASSESSMENT ON CT-SCANNED SANDWICH CORE COUPONS

CT scans were performed via Actis5 X-ray micro-CT scanner at Utah Composites Laboratory at the University of Utah. This system consists of an X-ray beam source, a rotating and moving base on which the scanned sample is placed, and an image intensifier that converts the attenuated signals received by the detector into a grayscale image. For the CT scans on the sandwich core samples, a full $360°$ rotation of the base was employed and 3600 views in total were taken and each view was averaged from the acquisition of two images per view. Filtered back projection was utilized to eliminate artefacts arising from the different projections of the same object as the base spins. Regarding the X-ray source, the scans were performed using 80 kV voltage, 90 μu current. The scanning resolution per image was 1024 x 1024 pixels for all different scans.

A typical isometric view of three orthogonal slices passing through the center of cylindrical chamber on untested sandwich core sample is shown in Figure 3.1. For the scanned sample of

Figure 3.1, each resulting voxel measured 34 μm and the dimensions along ribbon and expansion directions were equal to 26.9 mm and 27.6 mm respectively. The resolution of each image was about 1,000 pixels along each orthogonal direction. Prior to flatwise compression, the sample was CT-scanned to obtain a baseline of the pristine imperfections inherited during core manufacturing and co-curing bonding processes. After initial scan, the core sample was compressed at 0.5 mm/min displacement rate until the onset of the crushing plateau as shown in Figure 3.2.

The data produced by the scanner are stored into a stack of images along the scanning direction and each image has a finite thickness equal to 34 μm. Figure 3.3 depicts a 3D view of the normal to the ribbon direction sectioned sandwich core before and after compression test. In the context of fracture and detachment of the fillet columns, small cavities were observed near the damaged regions as shown in Figure 3.3.

Images were stored in MATLAB in the form of a 3D array with color intensity entries. CT scan images exhibited an 8-bit depth, giving a range of 256 different color intensities. Depending on the region of interest, a 2D image representing a unique CT slice may be extracted from manipulation of the resulting 3D array. Figure 3.4, Figure 3.5, Figure 3.6 all show CT slices along all three orthogonal planes. Minor ring artefacts were attributed to misalignments between the X-ray source and the colinear detector. Figure 3.4 validates the hypothesis that the main damage mode is related to the detachment and fracture of the fillets from the wall geometry. Except for local distortion due to fillet failure, cell wall structure has kept its original shape. Figure 3.5 demonstrates CT slice at a plane with outer normal parallel to expansion direction in which localized single cell wall kinking occurred. On a similar comparison, the failure mode along the ribbon direction in Figure 3.6 is based on fillet fracture.

To illustrate the fact that fracture mostly occurs at the interface and within the fillets, cross sections along the fillets and walls were directly compared. CT slices along the ribbon direction shown in Figure 3.7 revealed that cavities were formed at the fillet region which appears to be thicker than the double walls. In Figure 3.7c, localized wall kinking on the double wall was present. Given the CT scan resolution, the bonding adhesive did not fail as double walls did not disbond from each other. This feature could be useful as the adhesive does not need to be explicitly accounted for in modeling. Similar type of cavities as well as missing components on fillets along the expansion direction are also shown in Figure 3.8. The qualitative results obtained from this non-destructive technique coincide with the phenomenological observations of the previous chapter and they both illustrated that fillet fracture constitutes the main damage mode which is ultimately associated with cell collapse.

3.4 IMAGE-BASED DISCRETIZATION OF CT-SCANNED CORE WALL STRUCTURE

Thus far, interpretation of CT scan data was qualitative by providing insight on the type of failure induced by flatwise compression. CT scan numerical interpretation utilizing template matching algorithm has been performed to explicitly model individual composite fibers and their angular misorientation at the micro-scale level [Czabaj et al., 2014, Sencu et al., 2016, Emerson et al., 2017]. In honeycomb cores, X-ray CT scans were utilized to characterize mean cell size and mean wall thickness [Dietrich, 2014].

Since the imported stack of images can be transformed into an array representing 3D space, the geometry of scanned samples can be numerically reconstructed by isolating basic features of the cellular structure. To this end, we are proposing an automated reconstruction scheme that was

implemented in MATLAB environment. The basis of the scheme lies on an image-based nodal discretization of each ribbon followed by B-spline surface and volume interpolations representative of the thin wall cells and triangular fillets respectively. The end result is a geometric model similar to Computer Aided Design (CAD) models produced by commercial design software packages. While honeycomb core representations are typically based on nominal dimensions provided by core manufacturers, the proposed model reflects the actual 3D shape of the honeycomb structure within scanner accuracy.

Since honeycomb cores consist of multiple ribbons stacked and bonded together, the discretization of the structure into multiple nodes will follow similar pattern. The image-based discretization scheme was implemented along the through-thickness direction. The basic feature of a typical CT scan slice shown in Figure 3.9 is that attenuation is stronger when X-rays transmit through fillets simply because they are thicker compared to cell walls. Due to higher attenuation, fillets exhibit average color intensity closer to white color thresholds compared to cellular wall structure. To enhance contrast between the fillets and the cell walls, GIMP free image processing software was utilized to filter original CT scan images. More specifically, the application of color curve and unsharp masking filters led to significant tonality of the fillets as shown in Figure 3.10. For clarity and better visualization, the color intensity in all figures shown herein was linearly inverted so that less attenuated signals appear in white. The resulting images were then imported into MATLAB. The applied filters indeed allowed the selection of two different threshold intensity values as shown by the color histogram of a single CT slice in Figure 3.11. Choice of high threshold value yielded a binary representation of the honeycomb structure without the fillets, while relatively lower threshold value allowed fillet segmentation as depicted in Figure 3.12 and Figure 3.13 respectively. Even though binary representation yielded thicker cell walls, honeycomb

structure was numerically modeled as a cluster of zero-thickness surfaces passing through the midpoints of each wall segment. Good correlation between the binary fillet image and the original CT scan slice may be observed in Figure 3.14. Binary thresholding imprinted 90% of the pixels representing the fillets, however the important feature was to properly capture the three corner regions.

After binary thresholding, flood-fill algorithm integrated within MATLAB environment was applied to store each triangular-shaped fillet as a separate object containing all the inscribed pixels. Each structured fillet was then sorted based upon its average column and row pixel location and a unique ID number was assigned to each fillet structure. Within each fillet, the three corners highlighted in red in Figure 3.15 were obtained by tracking their position. These corners were also used as intermediate points in ribbon reconstruction. On the binary image showing the fillets and the identified corner pixels shown in red, a connectivity array was established to connect neighboring elements. This array was constructed by drawing ellipses of increasing major axis lengths from each fillet sequentially until they intersect with three neighboring elements at most. Figure 3.16 demonstrates the applied procedure in which the angles of the three ellipses relative to the horizontal axis were governed by the angle formed between the fillet centroid coordinates and the three corresponding corners respectively. The connectivity array consists of 4 columns; the first one reflects the number of each individual components, the other three include the ID values of the neighboring fillet structures. For each fillet lying along the four edges of the sandwich core sample, one entry on the connectivity array was filled with zero values. Partial demonstration of the connectivity array is shown in Table 3.1. Given the connectivity array, the sequence of fillets mimicking each ribbon of base material may be obtained by ascendingly ordering the elements of each row of the connectivity array and tracking the position of each element sequentially. In Table

76

3.2, the connectivity array for a full single ribbon is demonstrated. Due to the existence of double walls as a result of the expansion process, it is obvious that fillet structures are repeated within two consecutive ribbons. If needed, fillet structures were artificially embedded on the west and east side of the honeycomb core to create two additional complete ribbons as shown in Figure 3.17. This definition helped with the reconstruction process, and the artificial fillets were removed on the B-spline reconstruction part to back out the original honeycomb core structure as will be later discussed in the subsequent sections. Once connectivity was established, out of the three corner points of each fillet, only the appropriate set of two data points for the reconstruction of each ribbon was ascendingly stored.

In this manner, a ribbon pattern has been created that will allow further discretization of the wall structure contained within each material ribbon. In the binary representation of cell walls excluding the fillets as shown in Figure 3.13, each cell wall segment connecting two consecutive fillet structures from the ribbon ID connectivity was isolated. This task was performed by tracking the pixel coordinates coming from the intersection of two circles centered around the centroids of the fillets under investigation and with radius slightly larger than the side of each fillet, and the cellular structure. Binary value 0 (black color) was assigned to the stack of the intersected pixel coordinates resulting in separation of the wall segment from the continuous honeycomb wall description. In this manner, the individual wall segment was identified as a separate structure entity when flood-fill algorithm was applied as shown in Figure 3.18. Depending on user defined value n_w, the isolated, yet continuous wall segment was discretized into at most n_w nodes to accurately represent the wall path. As expected, the lower the chosen value, the lower the accuracy of the discrete wall representation. This automated discretization was performed using pixelated circles with prescribed radii and centers the last converged discrete point. The procedure was repeated

until the end of the isolated wall segment as partially demonstrated in Figure 3.19. In the unlikely event of 3-point intersection between the circle and the wall segment due to significant wall curvature, the radius was automatically decreased until 2-point intersection was attained. The above procedure was repeated on all wall segments of each ribbon, and nodal coordinates were stored in vector format. The applied scheme looks similar to that of Figure 3.20, in which single and double walls were discretized in 6 and 2 discrete points respectively. As expected, double walls between two consecutive ribbons share the exact same discrete points. Finally, it is implied in this discretization scheme that the fillets were joined to the wall structure, meaning that possible local disbond due to compression was not accounted for. The advantage of this procedure is that the required number of data points required to accurately reconstruct the geometry of the scanned sample is roughly three orders of magnitude less than scan resolution. This process is also useful for modelling cell wall behavior with zero thickness shell finite elements. The step after honeycomb discretization includes the implementation of B-spline surfaces and volumes in order to obtain a geometric numerical model.

3.5   FEATURES OF B-SPLINE THEORY

3.5.1   Lagrange Interpolation and Bézier Curves

The mathematical representation of geometric curves and surfaces can be performed by utilizing either implicit equations or parametric functions. For implicit schemes, the coordinates x, y of a curve in 2-D space are related through an equation $f(x, y) = 0$. An example of implicit description of a curve is a unit radius circle as shown in equation (3.1). In computer-aided design (CAD) modeling, this scheme is rather inefficient since a nonlinear equation needs to be solved to find pairs of coordinates lying on the curve.

78

$$f(x, y) = x^2 + y^2 - 1 = 0 \tag{3.1}$$

On the other hand, parametric schemes feature the change of position of a single point along a curved path as a function of a parametric independent variable, u. The parametric variable, u and the associated function can be interpreted as a time variable and a position vector quantity $\mathbf{C}(u)$ in 2-D or 3-D space respectively. For instance, one of the parametric representations of a unit radius circle has the form of equation (3.2).

$$\mathbf{C}(u) = \begin{Bmatrix} x(u) \\ y(u) \end{Bmatrix} = \begin{Bmatrix} \cos(u) \\ \sin(u) \end{Bmatrix} \tag{3.2}$$

Polynomial parametric functions are adopted herein due to their simple nature and robustness at describing more complicated shapes. Lagrange polynomials are the simplest form of polynomial interpolation. Given a set of data points $\mathbf{Q}_i$ in 2-D or 3-D space, the interpolation function is given by (3.3).

$$\mathbf{C}(u) = \sum_{i=0}^{n} L_i(u) \mathbf{Q}_i = \sum_{i=0}^{n} \left(\prod_{j=0, j \neq i}^{n} \frac{u - u_j}{u_i - u_j} \right) \mathbf{Q}_i \tag{3.3}$$

Data points $\mathbf{Q}_i$ do not necessarily need to be uniformly distributed with respect to parametric variable, u. The Lagrange basis functions $L_i(u)$ of degree n are defined in a way that the resulting curve $\mathbf{C}(u)$ exactly passes through the given data points. An example of Lagrange interpolation is shown in Figure 3.21.

Despite the exact fitting at data points $\mathbf{Q}_i$, Lagrange interpolation does not provide geometrically insightful information of the shape of the curve elsewhere. To overcome this issue,

a mathematically equivalent representation of Lagrange interpolation can be obtained through Bézier curves. A nth Bézier curve is defined by equation (3.4).

$$C(u) = \sum_{i=0}^{n} B_{i,n}(u)P_i = \sum_{i=0}^{n} \binom{n}{i} u^i (1-u)^{n-i} P_i \qquad (3.4)$$

The geometric coefficients P_i are control points in 2-D or 3-D space and the piecewise linear interpolation of those points is known as the control polygon. The corresponding basis functions $B_{i,n}(u)$ are essentially Bernstein polynomials and they can be obtained in a recursive mode as shown in the schematic of Figure 3.22 for a cubic Bézier curve.

Based on the recursive pattern and by defining $B_{0,0} = 1$, the $B_{1,2}(u)$, Bernstein basis function will be given by equation (3.5). The main advantage of Bézier description relative to Lagrange polynomials is that the resulting curve $C(u)$ will lie on the convex envelope of the control polygon as shown in Figure 3.23. Moreover, the lines connecting the first and last two control points are tangent to the resulting curve at the starting and ending points respectively. The recursive nature of Bézier formulation is also geometrically evaluated for a fixed value of parametric variable u in Figure 3.23. This visual interpretation demonstrates that the entire set of control points affects the curved path at any time instance suggesting that the basis functions $B_{i,n}(u)$ have been globally defined over the full range of parametric variable.

$$B_{1,2}(u) = uB_{0,1}(u) + (1-u)B_{1,1}(u) = u(1-u) + (1-u)u = 2u(1-u) \qquad (3.5)$$

Fitting a Bézier curve on specific data points Q_i requires the solution of a system of equations in order to compute the corresponding control points P_i. However, the non-local control

of Bézier formulation can potentially create an ill-conditioned square matrix leading to spurious solutions. When a higher degree polynomial interpolation needs to be computed like the one in Figure 3.24, local peaks in between two consecutive data points can be observed. This abrupt deviation from data points is not desirable in computer-aided modeling, thus more robust design techniques were developed.

B-spline curve theory overcomes the need for fitting $(n+1)$ data points with a precisely n^{th} degree polynomial expression by adopting an interpolation of a series of lower degree polynomials. In Figure 3.24, the B-spline curve interpolation looks smoother compared to the ill-conditioned Bézier description due to the piecewise nature of those curves as will be thoroughly described in the following section. In reality, Bézier curves are a small subset of the generalized B-spline theory. Non-Uniform Rational B-spline (NURBS) curve theory is an even broader class of parametric functions that has been established to precisely model complicated shapes (i.e. arc of a circle) as a combination of rational polynomial expressions. However, selection of B-spline technique was deemed as accurate enough for the reconstruction of honeycomb cores. In their textbook, Piegl and Tiller have thoroughly compared the features and weaknesses of most polynomial parametric functions available in literature [Piegl and Tiller, 2012]. The key elements of B-spline theory that have been used to develop 3-D X-ray CT-scan segmentation will be presented in the next sections.

3.5.2 Formulation of B-spline Curves, Surfaces and Volumes

A pth B-spline curve $\mathbf{C}(u)$ is defined based upon coordinates of control points $\mathbf{P}_i$ and the relationship (3.6). For the remainder of the following sections, the parametric variable u will range from 0 to 1. Based on relationship (3.6), the order of polynomial $\mathbf{C}(u)$ does not need to be equal

to the number of control points. In the special case of $p = n$, Bézier formula will be obtained.

$$\mathbf{C}(u) = \sum_{i=0}^{n} N_{i,p}(u)\mathbf{P}_i \tag{3.6}$$

The trick here lies on the definition of the basis functions which may not seem so intuitive at first. As stated earlier, the main disadvantage of Bézier functions is the non-local control. The need for a high degree polynomial can be eliminated by narrowing down the span of each basis function $N_{i,p}(u)$ to specific partitioned parametric intervals while zero elsewhere. The boundary values of those parametric intervals are called knots and all knots are clustered in the knot vector U at an ascending order as shown in equation (3.7).

$$U = \left\{ u_0, \quad u_1, \quad ..., \quad u_{m-1}, \quad u_m \right\} \tag{3.7}$$

. The ith basis function $N_{i,p}(u)$ is defined by the set of equations (3.8). As expected, knot vector selection is crucial for the final shape of each basis function. Knots need not be spaced uniformly, in fact some knots can be intentionally repeated to reduce the order of continuity of the resulting B-spline curve. When a knot is repeated, the knot span degenerates into a single parametric point. The pth-degree basis functions have a recursive built-up character that requires knowledge of lower degree polynomials as shown in the truncated triangle of Figure 3.25. In this sense, an arbitrary basis function $N_{i,p}(u)$ will be non-zero for any $u \in [u_i, u_{i+p+1})$. However, quite a few basis functions in the truncated triangle are going to be zero for a predefined value u. The reason for this behavior is attributed to the local support of each 0th-degree step function $N_{i,0}(u)$ for knot spans containing two consecutive knots. In Figure 3.26, basis functions are only limited to a small parametric region illustrating the local character of the B-spline basis formulation. The

entire collection of functions $N_{i,p}(u)$ also serves the property of non-negativity and their values are bounded between zero and unity as illustrated in Figure 3.26.

$$N_{i,0}(u) = \begin{cases} 1, & \text{if } u_i \le u < u_{i+1} \\ 0, & \text{elsewhere} \end{cases}$$

$$N_{i,p}(u) = \frac{u - u_i}{u_{i+p} - u_i} N_{i,p-1}(u) + \frac{u_{i+p+1} - u}{u_{i+p+1} - u_{i+1}} N_{i+1,p-1}(u) \tag{3.8}$$

From equation (3.6) and the form of basis functions $N_{i,p}(u)$, a B-spine curve is dependent on three parameters, namely the coordinates and number of control points $\mathbf{P}_i$, the desired p degree of the curve and the knot vector U. Those parameters cannot be randomly picked but instead a constraint equation is linking them. A qualitative example will be demonstrated to establish the relationship among them. For a 3rd -degree Bézier curve, we need four control points and four 3rd -degree basis functions in total. The truncated triangle including all the basis functions is shown in Figure 3.27. Since Bézier curve displays a non-local support, the entire parametric field should be covered by a single knot span $[u_i, \ u_{i+1}]$. Intuitively, the knot span of interest is $[u_3, \ u_4]$ as the dashed triangle of Figure 3.27 mimics the Bernstein triangle of Figure 3.22. The rest of the basis functions do not need to be calculated, so the knots before u_3 and after u_4 could be set to zero and unity respectively. In this sense, knot values 0 and 1 are repeated $p+1$ times in the knot vector. The need for precisely $2p+2$ knots of 0 and 1 and $2p$ single point knot spans can be extended to any B-spline curve of desired degree p. As a result, for a knot vector $U = \{u_0 = 0, \ ..., u_p = 0, \ u_{p+1}, \ ..., u_{m-p-1}, u_{m-p} = 1, \ ..., u_m = 1\}$, relationship (3.9) needs to hold to prevent erroneous calculations.

$$m = n + p + 1 \tag{3.9}$$

In a nutshell, the following remarks can be made regarding B-spline formulation:

- The resulting p^{th} -degree B-spline curve is a piecewise polynomial expression that has C^{p-1} continuity if knot values in knot vector are not duplicated.

- Owing to the non-negativity property of basis functions $N_{i,p}(u)$, B-spline curve is fully contained within the control polygon connecting the control points.

- Given a set of control points $\mathbf{P}_i$, the B-spline curve approaches the control polygon as the degree p decreases. If $p = 1$, the piecewise control polygon is obtained. Finally, if $p = 2$, the control polygon lines are locally tangent to the resulting curve. Examples of different degree B-spline curves are shown in Figure 3.28.

- For a given set of control points $\mathbf{P}_i$, selection of different knot vectors can change the shape of the curve as illustrated in Figure 3.29. Depending on how non-uniform the knots on the full parametric domain $u \in [0,\ 1]$ are, a single point may travel faster or slower along the curve compared to a uniform knot distribution. The effect of knot vector selection is particularly important for B-spline interpolation as there are many constraints than need to be satisfied.

A B-spline surface $\mathbf{S}(u,v)$ can be created by defining a patch of control points $\mathbf{P}_{i,j}$ and a set of knot vectors in 2-dimensional parametric space as shown in equation (3.10). The control patch has $(n+1)\times(l+1)$ entries and the polynomial degrees are equal to p and q in u and v parametric spaces respectively. In other words, a single point starting from one corner control point

$\mathbf{P}_{0,0}$ will travel along a generally non-planar surface to finally reach the opposite control point $\mathbf{P}_{n,l}$. Following the same principles of B-spline curve formulation, the knot vector V in v parametric space has the form of relationship (3.11). The size of the knot vector will be related to the degree q and the number of control points along v - direction through relationship (3.12).

$$\mathbf{S}(u,v) = \sum_{i=0}^{n}\sum_{j=0}^{l} N_{i,p}(u)N_{j,q}(v)\mathbf{P}_{i,j} \tag{3.10}$$

$$V = \left\{v_0 = 0,\ ...,\ v_q = 0,\ v_{q+1},\ ...,\ v_{s-q-1},\ v_{s-q} = 1,\ ...,\ v_s = 1\right\} \tag{3.11}$$

$$s = l + q + 1 \tag{3.12}$$

The properties of B-spline surfaces are very similar to the ones described for B-spline curves. An example of surface given a patch of control points $\mathbf{P}_{i,j}$ is shown Figure 3.30. The corresponding heating map reflects the absolute displacement magnitude as the square root of the sum of the squares of each displacement component with respect to a reference surface based upon bilinear interpolation of the four corner points. B-spline surface formulation is going to be used to reconstruct cellular wall geometry based on X-ray CT-scan data.

By adding a third parametric variable w and a volumetric set of control points, B-spline volumes are obtained as shown in equation (3.13). The eight vertices of the resulting volume correspond to the vertices of the control point volume set. Given a polynomial degree r, the generally non-uniform knot vector associated with the third parametric variable will be given by equation (3.14).

$$\mathbf{V}(u,v,w) = \sum_{i=0}^{n}\sum_{j=0}^{l}\sum_{k=0}^{t} N_{i,p}(u)N_{j,q}(v)N_{k,r}(w)\mathbf{P}_{i,j,k} \tag{3.13}$$

$$W = \left\{ w_0 = 0, \ ..., \ w_r = 0, \ w_{r+1}, \ ..., \ w_{o-r-1}, \ w_o = 1, \ ..., \ w_o = 1 \right\} \qquad (3.14)$$

Relationship (3.15) needs to hold to keep knot vector size and control point size consistent with respect to parametric variable w. An example of B-spline volume is shown in Figure 3.31. This formulation is going to be utilized to reconstruct the filleted columns as captured by CT-scans and optical microscopy images.

$$o = t + r + 1 \qquad (3.15)$$

3.5.3 Fitting Procedure for B-spline Curves and Surfaces Interpolation

B-spline formulation allows for an interactive shape construction by allowing user-defined selection of control points. On the other hand, fitting data points in space with a B-spline curve requires an inverse procedure. A B-spline curve of degree p should precisely pass through a given data point $\mathbf{F}_\xi$ if equation (3.16) holds at $u = \hat{u}_\xi$. There is a need for exactly $n+1$ equations of different data points $\mathbf{F}_\xi$ to be able to compute control points $\mathbf{P}_i$.

$$\mathbf{F}_\xi = \sum_{i=0}^{n} N_{i,p}(\hat{u}_\xi) P_i, \ \text{for } \xi = 0, \ 1, \ ..., \ n \qquad (3.16)$$

Typically, the only known part when trying to fit a curve is the coordinates of the $n+1$ data points. The system of equations cannot be solved directly because both the knot vector U and the collection of parametric values $\hat{u}_\xi$ are thus far unknown. One approach to determine the set of $\hat{u}_\xi$ is to equally space them based on the number of data points as shown in equation (3.17).

$$\hat{u}_\xi = \frac{\xi}{n}, \ \text{for } \xi = 0, \ 1, \ ..., \ n \qquad (3.17)$$

However, if data points $\mathbf{F}_\xi$ are not uniformly spaced, the B-spline interpolation may exhibit local peaks between two consecutive data points. In set of equations (3.18), a non-uniform distribution based on the distances between the given data points is established. Both methods have been used for the interpolation of cellular wall data obtained from X-ray CT-scans.

$$\hat{u}_0 = 0,$$
$$\hat{u}_\xi = \hat{u}_{\xi-1} + \frac{\sqrt{\left|\mathbf{F}_\xi - \mathbf{F}_{\xi-1}\right|}}{\sum_{\xi=1}^{n}\sqrt{\left|\mathbf{F}_\xi - \mathbf{F}_{\xi-1}\right|}}, \quad \text{for } \xi = 1, \ ..., \ n \tag{3.18}$$

The next step requires the calculation of the knot vector. Knots can be distributed evenly based on the number of data points as presented in equation (3.19). Alternatively, knots can be determined by averaging the parametric values $\hat{u}_\xi$ based on the scheme of (3.20). For simplicity, the knots corresponding to zero and unity are not included in both equations. The uniform distribution of knots is not a safe option when it is combined with a uniform collection of $\hat{u}_\xi$ (see equation 3.18), as the resulting matrix of basis functions may not be positive definite.

$$u_{i_f + p} = \frac{i_f}{n - p + 1}, \quad \text{for } i_f = 1, \ ..., \ n - p \tag{3.19}$$

$$u_{i_f + p} = \frac{1}{p}\sum_{j_f = i}^{i_f + p - 1} \hat{u}_{j_f}, \quad \text{for } i_f = 1, \ ..., \ n - p \tag{3.20}$$

Once the parametric values $\hat{u}_\xi$ and the knot vector U have been determined, the linear system of equations can be solved for the unknown control points $\mathbf{P}_i$ establishing in this way a unique B-spline curve passing through the given data points. The non-uniform and uniform

87

descriptions of knot vector and set of parametric values $\hat{u}_{\xi}$ respectively may produce different interpolation curves for the same dataset as depicted in Figure 3.32. The red curve demonstrates significant oscillatory behavior, while the blue curve fully adapts to the random position of data points proving that non-uniform knot distribution is more appropriate. An application of the fitting scheme on the reconstruction of a cell wall based obtain from X-ray CT-scan image is shown in Figure 3.33. The uniform distribution of knots as well as the set of parametric values $\hat{u}_{\xi}$ produces a fitted curve which is highly erratic close to the intersection of single and double walls.

The curve interpolation presented herein can be extended to a patch of data points $\mathbf{F}_{\xi,\zeta}$ to obtain a fitted B-spline surface of degree p and q along u and v parametric spaces respectively as shown in equation (3.21). In this case, the parametric set of values $\hat{u}_{\xi}$ and $\hat{v}_{\zeta}$ may be calculated as the average among each point of v and u parametric directions respectively. The corresponding knot vectors U and V will then be obtained from equation (3.19), and equation (3.20) respectively. Since the number of equations is equal to $(n+1)\times(l+1)$, it is easier to split the procedure in two steps by solving equation (3.16) twice, one for each independent parametric variable, and ultimately compute the patch of control points $\mathbf{P}_{i,j}$. This scheme is used to reconstruct the honeycomb cell walls with their inherent imperfections during manufacturing and co-curing processes. Figure 3.34 shows an example of surface fitting in which the heating map represents the absolute displacement magnitude as the square root of the sum of the squares of each displacement component with respect to a reference surface based upon bilinear interpolation of the four corner points. In surface fitting, knots along u and v direction as well the set of parametric values $\hat{u}_{\xi}$ and $\hat{v}_{\zeta}$ could be independently chosen using either uniform or non-uniform distribution.

$$\mathbf{F}_{\xi,\zeta} = \sum_{i=0}^{n}\sum_{j=0}^{l} N_{i,p}(\hat{u}_{\xi})N_{j,q}(\hat{v}_{\zeta})\mathbf{P}_{i,j}, \text{ for } \xi = 0,\ 1,\ ...,\ n \text{ and } \zeta = 0,\ 1,\ ...,\ l \qquad (3.21)$$

3.5.4 Fitting Data Points with Predefined End Derivatives

In many cases, the fitting technique described in the previous section requires additional constraints mainly related to the first derivatives at the end points of the resulting curve. The first derivative of a B-spline curve is obtained by differentiation of the basis functions. It can be shown that the slopes at the two ends of the curve are given by the set of equations (3.22). As a result, the lines connecting the first and last two control points are always tangent to the B-spline curve at both ends. The slope of the curve at the two ends is determined by the ratio between the X and Y coordinates of the derivative vector. However, its magnitude dictates how far away the second and second to last control points are located with respect to the coordinates of the end control points.

$$\mathbf{C}'(0) = \frac{p}{u_p + 1}(\mathbf{P}_1 - \mathbf{P}_0),$$

$$\mathbf{C}'(1) = \frac{p}{1 - u_{m-p-1}}(\mathbf{P}_n - \mathbf{P}_{n-1}) \qquad (3.22)$$

A fitting scheme with $n+1$ data points $\mathbf{F}_{\xi}$ and user defined end derivatives $\mathbf{D}_0$, $\mathbf{D}_1$ thus requires $n+3$ control points. The additional set of derivative equations can be solved directly through forward or backward substitution to compute the second and second to last control points $\mathbf{P}_1$, $\mathbf{P}_{n+1}$. It should be noted that the set of parametric variables $\hat{u}_{\xi}$ should not change with the addition of the two extra equations. Only the knot vector U needs to be evaluated to account for the two extra control points. An example of the modified scheme is shown in Figure 3.35. The slope of the chosen end derivative vectors mimics the slope of the lines connecting the first and

last two data points $\mathbf{F}_\xi$ respectively. In this way, specifying the end derivatives of the single cell walls enables the formation of a finite angle at the intersection of two consecutive single walls. This finite angle is particularly important to finite element modeling of the honeycomb structure as the chance of excessively distorted solid elements at the fillet regions is mitigated. Finally, in Figure 3.36, high magnitude derivative vectors lead to a spurious fitting curve suggesting that the scale factor associated with those vectors should be judiciously chosen to avoid this kind of phenomena.

3.5.5 Knot Refinement

As have been stated earlier, a pth-degree B-spline curve is dependent on the coordinates of the control points $\mathbf{P}_i$ and the selection of knot vector U. Given those parameters, the same curve $\mathbf{C}(u)$ can be reproduced by knot insertion technique which utilizes the position of an additional knot value into the existing knot vector U. When a new fixed knot value $\bar{u}$ is being added, it should be placed in an ascending order to form the augmented knot vector $\bar{U}$ of equation (3.23). The problem comes down to the computation of a set of $n+2$ control points $\mathbf{R}_i$ given the augmented knot vector $\bar{U}$ as shown in equation (3.24).

$$\bar{U} = \left\{ u_0,\ u_1,\ ...,\ u_{i_k},\ \bar{u},\ u_{i_k+1},\ ...,\ u_m \right\} \tag{3.23}$$

$$\sum_{i=0}^{n} N_{i,p}(u)\mathbf{P}_i = \sum_{i=0}^{n+1} \hat{N}_{i,p}(u)\mathbf{R}_i \tag{3.24}$$

Based on the recursive definition of a B-spline curve, the terms on the series that are going to be affected are displayed in equation (3.25). The remaining terms including both the basis

functions and the associated control points are going to be identical before and after knot insertion. Finally, the intermediate control points are computed as a recursive linear combination of the current set of control points. The computation of the knot inserted control points is depicted in set of equations (3.26).

$$\sum_{i=i_k-p}^{i_k} N_{i,p}(u)\mathbf{P}_i = \sum_{i=i_k-p}^{i_k+1} \hat{N}_{i,p}(u)\mathbf{R}_i \qquad (3.25)$$

$$\begin{aligned} \mathbf{R}_i &= \mathbf{P}_i, \ \text{for } i = 0, \ ..., \ i_k - p \\ \mathbf{R}_i &= \frac{\bar{u} - u_i}{u_{i+p} - u_i}\mathbf{P}_i + \frac{u_{i+p} - \bar{u}}{u_{i+p} - u_i}\mathbf{P}_{i-1}, \ \text{for } i = i_k - p + 1, \ ..., \ i_k \\ \mathbf{R}_i &= \mathbf{P}_{i-1}, \ \text{for } i = i_k + 1, \ ..., \ n+1 \end{aligned} \qquad (3.26)$$

Insertion of knot value $\bar{u}$ may be repeated multiple times a technique mostly well known as knot refinement. In knot refinement, a knot is inserted p times and the new control points $\mathbf{R}_i$ are calculated sequentially according to the set of equations (3.26) by adding one knot at a time. This procedure has several applications including the partition of a single B-spline curve into finer B-spline segments as illustrated in Figure 3.37, and the creation of finer mesh models in advanced computational methods [Hughes et al., 2005].

Since the shape of the edges of the filleted regions at honeycomb cells complies with the single cell wall geometry during dipping and resin curing process, knot refinement can be utilized to precisely model those edges as illustrated by the orange curve in Figure 3.38. In general, the boundaries of the edges of two consecutive fillets are determined by the first and last two fitted points of the single cell wall connecting them. For the 3rd-degree B-spline single cell wall of Figure 3.38, the parameter value $\hat{u}_\zeta$ fitting the second to last data point was found to be equal to 0.91.

91

This value was also selected for the knot refinement procedure to ensure that the resulting curve precisely fits the two last two data points when U is equal to 0.91 and 1. Thus, the modified knot vector is equal to $\bar{U} = \{0, 0, 0, 0, 0.27, 0.42, 0.56, 0.69, 0.80, 0.91, 0.91, 0.91, 1, 1, 1, 1\}$ and the number of control points $\mathbf{R}_i$ increased by 3. However, a splitting operation is necessary to recover only the last segment of the curve corresponding to the edge of the fillet. The resulting 3rd-degree curve of interest ultimately has a knot vector $\bar{U} = \{0.91, 0.91, 0.91, 0.91, 1, 1, 1, 1\}$ and four control points as depicted in Figure 3.38.

3.6 IMPLEMENTATION OF B-SPLINE THEORY ON DISCRETIZED HONEYCOMB CORES

The entire list of geometric modeling tools presented so far was used to geometrically reconstruct different honeycomb core coupons given an image-based discretization. The main features of the reconstruction process are evaluated for a single CT-scan slice and extrapolation to multiple slices can be performed through surface fitting. Figure 3.39 shows that the v parametric variable reflects shape changes along the thickness of the core while change of coordinates at fixed elevation is dependent upon u parametric variable. The image-based discretization scheme is applied at $(l+1)$ CT-scan slices to form a grid of fitted points. The number of CT-scan slices used ranges from 10 up to 20 slices to cover the entire core thickness excluding the core parts in which the adhesive film has pooled into. The X-ray CT resolution along the through thickness direction is about 700 pixels, thus a significant reduction in post-processing computation cost is attained by discretizing almost two orders of magnitude fewer images. Cell wall data points are stored according to the geometry of a material ribbon as physically obtained during adhesive node bonding and expansion process. Figure 3.40 demonstrates a ribbon of finite data points at a specific

CT-scan slice.

Given the data points of a ribbon entity, a single B-spline zig-zag surface can be theoretically constructed using the interpolation principles developed in the previous sections. However, a couple of technical downsides arise by directly applying the fitting scheme. Firstly, the angle at the intersection between single and double walls cannot be easily controlled. Not only are the discretized fillets possibly going to be highly distorted during finite element analysis, but also adjacent ribbons may locally inter-penetrate to each other. In reality, bonded regions should follow the same geometry because the adhesive nodes joining the individual ribbons are locally constraining relative displacements. These issues are overcome by applying the fitting scheme in segments. Each segment represents either a single or double wall of a cell. The ending node of one segment is the starting node of the next one, thus the continuity of the modeled ribbon is guaranteed. The list of steps required for geometric reconstruction of honeycomb core from $(l+1)$ CT-slices are the following:

i. Nodal coordinates of a single ribbon are extracted from the collection of data points stored during image-based wall discretization.

ii. Ribbon entity is segmented into multiple single or double wall parts. End nodes are shared between consecutive segments. The number of nodes for single and double walls is determined at the stage of image-based discretization.

iii. Given a grid of segmented nodes, the control points and the corresponding knot vectors of a B-spline surface of degree p in u parametric space and degree q in v parametric space (through thickness direction) are computed in accordance with section 3.5.3. Both degrees p and q should be at most equal to the number of fitted points per

segment. An additional $(l+1)$ set of derivative vectors needs to be defined to control the angle of the walls at both ends if needed. Special care should be taken regarding the absolute magnitude of the chosen vectors.

iv. Once the basic features of the interpolation surface are obtained, a fine set of parametric variables ranging from zero to unity is selected to visualize the shape of each surface.

v. Next wall segment can be interpolated. Owing to the described segmentation process, C^0 continuity along u parametric direction applies at the node linking two consecutive segments. Within each segment, the surface is $C^{(p-1)}$ and $C^{(q-1)}$ continuous at both parametric directions respectively. However, the connecting edges along the through thickness direction of two consecutive segmented surfaces are precisely identical if and only if the set of parametric variables $\hat{v}_\zeta$ and the corresponding knot vectors V are uniformly distributed in v parametric domain. A non-uniform parametric variable distribution $\hat{v}_\zeta$ is dependent on the coordinates of the nodes of each wall segment. This feature leads to slightly different control points which practically means that the vertical edges of adjacent segments will never be coincident. The out-of-plane wall perturbations are fairly small compared to the thickness of the core and as result the chance of local wiggles due to even knot distribution is minimized. In this manner, $C^{(q-1)}$-continuity is satisfied in the through thickness direction.

vi. For each constructed single wall surface, the edges of the triangular fillets are determined through knot refinement. For each CT-slice used, selected knot values are equal to the parametric values $\hat{u}_\zeta$ of the second and second to last data point of the wall segment under examination. Alternatively, user defined knot values may be

established. The two corner points of each fillet are linearly connected. Once two adjacent ribbon surfaces have been fully developed, a linear interpolation is carried out within the triangular filleted zones at each slice to define a volume of control points $\mathbf{P}_{i,j,k}$. B-spline volume formulation is then used to compute nodes throughout the entire height of the fillets. This step is particularly important in finite element modeling as the nodes of the volume spline are the vertices of solid elements.

vii. Steps a) through f) are repeated for next ribbons. When the control points of a wall segment cross one of the four user-defined boundary limits, knot refinement is applied to split the wall segment and keep only the part that is fully contained within the prescribed limits. As a result, step c) is modified appropriately to account for the boundaries. Finally, the boundaries need not coincide with the boundaries of the imaged-based discretization step and smaller portions of the scanned core sample may be extracted.

The list of steps described above is graphically illustrated in Figure 3.41. The degree of the B-spline surfaces along each CT-scan slice is equal to $p = 3$ for this example. The red dots representing the discretization on the double wall segment are repeated twice such that the two resulting surfaces are identical in the bonded region. This definition is appropriate as the two identical surfaces can be either tie-constrained or interfaced with zero-thickness cohesive zones in finite element modeling to effectively account for the increased cell wall stiffness. The end derivatives of each of the three wall segments are predefined such that the angle of the fillet at the shared node is finite and larger than 35° degrees.

Since the edges of a honeycomb core sample are trimmed due to the tile saw cutting, four

boundary limits should be defined. These limits do not necessarily have to coincide with the boundary during the image discretization process and as a result a subset of the physical sample may be obtained. The process of trimming the edge ribbons involves a combination of the techniques that have already been described. We start off by finding data points corresponding to the intersection of the fitted B-spline curve and the boundary limit for each CT-scan slice separately. The entire set of boundary nodes is then added on the patch of fitted points obtained during image-based discretization. The expanded patch of data points is interpolated by a B-spline surface and the parametric value u_b at the boundary limit is tracked. This parametric value u_b serves as the knot value for the knot refinement applied on the interpolated surface. The knot refinement process is repeated as many times as the degree of the interpolated wall segment. Finally, the resulting knot refined surface is partitioned so that only the portion contained within the specified boundary limits remains. Figure 3.42 shows how a curve at a specific CT-scan slice is trimmed following the steps above. The trimmed surface should be treated as a geometric object described by a patch of control points, the appropriate knot vectors and the end derivative vectors if specified.

Superimposed ring artifacts during X-ray CT-scanning may be present when the axis of one of the detectors is not colinear to the line connecting the center of the cylindrical chamber and the revolving X-ray transducer. Image post-processing aims to alleviate these ring phenomena on the entire volume of the core samples but even after this procedure, there is still a chance of some remaining artifacts. If the color intensity of this scan-based noise is at the same range with the one of the scanned cell walls, binary thresholding locally fails and as a result discontinuous cell wall segments exist as illustrated in Figure 3.43. The cell wall under investigation is described by only eight data points (green dots) due to the missing wall part interfering with the ring artifacts. Since

the number of data points for this particular CT-scan slice is less than the user-defined value, the grid of data points will be inconsistent along v parametric space. This mismatch can be overcome by artificially adding a set of data points shown in red in Figure 3.43. We start off by identifying the CT-scan slice at which the number of data points is the largest. A set of base parametric variables $\hat{u}_{\xi,b}$ is calculated based upon equation (3.18). A B-spline interpolation on all the CT-scan slices having smaller number of data points leads to different sets of parametric variables $\hat{u}_{\xi}$. Given the B-spline control points and corresponding knot vectors, the resulting B-spline curve is evaluated only at the base parametric variables $\hat{u}_{\xi,b}$ that have the largest absolute distance from the set of parametric variables $\hat{u}_{\xi}$. In this manner, additional data points are obtained as illustrated in Figure 3.43 and ultimately the grid of data points gets uniform along the thickness direction. The B-spline surface interpolation scheme can finally be applied on the augmented grid of data points. This procedure is not necessary when the number of data points is consistent throughout the CT-scan slices during image-based discretization.

3.7   APPLICATIONS OF NUMERICAL GEOMETRIC RECONSTRUCTION

3.7.1   Metrics of Manufacturing Induced Irregularities on Sandwich Core Samples

The proposed two-step image procedure can be utilized on untested sandwich core coupons to establish metrics of the inherent geometric imperfections. The focus is on irregularities related to the waviness of the cell walls throughout core thickness, and the size of the triangular fillet regions. The out-of-plane core wall imperfections are attributed to the core manufacturing process itself and the sandwich co-curing process. In co-curing process, uncured composite pre-impregnated facesheets are solidified and adhesively bonded to the core structure at the same time.

Vacuum pressure is applied to the entire assembly to ensure composite skin void removal and full bonding of adjacent plies. The applied pressure can potentially create local distortions on the thin wall structure especially when the sandwich part is cured inside an autoclave and the pressure levels are even higher. As will be later shown, single wall regions exhibited the largest waviness. X-ray computed tomography in conjunction with the proposed reconstruction scheme can serve as a non-destructive tool to quantitively assess the extent of these co-curing induced imperfections. Except for the establishment of metrics which is an important feature for quality control, these irregularities can be included into computational models that are essentially representative of the actual structure. The latter process will be presented in the following chapter.

The irregularities on a CT-scanned sample are defined based upon a linear fit baseline between the top face CT slice of the core and the bottom one. The coordinates of the linear baseline as well the 4th -degree through-thickness interpolation for a particular CT scan slice along the expansion direction are shown in Figure 3.45. The pristine imperfections (%) were defined as the absolute difference of coordinates between the linear baseline and the 4th degree through interpolation normalized by the 25.4 mm nominal core thickness. Even though the selection of a 4th degree surface along the thickness direction yielded slightly larger magnitude imperfections compared to a 2nd degree interpolation, the 4th degree interpolation still provided a smoother transition between the chosen CT scan slices as shown in Figure 3.46. Figure 3.47 shows a 3D map of the imperfections as calculated in the numerical reconstruction scheme. For this particular sandwich core sample, 25 CT-slices were utilized to fully reconstruct its geometry. The degree of B-spline surfaces along each CT-slice was selected to 3 and 2 for the single and double walls respectively. Large imperfections were accumulated in one of the corners possibly due to the tile saw cutting. Figure 3.48 and Figure 3.49 show a direct comparison between raw CT scan slices

and the reconstruction scheme along the expansion and ribbon orthogonal planes respectively. Relative displacements for single and double walls are graphically illustrated in Figure 3.50 and Figure 3.51 respectively. The term relative displacement means the algebraic subtraction of the linear baseline interpolation from the nodal coordinates of the fitting surfaces. Some of the observed oscillations were attributed to the noise arising from the ring artefacts, the noise of the digital image, and the binary thresholding procedure.

Since the largest imperfections were accumulated on one of the edges of the scanned coupon, the 3D map in Figure 3.47 does not provide enough information about the overall metrics on the single and double walls. Figure 3.52 shows a cross-sectional pattern along which the coordinates were fully computed throughout the core thickness utilizing knot refinement technique. Based on the cutting pattern, 24 double and 48 single walls were evaluated in total, and the imperfections normalized to core thickness are summarized in Figure 3.53 and Figure 3.54 respectively. As expected, double walls exhibited less waviness and the average imperfection throughout the entire thickness was equal to 0.096% which is less than the pixel noise normalized by the core thickness. Regarding the single walls, average imperfections were 0.23%, however the peak imperfection approached 1.5% close to the corner. Finally, the area of the triangular-shaped fillets was calculated throughout the core thickness. The results shown in Figure 3.55 reveal that the variation of the fillet area is higher than the variation of waviness. This larger variation was attributed to the non-consistent image processing of each CT slice as a result of the ring artifacts, and the fact that only three corner points were utilized to numerically reconstruct each fillet. The average fillet size was equal to 0.138 mm^2.

3.7.2 Metrics of Residual Displacements on post-tested scanned specimens

The reconstruction scheme described in the previous section was applied on two different core coupons that were initially compressed and then were X-ray CT scanned to determine metrics of residual deformations. The mechanical response of those two coupons is shown in Figure 3.56. Upon loading, displacement reversal/reloading was manually triggered to make sure that the two tests were stopped slightly before and slightly after the peak response. More specifically, the core coupon with ID number CCB-084 was unloaded before the expected peak, while specimen with CCB-085 ID was unloaded at the onset of the softening branch.

The 3D map of the residual displacements for test case CCB-084 is shown in Figure 3.57. Since the X-ray CT scans were performed after the compression tests and pristine imperfections were not tracked via an initial scan, the term residual refers to the subtraction of the linear baseline coordinates from the 3D coordinates obtained by a 4th degree through-thickness spline fitting. For the 3D map of Figure 3.57, the absolute residual displacements were normalized to core thickness. Based on the front face of the 3D map, there were no significant damages within the scanner resolution. The residual displacements of a representative single wall section are shown in Figure 3.58. In this figure, wall #1 is on the verge of fracturing, but the curvature of the B-spline is not that concentrated to speculate that wall kinking was present. The average and peak residual displacements on 24 double and 48 single wall cross-sections are summarized in Figure 3.59 and Figure 3.60 respectively. As expected, double walls showed on average less amount of residual displacements relative to the single walls. The reported peak displacements did not reveal any major single wall damage.

On the other hand, the 3D map of the residual displacements of test case CCB-085 reported

in Figure 3.61 revealed significant localized residual displacement at one of the single walls. The peak residual displacement for test CCB-085 is 25% higher than that of the nearly-crushed test CCB-084. This feature should be a sign of wall kinking very close to the intersection with the fillet. A closer view of the possible damaged region is shown in Figure 3.62 by taking a cross-section along the ribbon direction. In Figure 3.62, wall #1 corresponding to the damaged wall of the 3D map of Figure 3.61 developed significant kinking as illustrated by the large local curvature accompanied by the high residual magnitude. Finally, the average and peak residual displacements on 24 double and 48 single wall cross-sections for case study CCB-085 are summarized in Figure 3.63 and Figure 3.64 respectively. The average trends for 24 double and 48 single wall cross-sections are very similar to those of test case CCB-084. In general, the 3D map of the residual displacements gives the clearest picture of possible localized damage. On the other hand, metric plots such as the one in Figure 3.64 provide an estimate of the average residual displacements and imperfections.

3.7.3   In-situ X-ray CT scan on Progressively Compressed Coupon

An in-situ portable load frame was designed at Utah Composite Mechanics Lab to enable X-ray CT scanning at different load stages. A snapshot of the actual fixture is shown in Figure 3.65 and it is equipped with a stepper motor with rated maximum load of about 900 N. Due to the size limitations of the in-situ frame and the supporting base, a core sample of 4 fully enclosed cells was scanned. The effective stress vs. out-of-plane strain curve is shown in Figure 3.66 along with the 4 different displacement increments at which test progression was paused for X-ray CT scanning. The last scan was performed immediately after peak load. The displacement data was shifted along the x-axis based upon a linear regression of the elastic portion of the curve. The slight load drop after each scan was attributed to material relaxation. X-ray CT scans at the 4 distinct

displacement increments are summarized in Figure 3.67, Figure 3.68, and Figure 3.69.

In Figure 3.67, outer free-edge single walls start moving inwards even at the lowest strain increment. At the collapse limit state, fillet fracture and detachment has occurred at the bottom right corner. The adjacent cell walls started peeling off from the adhesive node lines in the double wall region as a result of the instability caused by the fillet detachment. Finally, there is no evidence of double wall region crushing. In Figure 3.68, the out-of plane behavior of the single walls is shown. At strain increment "1", minor buckling of single cell walls has initiated, but the amount, thus no change in specimen stiffness was observed. At strain increment "2", buckling has propagated, and the stiffness of the specimen starts hardening. Localized kinking may be observed at wall #2. At strain increment "3", the far-right wall has clearly fractured. Figure 3.69 shows the test progression of the double wall regions. There is no sign of buckling in the first two strain increments. At strain increment "3", visible buckling has occurred, but no compression failure in the form of compression crushing is evident at this CT scan slice. The reconstruction scheme was applied at strain increments "1" and "2" to numerically capture the displacement contours as shown in Figure 3.70 and Figure 3.71. Due to high distortions imposed by the X-ray CT scan noise, the fillets exhibited major variations through the thickness direction as can be observed in the figures. On the other hand, the cell wall geometry was accurately tracked. Since the reconstruction scheme assumes that fillets are always attached to the paper ribbons, strain increment "3" was not numerically post-processed.

In conclusion, X-ray computed tomography is one of the most reliable and high-fidelity imaging techniques, particularly for fully enclosed systems such as honeycomb cores. In this sense, damage morphology can be captured within the scanner resolution in a non-destructive manner. In addition, the proposed reconstruction scheme allows a quantitative interpretation of the pixelated

102

data, which can be used as a tool for numerical model generation accounting for local defects.

Chapter 3, in part is currently being prepared for publication of the material. Anagnostopoulos, K., Czabaj, M. W., Kim, H. The dissertation author is the primary investigator and author of this material.
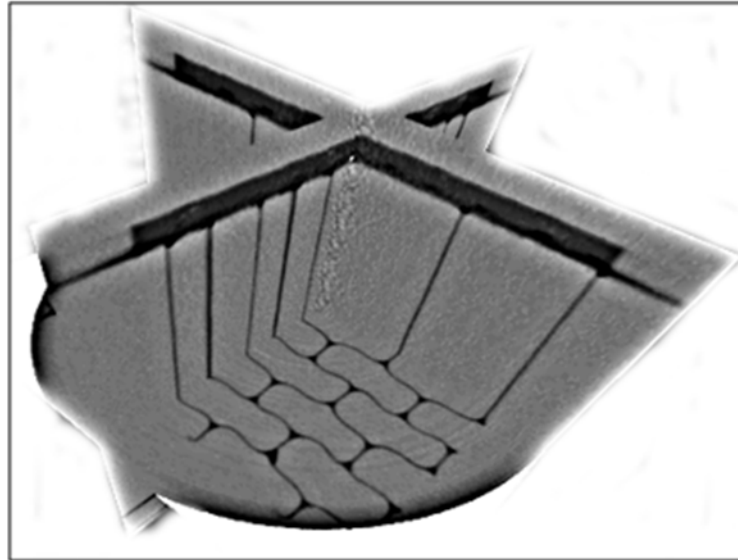
Figure 3.1. Isometric CT scan view of mutually orthogonal planes
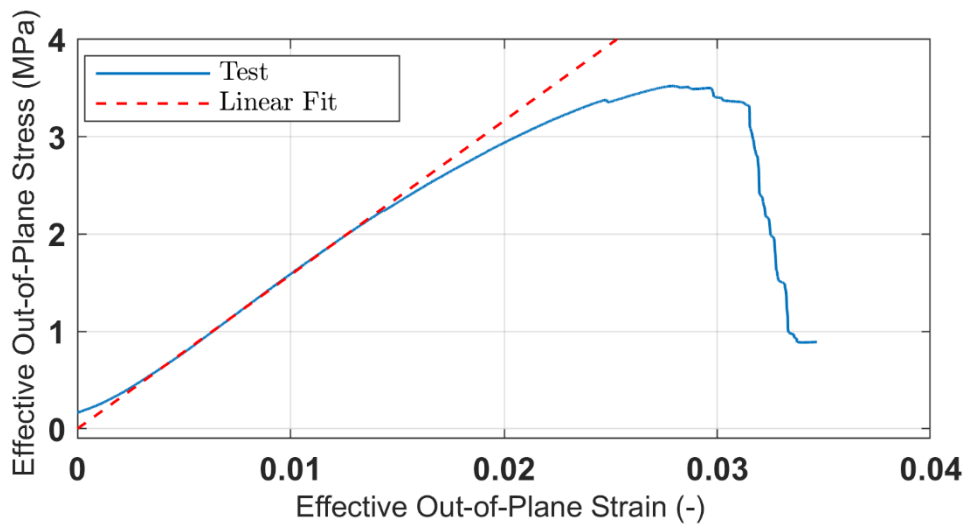
Figure 3.2. Effective stress vs strain on CT scanned sandwich core sample
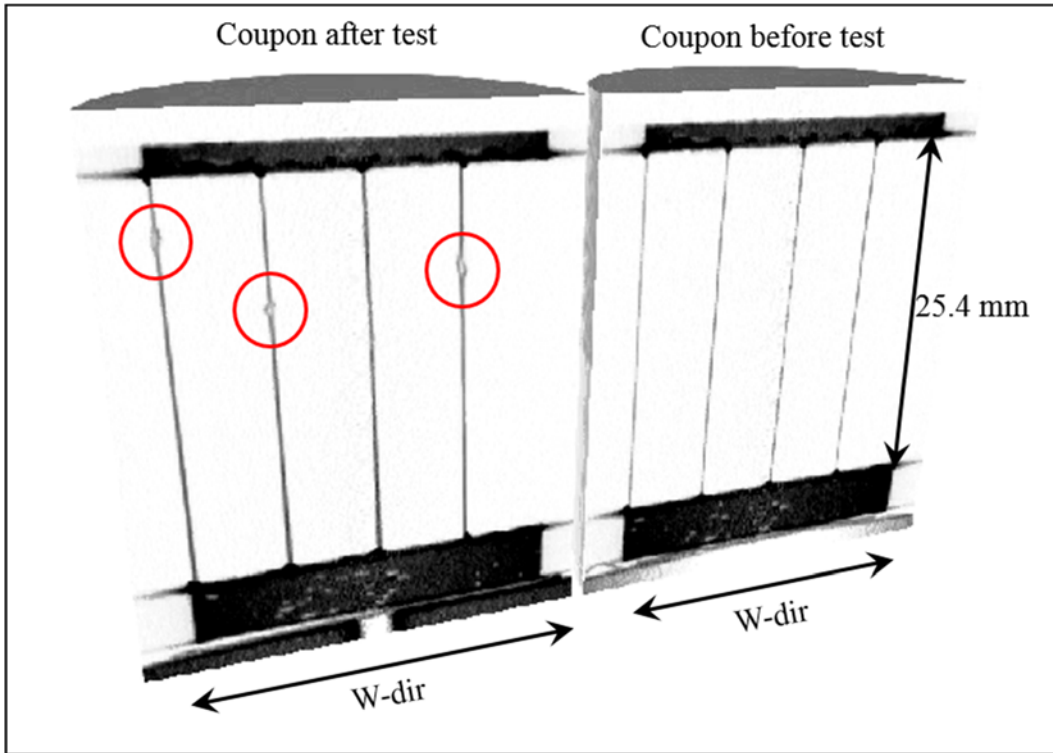
Figure 3.3. CT scan comparison before and after testing
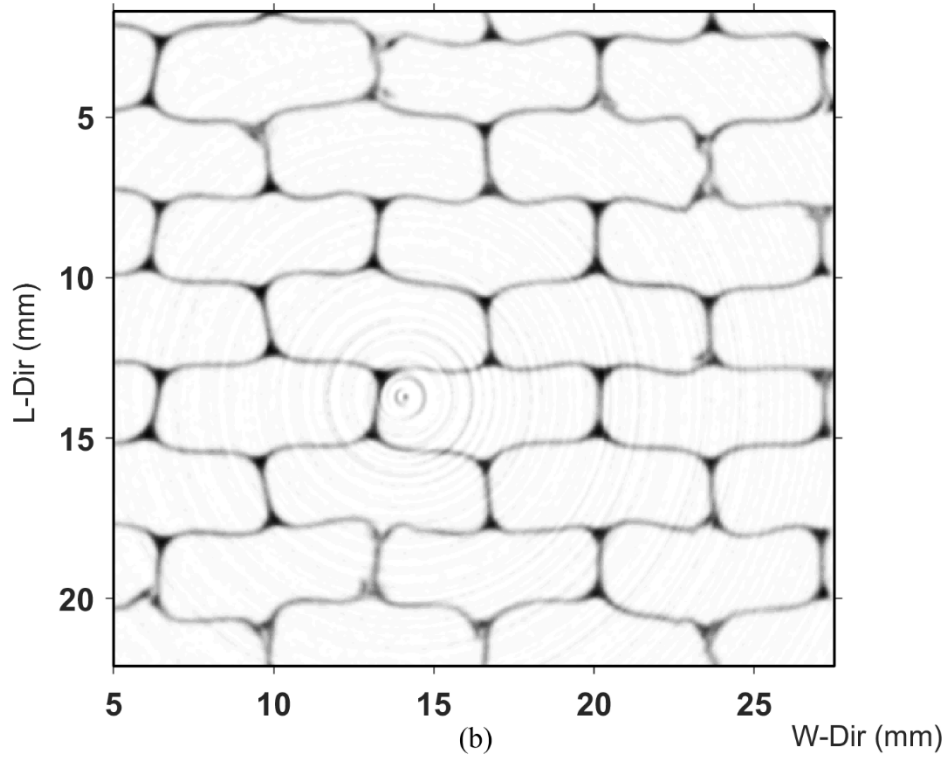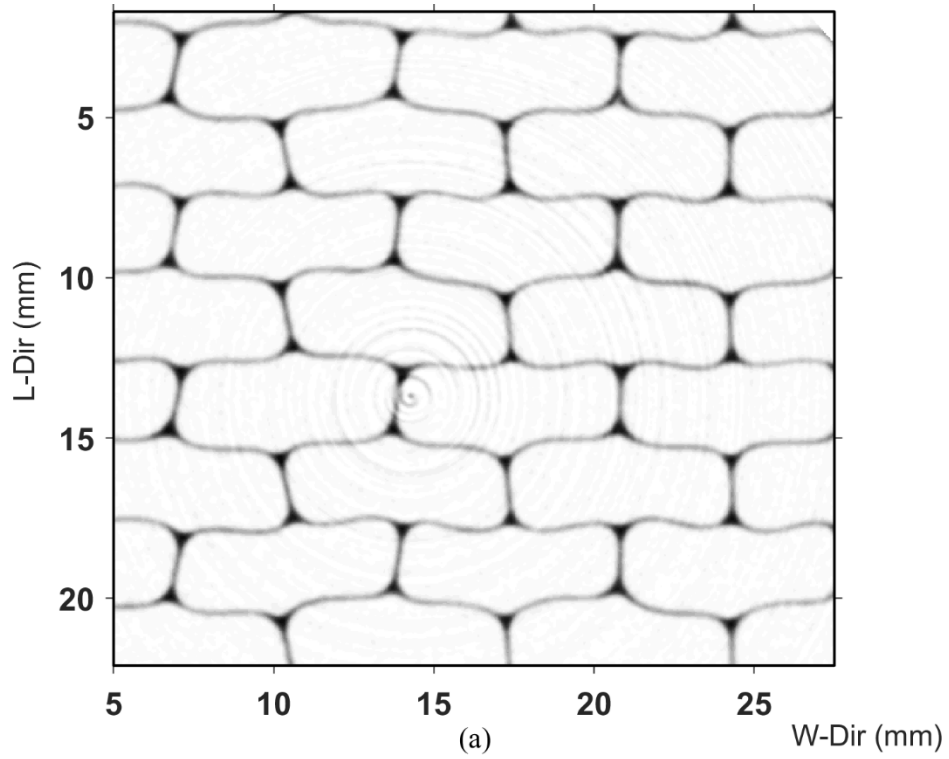
Figure 3.4. Through-thickness slice at 21.4 mm elevation from top: (a) Before test; (b) After test
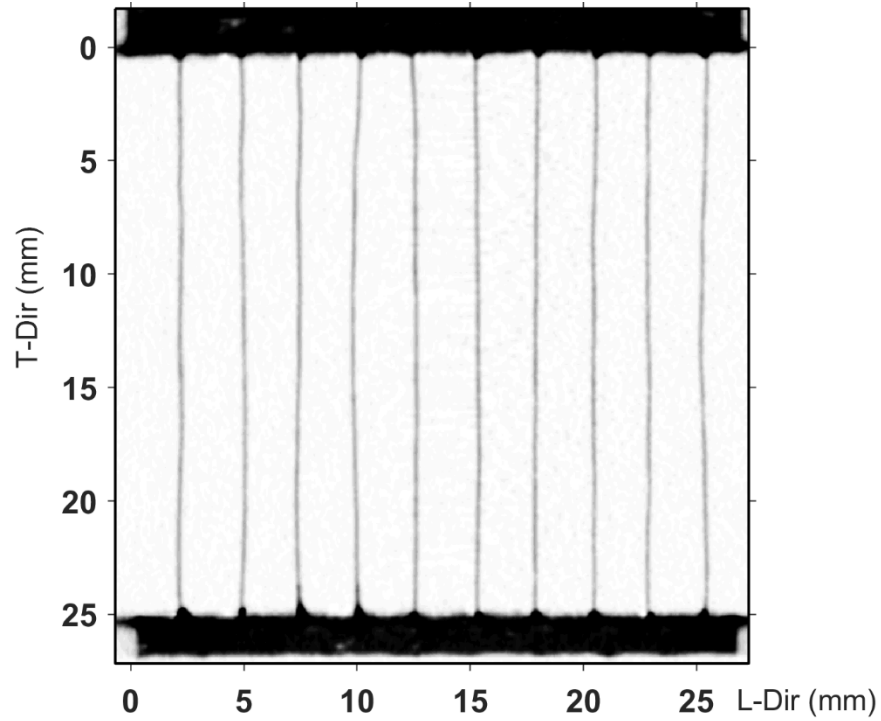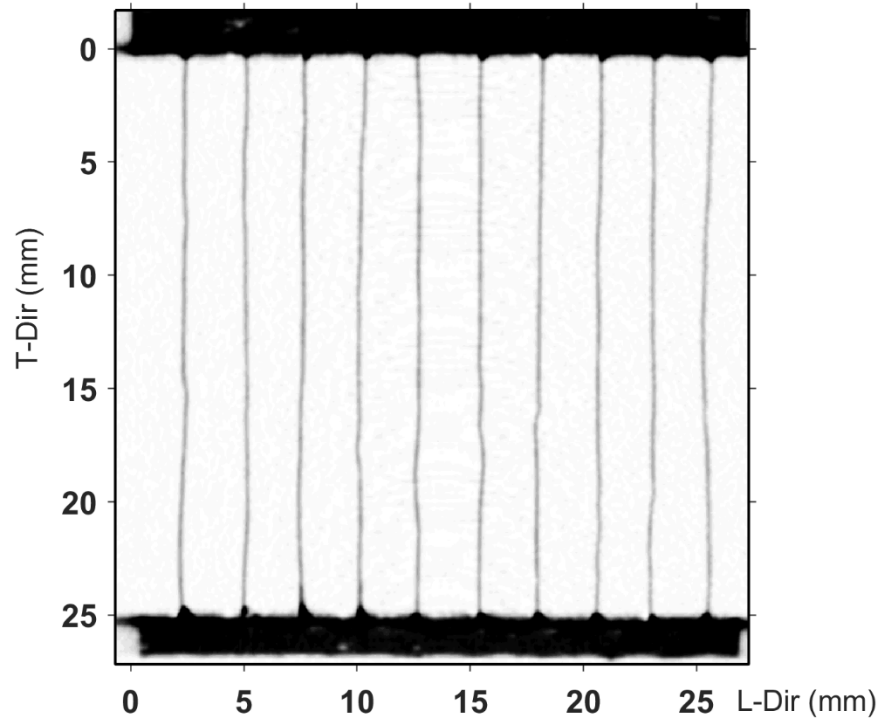
Figure 3.5. CT scan slice normal to expansion direction: (a) Before test; (b) After test

106
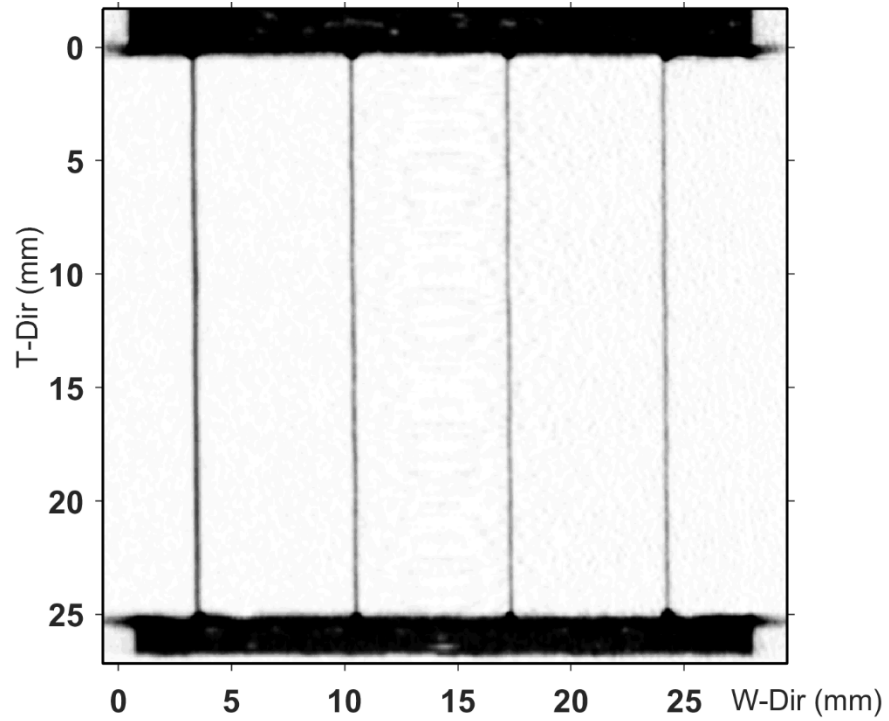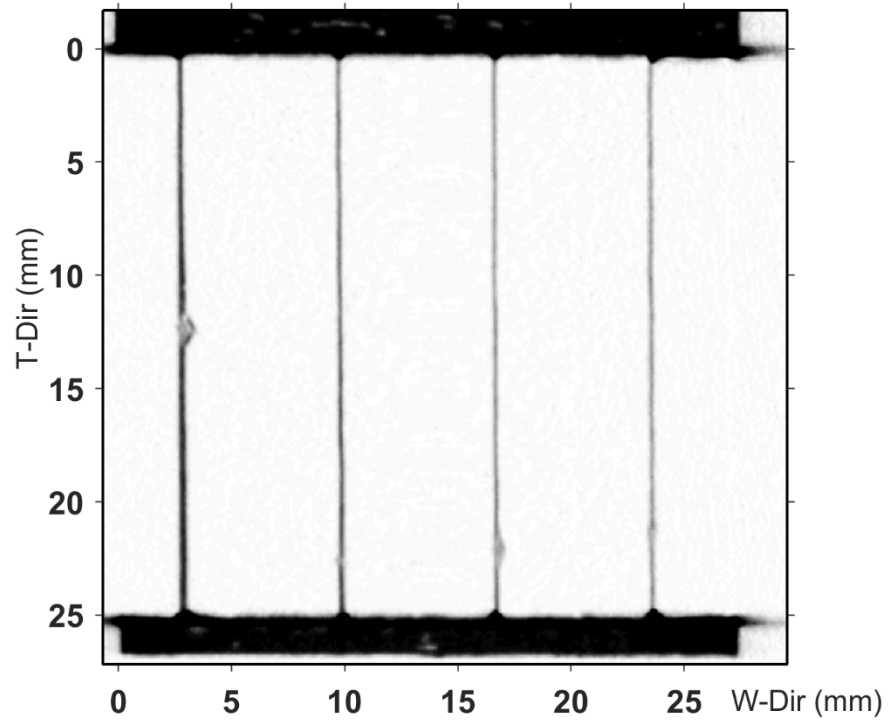
Figure 3.6. CT scan slice normal to ribbon direction: (a) Before test; (b) After test

107
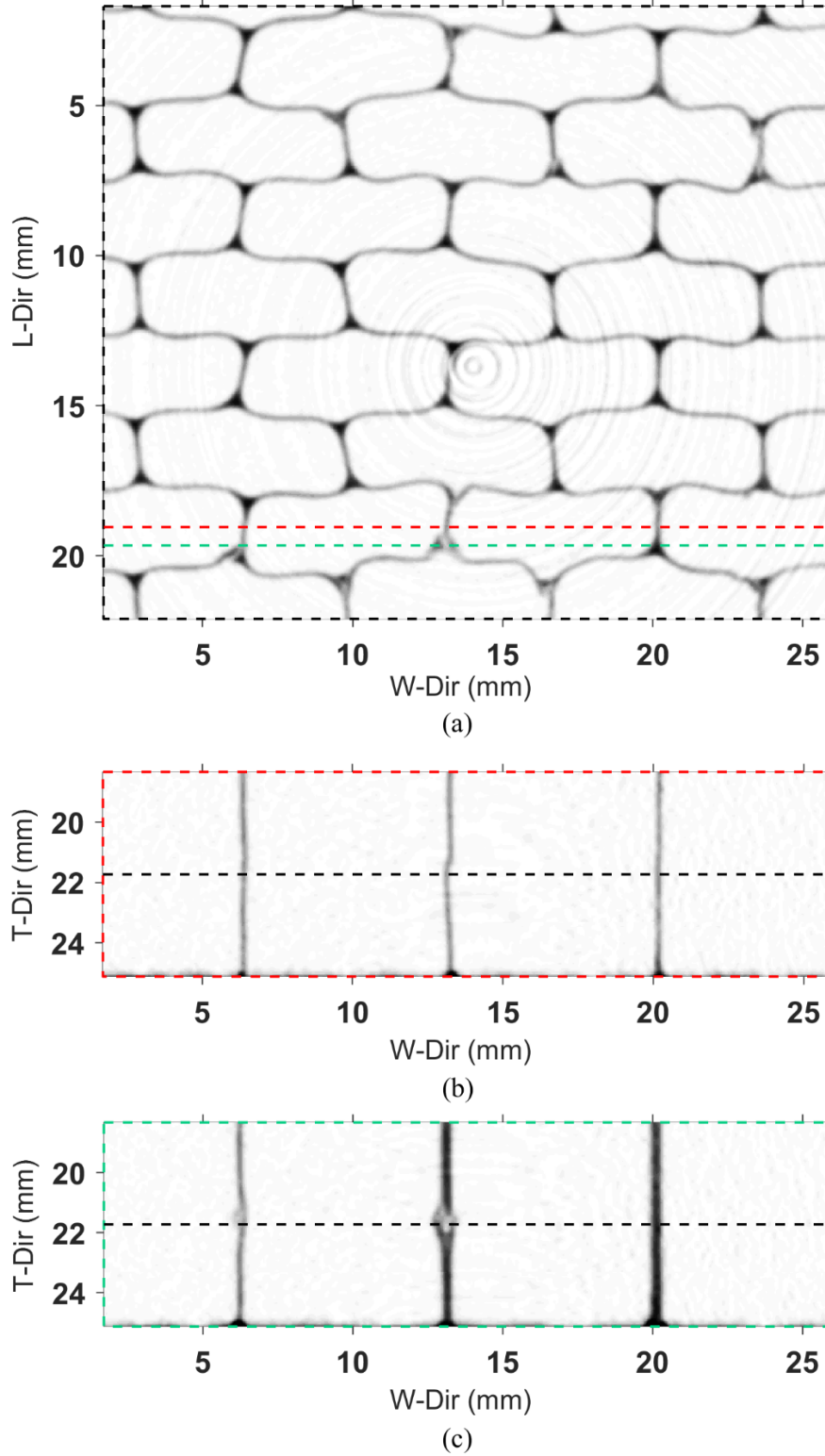
Figure 3.7. Damage comparison on CT scan slices normal to ribbon direction: (a) Through-thickness slice; (b) Slice through fillet; (c) Slice through double walls
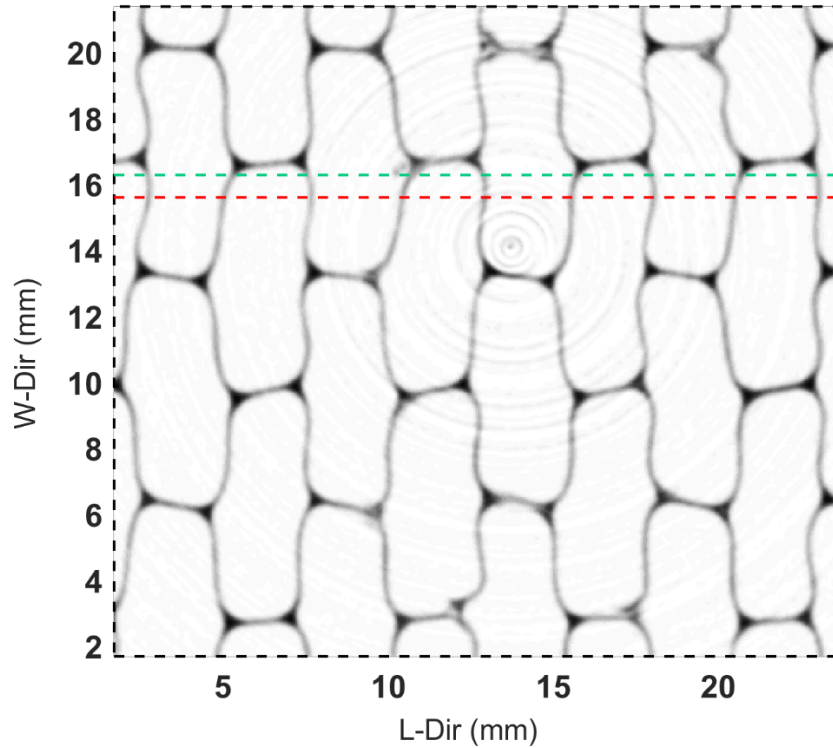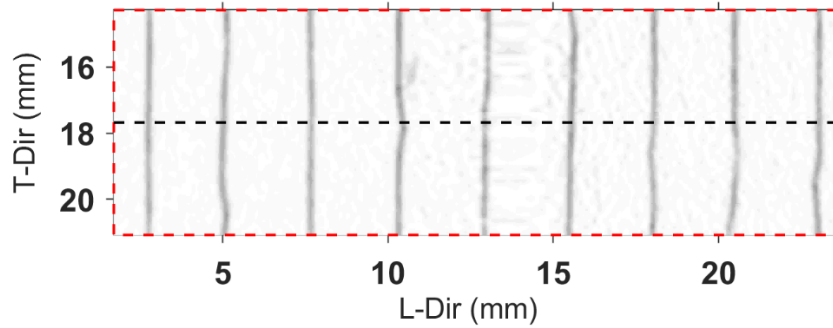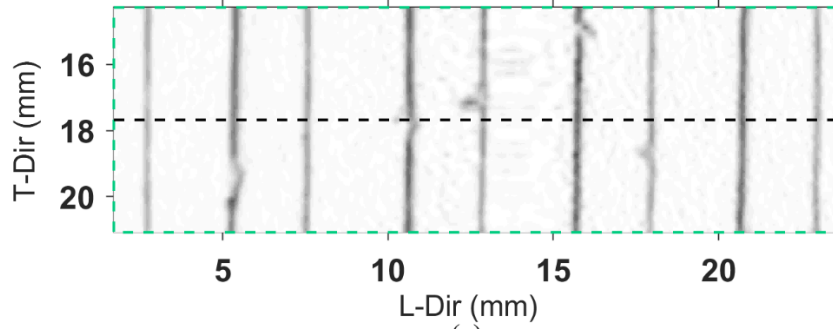
Figure 3.8. Damage comparison on CT scan slices normal to expansion direction: (a) Through-thickness slice; (b) Slice through fillet onset; (c) Slice through single walls
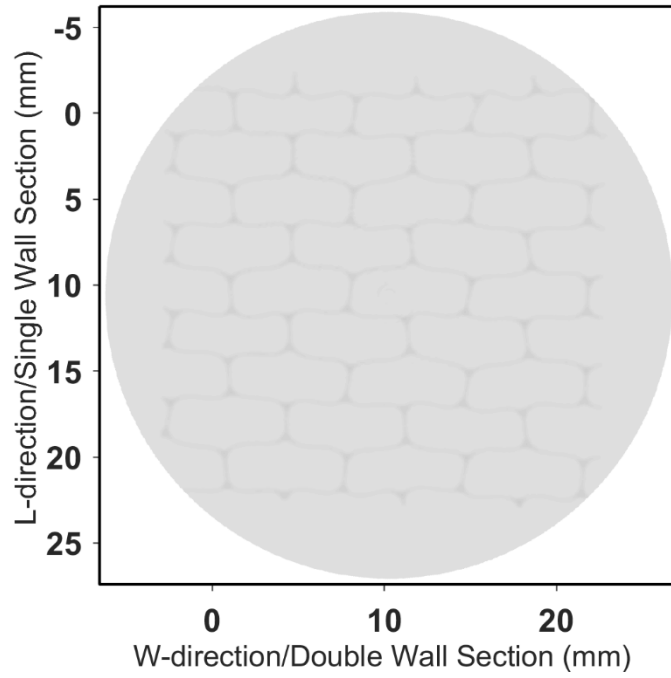
Figure 3.9. Linearly color inverted raw CT scan slice
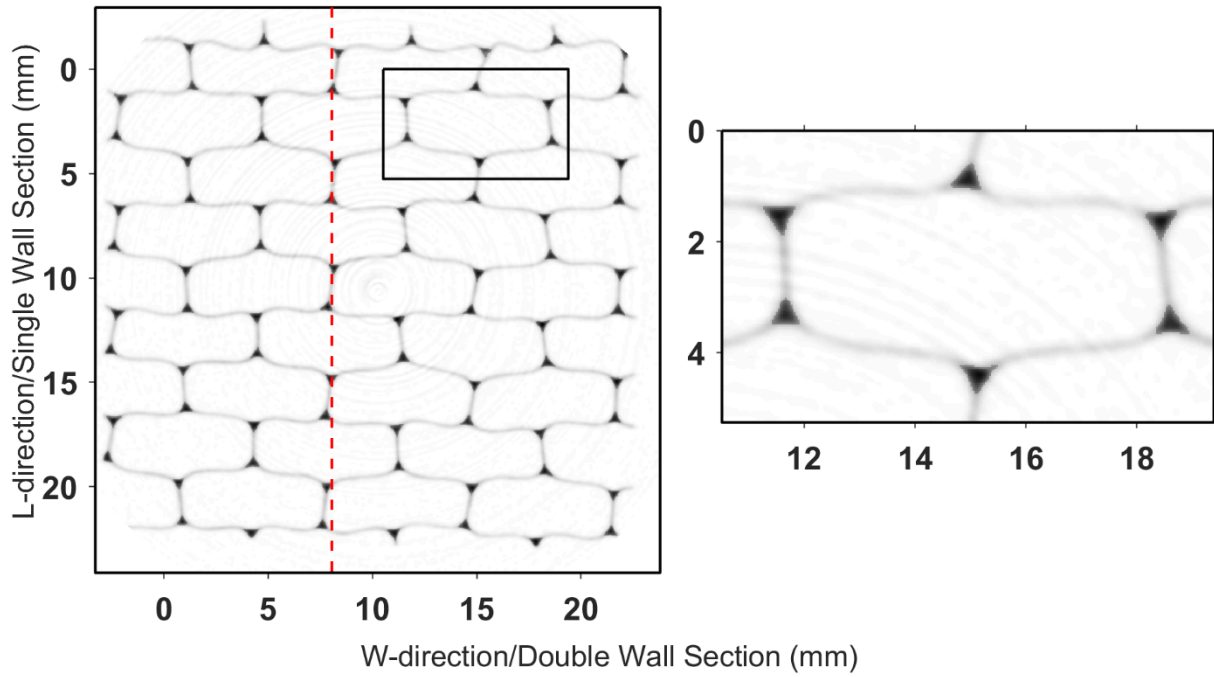
Figure 3.10. Higher contrast CT scan slice and close-up view of entire cell
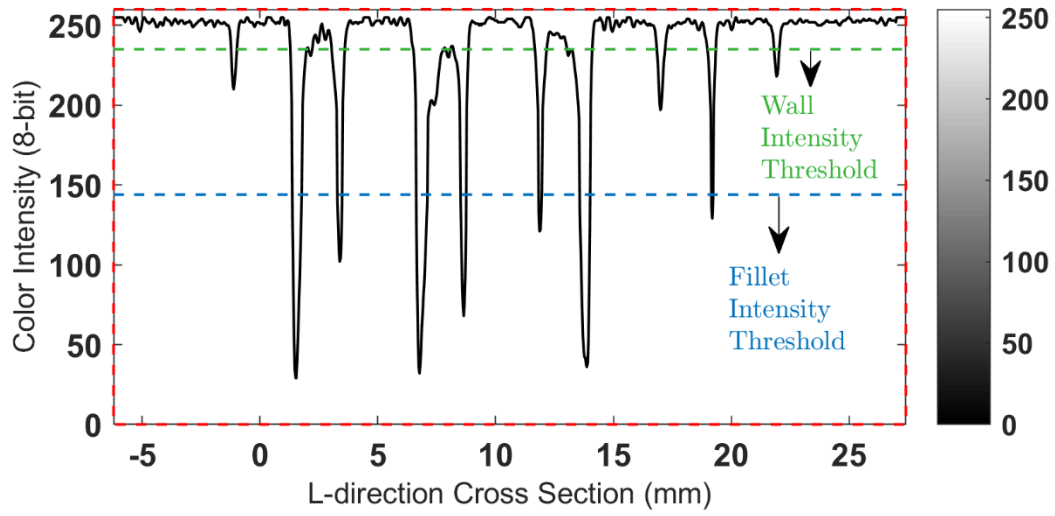
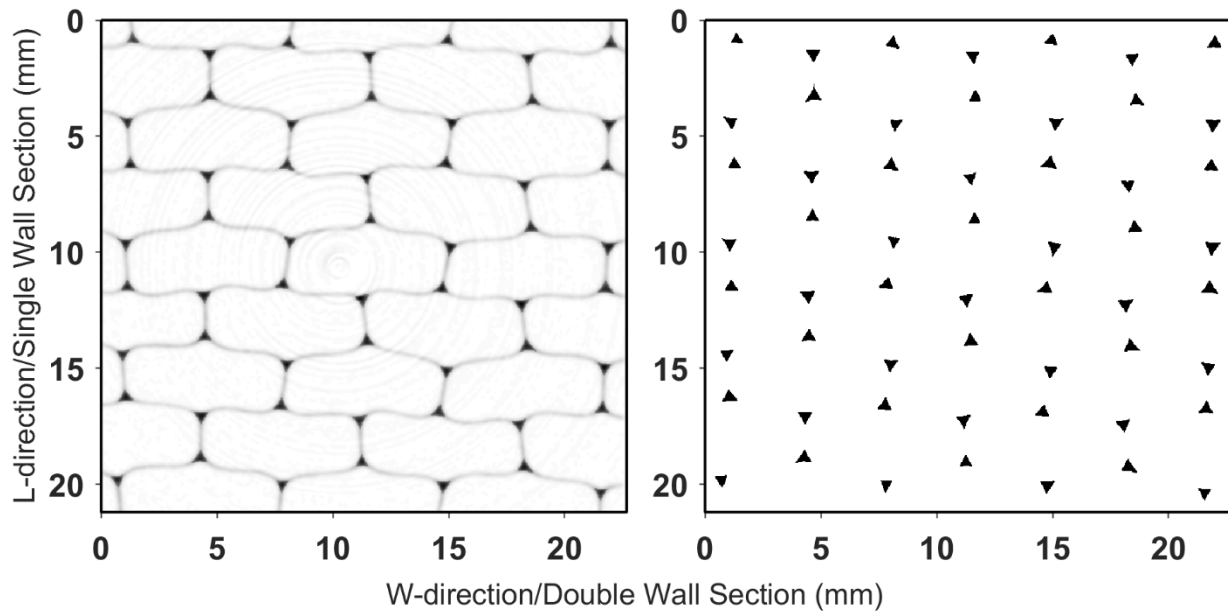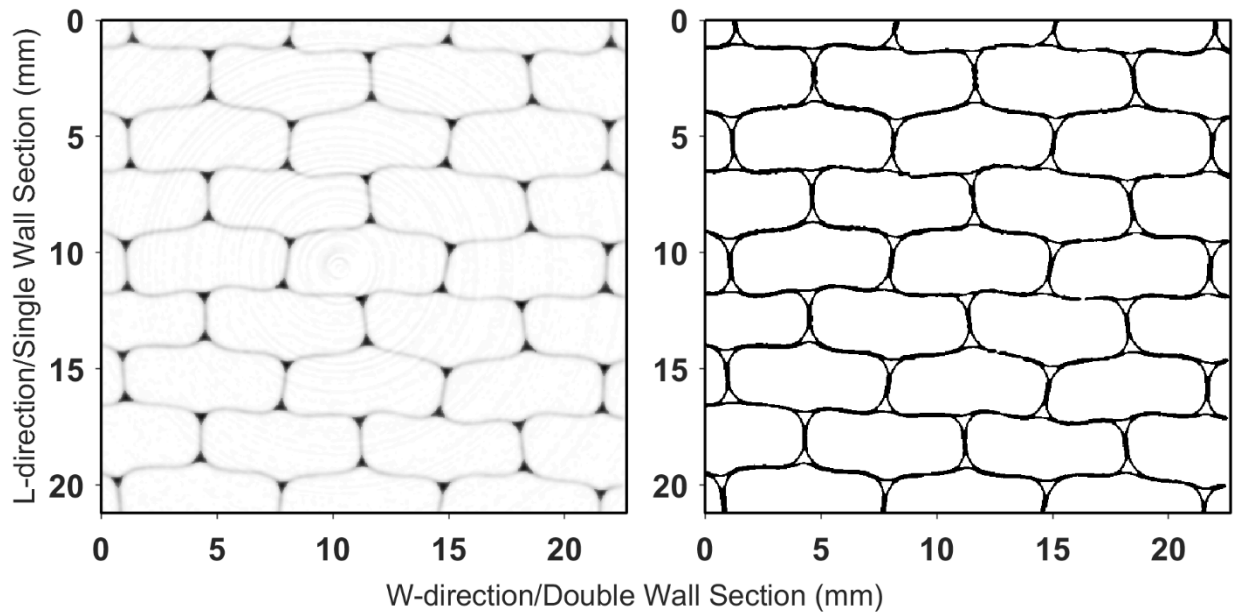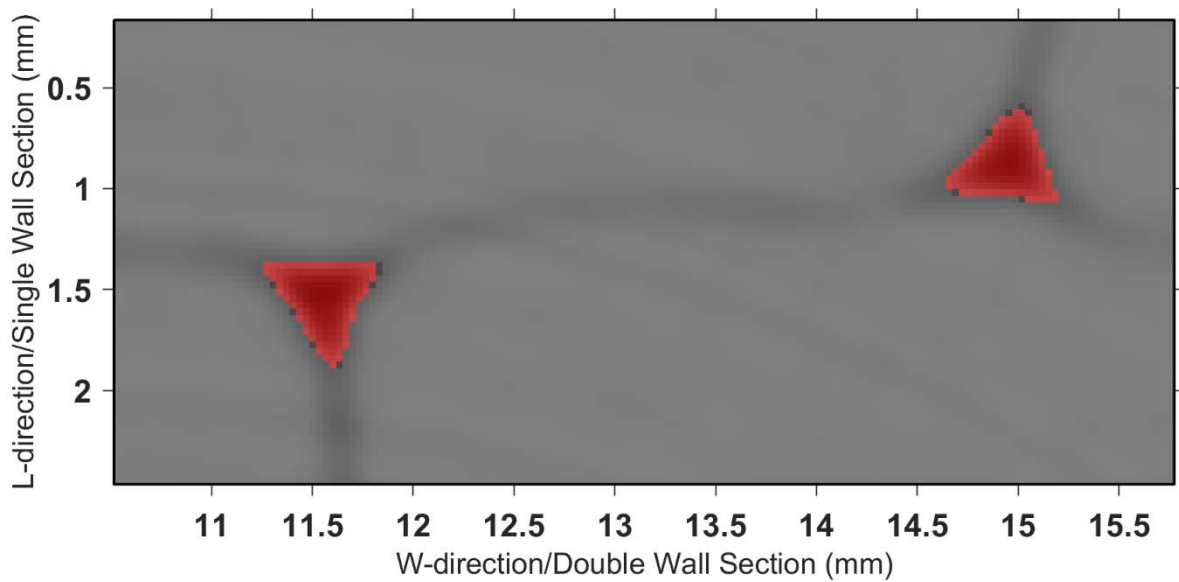**Figure 3.11. Typical color intensity distribution along ribbon direction**

Figure 3.12. Application of binary color intensity threshold for isolation of fillets

Figure 3.13. Application of binary color intensity threshold for wall structure isolation

Figure 3.14. Overlay between raw CT scan image and binary image of fillets (fillet geometry obtained from binary thresholding are represented with red color tonalities)
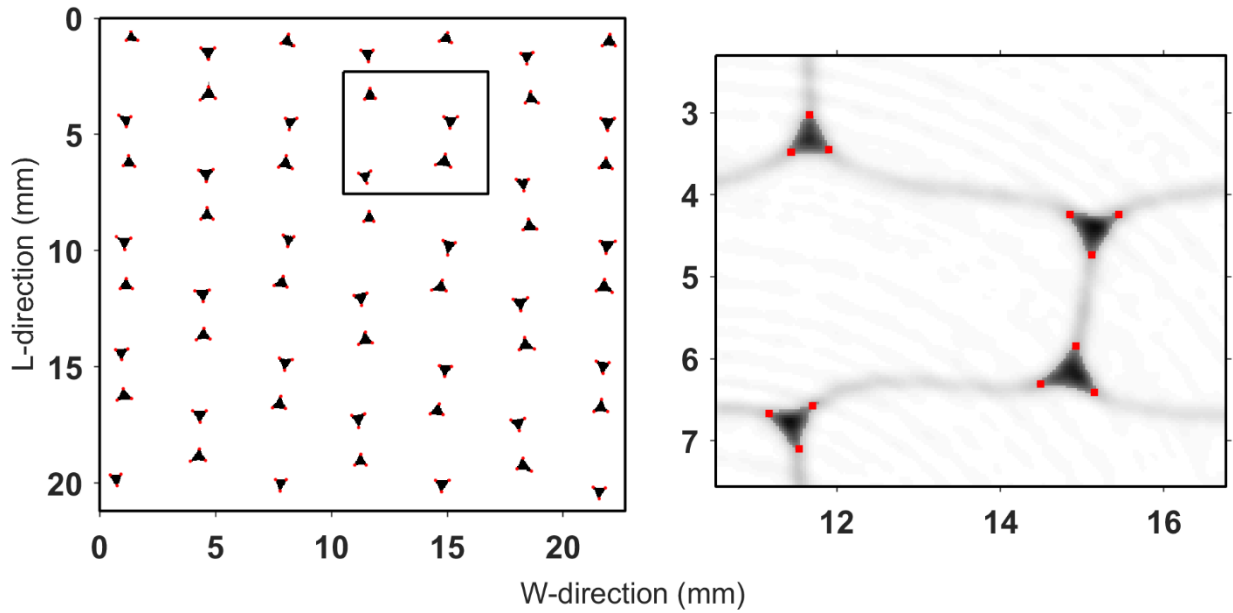
Figure 3.15. Automatic selection of corner points of individual fillets
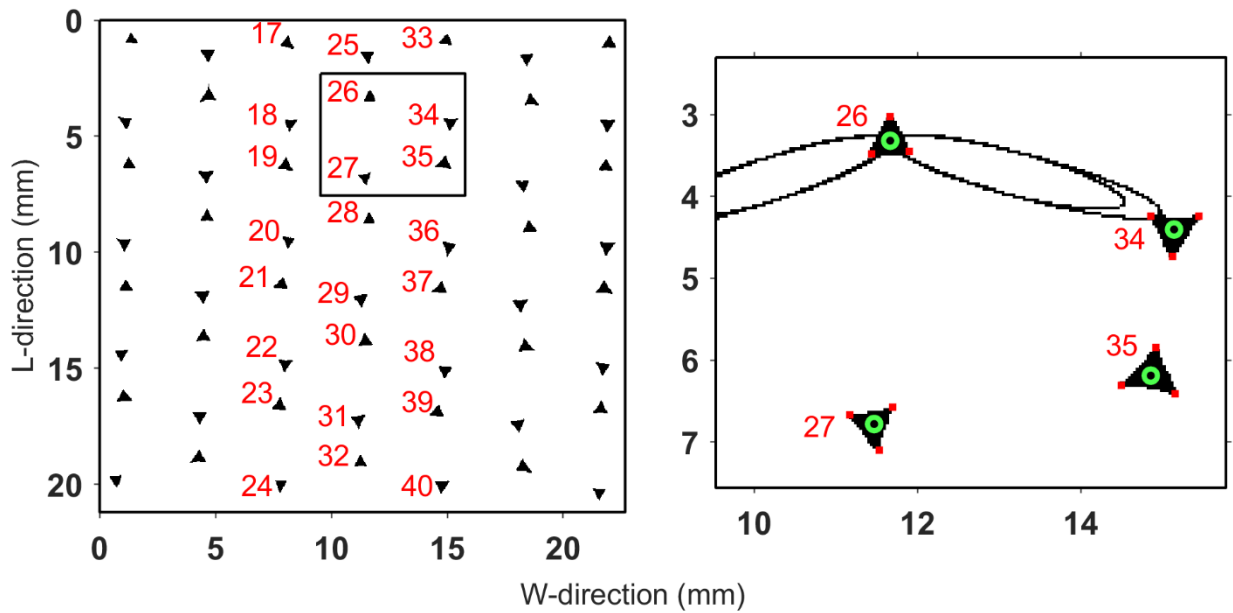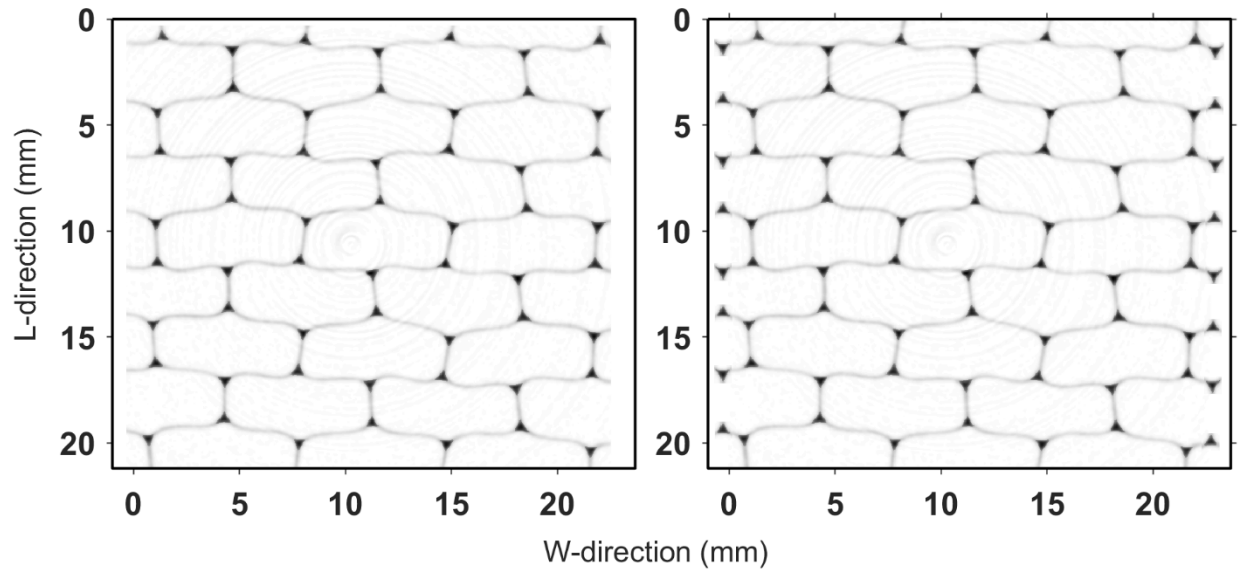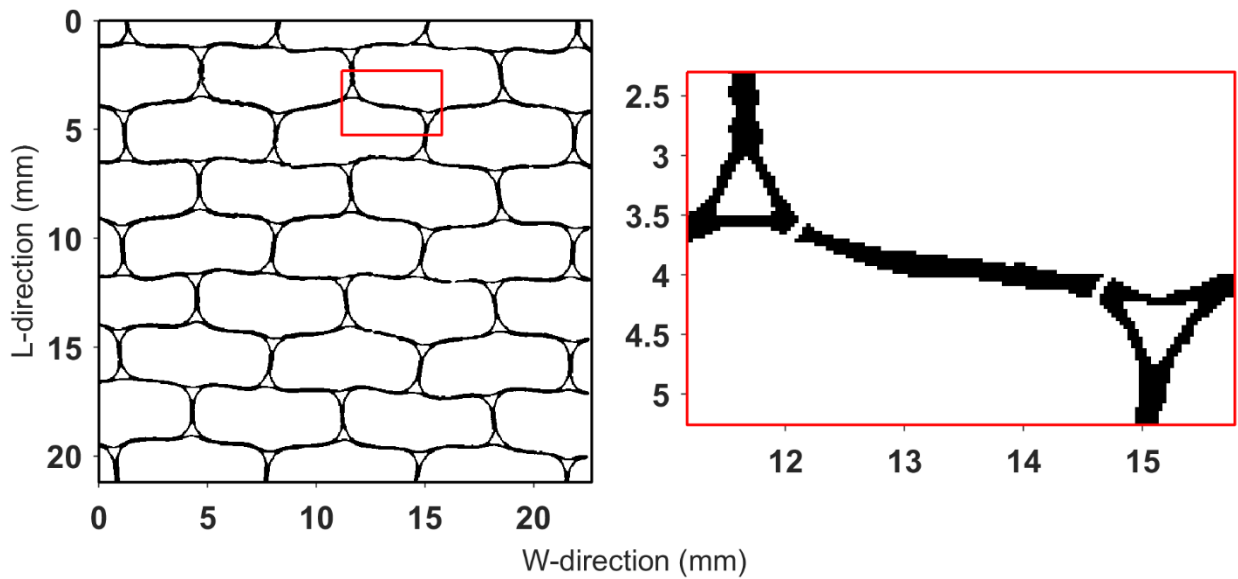

Figure 3.16. Construction of connectivity array among all fillets based upon intersection of neighboring fillet with increasing size ellipses (node 26 is connected to node 34)

Figure 3.17. Artificial insertion of fillets for creation of full ribbon connectivity on the left and right boundaries

Figure 3.18. Isolation of an arbitrary wall segment after construction of the ribbon connectivity array
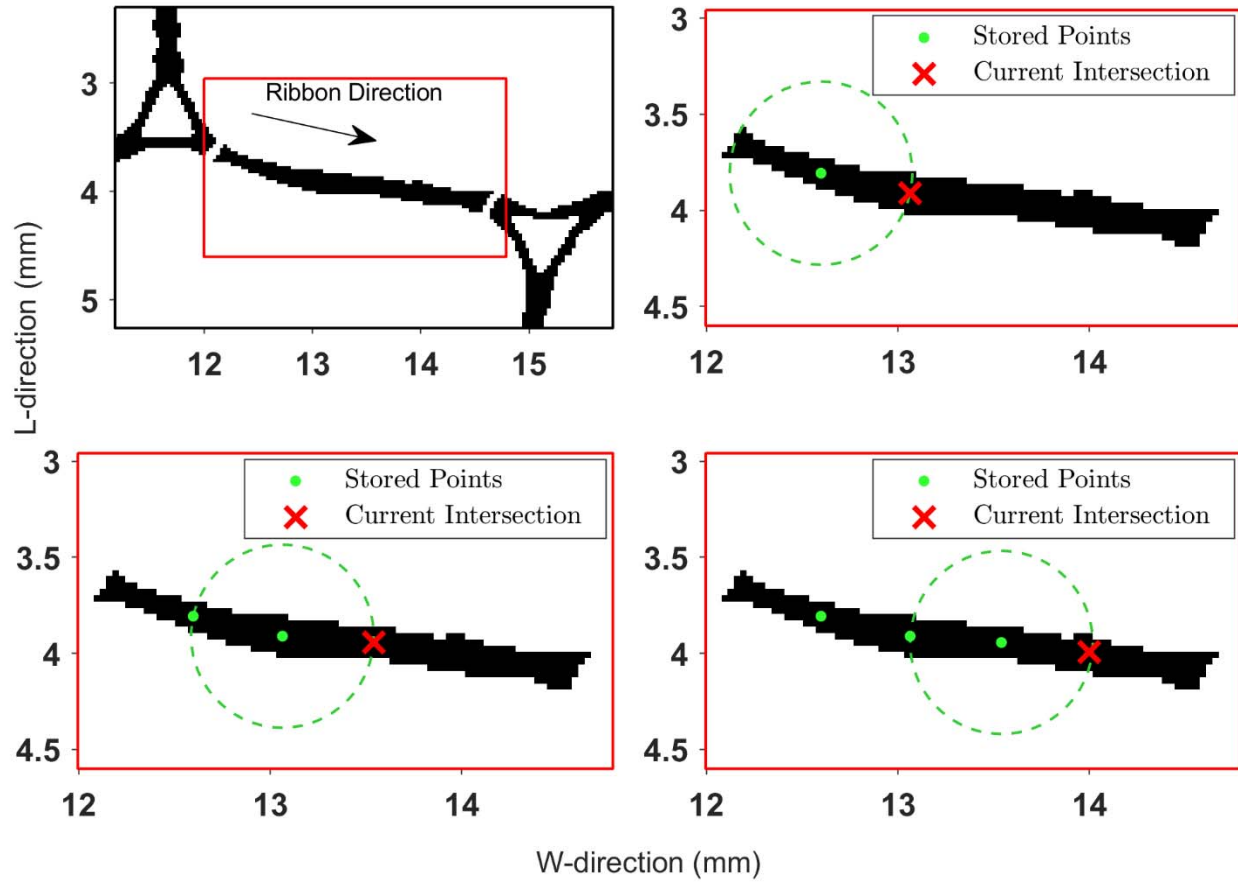
114

Figure 3.19. Progression of wall discretization using moving circle intersections

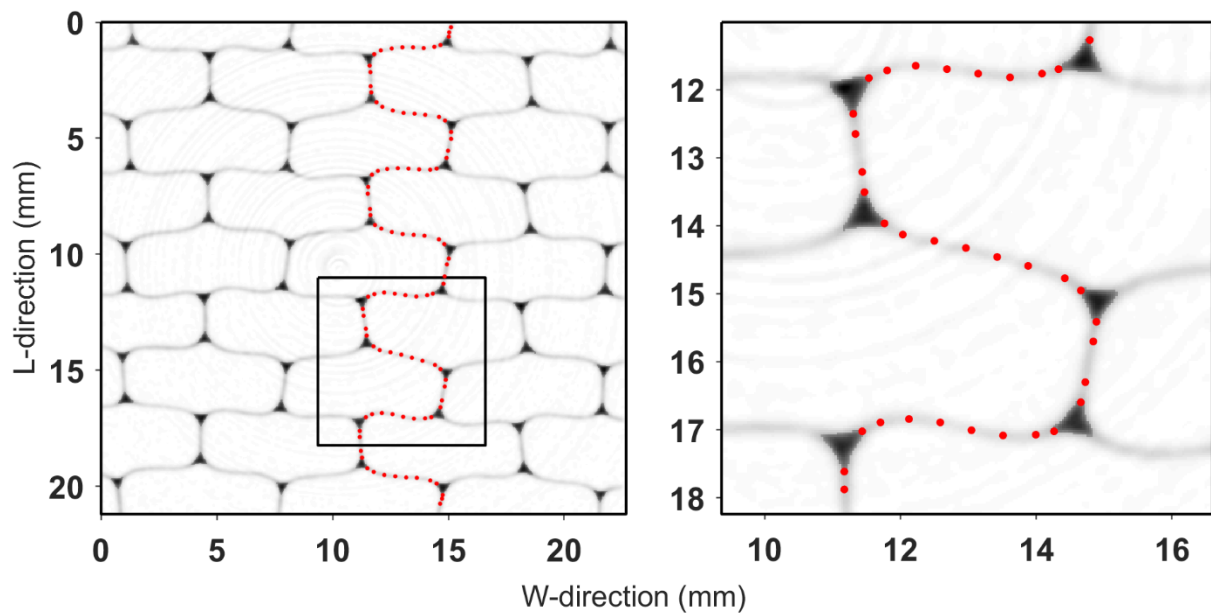**Figure 3.20. Automated fully discretized CT scanned ribbon and close-up view**

115
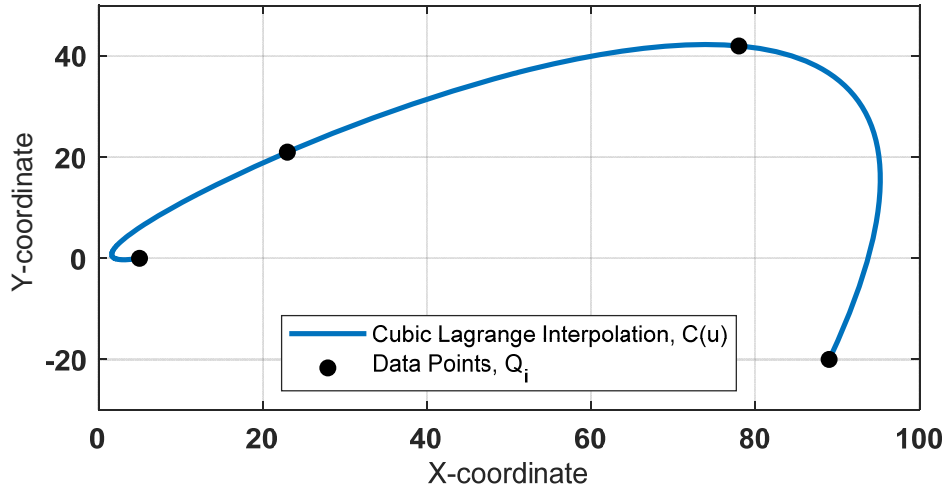
Figure 3.21. Cubic Lagrange interpolation
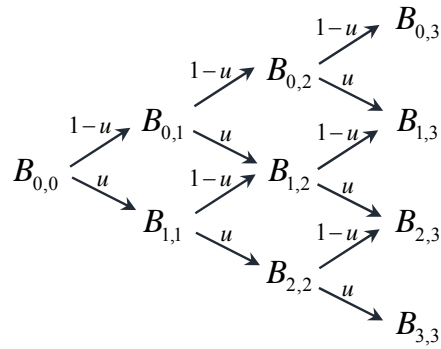
Figure 3.22. Schematic of recursive algorithm for Bernstein basis functions
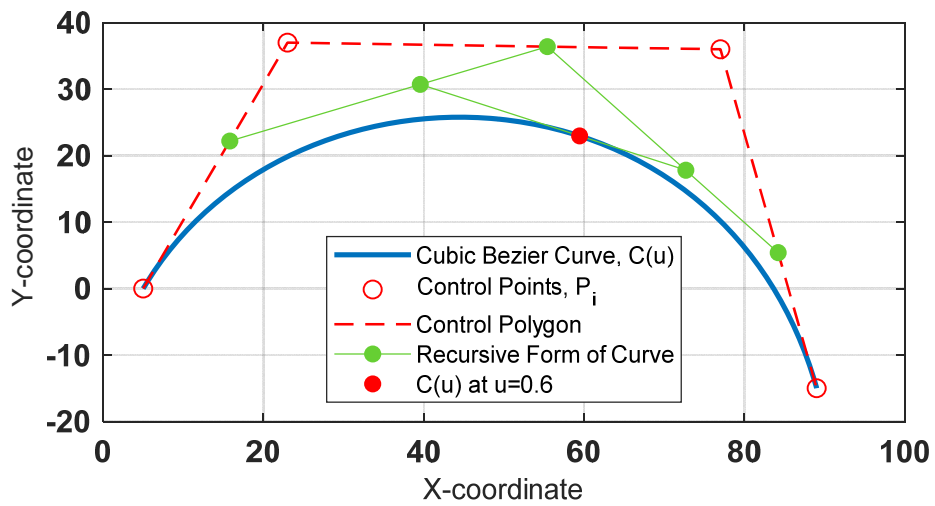
Figure 3.23. Construction of a cubic Bézier curve
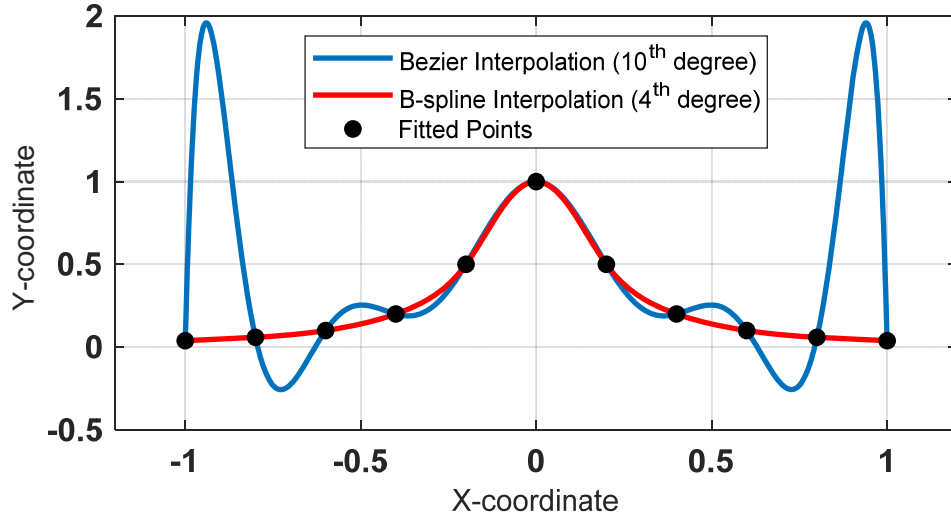
Figure 3.24. Comparison of Bézier and B-spline interpolations
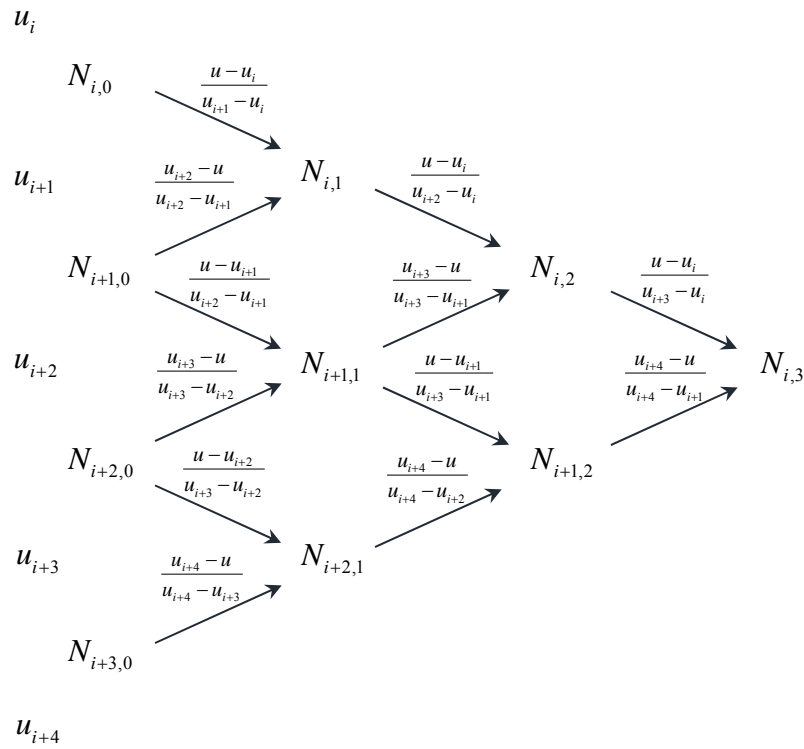
Figure 3.25. Truncated triangle for calculation of B-spline basis functions

117
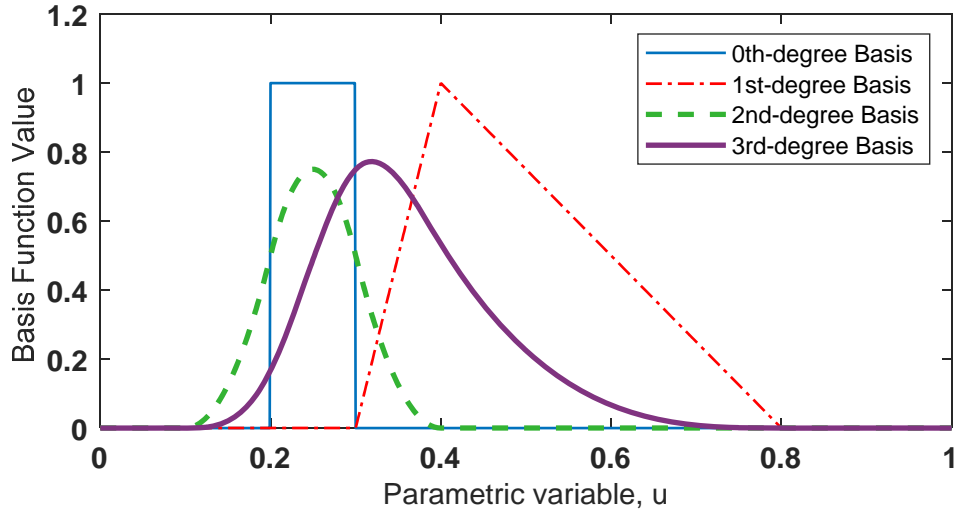
Figure 3.26. Selective collection of basis functions $N_{i,p}$ (u) for knot vector U= {0, 0, 0, 0, 0.1, 0.2, 0.3, 0.4, 0.8, 1, 1, 1, 1}
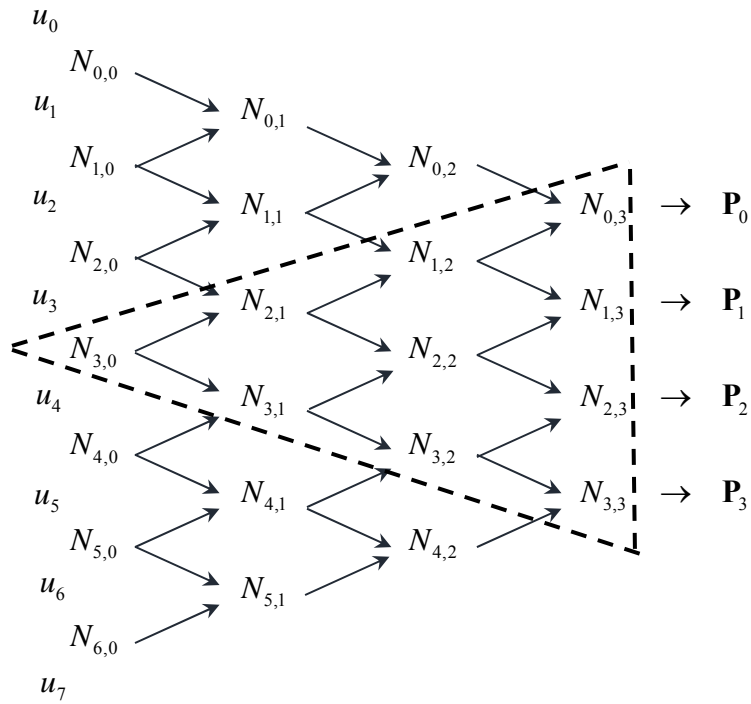
Figure 3.27. Truncated triangle for 3rd-degree B-spline curve
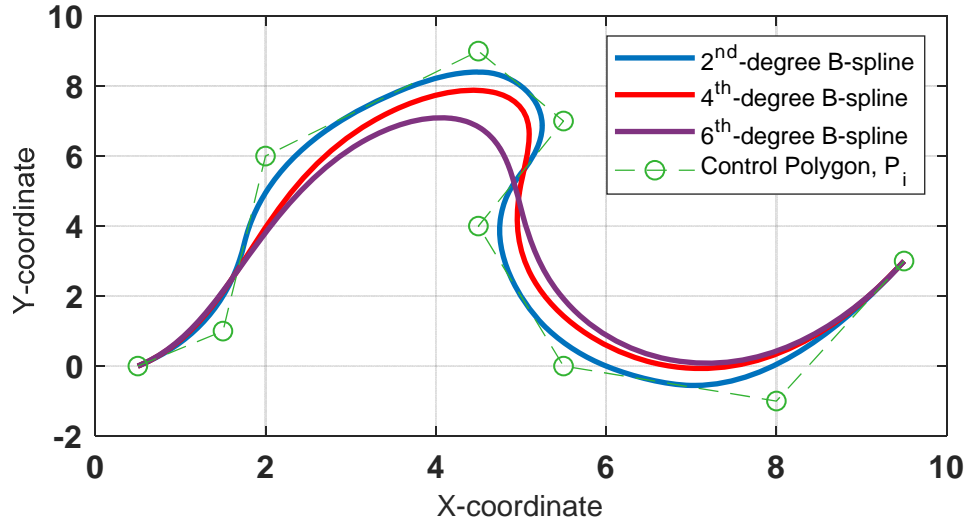
Figure 3.28. B-spline curves of different degree p for uniformly spaced knot vectors and given set of

P_i control points
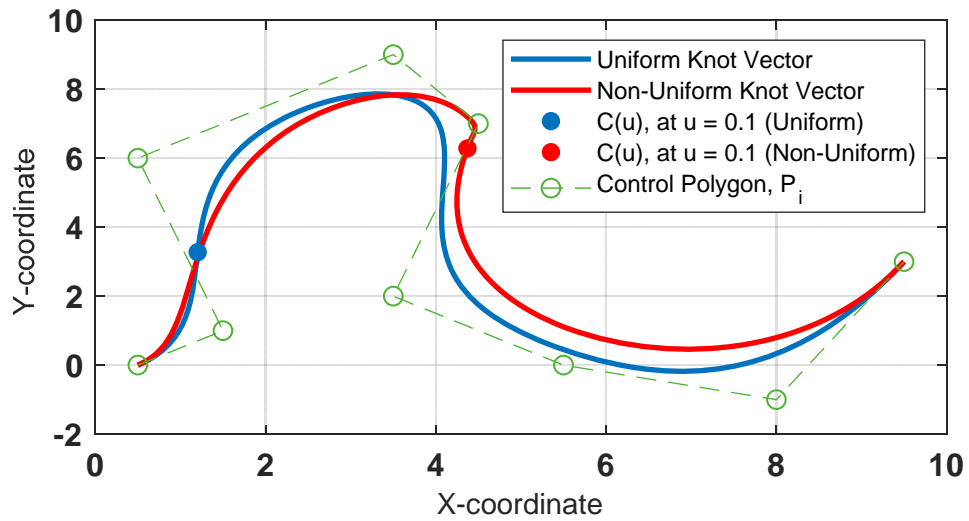
Figure 3.29. B-spline curve of 4th degree for uniform and non-uniform knot vectors U={0, 0, 0, 0, 0, 0.2, 0.4, 0.6, 0.8, 1, 1, 1, 1, 1} and U={0, 0, 0, 0, 0, 0.05, 0.06, 0.07, 0.08, 1, 1, 1, 1, 1} respectively
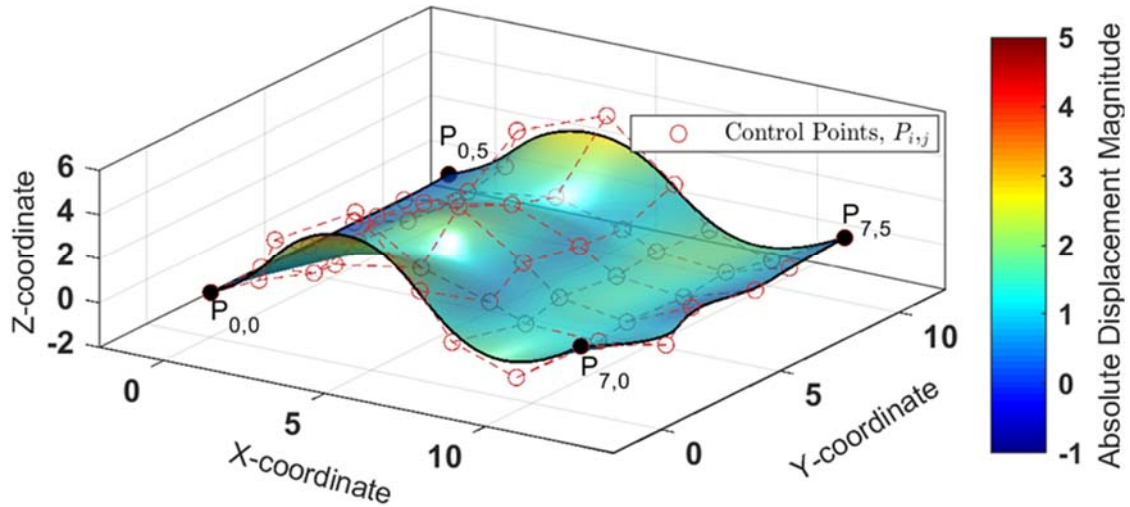
Figure 3.30. B-spline surface of degrees p=4, q=2 obtained from 8x6 control patch and knot vectors U= {0, 0, 0, 0, 0, 0.25, 0.50, 0.75, 1, 1, 1, 1, 1}, V= {0, 0, 0, 0.25, 0.50, 0.75, 1, 1, 1} respectively
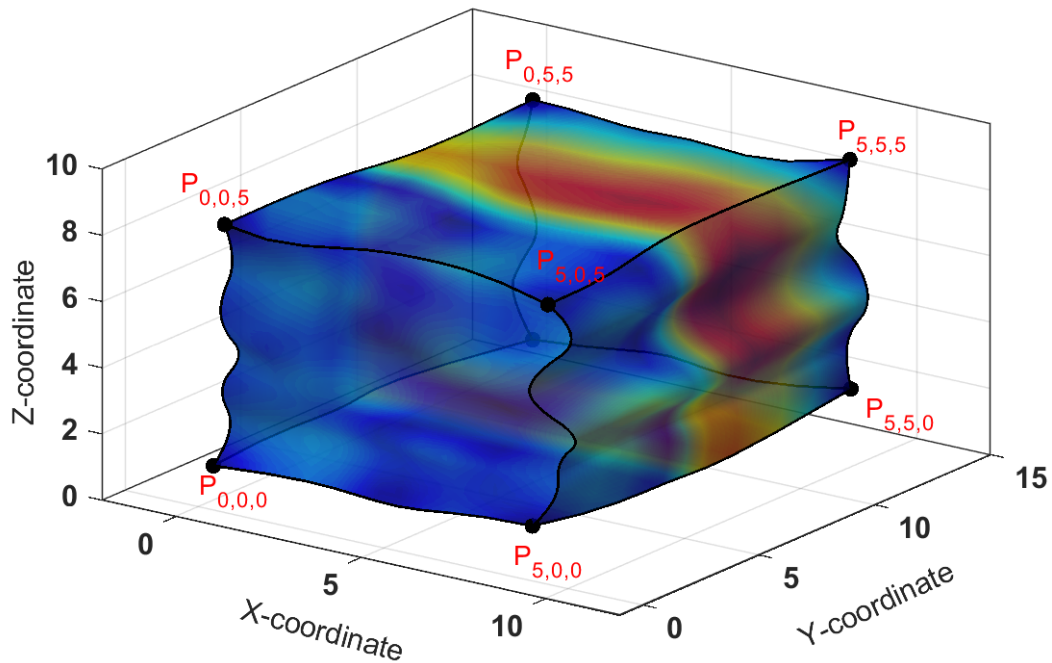
Figure 3.31. B-spline volume of degrees p=3, q=4, r=2 obtained from 6x6x6 control volume and knot vectors U={0, 0, 0, 0, 0.33, 0.66, 1, 1, 1, 1}, V={0, 0, 0, 0, 0, 0.50, 1, 1, 1, 1}, W={0, 0, 0, 0.166, 0.333, 0.500, 0.666, 0.833, 1, 1, 1} respectively
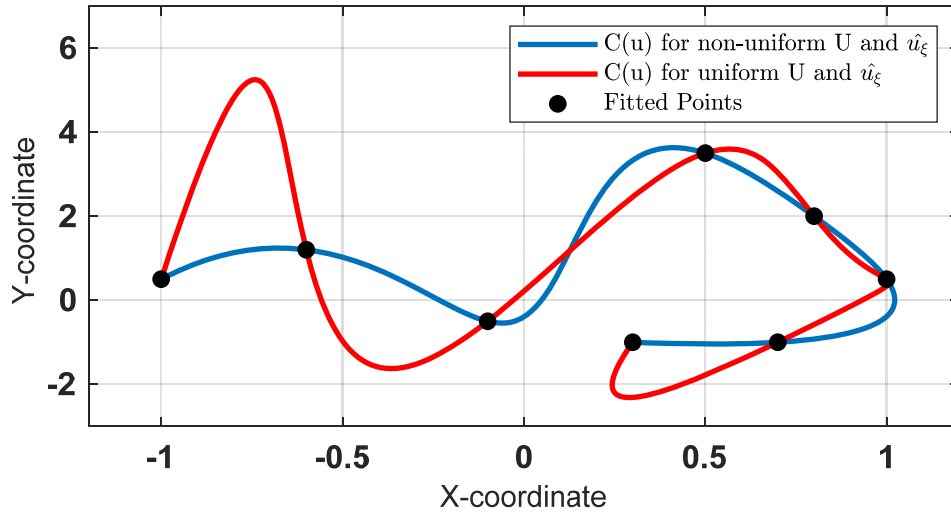
Figure 3.32. Comparison between uniform and non-uniform selection of knots and parametric values for a 4th – degree B-spline curve interpolation
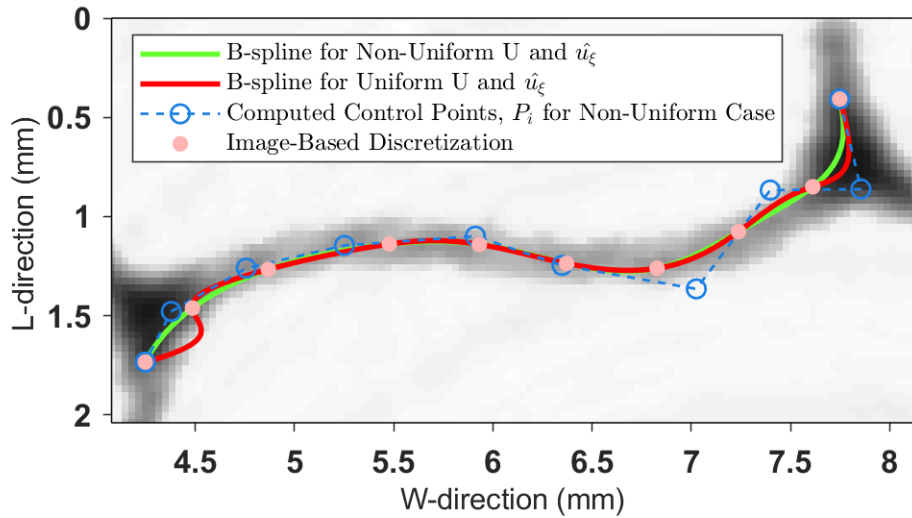
Figure 3.33. B-spline 4th – degree curve interpolating discretized single cell wall segment
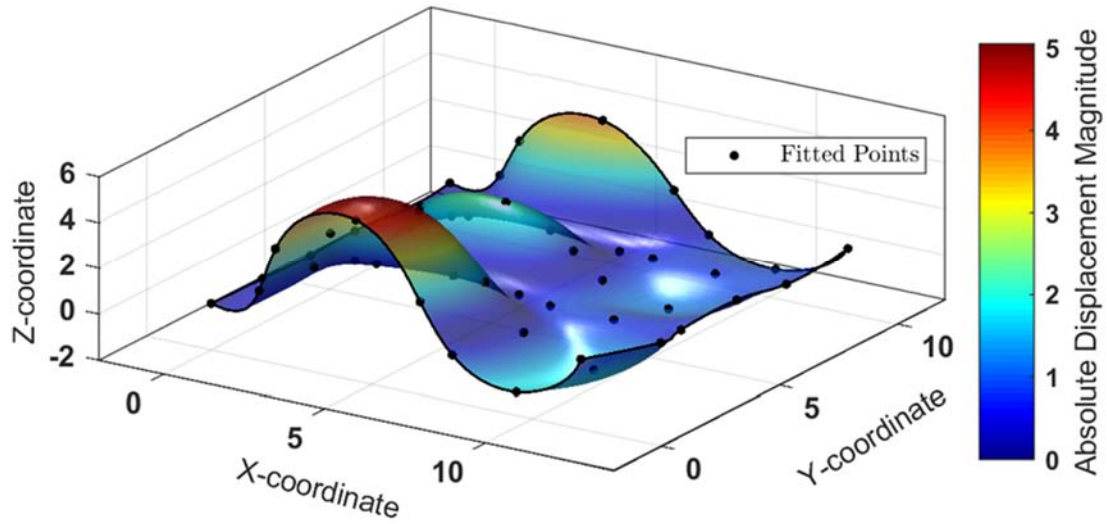
Figure 3.34. B-spline surface interpolation of degree p=4 and q=2 on 8x6 grid of fitted data points
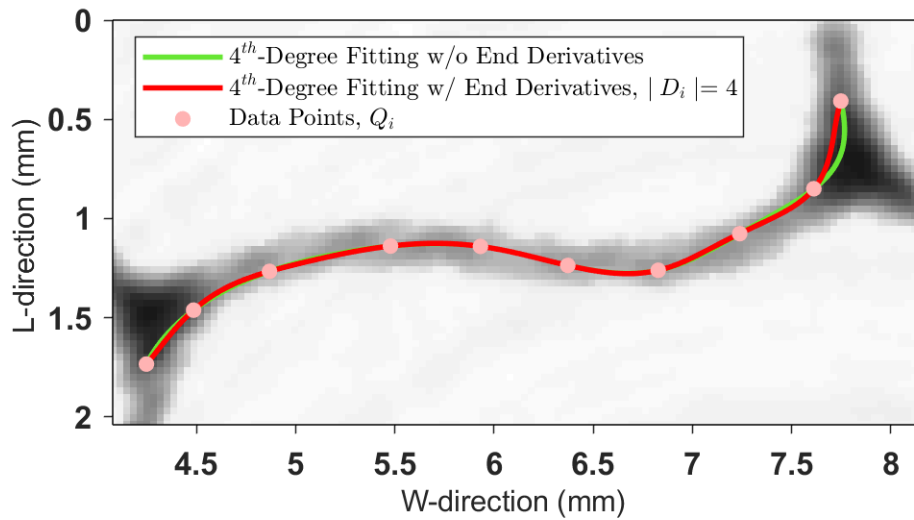
Figure 3.35. B-spline interpolation curves with and without end derivatives specified
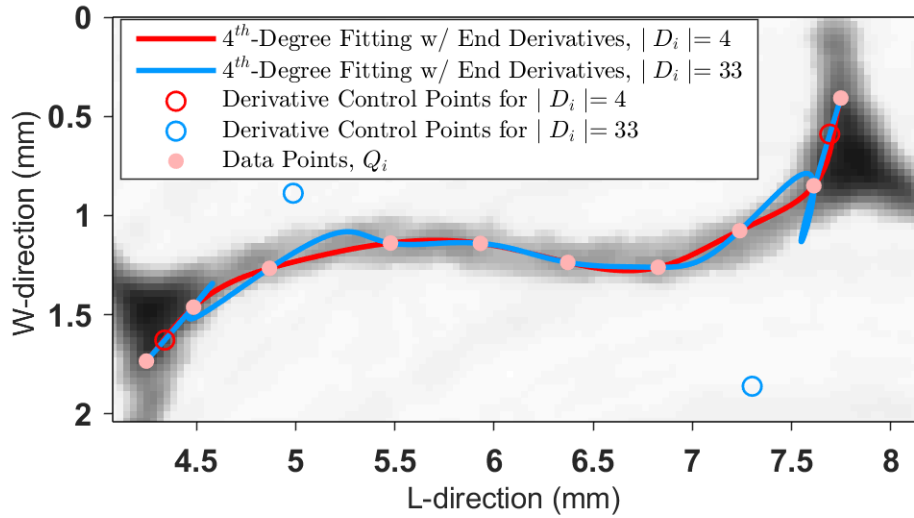
Figure 3.36. B-spline interpolation curves with different magnitude end derivatives
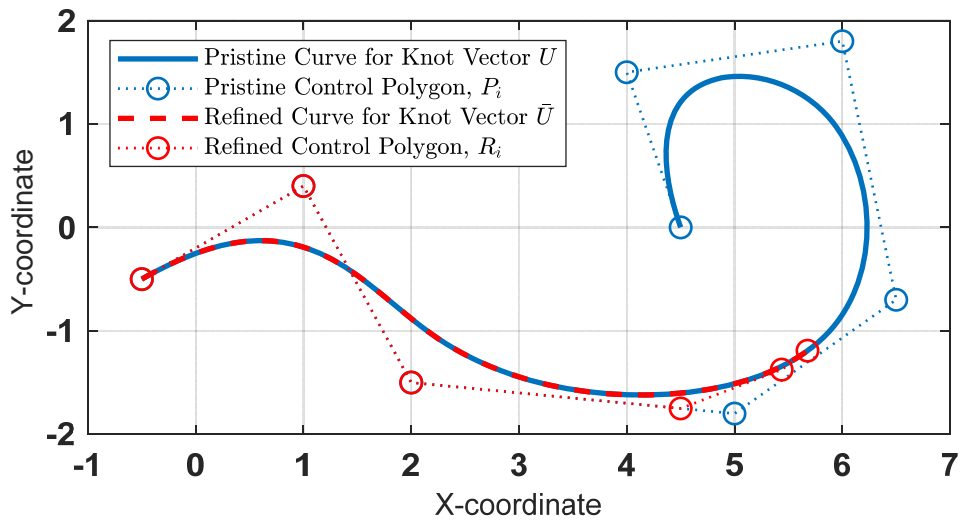
Figure 3.37. Application of knot vector refinement, Ū= {0, 0, 0, 0, 0.2, 0.4, 0.5, 0.5, 0.5, 0.5}, for segmentation of the first half of a 3ʳᵈ-degree B-spline curve
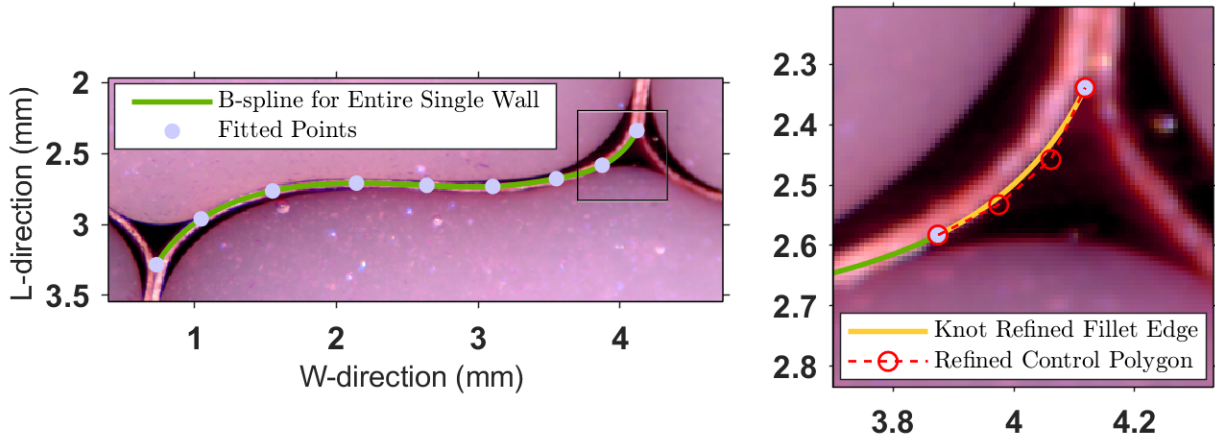
Figure 3.38. Application of interpolation scheme at: (a) single cell wall fitted by 3ʳᵈ-degree B-spline curve, (b) knot refined fillet edge
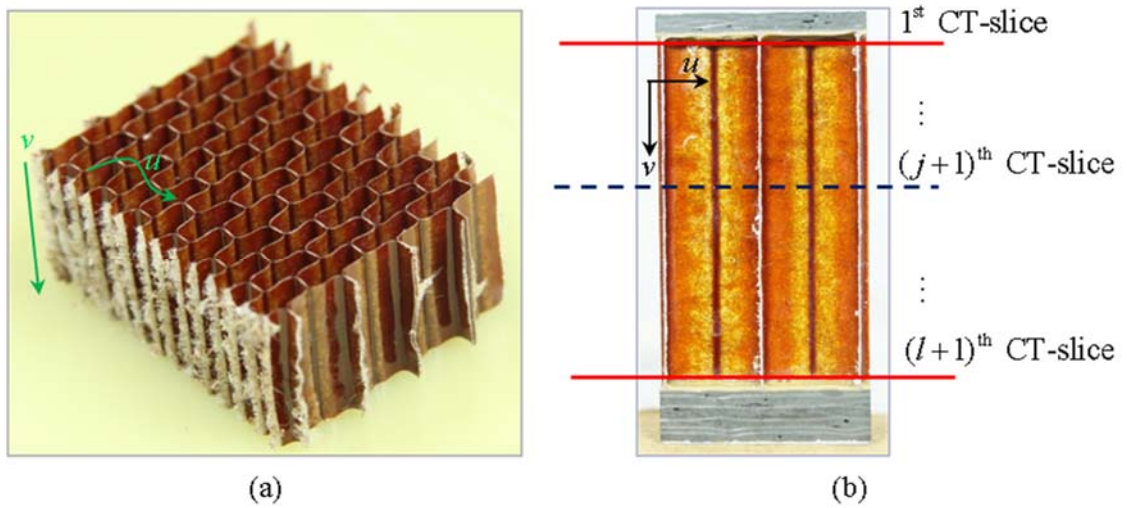
Figure 3.39. (a) Direction of B-spline parametric variables for honeycomb core coupons, (b) Numbering convention of CT-slices used for cellular discretization
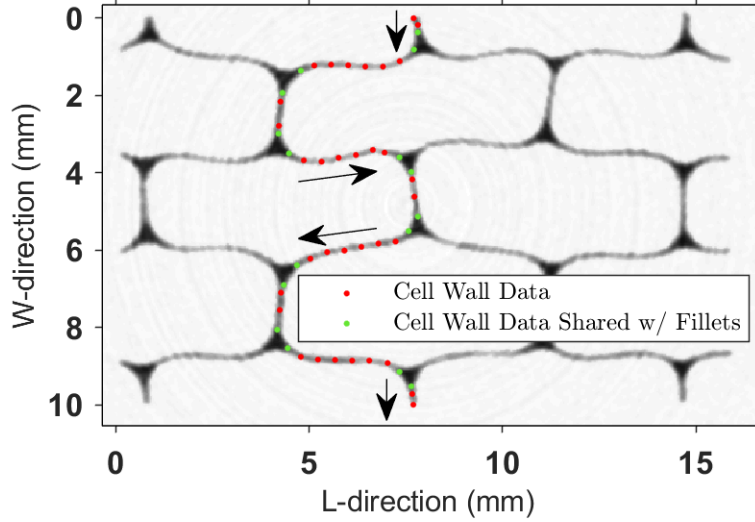
Figure 3.40. Ribbon wall discretization at CT-slice #577
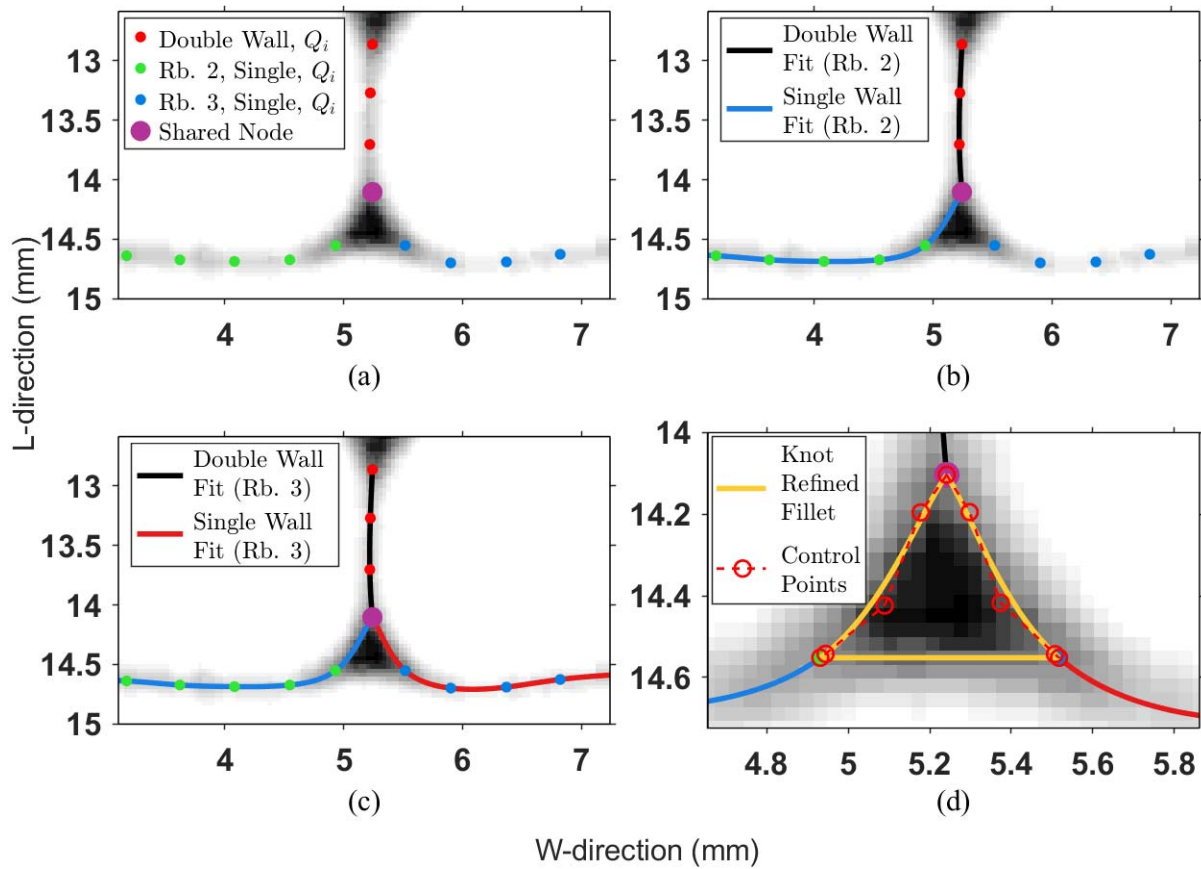
Figure 3.41. Step by step application of B-spline theory on CT-scan slice #750
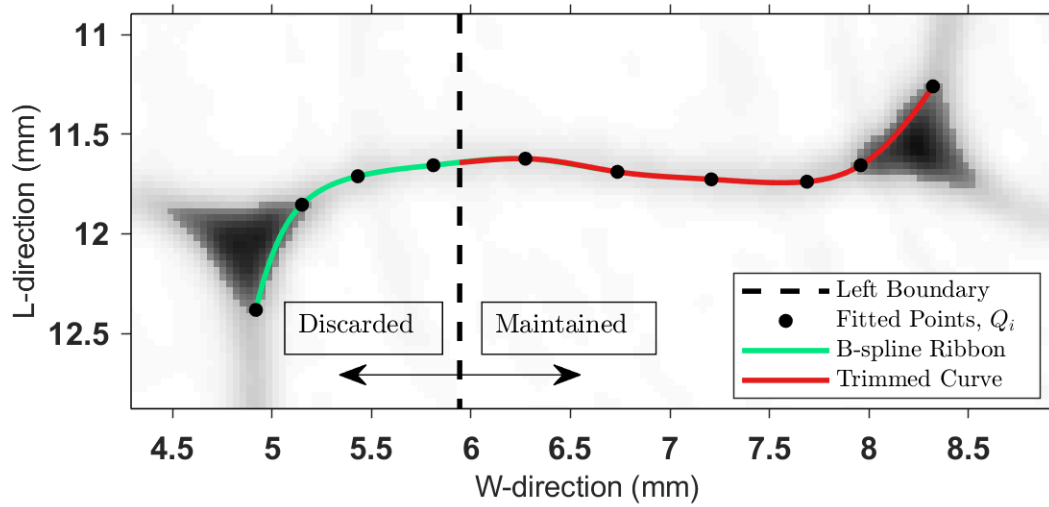
Figure 3.42. Trimmed B-spline curve imposed by boundary limits
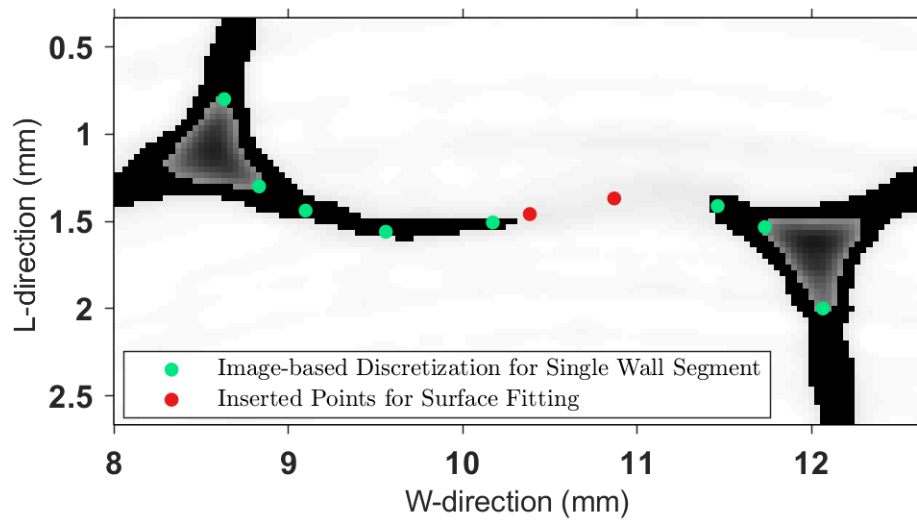
Figure 3.43. Data point insertion at discontinuous wall segments using B-spline curve interpolation

on raw data (green dots)
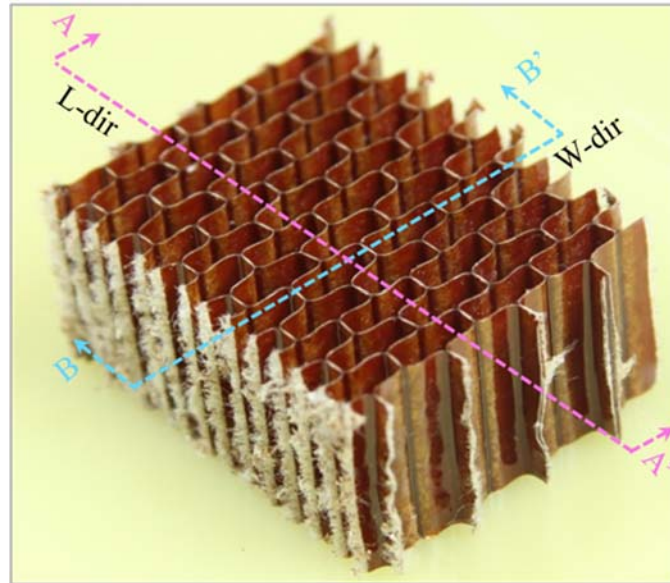
Figure 3.44. Isometric view of honeycomb core and corresponding cross section directions
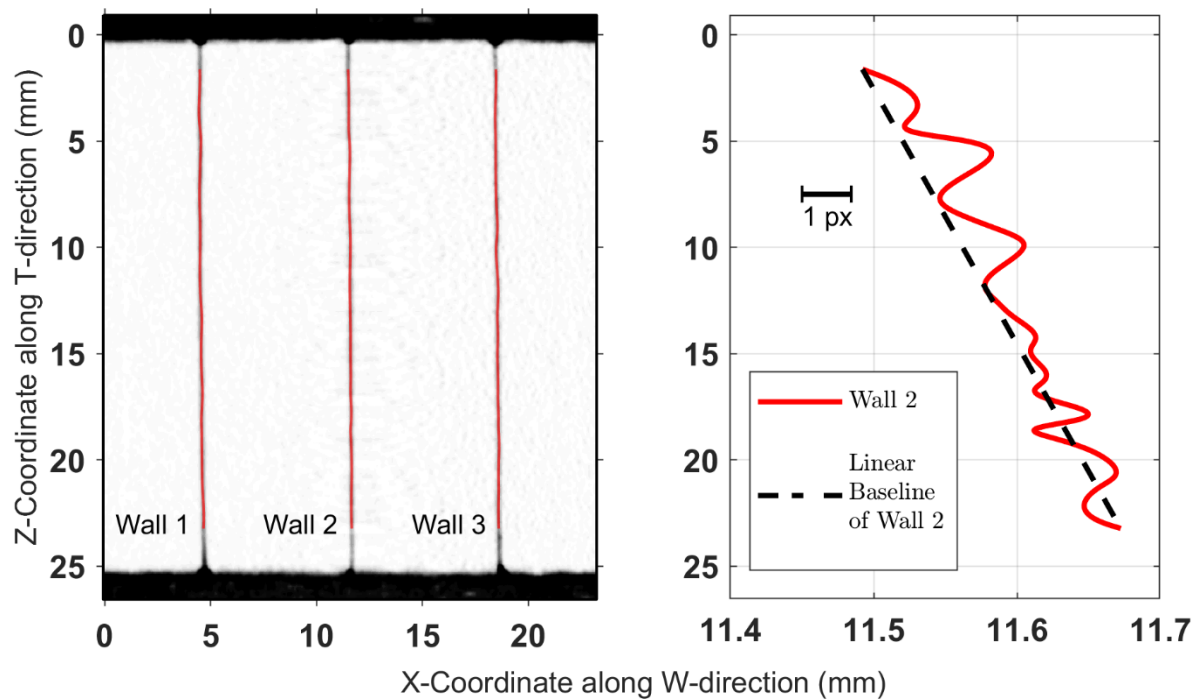
Figure 3.45. Linear baseline between top and bottom CT slices from which coordinates are subtracted from to obtain metrics of imperfections
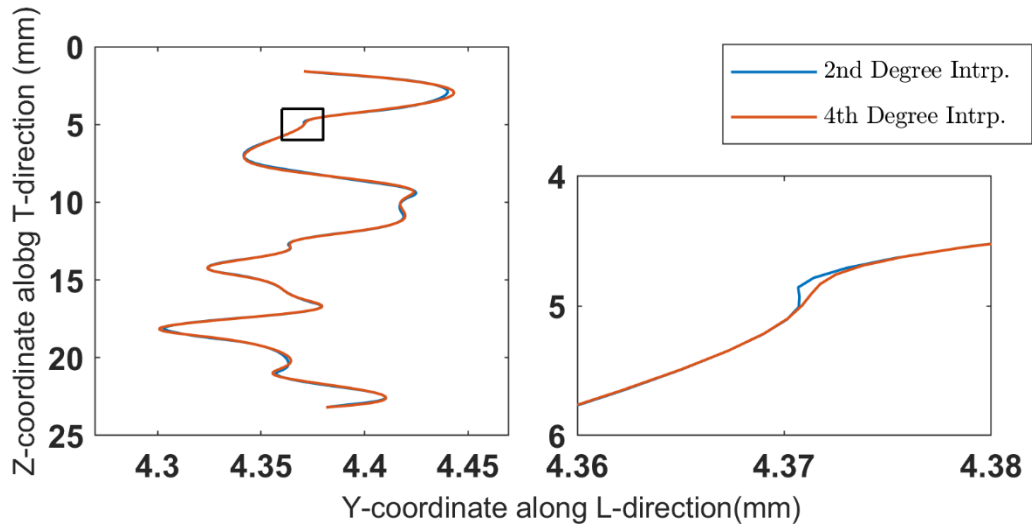
Figure 3.46. 2nd vs. 4th -degree interpolation through the thickness direction
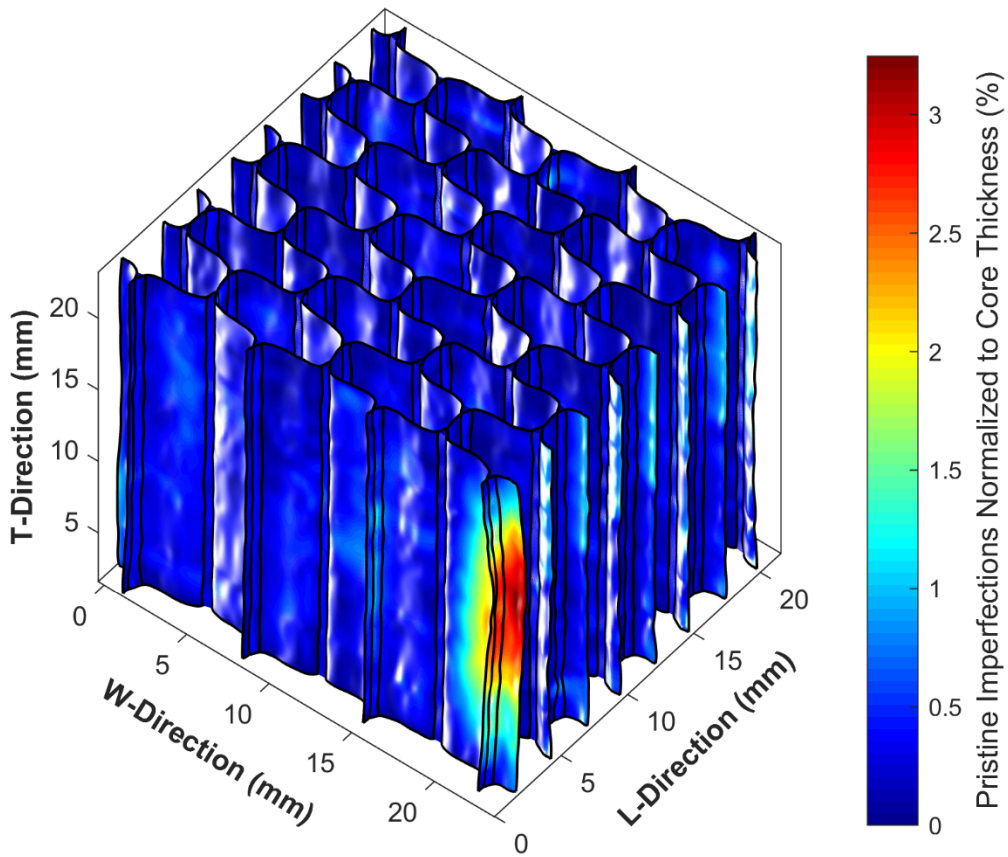
Figure 3.47. Core imperfections normalized to its thickness (25.4 mm)

128
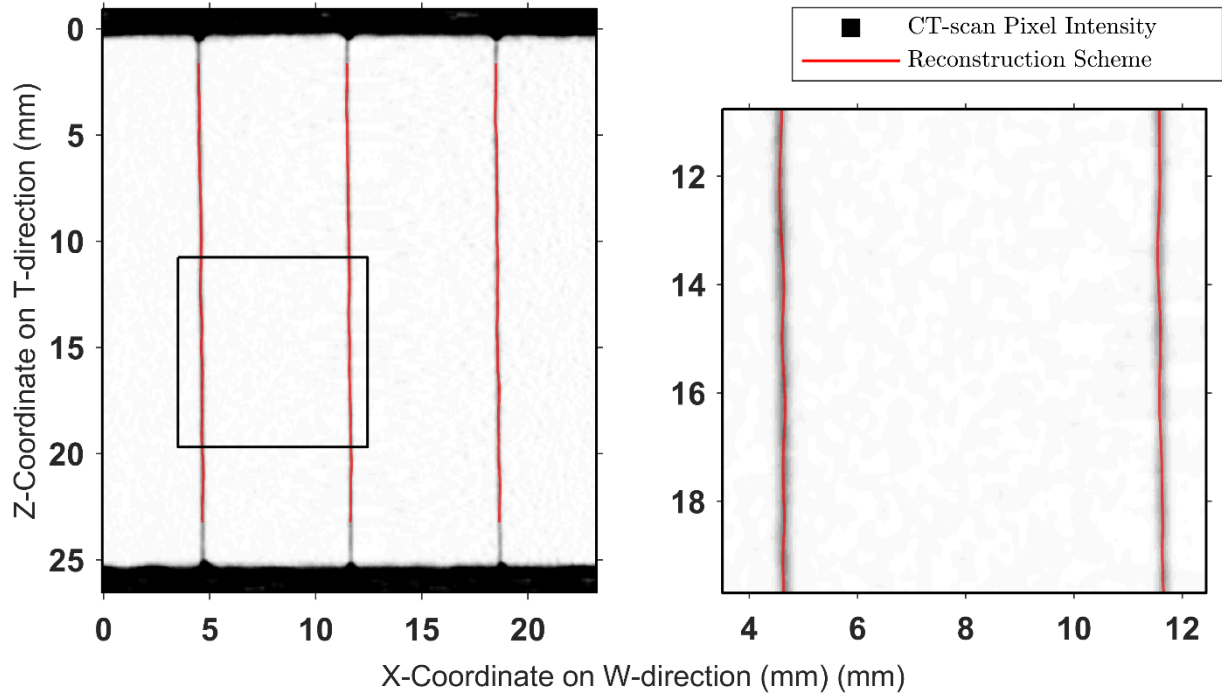
Figure 3.48. Comparison between double wall cross-sectional CT slice and reconstruction scheme
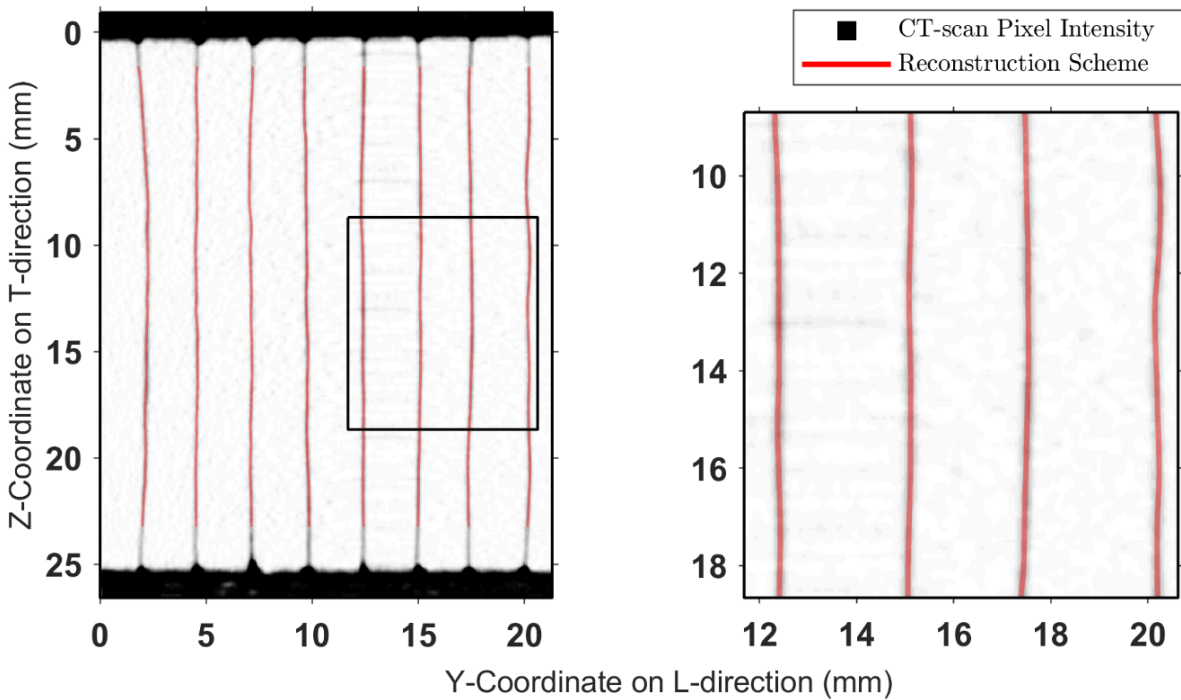
Figure 3.49. Comparison between single wall cross-sectional CT slice and reconstruction scheme

129
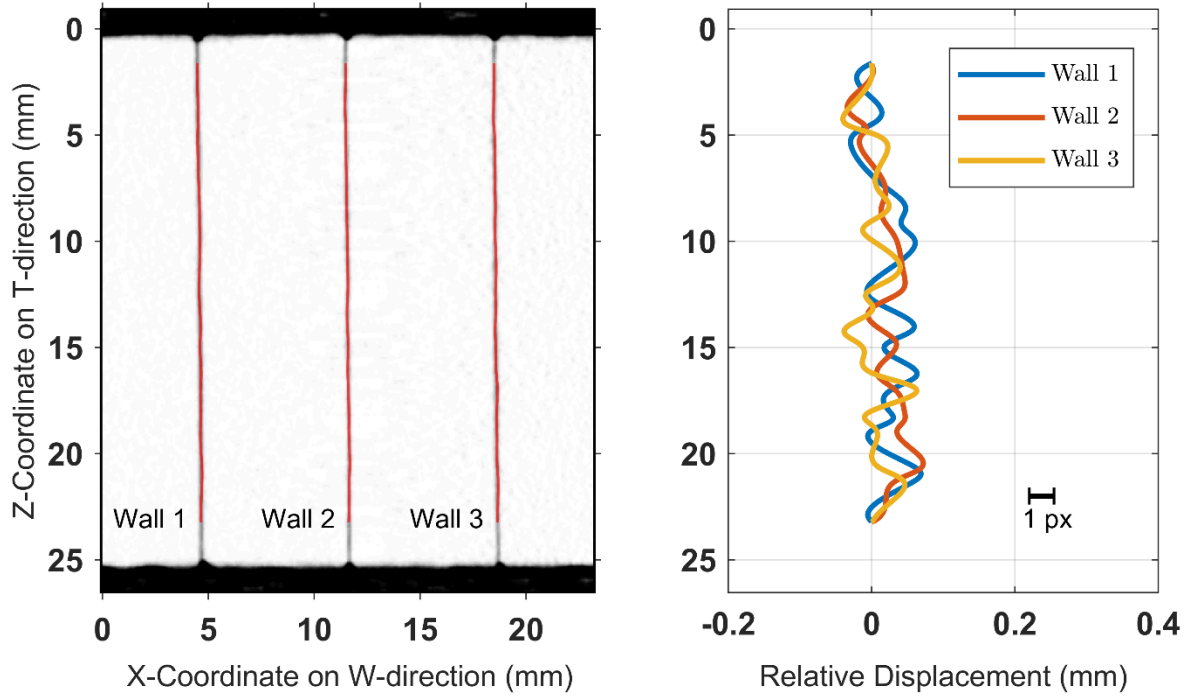
Figure 3.50. Representative relative displacements on double walls
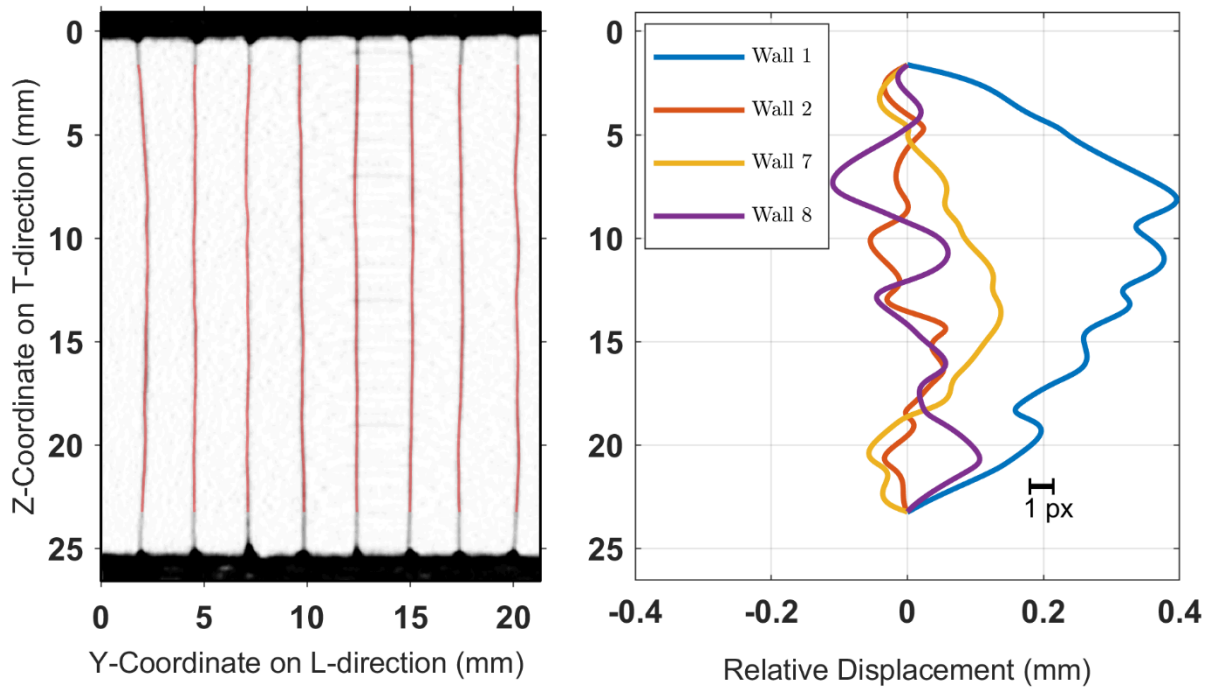
Figure 3.51. Representative relative displacements on single walls (wall numbering starts from left to right)

130
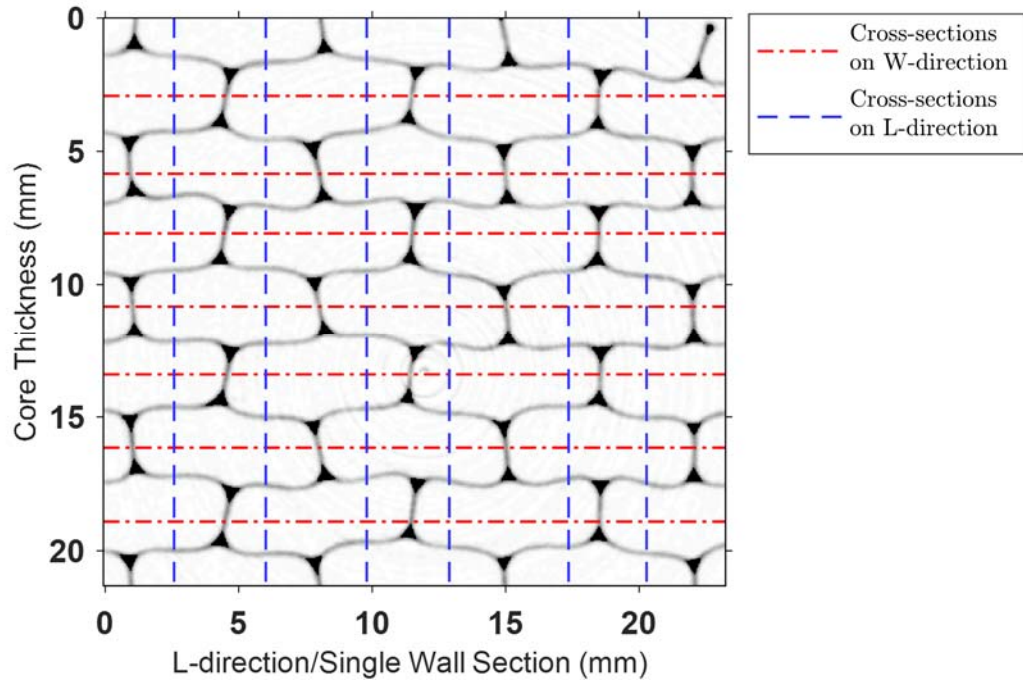
Figure 3.52. Orthogonal slice pattern for extraction of statistical information of the imperfection metrics
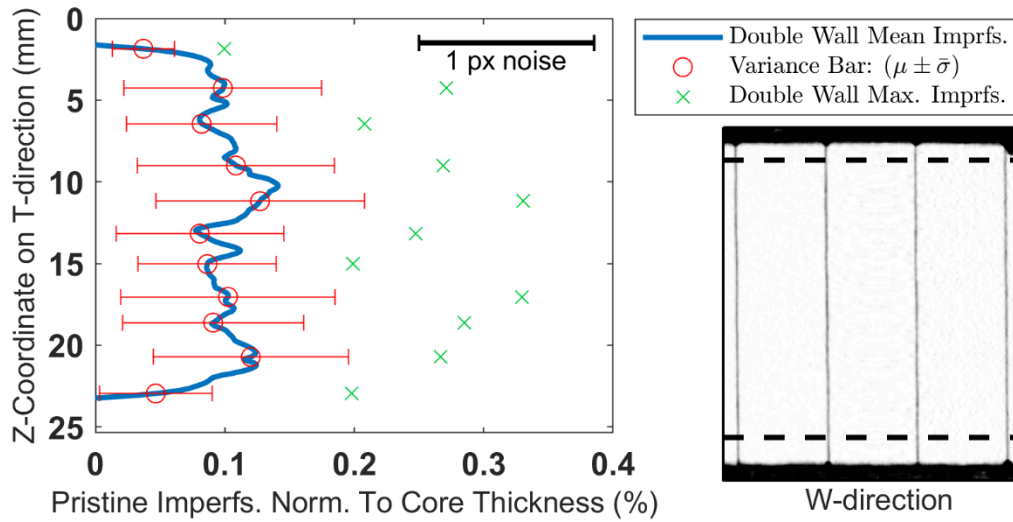
Figure 3.53. Metrics of double wall imperfections
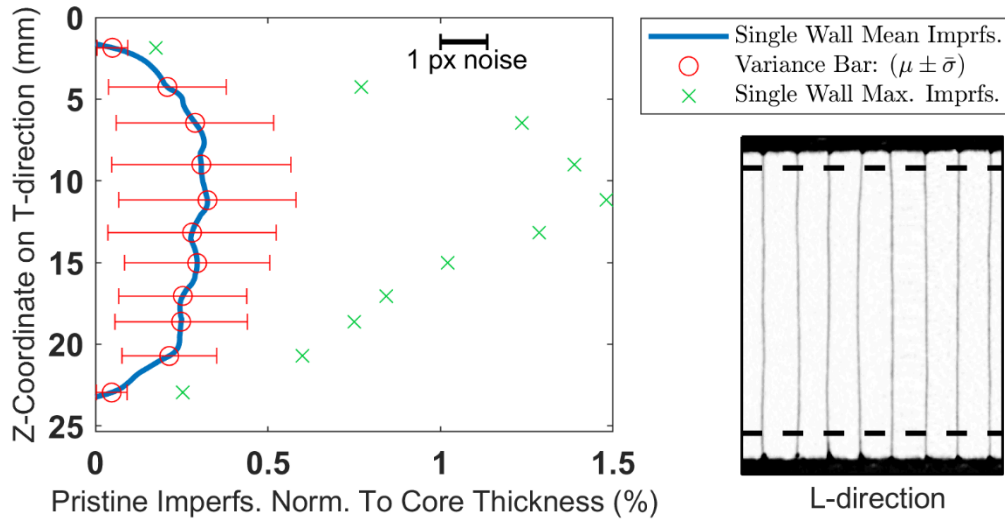
Figure 3.54. Metrics of single wall imperfections
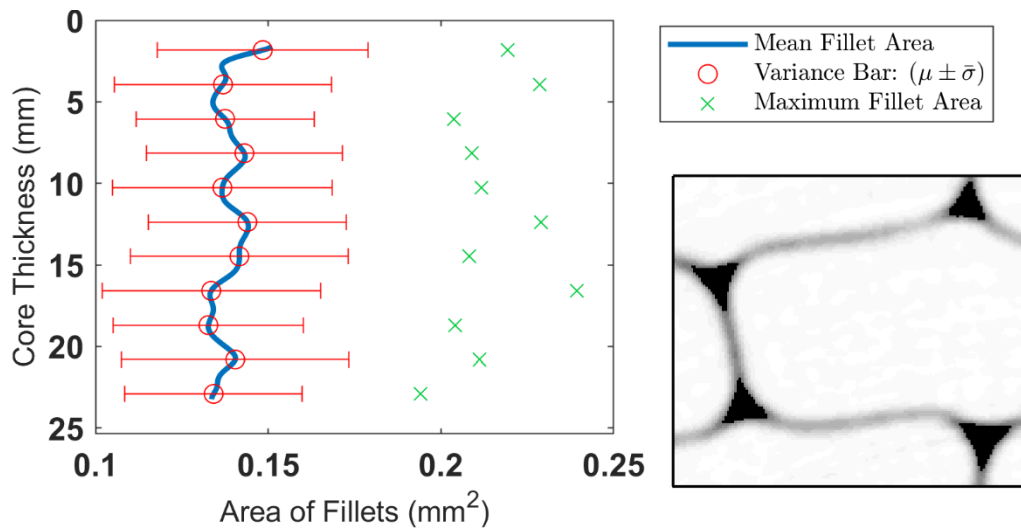
Figure 3.55. Metrics of fillet size irregularities
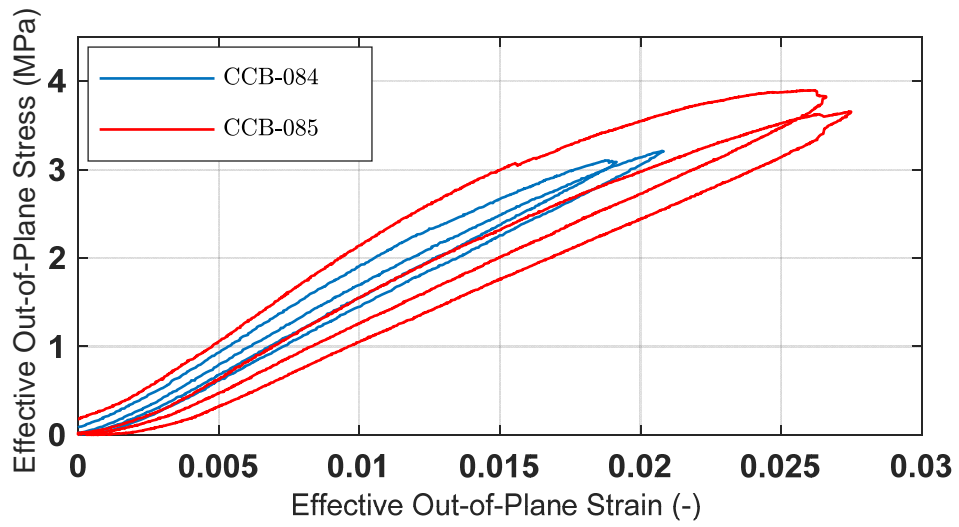
Figure 3.56. Flatwise compression response on posteriori CT-scanned core specimens
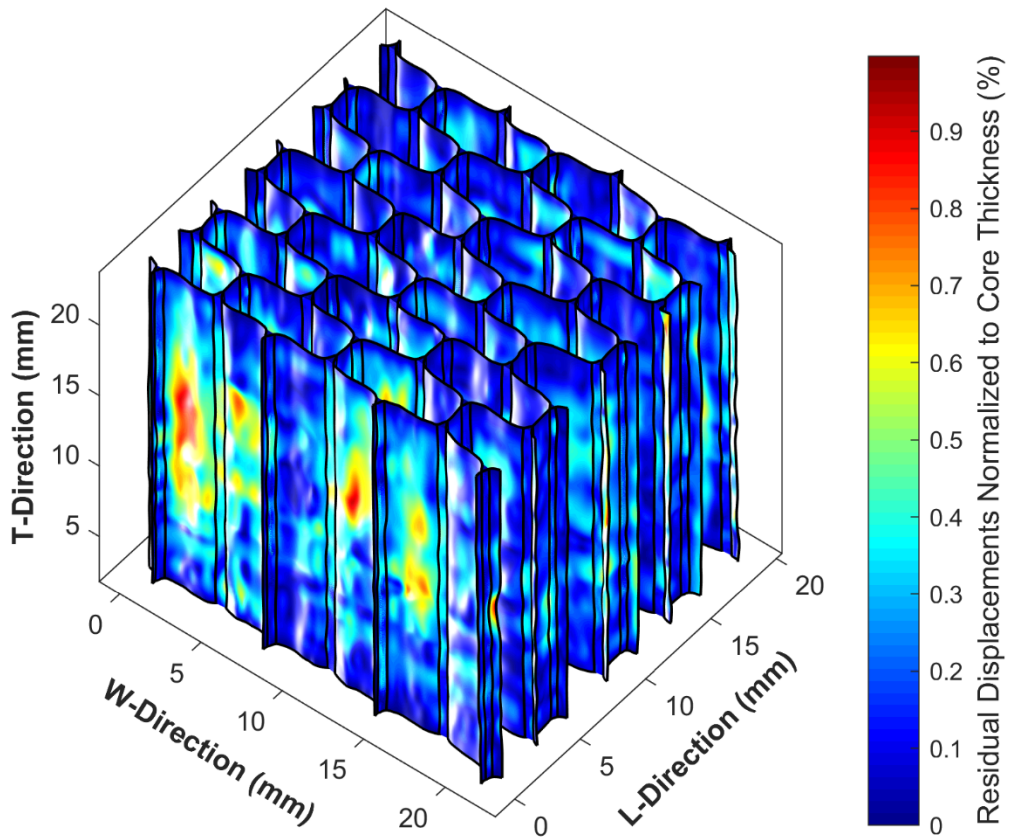
Figure 3.57. 3D residual absolute displacements map for CCB-084 tested coupon
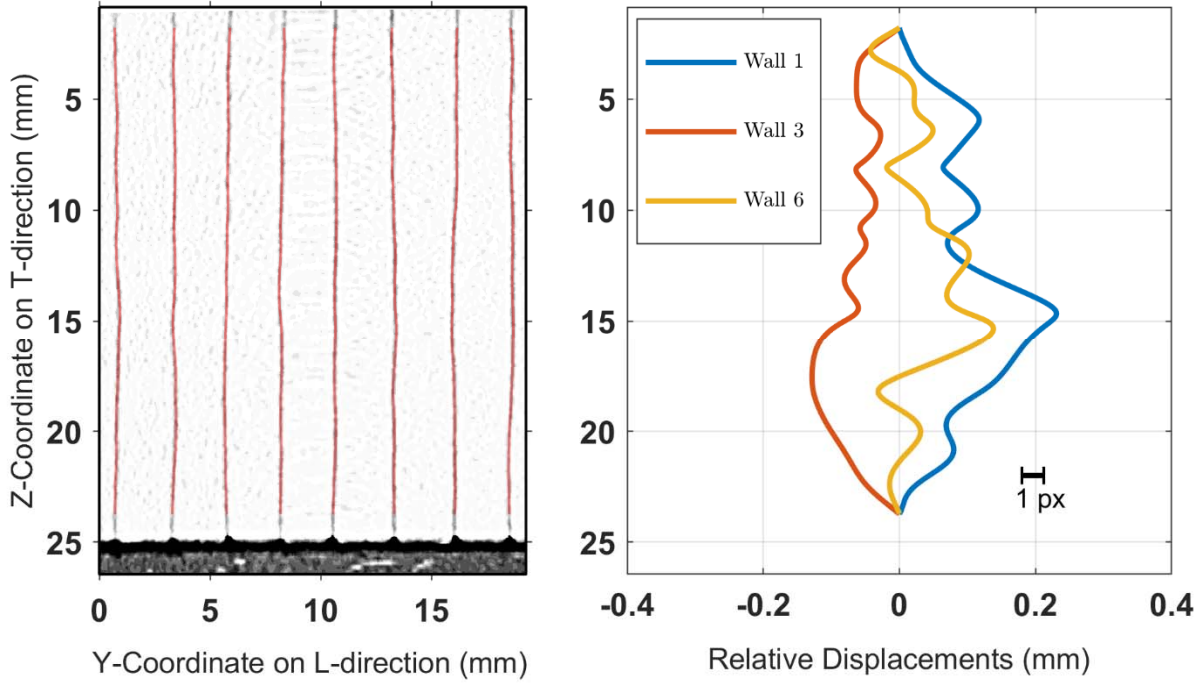
Figure 3.58. Representative single wall residual displacements along specific CT-slice of CCB-084

(wall numbering starts from left to right)
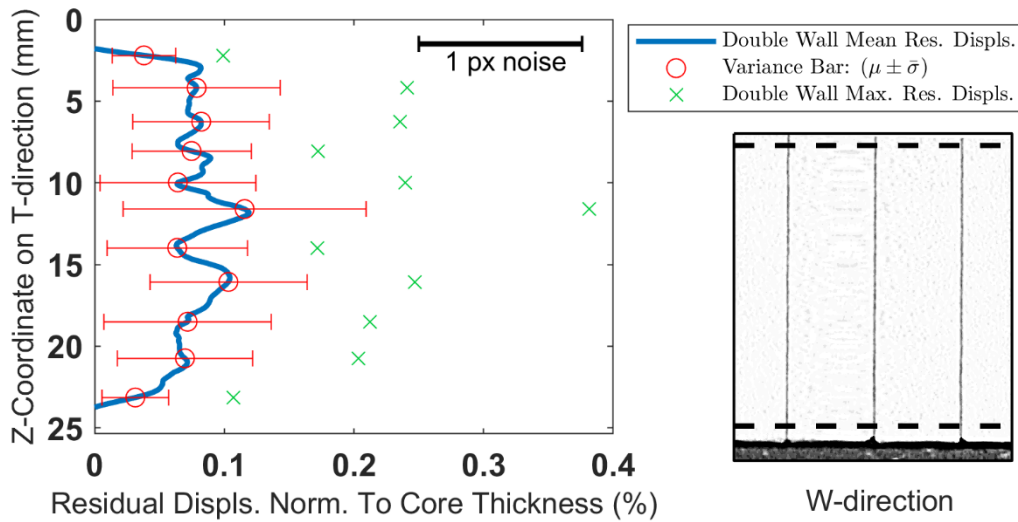
Figure 3.59. Metrics of double wall residual displacements on 24 double sectioned walls for coupon
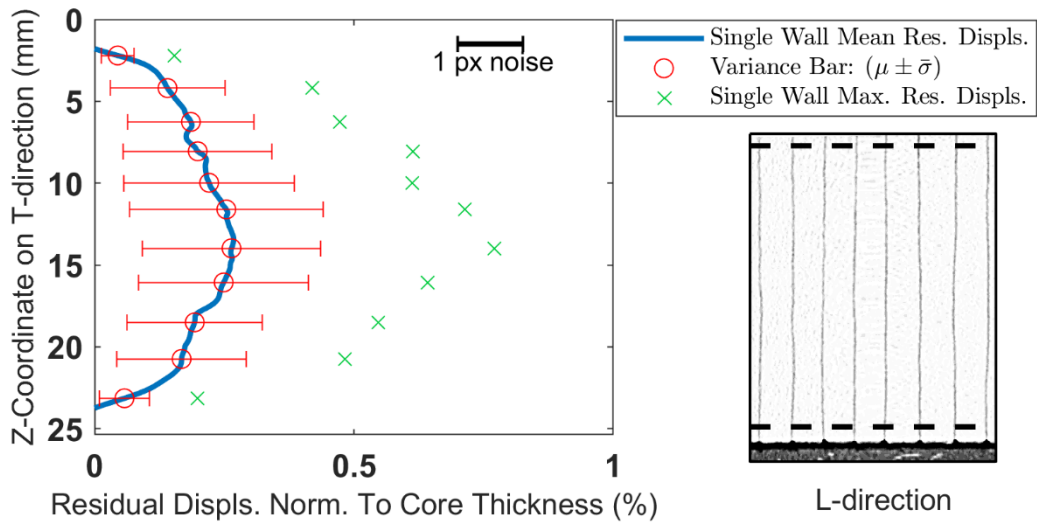
CCB-084

Figure 3.60. Metrics of double wall residual displacements on 48 single sectioned walls for coupon
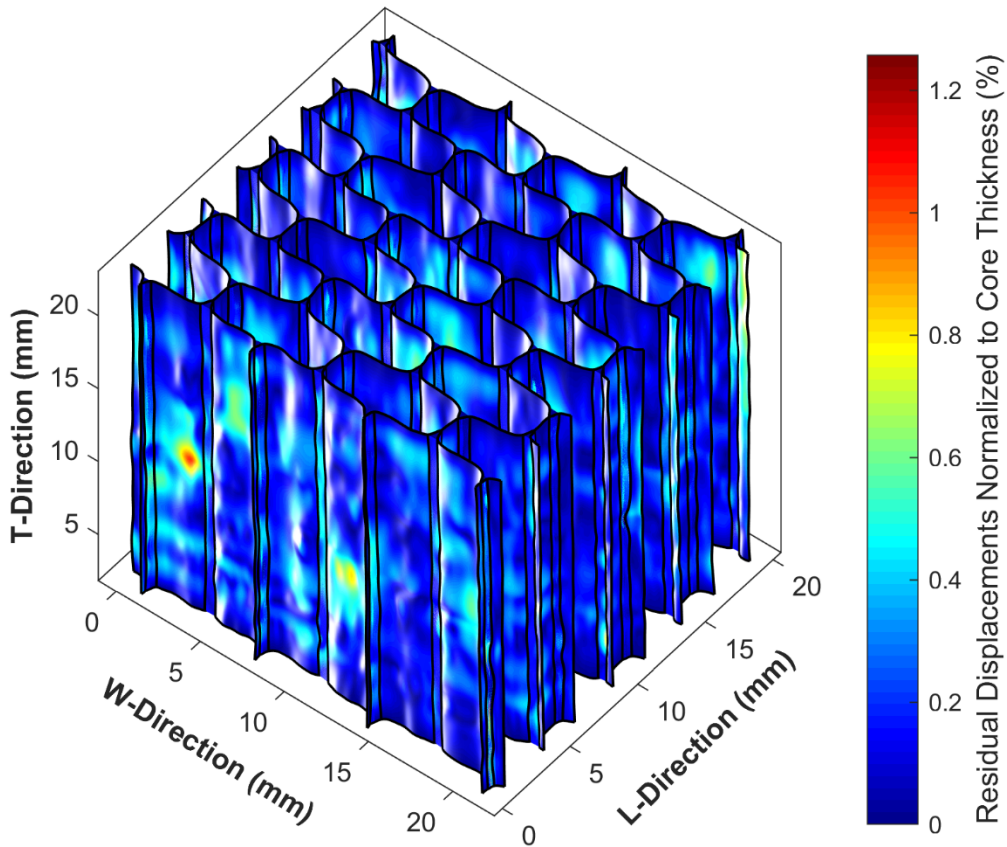
CCB-084

Figure 3.61. 3D residual absolute displacements map for CCB-085 tested coupon
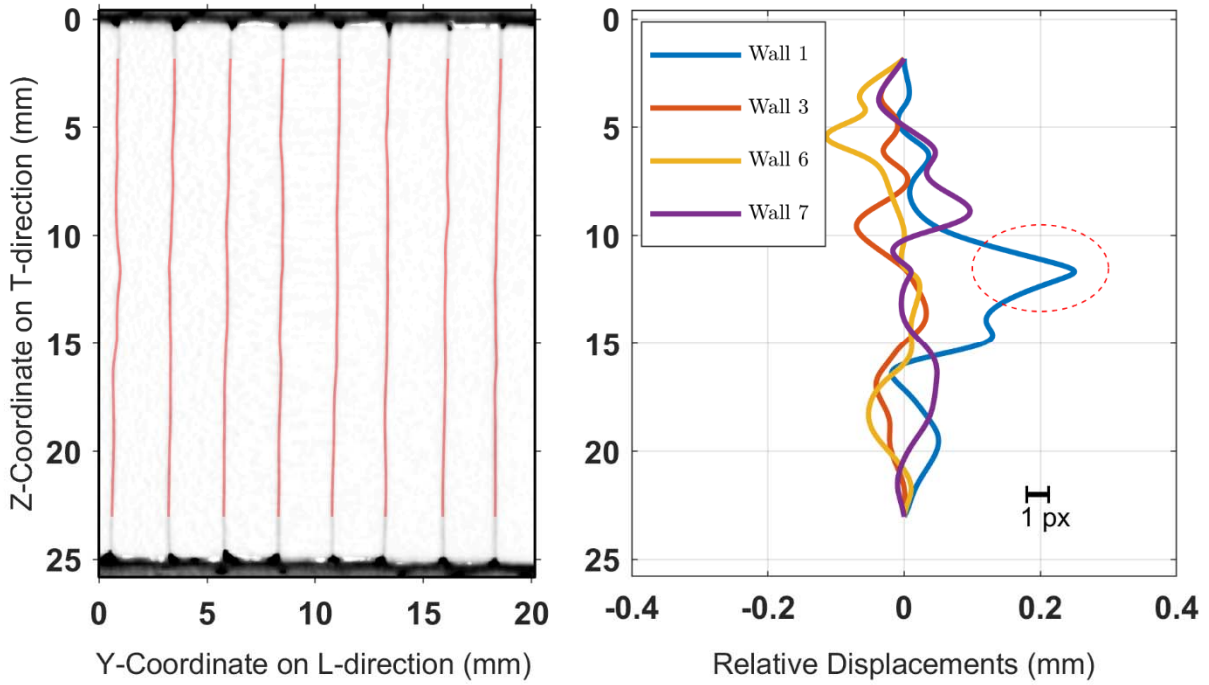
Figure 3.62. Representative single wall residual displacements along specific CT-slice of CCB-085

(wall numbering starts from left to right)
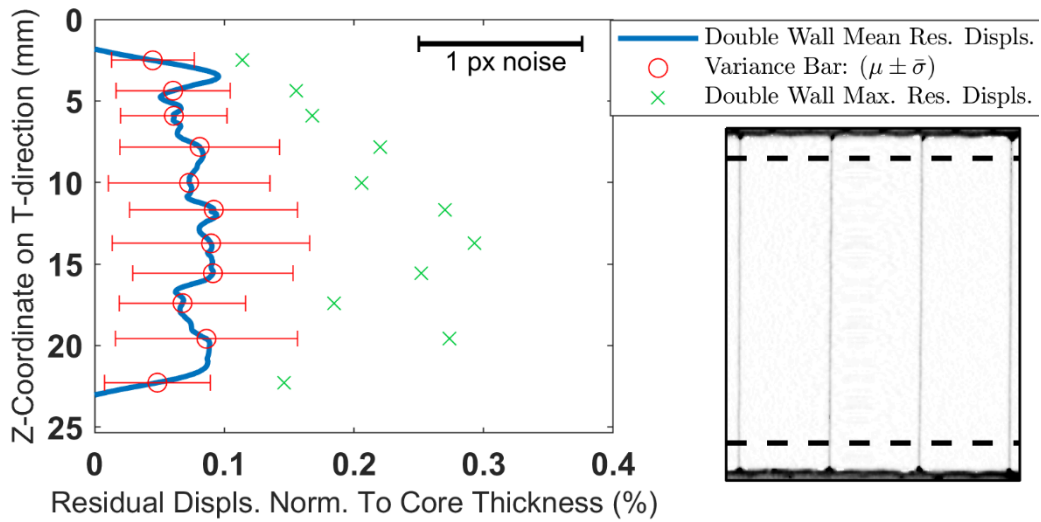
Figure 3.63. Metrics of double wall residual displacements on 24 double sectioned walls for coupon

CCB-085

136
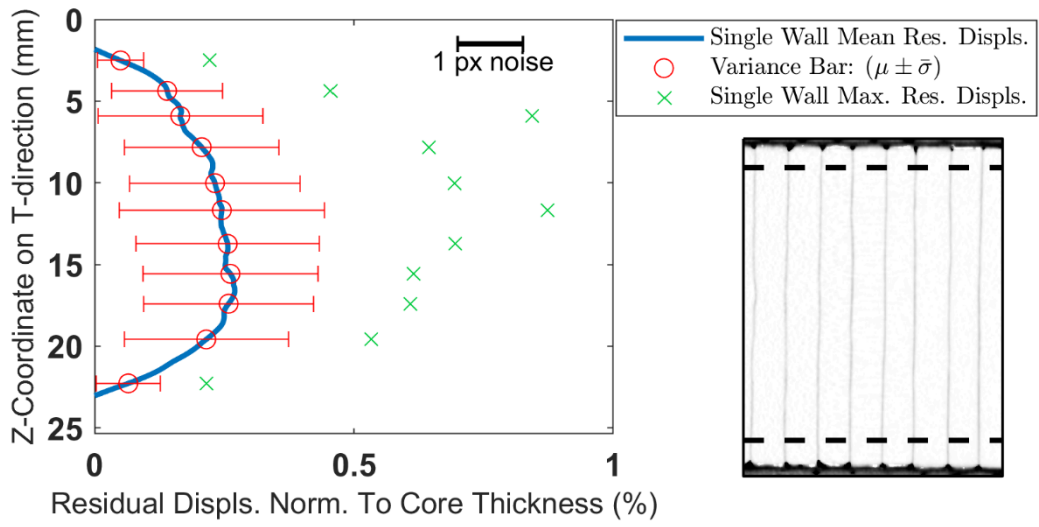
Figure 3.64. Metrics of single wall residual displacements on 48 single sectioned walls for coupon CCB-085

Figure 3.65. In-situ load frame
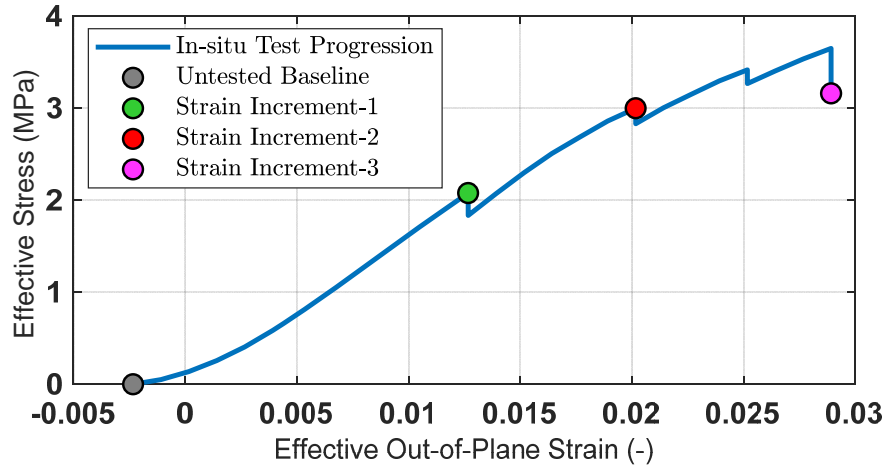
Figure 3.66. In-situ effective stress vs. strain data and strain increments for X-ray CT scanning
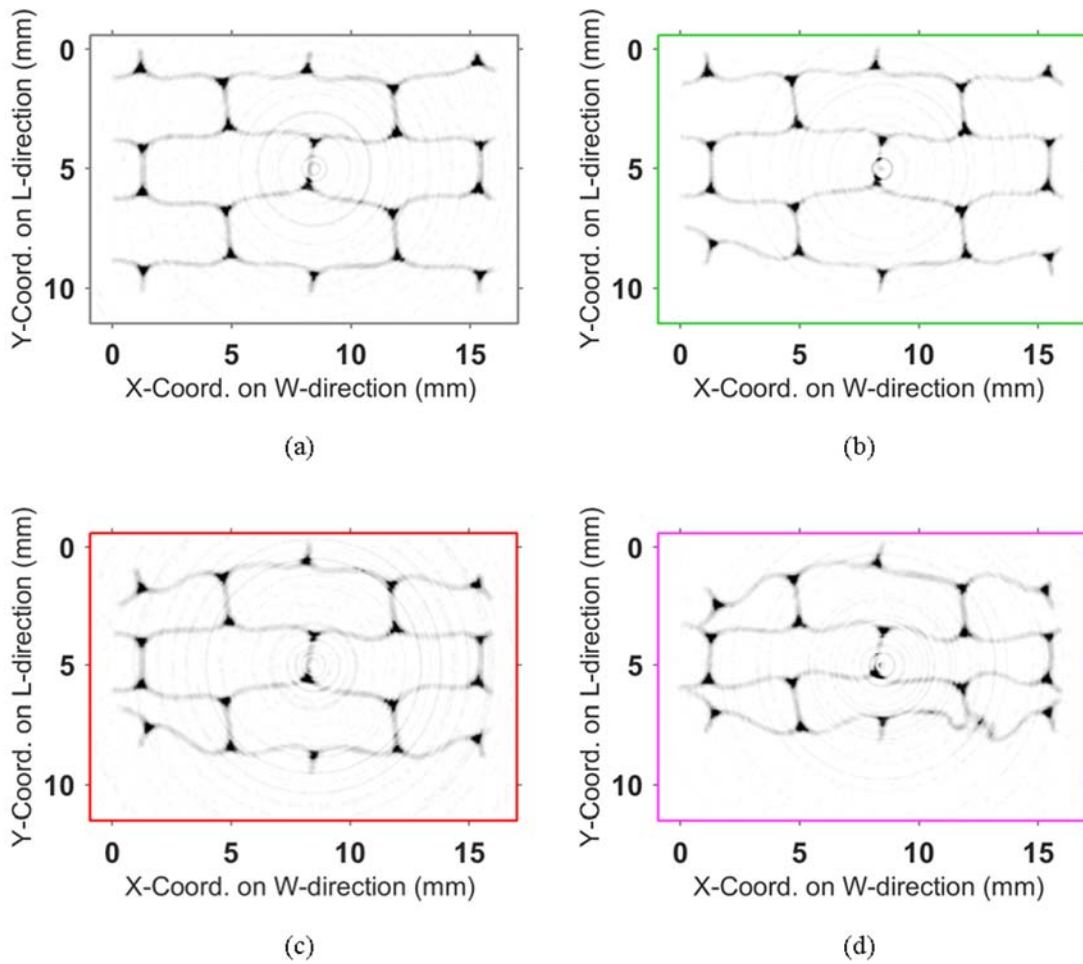
Figure 3.67. CT slices on thickness direction: (a) Baseline; (b) Strain increment "1"; (c) Strain

increment "2"; (d) Strain increment "3"

138
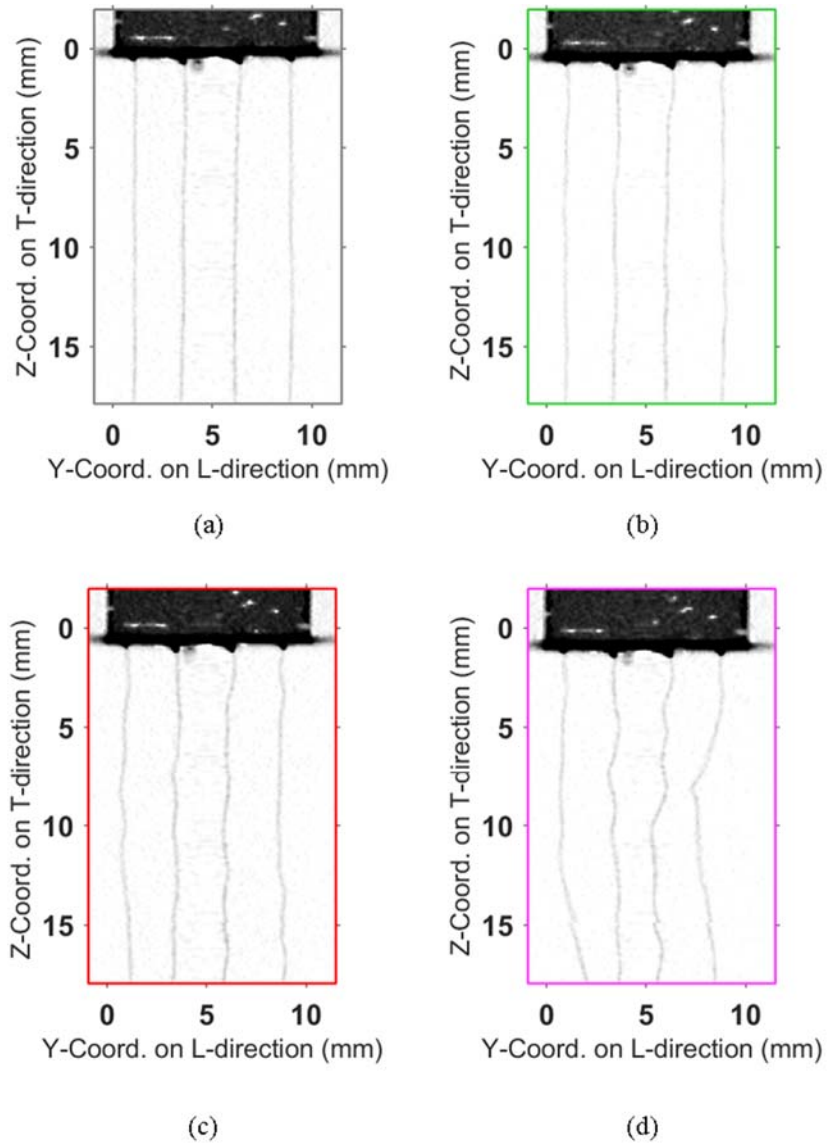
Figure 3.68. CT slices on ribbon direction: (a) Baseline; (b) Strain increment "1"; (c) Strain increment "2"; (d) Strain increment "3"
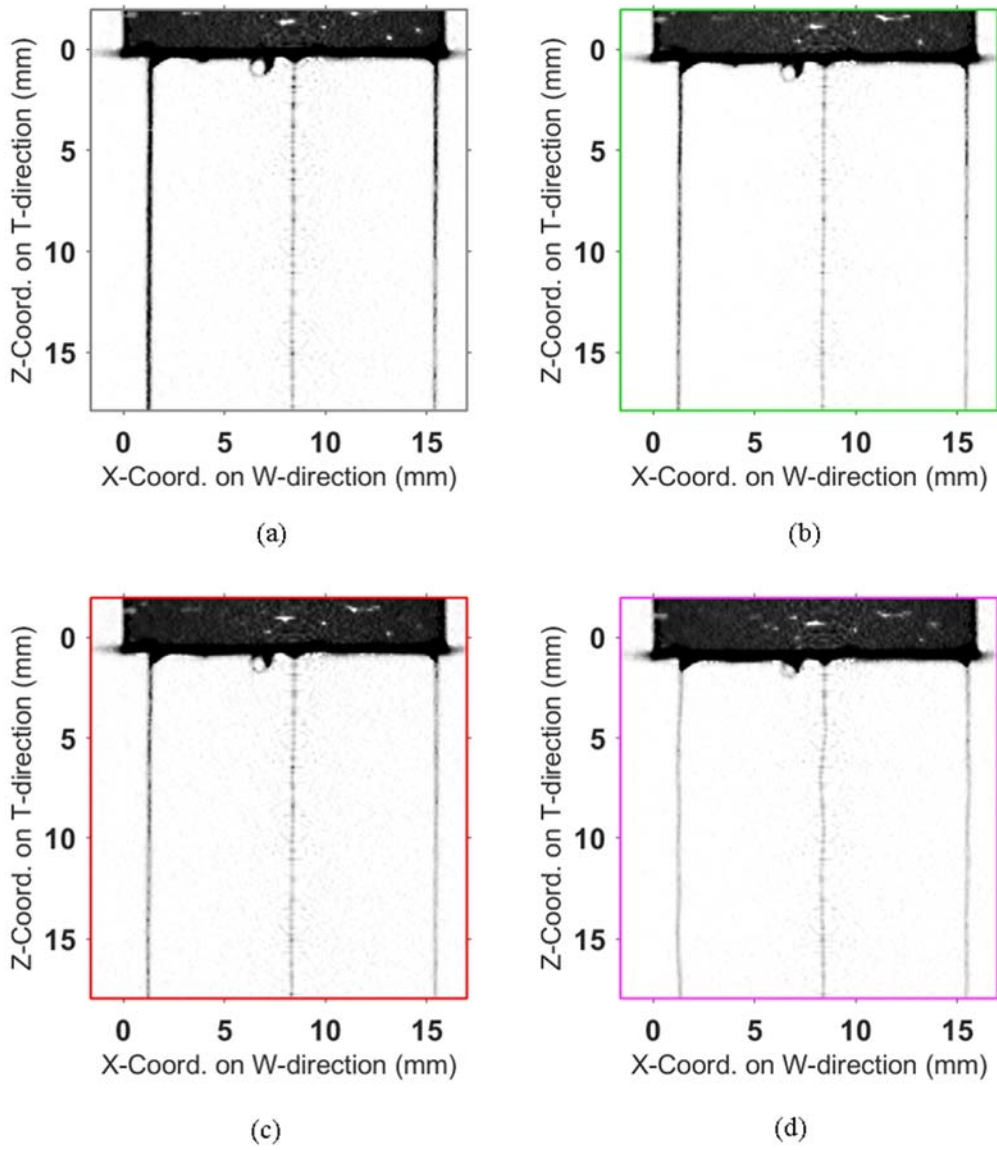
Figure 3.69. CT slices on expansion direction: (a) Baseline; (b) Strain increment "1"; (c) Strain increment "2"; (d) Strain increment "3"
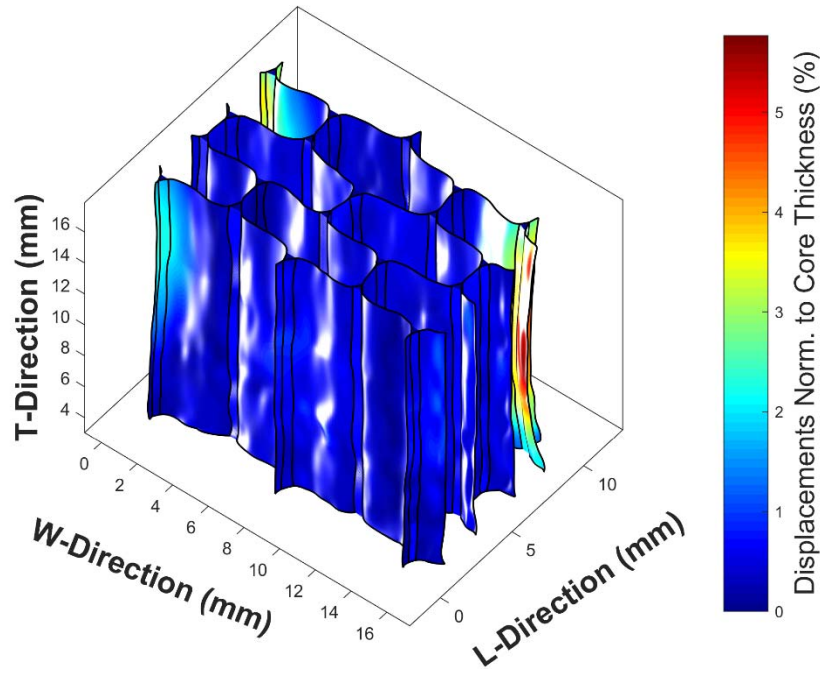
Figure 3.70. Reconstruction scheme applied on strain increment "1"
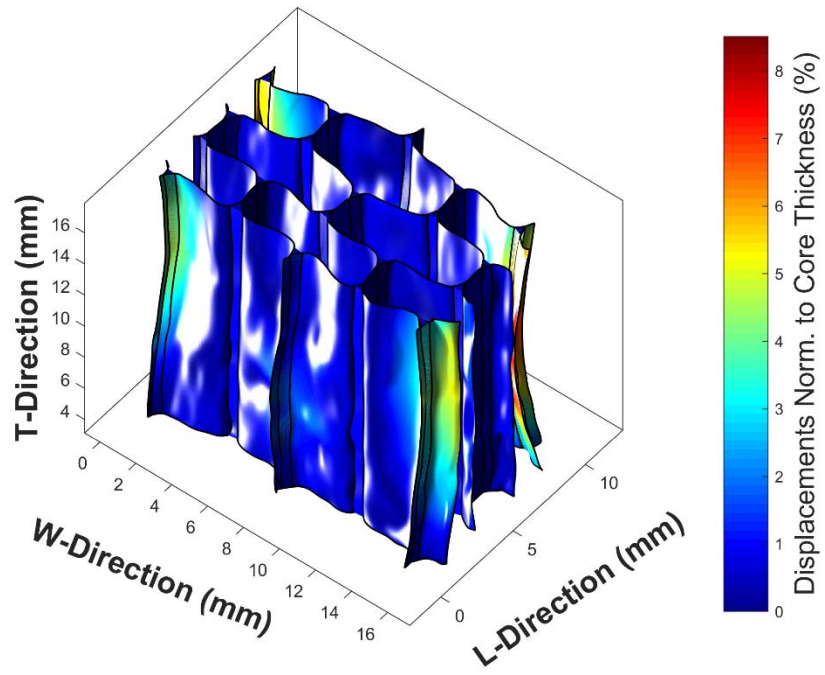
Figure 3.71. Reconstruction scheme applied on strain increment "2"

Table 3.1. Partial demonstration of fillet connectivity array

Fillet Structure ID	Neighboring Fillet Structures Based on Ellipse Intersection		
25	26	17	33
26	25	18	34
27	28	19	35
28	27	20	36
29	30	21	37
30	29	22	38
31	32	23	39
32	31	24	40

Table 3.2. Sequence of connected fillets

Ribbon ID #3	Ribbon ID #3 (cont'd)	Ribbon ID #4	Ribbon ID #4 (cont'd)
17	21	33	37
25	29	25	29
26	30	26	30
18	22	34	38
19	23	35	39
27	31	27	31
28	32	28	32
20	24	36	40

CHAPTER 4: VALIDATION WITH FINITE ELEMENT MODELING

4.1   OVERVIEW

Finite element models were carried out to validate the arguments regarding the effect of the phenolic resin fillets to the global stability of the meso-system under out-of-plane compression. Since the out-of-plane compressive behavior of honeycomb cores involves post-buckling phenomena, random node shaking and buckling eigen-vector mode shaping are commonly used to artificially include imperfections on an axially compressed computational models. Explicit geometric modeling of honeycomb cells was attained through MATLAB scripting by extending the reconstruction scheme presented in the previous chapter and create a finite element model. In this sense, realistic imperfections in terms of the wall waviness and fillet areas were accounted for. For non-metallic cores, base material properties are limited in literature. To this end, in-situ strips of honeycomb impregnated walls were extracted and tested under tension to calibrate base material properties. Due to the small cross-sectional area of those coupons, geometric features were extracted from optical microscopy and Voigt micromechanics approach. Finally, the versatility of the reconstruction scheme allowed for a parametric study with and without the fillets to further validate the experimental observations.

4.2   PREVIOUS WORK ON NON-METALLIC HONEYCOMB CORE MODELING

Honeycomb core in sandwich panels can be modelled either as a homogeneous thick layer of 3D elements with effective homogenized properties obtained from mechanical testing or by explicitly modeling core geometry with shell elements. The latter approach is computationally demanding for the analysis of a decent size sandwich panel. However, discretization of the core geometry at relatively small scale can provide useful insight on their performance under basic

types of loading. Virtual numerical experiments using explicit time integration schemes were performed on Nomex® paper honeycomb cores and validated through flatwise compression tests [Heimbs, 2009, Liu et al., 2015]. In a thorough numerical study on the different damage states, periodic boundary conditions on an aluminum representative volume element were applied to decrease the physical domain and the number of cells [Wilbert et al., 2011]. Imperfections were also introduced by means of first few buckling eigen-modes multiplied by reduction scalar factors. On a different approach on Nomex® paper cores, geometrical and material imperfections were introduced via a Gaussian distribution of the elastic moduli and the cell wall thickness respectively at each shell element [Asprone et al., 2013]. Collapse limit was affected more by the coefficient of variation of the paper thickness. Random perturbations through artificial node shaking were introduced in the cellular structure for the prediction of the indentation response of aluminum honeycomb sandwich panels [Czabaj, 2010]. A semi-adaptive coupling technique in the form of single particle hydrodynamics after local failure was employed in order to decrease computational cost and replace honeycomb structure with homogenized 3D elements [Aktay et al. 2008].

Regarding material constitutive behavior, uniaxial tension, stacked cylinder compression, and bending tests were conducted to characterize the mechanical properties of generic aramid paper [Fischer et al. 2009]. For this type of paper, there was no strong orthotropy along the paper sheet principal directions and the reported Young's modulus in both material directions was roughly equal to 8,000 MPa. Raw Nomex® tensile coupon tests were conducted, but the results were reported in force vs. strain format [Foo et al., 2007]. Base material properties of Nomex® paper along both material directions were determined via tensile tests on raw paper and phenolic resin impregnated coupons [Roy, 2014]. Multi-layer approach was utilized to model Nomex® paper separately from the phenolic resin coating, and despite the fillet accumulations, phenolic

resin was uniformly distributed along each cell wall [Seemann and Krause, 2017]. Tensile constitutive elastoplastic and elastic with linear softening curves were provided for aramid paper and phenolic resin respectively [Liu et al., 2015]. In this study, adhesive nodes were also modelled via cohesive interfaces with a bilinear traction separation law. Ductile material damage model was utilized to capture brittle fracture of phenolic resin coating on impregnated aramid paper cores [Giglio et al., 2011]. Based on the literature review, fillets have not been explicitly accounted for in the analysis of the honeycomb meso-structure of phenolic resin impregnated aramid paper core. Since most of the discussed studies rely on an idealized core geometry with some sources of artificial imperfections and irregularities, image-based model generation via X-ray CT data is a suitable technique to model the actual geometry of honeycomb cores.

4.3   MODEL GEOMETRY EXTRACTED FROM CT RECONSTRUCTION SCHEME

4.3.1   Mesh Generation through B-spline Reconstruction Scheme

The proposed reconstruction scheme was extended to create a finite element mesh which was compatible to Abaqus/Explicit® commercial finite element solver. This task was performed in MATLAB on pristine X-ray CT-scanned cores. Once the control points and corresponding knot vectors describing each cell wall and filet were identified, node spacing along the planar and through-thickness direction were user defined. These basic parameters along with Abaqus keyword commands *NGEN and *NGEN, allowed for the conversion of each B-spline into a finite element mesh within MATLAB environment. Regarding the fillets, each centroid was used as the basis for the partition of each   triangle of specific elevation into 3 quadrilaterals. The entire procedure starting from the image-based wall discretization all the way up to the end finite element mesh in Abaqus graphical interface is shown in Figure 4.1. Zero-thickness 4-node conventional

shell elements were chosen as a result of the B-spline surface formulation. On the other hand, fillets were modeled with 8-node brick elements. The details of the chosen element types and integration schemes are going to be discussed in the following sections.

During-image based discretization of each ribbon, the individual data points between consecutive CT-scan slices were not spaced uniformly. Since the parametric variables of B-spline theory represent time variable, the discrete points along a predefined size patch of the B-spline surface are also unequally spaced resulting in an uneven mesh in the through-thickness direction. This irregularity is overcome by imposing equal distances between consecutive nodes as graphically shown in Figure 4.2 for a half-sinusoidal wave case study in which initial raw data points were randomly spaced. The random spacing between the raw data points has been exaggerated for graphical purposes and by no means does it reflect the actual spacing between consecutive CT scan slices. Figure 4.3 illustrates the finalized mesh before and after the application of equal distance constraint. As can be observed, the imposed constraint resulted in a more structured mesh.

The reconstruction scheme was applied to CT-scan slices that did not fully span the entire nominal core thickness of 25.4 mm due to uneven blending of the adhesive film into the honeycomb core as illustrated by two different slices in Figure 4.4. The top and bottom CT-slices of the image-based reconstruction scheme were extruded and fitted through B-spline surfaces to attain the prescribed core thickness of 25.4 mm. In addition, first derivative along the through-thickness direction was predefined to attain a smooth transition from the extruded slices as shown in Figure 4.5.

4.3.2   Distribution of Phenolic Resin through Optical Microscopy Measurements

As stated earlier, B-spline surface cell walls were modeled with 4-node zero-thickness shell elements. Within each element, a composite layup section was defined to account for the composite nature of the phenolic resin impregnated Nomex® paper walls. The thicknesses of the phenolic resin coating and the paper were determined via optical microscopy. The cross-sectional view consisted of multiple microscopy images tiled up together is shown in Figure 4.6. After taking the microscopy images, the measuring scale shown in Figure 4.7 established a scale factor to convert pixels into physical dimensions. First, we apply k-means clustering to segment the entire image into 3 regions, namely the paper walls, the phenolic resin coating and fillets, and the surrounding cell voids. Three different grayscale intensities were assigned to obtain the segmented image similar to that of Figure 4.8. Paper thickness may be directly calculated by counting the number of pixels along its thickness direction. This method is not so accurate because the paper section is relatively thin and subjected to round-off errors. The best way to calculate the paper thickness is to divide the number of gray color pixels by the length of the examined wall as calculated from B-spline fitting curve shown in Figure 4.9. This procedure was repeated for multiple single wall segments and the average paper thickness was equal to 45 μm. For the phenolic resin coating on the single walls, the same procedure was followed, and the average thickness was equal to 32 μm. Double walls exhibited a very small portion of phenolic resin coating. The phenolic resin coating on the single walls was equally distributed along the length of the cell wall. For the first half of each single wall segment, the coating was distributed either above or below the paper section and the opposite direction was chosen for the other half.

Based on the measurements and the meso-structure, single and double walls were modeled as zero-thickness shells with a composite layup section definition. Table 4.1 should be used in

147

conjunction with the reference microscopy image shown in Figure 4.10 in which the ply ID number of each shell element increases along the direction of the shell element normal. Double wall region is split into two separate entities with identical coordinates, each having a thickness of 45 μm, and these entities are tie-constrained to mimic the adhesive node bonding. Offset distances normalized to total laminate height were defined to properly constrain the surfaces of the double wall region. Since the adhesive printed lines have a finite peel-off strength, cohesive interfaces with a bilinear traction separation laws could have been defined, but this feature is beyond the scope of this research work as a result of the limited experimental data on the cohesive bond strength.

4.4   BASE MATERIAL MECHANICAL PROPERTIES

4.4.1   Calibration of Material Parameters based on Uniaxial Tensile Testing

Uniaxial testing was performed on aramid paper coupons as well as in-situ strips of single walls extracted from sandwich core samples via fine saw. Regarding the aramid paper coupons, the tensile coupons were laser cut through 40 W CO_2 Orion Motor Tech model to create dog bone coupons. The laser intensity was minimal, and a fine line of the coupon perimeter was engraved on the aramid paper sheet which was then carefully cut with a razor blade. Because the phenolic resin coated paper coupons extracted from the sandwich cores were very small, a large as well as a small configuration of aramid paper tensile coupons were created to check out any possible edge effects. The three types of specimens shown in Figure 4.11a were all tested in TestResources 100-Series load frame equipped with a 500 lbf actuator. To prevent local failure of large size aramid paper coupons in the gripped region, rubber paste was utilized to bond square tabs onto the tensile coupon. The bonding procedure was done under vacuum to squeeze out the excessive amount of rubber paste and attain uniform total tab thickness. Regarding the in-situ phenolic resin

impregnated coupons, the load frame grips held the specimens from the attached sandwich composite skins to eliminate any chance of local failure in the gripped zone.

The entire test apparatus is shown in Figure 4.11b. Strain measurements on aramid paper coupons were attained via the actuator displacement as well as non-contact EIR Model LE-05 laser extensometer. Laser extensometer tracks the distance between two reflective tapes attached on the tested coupon. The cross-sectional area of each coupon was measured through imaging and micrometer with measuring increment of 0.001 mm.

Only the actuator displacement channel was utilized for the in-situ phenolic resin tensile coupons because the reflective tapes could stick well on the surface. In this case, longitudinal strain was calculated by normalizing the displacement channel by the free length of the core between the two adhesive film layers. The cross-sectional area for of each phenolic impregnated coupon was determined via optical microscopy due to the composite nature of the tested samples.

As a result of the paper sheet orthotropy, machine principal material direction was oriented at 0°, 45°, and 90° degrees with respect to the axis of the coupon, to fully characterize the 4 independent elastic properties of the aramid paper under plane stress conditions. These four properties are the Young's modulus in 1-direction, E_1, the Young's modulus in 2-direction E_2, the in-plane shear modulus, G_{12}, and finally the Poisson's ratio due to loading along 1-direction, v_{12}. In this case, the 1-direction corresponds to the stronger material principal direction which is also coincident to the machine paper sheet direction. Typical stress-strain relationship for a large size aramid paper coupon is shown in Figure 4.12. The normalized strain levels obtained from the actuator displacement channel were slightly underestimated compared to the local laser measurements. Since, local measurements are more representative of the strains in the slender

149

portion of the dog-bone coupons, laser extensometer was utilized for strain calculations of aramid paper samples. Typical uniaxial tensile curves in the three different orientations for the large coupon configuration are shown in Figure 4.13, in which all the stresses and strains have been normalized with respect to the peak stress and strain along the 0° orientation. In total, 10 specimens along the 0° and 90° orientations were tested, and 5 coupons along the 45° direction were conducted. For the 0° orientation, digital image correlation software VIC-2D was used to calculate Poisson's ratio v_{12}. The speckle pattern was hand-drawn with a fine sharpie as shown in Figure 4.14. Having the four average elastic constants E_1, E_2, v_{12}, and $E_{45°}$ from the tensile tests conducted on three different orientations, Equation (4.1) from lamina plane stress theory for $\theta=45°$ was utilized to back out the in-plane shear modulus G_{12}.

$$\frac{1}{E_{45°}} = \frac{1}{E_1}\cos^4\theta + \left(\frac{1}{G_{12}} - 2\frac{v_{12}}{E_1}\right)\sin^2\theta\cos^2\theta + \frac{1}{E_2}\sin^4\theta \tag{4.1}$$

Figure 4.15 shows a direct comparison of the tensile response normalized to peak stress and strain between large and small aramid paper coupons tested at 0° orientation. The observed good correlation suggests that the size of the in-situ phenolic resin impregnated paper coupons (refer to Figure 4.11a) is suitable enough for backing out the elastic modulus of just the phenolic resin constituent. Figure 4.16 illustrates the global stress vs. strain of 5 different in-situ phenolic resin impregnated paper coupons. The elastic modulus does not show significant variation among the different tensile tests. In Figure 4.16, phenolic resin fracture occurred when the average stress exhibited a small drop. Then, strain localizes on the damaged region until the point where the paper also fractures. The behavior was linear elastic until initial failure, indicating that the phenolic resin behaves in a brittle material.

The total cross-sectional area was calculated based upon optical microscopy. More specifically, after the fracture of each specimen due to tensile loading, Buehler SamplKwick acrylic resin system was casted around each specimen. Once the resin was cured, the assembly was cut under the fine precision saw to allow for clean and high-contrast microscopy images as the one shown in Figure 4.17. Since microscopy image was taken from one cross section for each coupon, cross-sectional area was assumed to be the same along the entire length. The phenolic resin Young's modulus, E_r, and tensile strength, f_r^T were determined by assuming Voigt micromechanics model. This model implies strain compatibility along the loading direction, meaning that the strains of the composite layup and the two constituents are equal. In this sense, the effective stress and modulus of the composite are related to the base material corresponding properties through the volumetric/area fractions as illustrated in the generalized Equation (4.2). In Equation (4.2), the generic symbol C_i represents either the elastic modulus or the tensile strength, and V_{paper} reflects the area fraction of the paper relative to the total area of the phenolic resin impregnated paper wall.

$$C_{\text{comp.}} = C_{\text{paper}}V_{\text{paper}} + C_{\text{phenol}}(1 - V_{\text{paper}}) \qquad (4.2)$$

Given the volumetric/area fractions of each constituent, and the effective stresss-strain curves of the raw aramid paper and composite in-situ coupons, the phenolic resin elastic modulus and tensile strength were backed out through the application of the basic Voigt model. For the in-situ phenolic impregnated paper tensile coupons, it was assumed that the machine direction (1-direction) of the paper was parallel to the sandwich core thickness direction. Table 4.2 summarizes the calculation of the elastic Young's modulus of the phenolic resin for all 5 tensile tests. Finally, the average tensile strength f_r^T was calculated as 43 MPa, a value that is underestimating the true

strength. Possible reason for this low value is the complex geometry and narrowness of each tensile coupon.

4.4.2 Material Modeling in Abaqus

Brittle damage initiation and evolution of phenolic resin was incorporated through a ductile damage criterion available in Abaqus 6.14 for metal plasticity. By using this ductile damage feature, it is assumed that material will yield based upon Von-Mises criterion in which yielding of an element under combined stress state is triggered when its distortion energy density reaches the corresponding critical value at yield in uniaxial tension. Ductile damage model is available in Abaqus/Explicit®, which is the type of solver used in this research work.

A schematic of the constitutive yielding behavior is shown in Figure 4.18. At a certain user defined yielding stress, damage initiation occurs, and scalar damage index starts getting non-zero values beyond this point. This yielding stress corresponds to an equivalent plastic strain $\bar{\varepsilon}_{\text{pl}}^{0}$. If the value $\bar{\varepsilon}_{\text{pl}}^{0}$ is selected to be larger than the residual plastic strain after elastic unloading as shown in Figure 4.18, the material will keep yielding in a perfectly plastic manner until the equivalent strain value is met. For metal plasticity, the equivalent plastic strain at damage onset $\bar{\varepsilon}_{\text{pl}}^{0}$ is highly dependent upon the stress triaxiality and strain rates. Since there is no experimental data that validate this dependency on phenolic resin, both of these parameters were ignored by selecting a unique value of $\bar{\varepsilon}_{\text{pl}}^{0}$. Additionally, the artificial yielding branch of the phenolic resin constitutive behavior was very small to simulate a nearly brittle behavior. Post-damage initiation behavior was established through a linear softening branch in which both the yielding stress and elastic modulus are both reduced by a scalar damage variable D. The maximum value of D is

equal to unity and occurs when either the area underneath an equivalent traction-separation law reaches an experimentally obtained fracture toughness or the equivalent final plastic failure strain gets equal to $\bar{\varepsilon}_{\text{pl}}^{f}$ (see Figure 4.18). Equivalent plastic failure strain $\bar{\varepsilon}_{\text{pl}}^{f}$ was based on the uniaxial tensile tests of the in-situ impregnated coupons. To avoid mesh sensitivity issues due to strain localization in the post-damage initiation region, the failure equivalent plastic strain $\bar{\varepsilon}_{\text{pl}}^{f}$ is expressed in terms of element effective displacement $\bar{u}_{\text{pl}}^{f}$ using Equation (4.3) [Lapczyk and Hurtado, 2007]. In Equation (4.3), L^{e} is the characteristic length of the element. For shell elements, the characteristic length is equal to the square root of the area assigned per integration point, and the cubic root of the volume for 3D elements. For this study, the effective plastic failure displacement $\bar{u}_{\text{pl}}^{f}$ is related to the damage index D in a linear manner as shown in Figure 4.19. Finally, element removal was activated when the scalar degradation factor was equal to $D = 0.95$. The chosen material parameters are shown in Table 4.3 for the phenolic resin. Since the material behavior is quite brittle, a small isotropic hardening plateau was chosen. Depending on the mesh size, the equivalent plastic failure was manually calculated based upon a fixed value of failure strain.

$$\bar{u}_{\text{pl}}^{f} = L^{e} \bar{\varepsilon}_{\text{pl}}^{f} \tag{4.3}$$

Regarding the orthotropic behavior of Nomex® paper as observed in Figure 4.13, Hill yielding criterion was utilized which essentially accounts for anisotropic yielding based on Equation (4.4). Parameters F, G, H, L, M, N are obtained via uniaxial tests along the principal material directions and defined as in Equation (4.5). The terms with bar symbol represent the 6 different initial yield stresses and σ_{0} reflects a random reference value. Instead of definition of

these parameters, the ratios in Equation (4.6) must be calculated. Once initial yielding has occurred, all the 6 different yielding stress quantities are scaled proportionally to the R_{ij} ratios based on the reference isotropic hardening constitutive behavior. Since paper material was assigned in the zero-thickness shell formulation in which each element is subjected to plane stresses, the chosen values along the 3-direction do not matter. Ductile damage evolution was not utilized in paper material model.

$$F(\sigma_{22} - \sigma_{33})^2 + G(\sigma_{33} - \sigma_{11})^2 + H(\sigma_{11} - \sigma_{22})^2 + 2L\sigma_{23}^2 + 2M\sigma_{31}^2 + 2N\sigma_{12}^2 = 1 \qquad (4.4)$$

$$F = \frac{\sigma_0^2}{2}\left(\frac{1}{\bar{\sigma}_{22}^2} + \frac{1}{\bar{\sigma}_{33}^2} - \frac{1}{\bar{\sigma}_{11}^2}\right)$$

$$G = \frac{\sigma_0^2}{2}\left(\frac{1}{\bar{\sigma}_{33}^2} + \frac{1}{\bar{\sigma}_{11}^2} - \frac{1}{\bar{\sigma}_{22}^2}\right)$$

$$H = \frac{\sigma_0^2}{2}\left(\frac{1}{\bar{\sigma}_{11}^2} + \frac{1}{\bar{\sigma}_{22}^2} - \frac{1}{\bar{\sigma}_{33}^2}\right)$$

$$M = \frac{3\tau_0^2}{2\bar{\sigma}_{13}^2}$$

$$M = \frac{3\tau_0^2}{2\bar{\sigma}_{13}^2}$$

$$N = \frac{3\tau_0^2}{2\bar{\sigma}_{12}^2}$$

$$(4.5)$$

$$R_{11} = \frac{\bar{\sigma}_{11}}{\sigma^0},$$

$$R_{22} = \frac{\bar{\sigma}_{22}}{\sigma^0},$$

$$R_{33} = \frac{\bar{\sigma}_{33}}{\sigma^0},$$

$$R_{23} = \sqrt{3}\,\frac{\bar{\sigma}_{12}}{\sigma^0},$$

$$R_{13} = \sqrt{3}\,\frac{\bar{\sigma}_{13}}{\sigma^0},$$

$$R_{12} = \sqrt{3}\,\frac{\bar{\sigma}_{12}}{\sigma^0}$$

(4.6)

4.5   ANALYSIS RESULTS

A fully enclosed cell was modeled to reduce the computational run time. One side of the honeycomb structure was fully clamped, and the other side was tie-constrained to a rigid plate. All the degrees of freedom on the rigid plate were restrained except for the displacement along the core thickness direction. Tie constraints were also applied on the double wall regions of two consecutive ribbons to effectively account for the increased stiffness. Additional tie constraints were applied between the fillets and the single cell walls. Cell walls were modeled with reduced integration zero-thickness shell elements (S4R), and the fillet elements were modeled with 3D brick elements (C3D8R). Finally, the through-thickness direction of the cell wall plates and fillet columns was seeded with 100 and 200 nodes respectively. A snapshot of the finalized mesh is shown in Figure 4.20. Explicit time integration was employed for this study, since the default convergence tolerance criteria on the implicit scheme were tight, thus not allowing convergence at the onset of buckling instability. A mass scaling factor of 10,000 was applied on the paper and phenolic resin densities to artificially increase the critical time step. This threshold value was chosen to reduce the kinetic energy less than 5% of the system strain energy. Mass proportional

damping was also applied to avoid any oscillatory behavior of the walls after local collapse.

The global effective stress vs. effective out-of-plane strain curve in plotted in Figure 4.21. As a comparison, two different flatwise compression tests on honeycomb cells with only one fully enclosed cell are also shown. It must be pointed out that the X-ray CT scan data used for the imported geometric model corresponded to core sample that was not ultimately compressed. The collapse at lower effective strain levels was attributed to the shape irregularities of the triangular fillets along the through thickness direction as illustrated in Figure 4.22. The primary reason for this irregular shape is the existence of ring artefacts that does not allow a more uniform discretization of the fillets along the core thickness direction. Discrepancies between the experiments and the computational results are due to the aforementioned ring artefacts and the characterization of the material properties under compression.

Figure 4.23 and Figure 4.24 demonstrate the deformed shape of the different stages of core crushing. In Figure 4.23, the behavior of the honeycomb sample is axially dominated as the displacement magnitude is decreasing linearly from the moving surface all the way up to the fixed base. Within this region, the analytical effective out-of-plane modulus matches the experimental one. In Figure 4.24, highly localized displacement contours on the analysis develop around the middle fillets that are not supported by double walls. At the same time, buckling induced deformation may be observed in the actual compression test but it is has not propagated as much compared to the simulation results.

The initial load drop in the simulation results of Figure 4.21 was further investigated in Figure 4.25 by taking snapshots of the deformed shape at two consecutive time steps. The fillet column locally fractured around the mid-height leading to a slight softening branch. A selection

of higher ultimate failure displacement threshold would not have drastically changed the results, as the load drop is mostly attributed to local instability due to excessive post-buckling behavior.

Since the modeled fillets exhibited significant areal variations, a linear interpolation between the top and bottom scanned CT slice was performed to reduce those effects. In Figure 4.26, the resulting curve is plotted on top of the experimental results and the simulation including the nonlinearly interpolated geometry. As expected, the effective out-of-plane strain at which local collapse first occurred, increased by 30% compared to the baseline analysis results, illustrating in this manner the need for the X-ray CT-scan ring noise removal.

To quantify the effect of the fillets on the collapse limit, models without the fillets were also simulated. In Figure 4.27, a comparison between the out-of-plane core response with and without the fillets is shown. The major contribution of fillets in the overall response is reflected on the 50% reduction of the collapse effective stress, when fillets are not explicitly accounted for. As a result, fillets play major role on the out-of-plane performance by providing additional stiffness and reducing the effective width of cell wall plates.
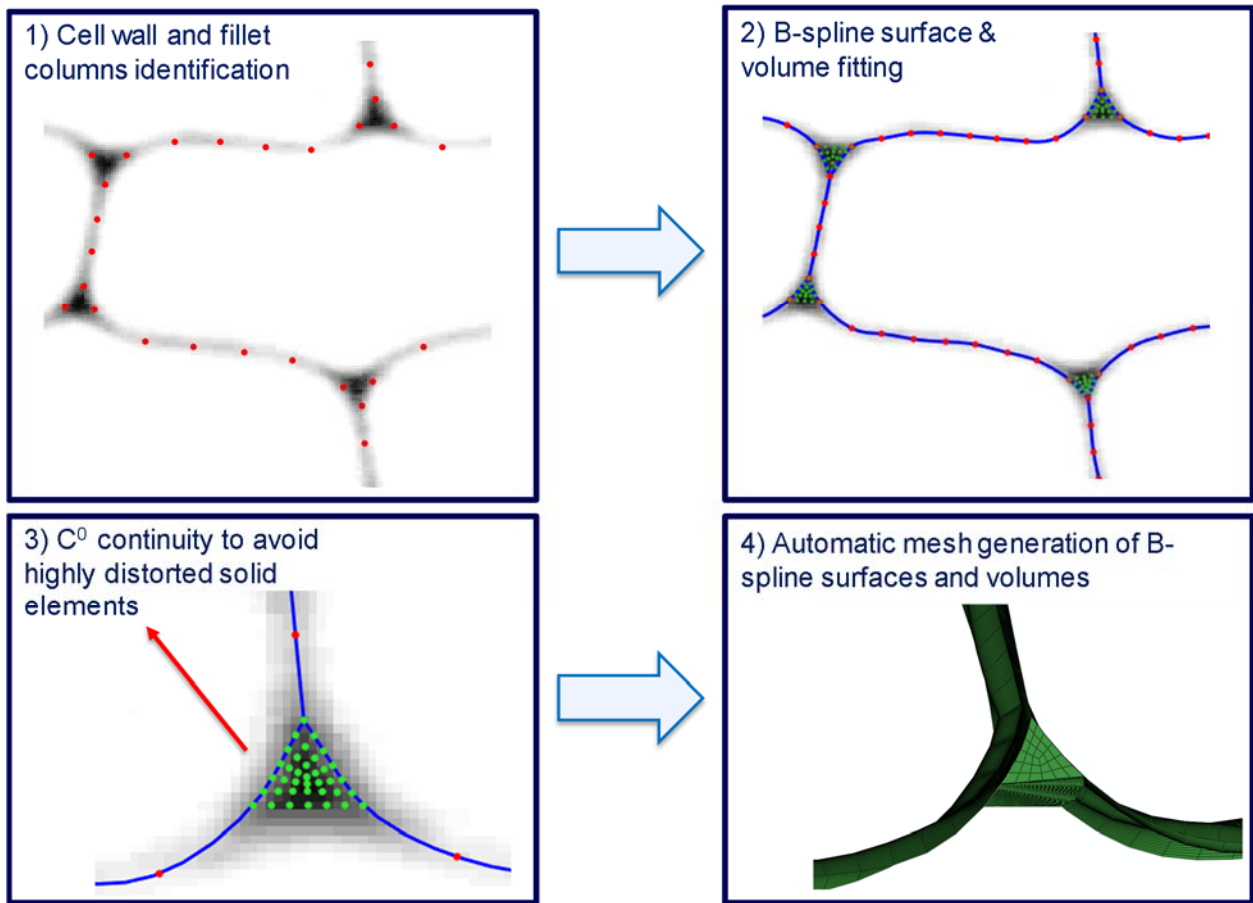
Figure 4.1. Schematic flow of reconstruction scheme extended to finite element model generation
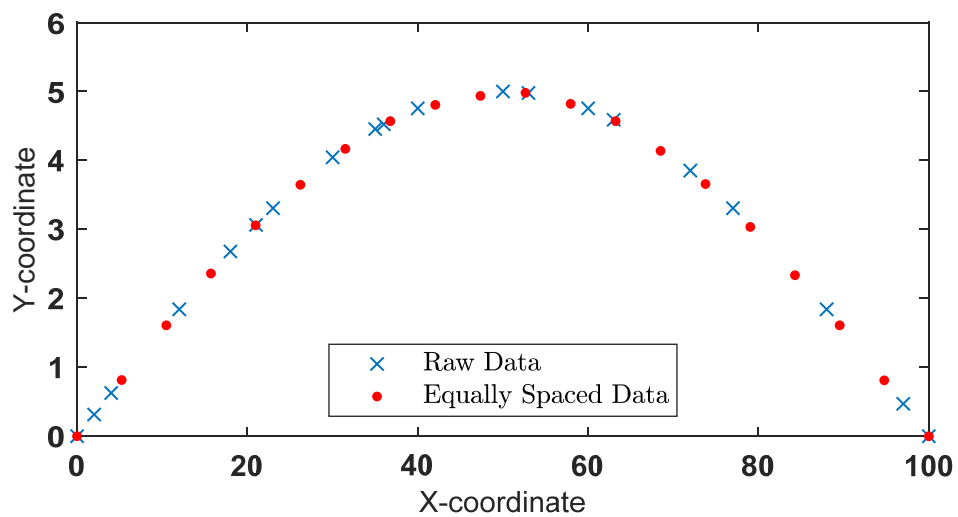
Figure 4.2. Representation of sinusoidal half-wave with unequally and equally spaced data points
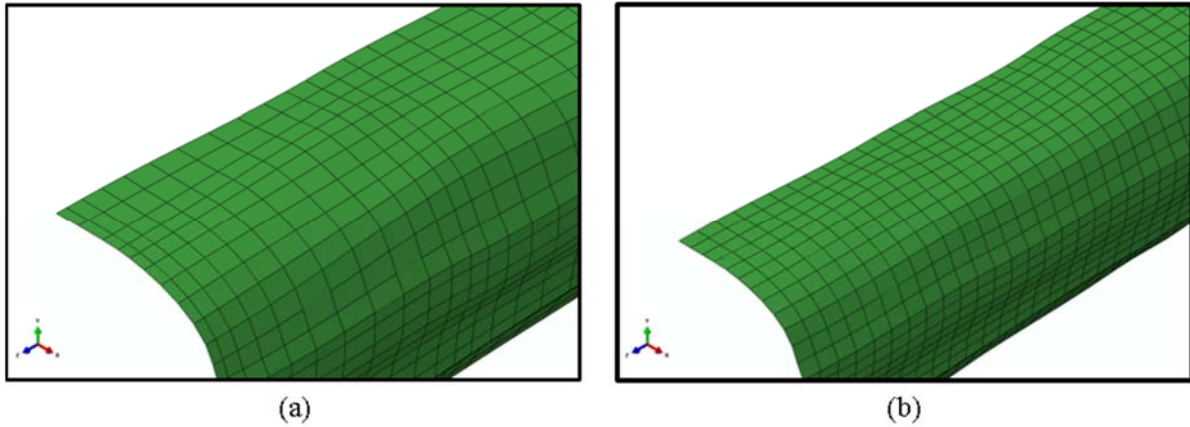
Figure 4.3. Finite element mesh, (a) Before application of equal spacing between nodes; (b) After application of equal spacing between nodes
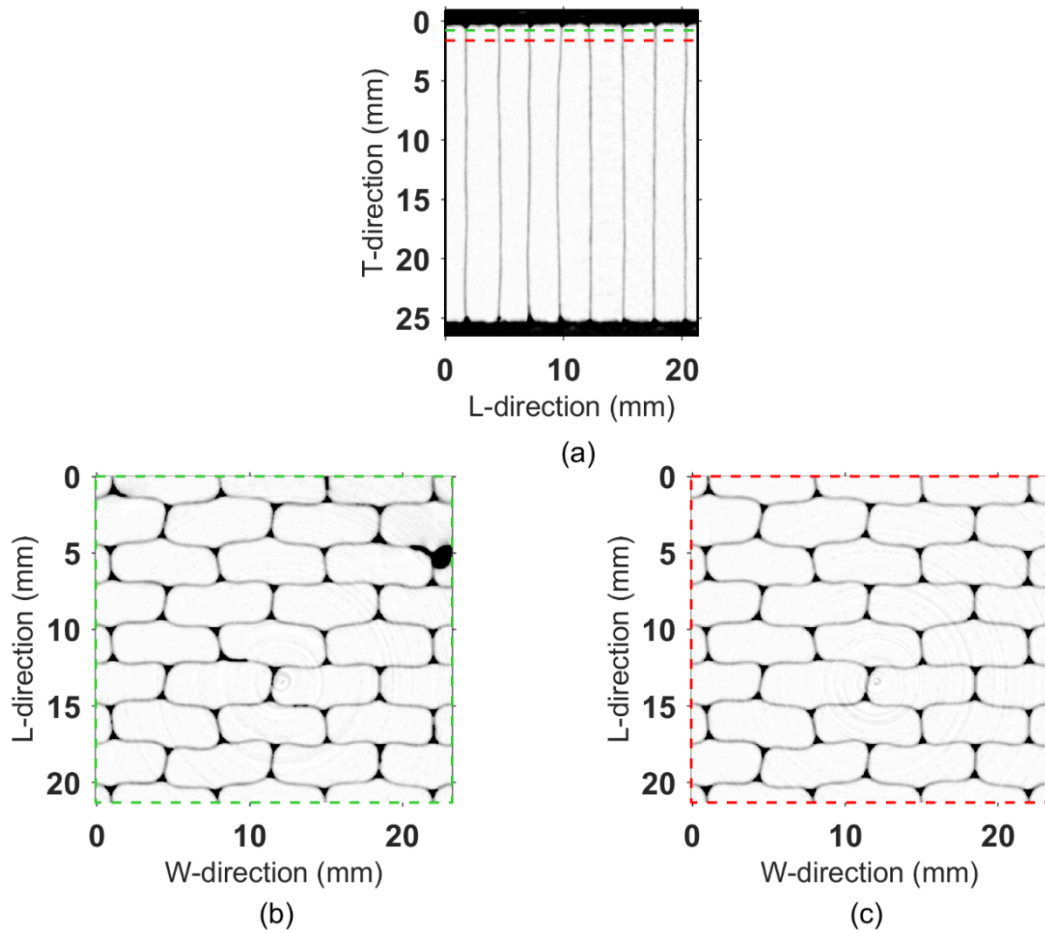
Figure 4.4. Overflow of adhesive film inside the honeycomb core: (a) Ribbon-direction cross-section; (b) Dripped adhesive film; (c) CT scan slice free of adhesive film

159
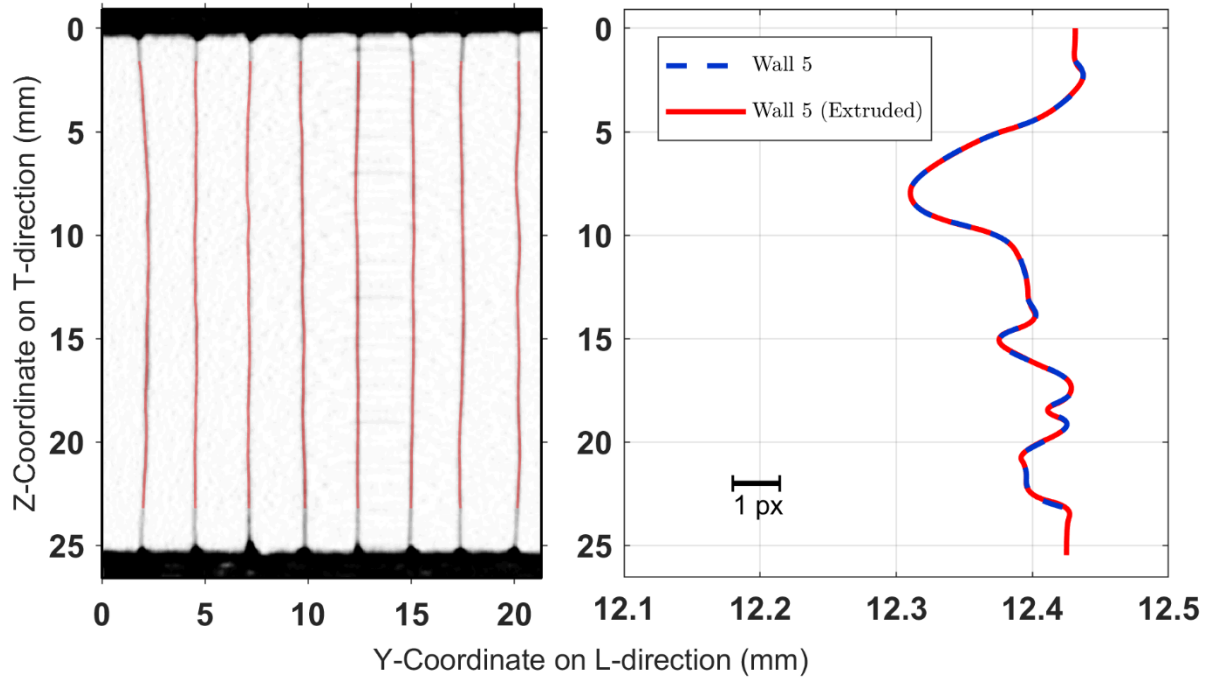
Figure 4.5. Extrusion of top and bottom CT scan slices for modeling the entire core thickness
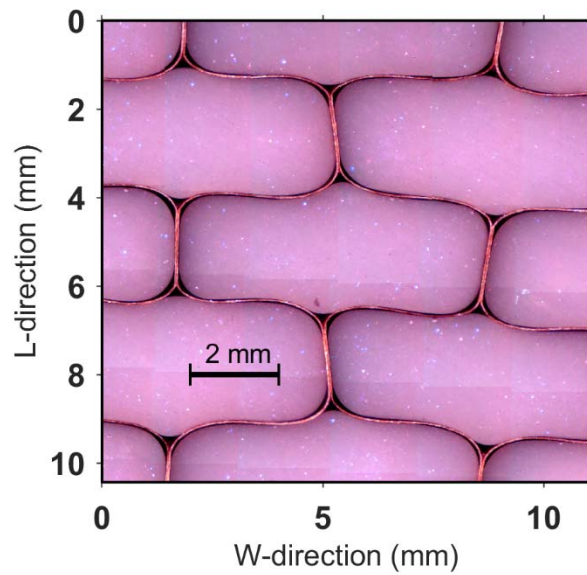
Figure 4.6. Microscopy view of over-expanded Nomex® core
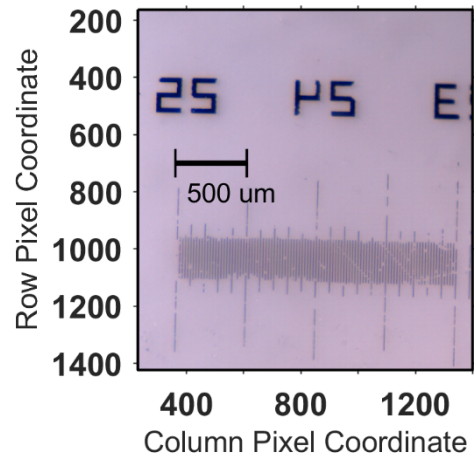
Figure 4.7. Measuring scale for conversion of pixelated data into physical dimensions
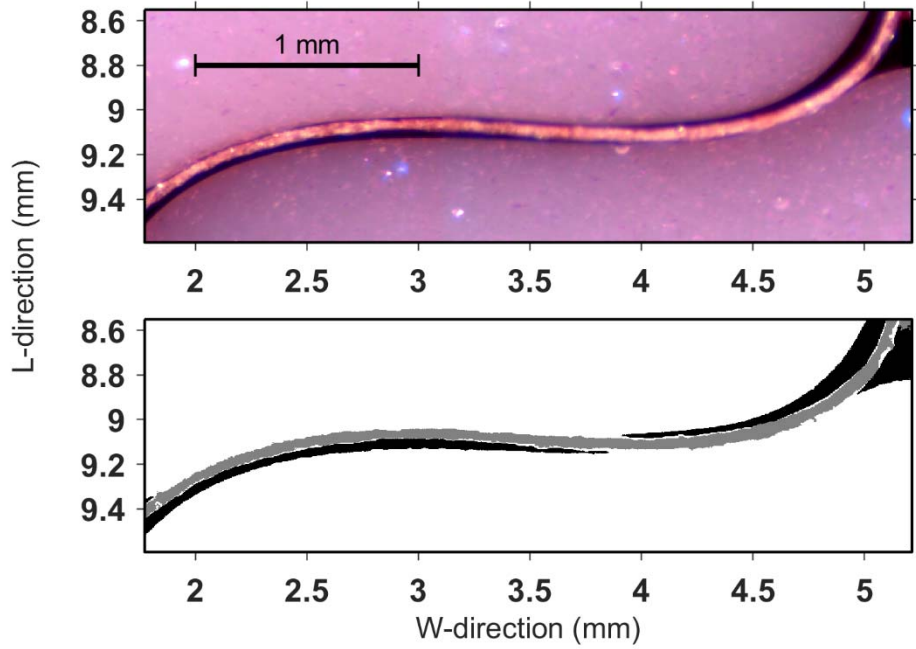
Figure 4.8. Application of K-means clustering algorithm for 3-object segmentation
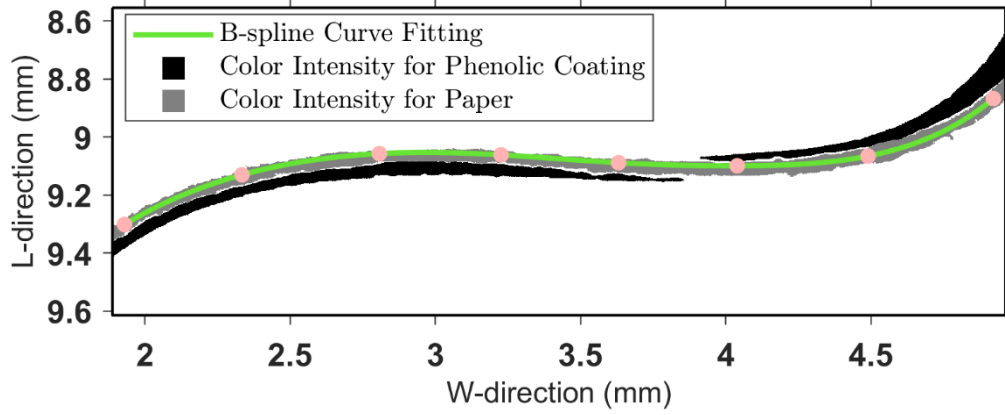
Figure 4.9. B-spline curve fitting for calculation of single wall segment length
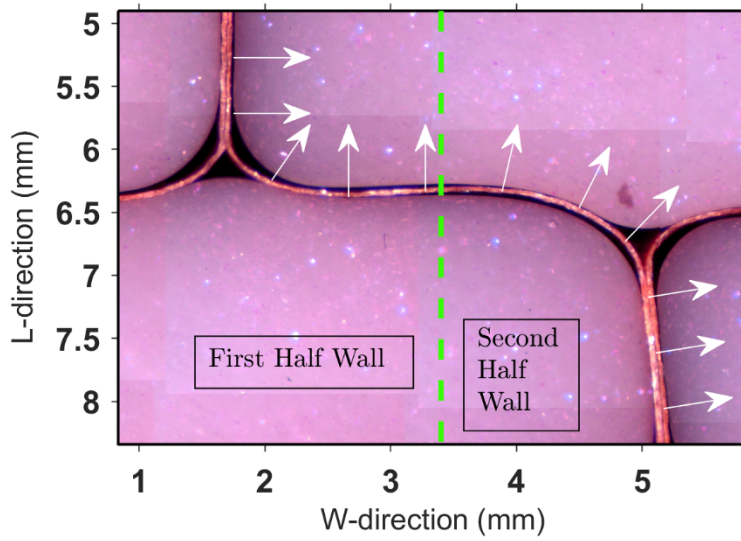
Figure 4.10. Variation of normal direction for specific material ribbon
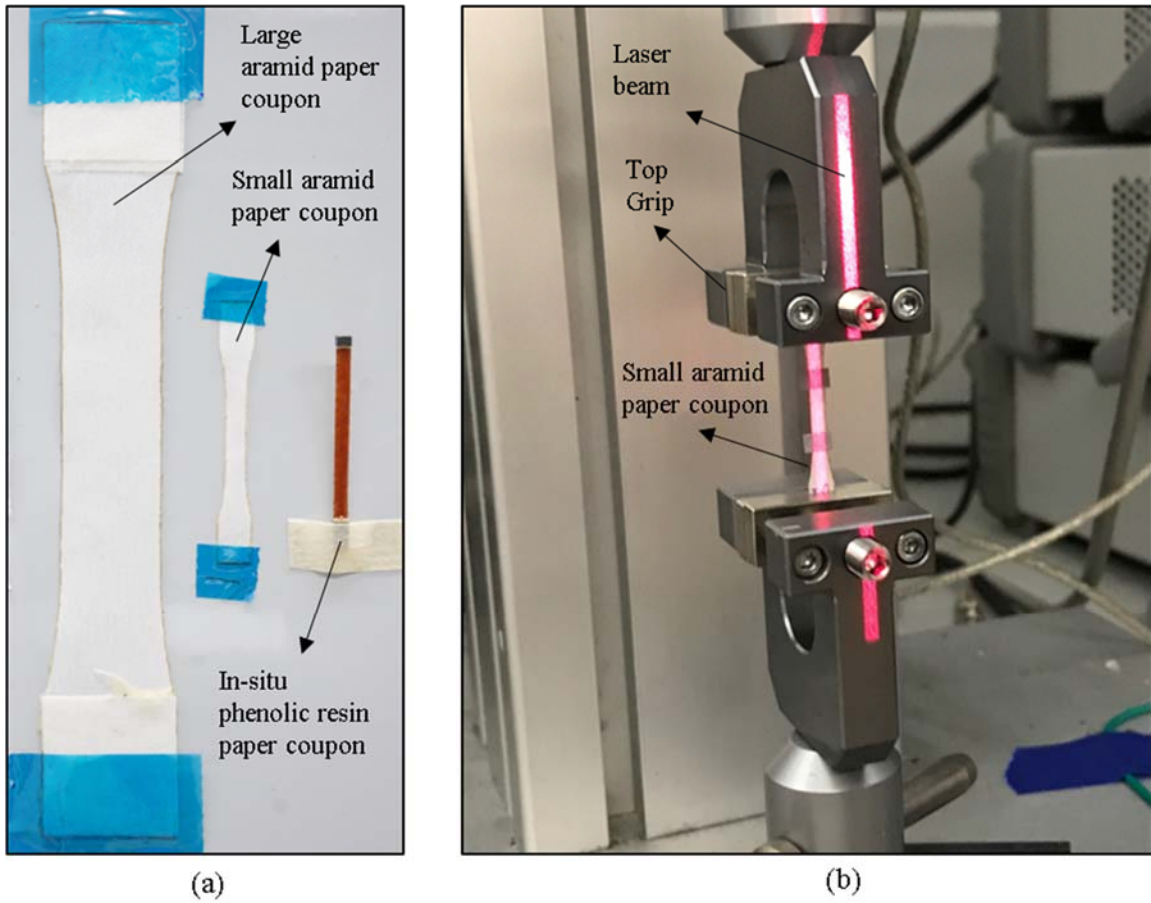
Figure 4.11. (a) Different tensile coupon configurations; (b) Test apparatus for small size aramid paper coupons
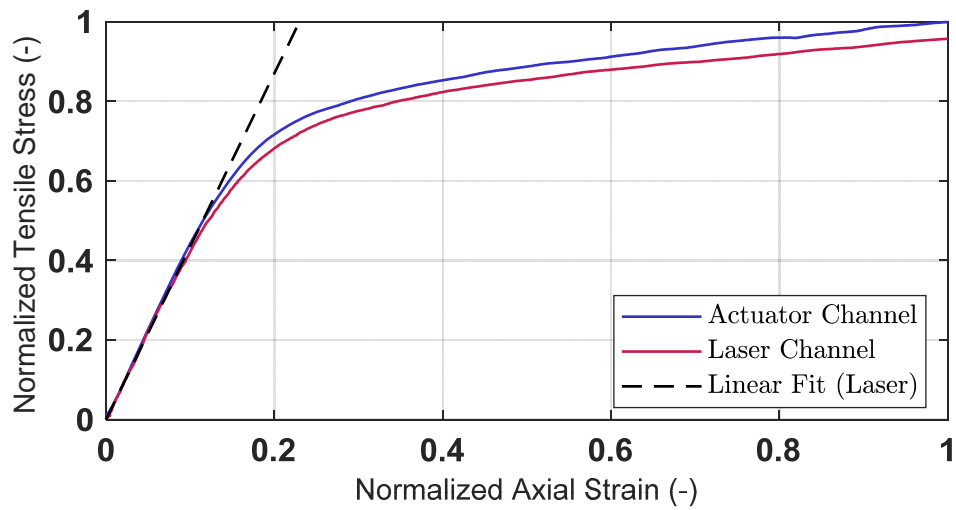
Figure 4.12. Normalized stress vs. strain for large size aramid paper coupon along 0° orientation
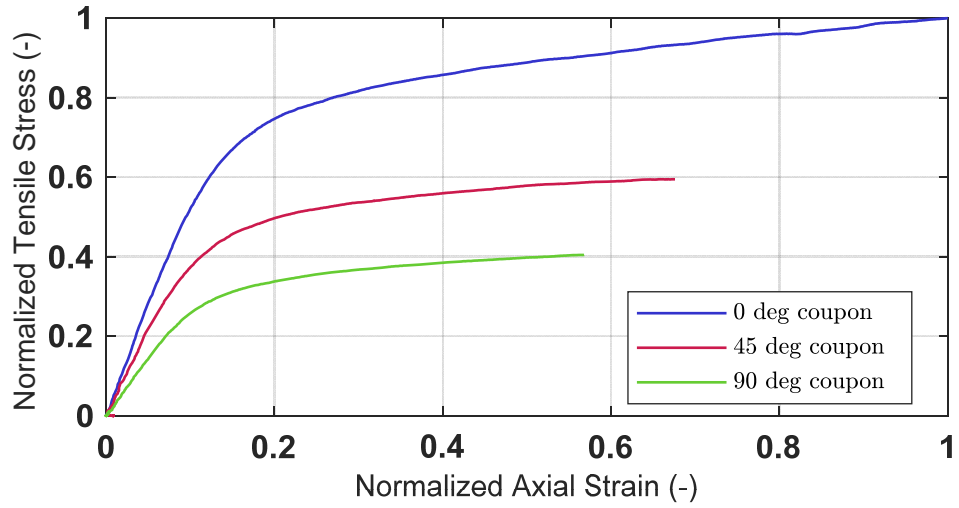
Figure 4.13. Normalized stress vs. strain for large size aramid paper coupon oriented at three different angles
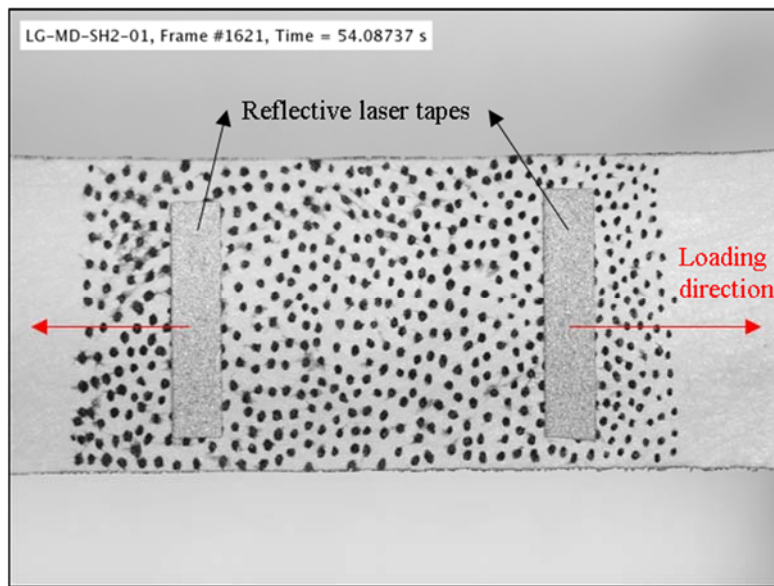
Figure 4.14. Speckle pattern of 0° orientation tensile coupon for calculation of Poisson's ratio v_{12} based on digital image correlation
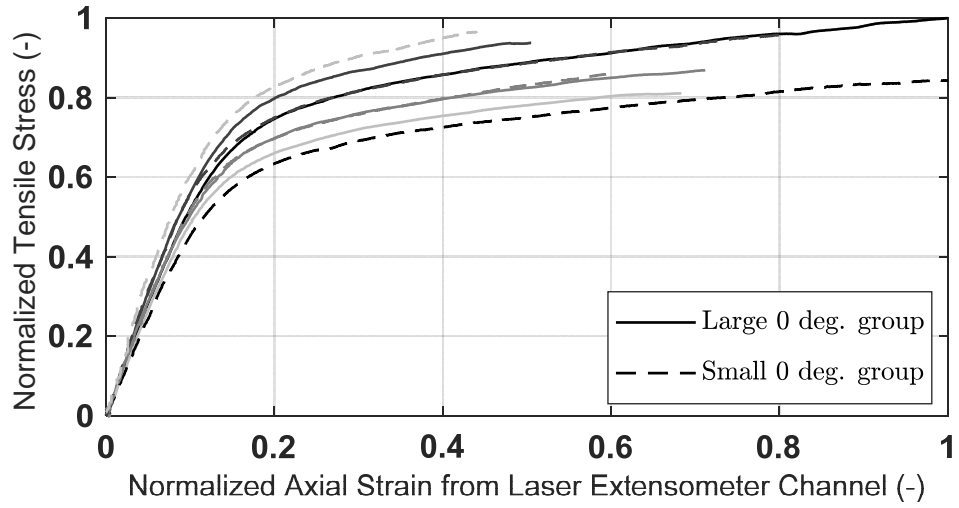
Figure 4.15. Normalized stress vs. strain for large and small size aramid paper coupons along 0°

orientation
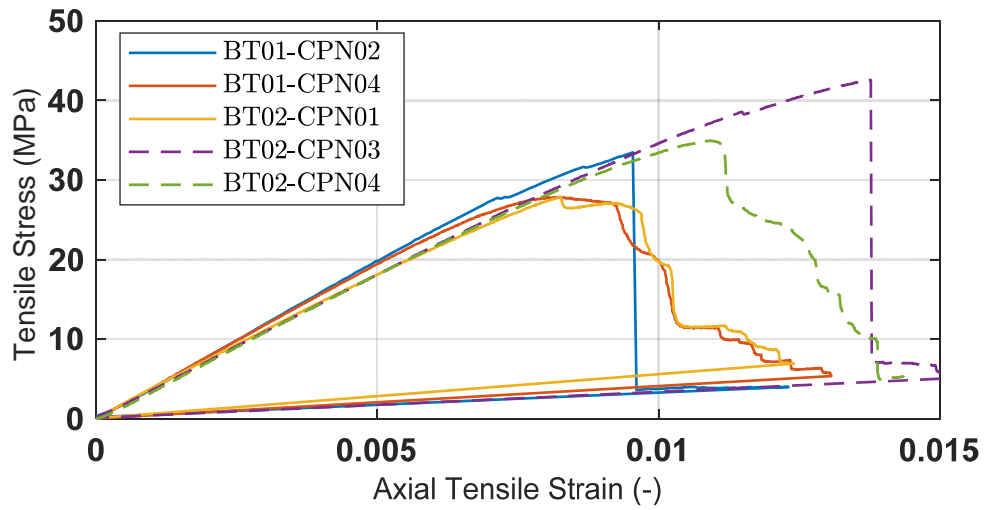
Figure 4.16. Effective stress vs. strain curves for in-situ phenolic resin impregnated tensile coupons
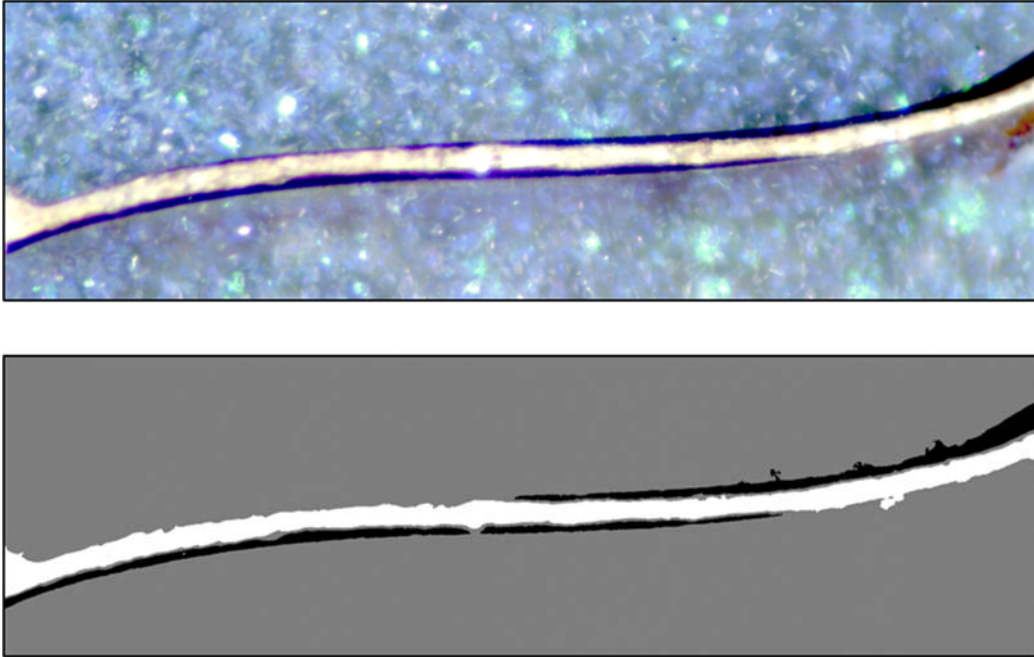
Figure 4.17. Segmentation of in-situ phenolic resin impregnated tensile coupons for calculation of constituent volume fractions and total cross-sectional area
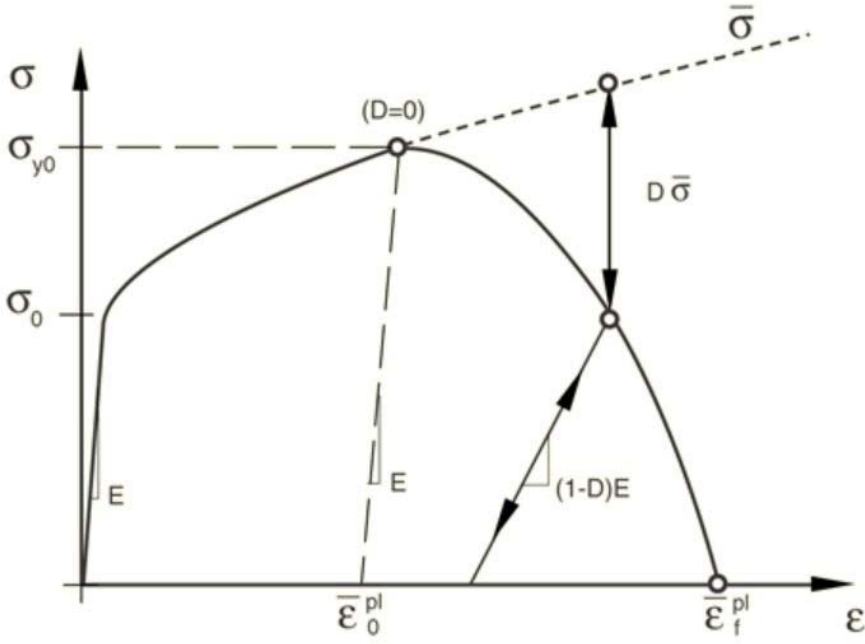
Figure 4.18. Schematic diagram of damage initiation and evolution in metal plasticity [Abaqus Theory Guide, 2014]
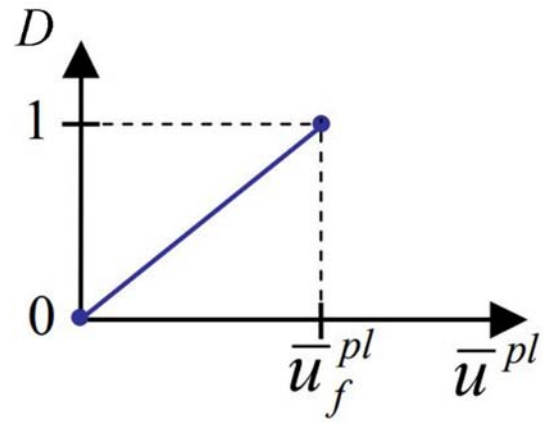
Figure 4.19. Linear damage evolution expressed in equivalent plastic displacement terms
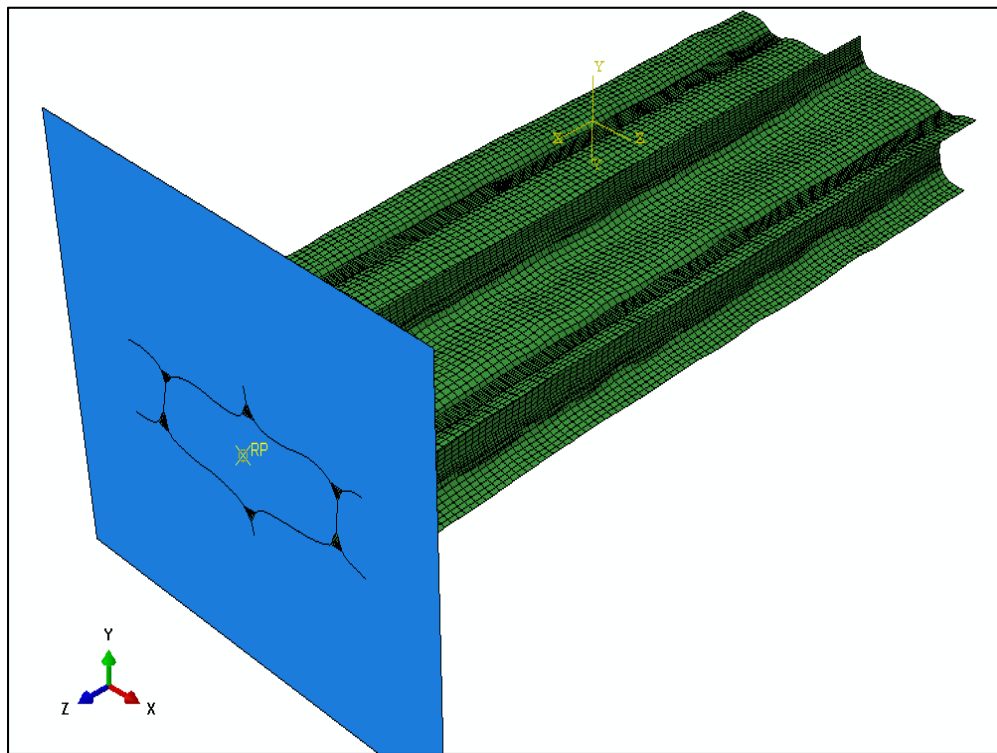
Figure 4.20. Finite element mesh in Abaqus interface
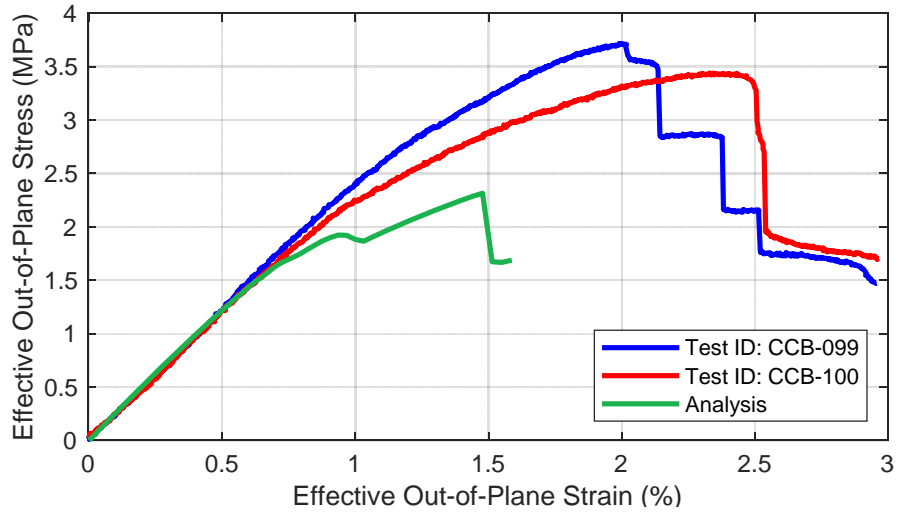
Figure 4.21. Comparison between test data and computational analysis output
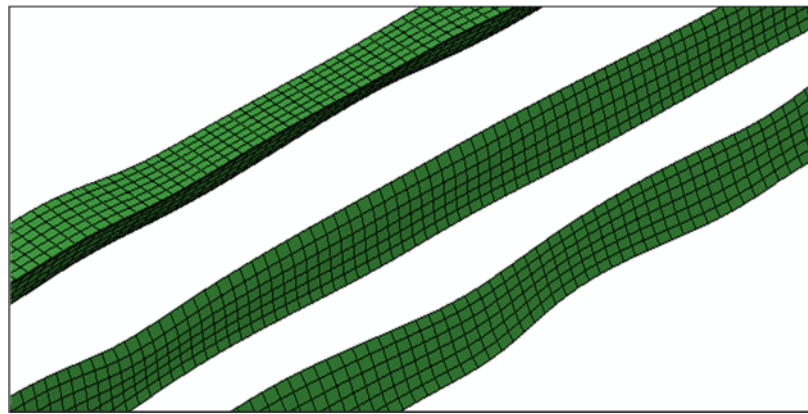
Figure 4.22. Through-thickness phenolic resin column irregularities as a result of X-ray CT-scan

ring artefacts
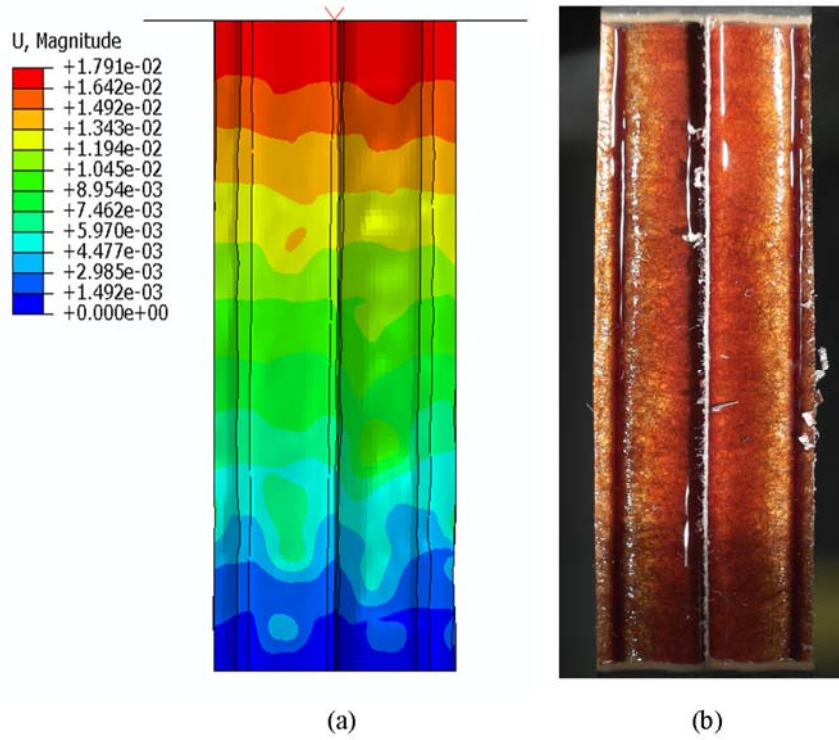
Figure 4.23. Deformed shape at 0.5% effective out-of-plain strain: (a) Analysis; (b) Experiment
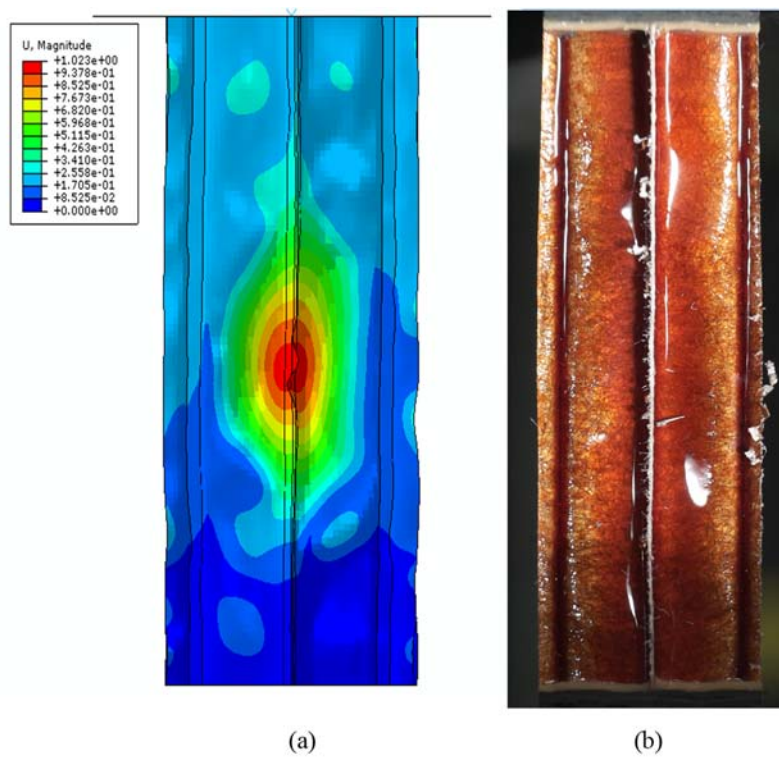
Figure 4.24. Deformed shape at 1.0% effective out-of-plain strain: (a) Analysis; (b) Experiment

169
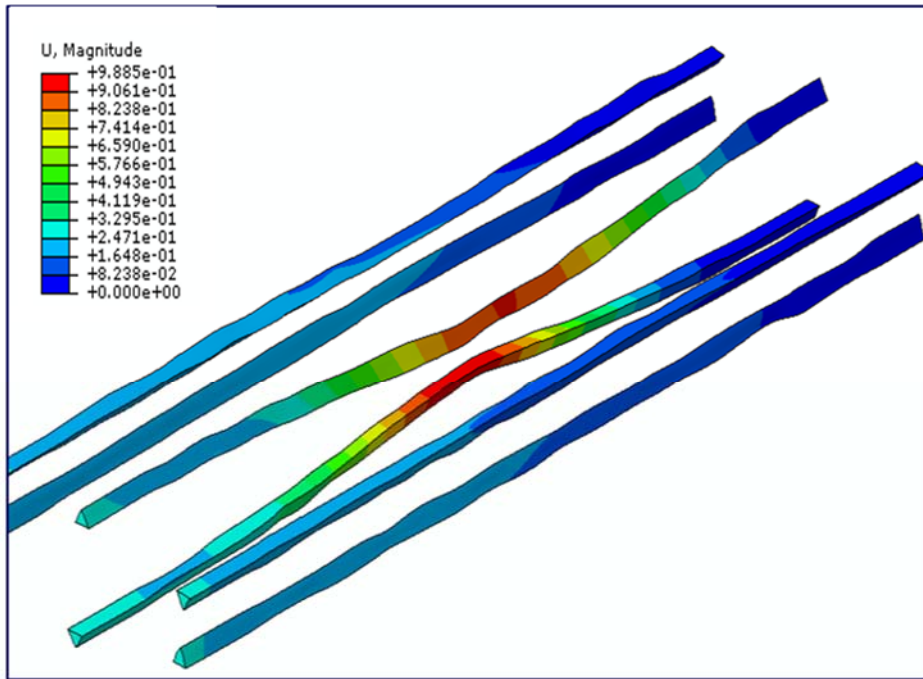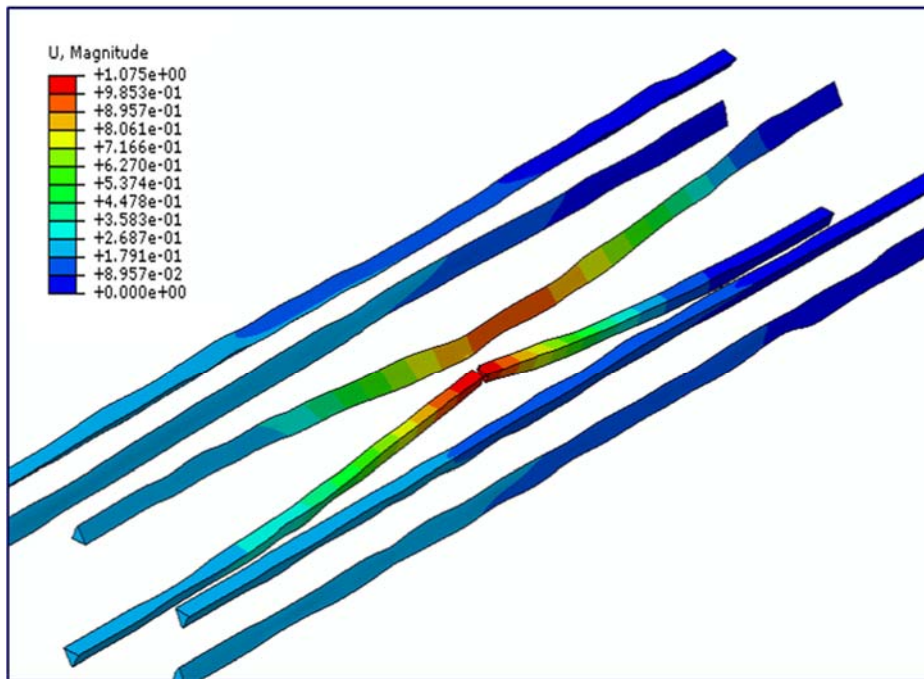
Figure 4.25. Fillet damage progression: (a) Buckling of intermediate fillets; (b) Onset of response softening as a result of brittle fracture of phenolic resin fillet (element deletion employed beyond maximum scalar damage index)
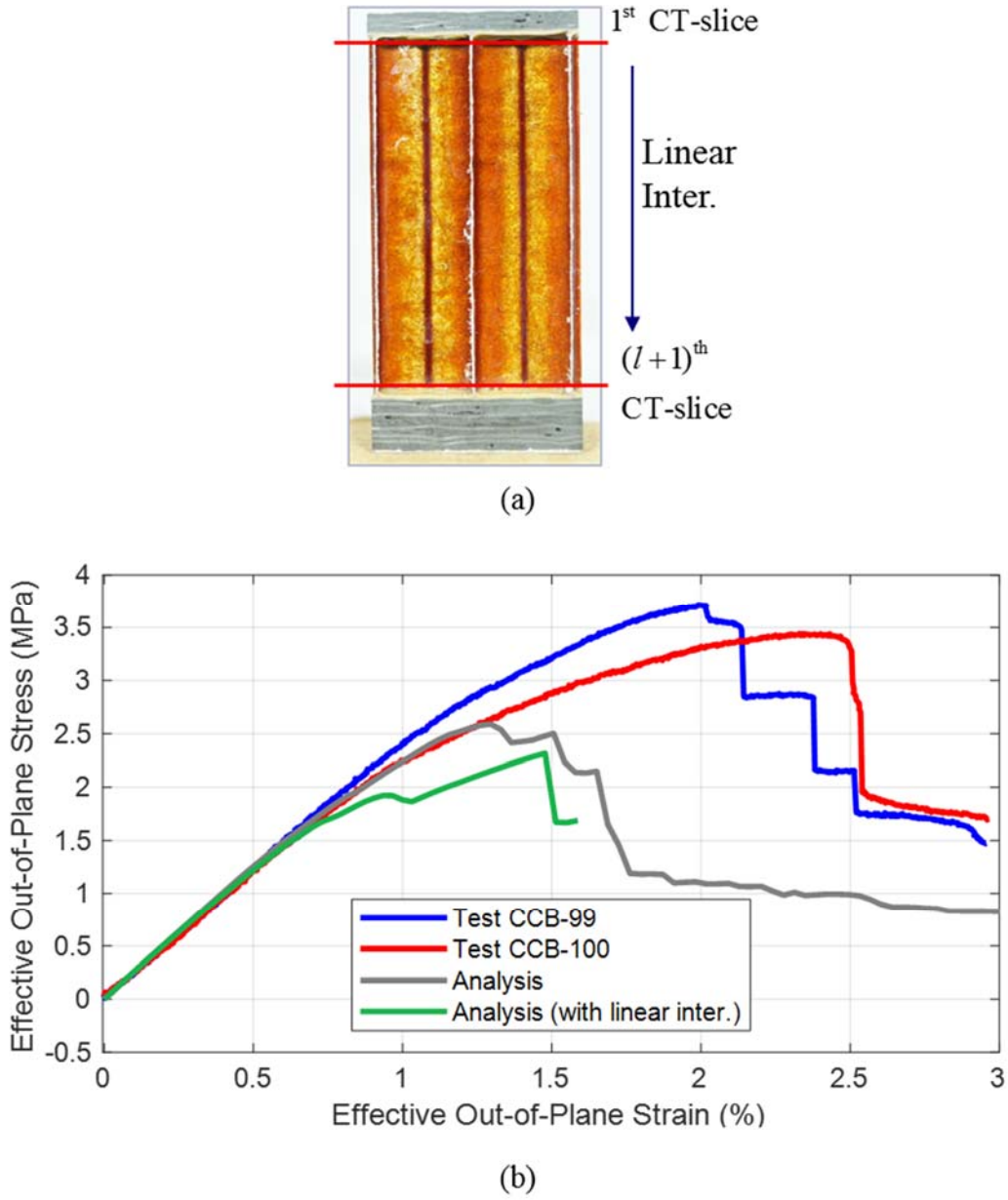
Figure 4.26. (a) Schematic view of linear interpolation between top and bottom through thickness

CT-slice; (b) Analysis results yielding higher collapse effective stress threshold
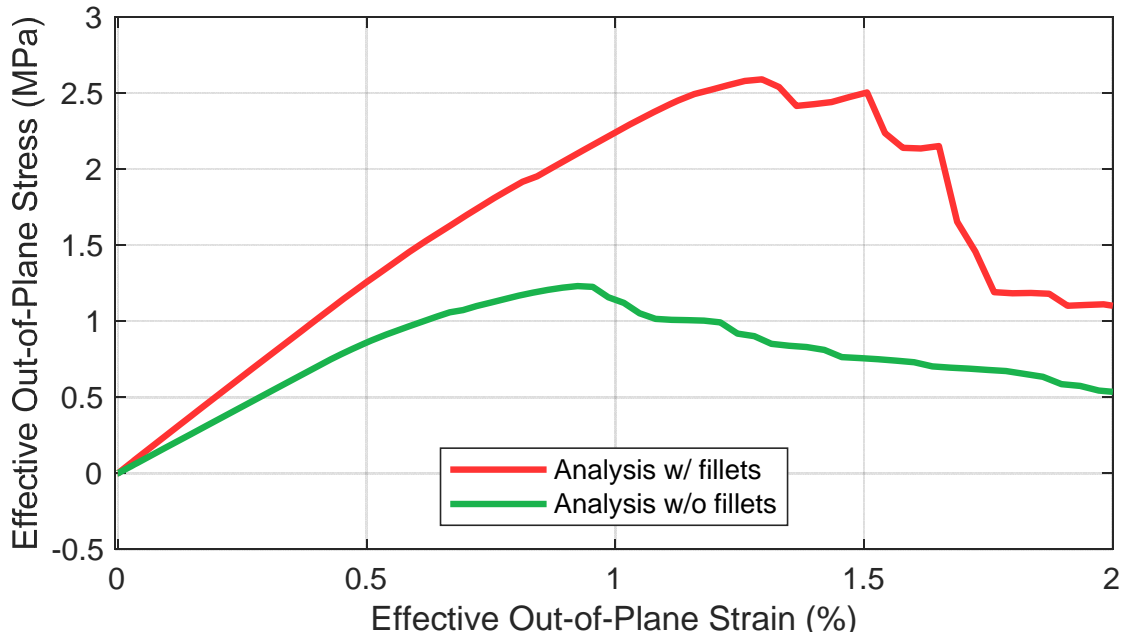
Figure 4.27. Effect of fillets on the out-of-plane buckling response of Nomex® honeycombs

Table 4.1. Thickness values for composite layup of single and double walls

Cell Wall Region	Ply ID	Measured Thickness (μm)
First half of single wall	#1	32
	#2	45
Second half of single wall	#1	45
	#2	32
Double wall	#1	45

Table 4.2. Elastic modulus calculation for phenolic resin

Coupon ID	Calculated Phenolic Resin Modulus (MPa)
BT01-CPN02	5,378
BT01-CPN04	5,177
BT02-CPN01	6,412
BT02-CPN03	4,426
BT02-CPN04	4,178
Average	**5,114**

Table 4.3. List of phenolic resin material properties

Material Property	Value
Young's Modulus, $E_{res.}$	5,100 MPa
Initial yield stress, σ_0	150 MPa
Yield stress at damage onset, σ_{y0}	152 MPa
Poisson' ratio, v	0.3
Density, ρ	1,300 kg/m^3

CHAPTER 5: CONCLUSIONS

A series of simulated hail ice gas gun impact tests was conducted to characterize honeycomb core damage extent on prefabricated Nomex® paper honeycomb core flat sandwich panels with carbon fiber prepreg skin configuration. Sandwich panel design was geared towards fuselage application, which is not a common industry practice yet, since sandwich construction is currently employed for control surfaces, nacelle doors, radomes and other applications. A 10° angle of attack was chosen to realistically simulate relative trajectories between a falling hail projectile and an operating aircraft. Terminal velocities were equal to 95 and 135 m/s, representative of smaller size aircraft descent. Tested sandwich panels exhibited minor residual dents, which could not be visually detected. Destructive sectioning of the panel revealed significant core crushing in terms of cell wall collapse that spanned up to 80 mm along the projectile direction. Delamination on the impacted skin was also observed for the most severe impact, but there was no correlation study upon its size compared to the core crushing extent.

Given the complexity of sandwich panels, the dynamic strain rate effects due to high-velocity impact, and the lack of proper in-situ measurements, core crushing phenomena were investigated at a smaller scale in a controllable manner. A proposed framework in the form of coupon level experiments, imaging techniques, and finite element modeling was established to better characterize the out-of-plane compressive behavior of phenolic resin impregnated Nomex® paper honeycomb cores used in sandwich composites. This type of honeycomb core is preferred to aluminum core design because of its lower density, comparable mechanical response, and formability into curved shapes. Through optical microscopy, Nomex® paper honeycomb walls consist of paper wall coated by a slightly thinner layer of phenolic resin. Furthermore, resin

accumulations also known as fillets, in the corners of adjacent ribbons also were observed, giving rise to skin supported by stringers analogy. Flatwise compression tests on 25.4 mm thick Nomex® paper cores revealed that partial collapse was attributed to local fillet detachment from the single walls immediately followed by rapid kinking at the unsupported region. This fracture propagated to the double stiffened walls, while single cell wall fracture could occur either before or after fillet kinking. From this phenomenological study, it was deduced that fillet fracture was a clear indication for cell wall crushing.

X-ray computed tomography was additionally utilized to visually assess 3D damage state on coupons subjected to flatwise tests. X-ray imaging validated that local fillet detachment in the form of small cavities is the prevailing failure mode. Single walls and especially outer walls also exhibited local kinking. Since X-ray computed tomography is one of the most accurate high-resolution non-destructive imaging techniques, an image-based reconstruction scheme was developed to numerically model the actual geometry of the scanned cellular structure including the fillets. The proposed automated scheme features basic image processing techniques to seed the pixelated cell wall structure into discrete nodes that are representative of the cell wall shape. A B-spline surface and volume interpolation was then programmed to connect those discrete nodes in a continuous form. The end product is similar to a Computer Aided Design entity in which inherent imperfections in terms of cell wall waviness, shape irregularities and fillet area have been explicitly quantified. The reconstruction scheme was fully programmed in MATLAB and its application is tailored to the given X-ray CT data. In the reconstruction scheme, roughly 20-25 CT scan slices along the core thickness direction were discretized, leading to a significant post-processing computational cost reduction.

The B-spline reconstructed geometric model was used to obtain metrics of pristine

imperfections. As expected, single cell walls exhibited larger waviness than the double walls which were straight within the CT scan resolution. The area of the fillets throughout core thickness exhibited larger variation compared to cell wall waviness, a fact that is attributed to the image quality of the X-ray CT scans and the image post-processing parameters. In-situ X-ray CT scanning on progressively compressed coupon allowed direct observations of the buckling propagation and fracture onset. Outer single walls single cell wall buckling was triggered on an early stage. Post peak CT scan revealed double wall buckling and fillet detachment.

The contribution of the phenolic resin fillets was validated through finite element modeling. The image-based reconstruction scheme was extended to create a finite element mesh that reflects the inherent imperfections. For base material mechanical characterization, uniaxial tensile tests on aramid paper and in-situ phenolic resin impregnated paper coupons were performed. From this test matrix, properties such elastic moduli, Poisson's ratio as well as tensile strengths were determined. Due to limited size of the in-situ tensile coupons, the tensile strength of the phenolic resin was underestimated, based on the results of early stage computational models. A parametric study on the effect of the phenolic resin fillets revealed that the collapse effective stress can be reduced by as much as 40% when the fillet columns were not included in the model. This major conclusion illustrates the significance of the fillets on the overall response and also suggests that explicit modeling of the cellular geometry should include these stiffened regions.

The major finding from this research study lies on the contribution of the phenolic resin accumulations of impregnated Nomex® medium-weight cores on the stability of the honeycomb system. This trend was observed via testing, imaging and numerical modeling. Even though honeycomb core manufacturers do not report metrics of the size of the fillets, research studies on the simulation of explicitly modeled Nomex® core geometries should account for these junctions.

The proposed framework of combining coupon level testing under simple loading conditions, advanced imaging techniques, and finite element modeling allows major honeycomb core manufacturers increase core structural performance, especially against transverse impact loading. X-ray computed tomography is one of the most established imaging techniques, and its application on honeycomb core industry can serve as quality check of the manufacturing process.

In addition, X-ray computed tomography in conjunction with the proposed reconstruction scheme can be further applied on sandwich parts that have been co-cured inside or outside an autoclave to assess cell wall waviness induced by the applied consolidation pressure. For this research study, single walls exhibited minor curing-induced waviness that ultimately did not affect the out-of-plane collapse state, but it must be pointed out that the co-curing process was performed under vacuum conditions only. In this sense, cell wall waviness especially on the double walls may be an issue for either light-weight Nomex® cores that have less amount of phenolic resin coating or autoclave co-curing processes. Lastly, it is the proposed reconstruction scheme applied on either X-ray CT data or optical microscopy images that allows direct representation of in-situ geometric features of honeycomb cores that are otherwise assumed in numerical modeling. However, ring artefacts should be calibrated and eliminated from the stack of images in order to increase the accuracy of the numerical modeling results. Finally, the reconstruction scheme applied to X-ray CT data can be utilized to quantitively assess local defects. When also used in conjunction with in-situ testing protocols, the image-based reconstruction scheme applied on different stages of deformation will allow more accurate calibration of numerical modeling parameters.

Since localized impact response involves bi-axial effective stress state on honeycomb core, the research study presented herein should be extended to transverse shear loading. In the explicit honeycomb core computational modeling, the proposed B-spline image-based geometry

177

reconstruction scheme can be combined with isogeometric analysis that also incorporates non-uniform rational B-spline shape functions to ultimately increase solution accuracy and minimize computational cost relative to traditional finite element modeling.

LIST OF REFERENCES

Abrate, S. (1997). Localized Impact on Sandwich Structures with Laminated Facings. ASME. *Appl. Mech. Rev*. February 1997; 50(2): 69–82.

Aktay, L., Johnson, A. F., & Kröplin, B. H. (2008). Numerical modelling of honeycomb core crush behaviour. *Engineering Fracture Mechanics*, *75*(9), 2616-2630.

Aminanda, Y., Castanié, B., Barrau, J. J., & Thevenet, P. (2005). Experimental analysis and modeling of the crushing of honeycomb cores. *Applied Composite Materials*, *12*(3-4), 213-227.

Anderson, T., & Madenci, E. (2000). Experimental investigation of low-velocity impact characteristics of sandwich composites. *Composite structures*, *50*(3), 239-247.

Appleby-Thomas, G. J., Hazell, P. J., & Dahini, G. (2011). On the response of two commercially-important CFRP structures to multiple ice impacts. *Composite Structures*, *93*(10), 2619-2627.

Asp, L. E., & Juntikka, R. (2009). High velocity impact on NCF reinforced composites. *Composites Science and Technology*, *69*(9), 1478-1482.

Asprone, D., Auricchio, F., Menna, C., Morganti, S., Prota, A., & Reali, A. (2013). Statistical finite element analysis of the buckling behavior of honeycomb structures. *Composite structures*, *105*, 240-255.

ASTM International. (2016). ASTM F320-16: Standard test method for hail impact resistance of aerospace transparent enclosures. West Conshohocken, PA: American Society for Testing and Materials. doi: https://doi.org/10.1520/F0320-16

Bitzer, T. (1997). *Honeycomb technology*. Glasgow: Springer, Dordrecht.

Caldemeyer, K. S., & Buckwalter, K. A. (1999). The basic principles of computed tomography and magnetic resonance imaging. *Journal of the American Academy of Dermatology*, *41*(5), 768-771.

Castanié, B., Bouvet, C., Aminanda, Y., Barrau, J. J., & Thévenet, P. (2008). Modelling of low-energy/low-velocity impact on Nomex honeycomb sandwich structures with metallic skins. *International Journal of Impact Engineering*, *35*(7), 620-634.

Chai, G. B., & Zhu, S. (2011). A review of low-velocity impact on sandwich structures. *Proceedings of the Institution of Mechanical Engineers, Part L: Journal of*

Materials: Design and Applications, *225*(4), 207-230.

Chan, M. K. (2014). *Low Velocity Blunt Impact on Lightweight Composite Sandwich Panels* (Master's thesis, University of California, San Diego). Retrieved from https://escholarship.org/uc/item/00p8828q

Composite Materials Handbook-17 (CMH-17). (2013). *Composite Materials Handbook, Volume 6 - Structural Sandwich Composites (CMH-17).* SAE International on behalf of CMH-17, a division of Wichita State University.

Crupi, V., Epasto, G., & Guglielmino, E. (2011). Computed Tomography analysis of damage in composites subjected to impact loading. *Frattura ed Integrità Strutturale*, *5*(17), 32-41.

Crupi, V., Epasto, G., & Guglielmino, E. (2013). Comparison of aluminium sandwiches for lightweight ship structures: honeycomb vs. foam. *Marine structures*, *30*, 74-96.

Crupi, V., Epasto, G., & Guglielmino, E. (2016). Internal damage investigation of composites subjected to low-velocity impact. *Experimental Techniques*, *40*(2), 555-568.

Crupi, V., Epasto, G., Guglielmino, E., Mozafari, H., & Najafian, S. (2014). Computed tomography-based reconstruction and finite element modelling of honeycomb sandwiches under low-velocity impacts. *Journal of Sandwich Structures & Materials*, *16*(4), 377-397.

Czabaj, M. (2010). *Damage and damage tolerance of high temperature composites and sandwich composite structures* (Doctoral dissertation, Cornell University). Retrieved from https://ecommons.cornell.edu/handle/1813/17694

Czabaj, M. W., Riccio, M. L., & Whitacre, W. W. (2014). Numerical reconstruction of graphite/epoxy composite microstructure based on sub-micron resolution X-ray computed tomography. *Composites Science and Technology*, *105*, 174-182.

Daggett, S. S., & Fuller, J. J. (2016). Thermal and thickness effects in para-aramid core. *Proceedings of American Society for Composites: Thirty-First Technical Conference. Williamsburg, Virginia. DEStech Publications, Inc., CD-ROM-10pp.*

Das, M., Oterkus, E., Madenci, E., & Razi, H. (2009). Residual strength of sandwich panels with hail damage. *Composite Structures*, *88*(3), 403-412.

Dear, J. P., Lee, H., & Brown, S. A. (2005). Impact damage processes in composite sheet and sandwich honeycomb materials. *International Journal of Impact Engineering*, *32*(1-4), 130-154.

Dietrich, S., Weidenmann, K., & Elsner, P. (2014). 3D tomographic characterization of sandwich structures. *NDT & E International*, *62*, 77-84.

Emerson, M. J., Jespersen, K. M., Dahl, A. B., Conradsen, K., & Mikkelsen, L. P. (2017). Individual fibre segmentation from 3D X-ray computed tomography for characterising the fibre orientation in unidirectional composite materials. *Composites Part A: Applied Science and Manufacturing*, *97*, 83-92.

Fawcett, A. J., & Oakes, G. D. (2006, July). *Boeing composite airframe damage tolerance and service experience*. Presented at Composite Maintenance Workshop, Chicago, IL.

Fischer, S., Drechsler, K., Kilchert, S., & Johnson, A. (2009). Mechanical tests for foldcore base material properties. *Composites Part A: Applied Science and Manufacturing*, *40*(12), 1941-1952.

Foo, C. C. (2013). *Energy absorption characteristics of sandwich structures subjected to low-velocity impact* (Doctoral dissertation, Nanyang Technological University). Retrieved from https://repository.ntu.edu.sg/handle/10356/15558

Foo, C. C., Chai, G. B., & Seah, L. K. (2007). Mechanical properties of Nomex material and Nomex honeycomb structure. *Composite structures*, *80*(4), 588-594.

Foo, C. C., Seah, L. K., & Chai, G. B. (2008). Low-velocity impact failure of aluminium honeycomb sandwich panels. *Composite Structures*, *85*(1), 20-28.

Giglio, M., Manes, A., & Gilioli, A. (2012). Investigations on sandwich core properties through an experimental–numerical approach. *Composites Part B: Engineering*, *43*(2), 361-374.

Girolamo, D., Chang, H. Y., & Yuan, F. G. (2018). Impact damage visualization in a honeycomb composite panel through laser inspection using zero-lag cross-correlation imaging condition. *Ultrasonics*, *87*, 152-165.

Han, T. S., Ural, A., Chen, C. S., Zehnder, A. T., Ingraffea, A. R., & Billington, S. L. (2002). Delamination buckling and propagation analysis of honeycomb panels using a cohesive element approach. *International Journal of Fracture*, *115*(2), 101-123.

Hazizan, M. A., & Cantwell, W. J. (2003). The low velocity impact response of an aluminium honeycomb sandwich structure. *Composites Part B: Engineering*, *34*(8), 679-687.

Heimbs, S. (2009). Virtual testing of sandwich core structures using dynamic finite element simulations. *Computational Materials Science*, *45*(2), 205-216.

Heimbs, S., Middendorf, P., & Maier, M. (2006). Honeycomb Sandwich Material Modeling for

Dynamic Simulations of Aircraft Interior Components. *Proceedings of the 9th International LS-DYNA Conference, Detroit, USA*

Heimbs, S., Schmeer, S., Middendorf, P., & Maier, M. (2007). Strain rate effects in phenolic composites and phenolic-impregnated honeycomb structures. *Composites Science and Technology*, *67*(13), 2827-2837.

Herrmann, A. S., Zahlen, P. C., & Zuardy, I. (2005). Sandwich structures technology in commercial aviation. *In Sandwich structures 7: Advancing with sandwich structures and materials* (pp. 13-26). Springer, Dordrecht.

Herup, E. J., & Palazotto, A. N. (1998). Low-velocity impact damage initiation in graphite/epoxy/nomex honeycomb-sandwich plates. *Composites Science and Technology*, *57*(12), 1581-1598.

Hughes, T. J., Cottrell, J. A., & Bazilevs, Y. (2005). Isogeometric analysis: CAD, finite elements, NURBS, exact geometry and mesh refinement. *Computer methods in applied mechanics and engineering*, *194*(39-41), 4135-4195.

International Air Transportation Association. (2005). Ground damage prevention programme targets 10% cost reduction. *Industry Times*.

Iváñez, I., Moure, M. M., Garcia-Castillo, S. K., & Sanchez-Saez, S. (2015). The oblique impact response of composite sandwich plates. *Composite structures*, *133*, 1127-1136.

Kim, H., Welch, D. A., & Kedward, K. T. (2003). Experimental investigation of high velocity ice impacts on woven carbon/epoxy composite panels. *Composites Part A: applied science and manufacturing*, *34*(1), 25-41.

Lagace, P. A., Williamson, J. E., Wilson Tsang, P. H., Wolf, E., & Thomas, S. (1993). A preliminary proposition for a test method to measure (impact) damage resistance. *Journal of reinforced Plastics and Composites*, *12*(5), 584-601.

Lapczyk, I., & Hurtado, J. A. (2007). Progressive damage modeling in fiber-reinforced materials. *Composites Part A: Applied Science and Manufacturing*, *38*(11), 2333-2341.

Laxmi Narain Verma Memorial Society Group of Institutes. (2007). Airframe and aircraft components. New Delhi: Laxmi Narain Verma Memorial Society Group of Institutes.

Liu, L., Meng, P., Wang, H., & Guan, Z. (2015). The flatwise compressive properties of Nomex honeycomb core with debonding imperfections in the double cell wall. *Composites Part B: Engineering*, *76*, 122-132.

Liu, L., Wang, H., & Guan, Z. (2015). Experimental and numerical study on the mechanical response of Nomex honeycomb core under transverse loading. *Composite Structures*, *121*, 304-314.

Liu, T., Malcolm, A. A., & Xu, J. (2010). High-resolution X-ray CT inspection of Honeycomb Composites Using Planar Computed Tomography Technology. *2nd International Symposium on NDT in Aerospace*.

Luong, S. D. (2014). *Hail Ice Impact of Lightweight Composite Sandwich Panels* (Master's thesis, University of California, San Diego). Retrieved from https://escholarship.org/uc/item/8s80t06m

Manual, A. U. (2014). Abaqus theory guide. *Version*, *6*, 14.

Meguid, S. A., Mao, R. H., & Ng, T. Y. (2008). FE analysis of geometry effects of an artificial bird striking an aeroengine fan blade. *International Journal of Impact Engineering*, *35*(6), 487-498.

Meo, M., Vignjevic, R., & Marengo, G. (2005). The response of honeycomb sandwich panels under low-velocity impact loading. *International journal of mechanical sciences*, *47*(9), 1301-1325.

Moore, D. G., & Nelson, C. L. (2012). *Damage Assessment of Composite Honeycomb Material Using Advanced Inspection Technologies* (No. SAND2012-5975C). Sandia National Lab.(SNL-NM), Albuquerque, NM (United States).

Neidigk, S. O., Roach, D. P., Duvall, R. L., & Rice, T. M. (2017). *Detection and characterization of hail impact damage in carbon fiber aircraft structures* (Report No. DOT/FAA/TC-16/8). Retrieved from http://www.tc.faa.gov/its/worldpac/techrpt/tc16-8.pdf

Niu, M. C. Y. (1997). *Airframe stress analysis and sizing*. Granada Hills: Adaso/Adastra Engineering Center.

Olsson, R., Juntikka, R., & Asp, L. E. (2013). High velocity hail impact on composite laminates–modelling and testing. In *Dynamic Failure of Composite and Sandwich Structures* (pp. 393-426). Springer, Dordrecht.

Othman, A. R., & Barton, D. C. (2008). Failure initiation and propagation characteristics of honeycomb sandwich composites. *Composite Structures*, *85*(2), 126-138.

Piegl, L., & Tiller, W. (2012). *The NURBS book*. Springer Science & Business Media.

Rhymer, J. D. (2012). *Force criterion prediction of damage for carbon/epoxy composite panels impacted by high velocity ice* (Doctoral dissertation, University of California, San Diego). Retrieved from https://escholarship.org/uc/item/0nd3r7k6

Rhymer, J., Kim, H., & Roach, D. (2012). The damage resistance of quasi-isotropic carbon/epoxy composite tape laminates impacted by high velocity ice. *Composites Part A: Applied Science and Manufacturing*, *43*(7), 1134-1144.

Rinker, M., Krueger, R., & Ratcliffe, J. (2013). Analysis of an aircraft honeycomb sandwich panel with circular face sheet/core disbond subjected to ground-air pressurization. *NASA/CR-2013-217974, NIA Report No. 2013-0116*.

Robinson, P., & Davies, G. A. O. (1992). Impactor mass and specimen geometry effects in low velocity impact of laminated composites. *International Journal of Impact Engineering*, *12*(2), 189-207.

Rouse, M., Ambur, D. R., Bodine, J., & Dopker, B. (1997). Evaluation of a composite sandwich fuselage side panel with damage and subjected to internal pressure. *NASA-TM-110309, NAS 1.15:110309*.

Roy, R., Park, S. J., Kweon, J. H., & Choi, J. H. (2014). Characterization of Nomex honeycomb core constituent material mechanical properties. *Composite Structures*, *117*, 255-266.

Seemann, R., & Krause, D. (2017). Numerical modelling of Nomex honeycomb sandwich cores at meso-scale level. *Composite Structures*, *159*, 702-718.

Sencu, R. M., Yang, Z., Wang, Y. C., Withers, P. J., Rau, C., Parson, A., & Soutis, C. (2016). Generation of micro-scale finite element models from synchrotron X-ray CT images for multidirectional carbon fibre reinforced composites. *Composites Part A: Applied Science and Manufacturing*, *91*, 85-95.

Song, Z., Margetts, L., Lowe, T., Tse, B., Wang, Y., & Ahmed, M. X-ray tomography imaging of sandwich panels made of ramie fibre and carbon fibre. *The 10th International Conference on Green Composites November 7-9, 2018, Quanzhou, P. R. China*

Thévenin, R. (2007, May). *Aircraft composite structures - Perspectives on safe maintenance practice*. Presented at CACRC Workshop, Amsterdam.

Transportation Safety Board of Canada. (2005). *Aviation Investigation Report A05F0047*. Retrieved from https://www.tsb.gc.ca/eng/rapports-reports/aviation/2005/a05f0047/A05F0047.pdf

U.S. Department of Transportation, Federal Aviation Administration. (2009). *Advisory Circular*

(AC No. 20-107B). Retrieved from https://www.faa.gov/documentLibrary/media/Advisory_Circular/AC20-107B.pdf

Wadley, H. N. (2005). Multifunctional periodic cellular metals. *Philosophical Transactions of the Royal Society A: Mathematical, Physical and Engineering Sciences*, *364*(1838), 31-68.

Wang, W. (2004). *Cohesive Zone Model for Facesheet-Core Interface Delamination in Honeycomb FRP Sandwich Panels* (Doctoral Dissertation, West Vigrinia University). Retrieved from https://researchrepository.wvu.edu/etd/2578

Webb, S. (2017, July 31). *Dramatic moment pilot lands plane full of tourists 'blind' after giant hailstones shatter cockpit windscreen and 'severely' damage jet. Retrieved from https://www.thesun.co.uk/news/4136399/brave-pilot-emergency-lands-plane-blind-after-massive-hailstones-shatter-cockpits-windscreen*

Wilbert, A., Jang, W. Y., Kyriakides, S., & Floccari, J. F. (2011). Buckling and progressive crushing of laterally loaded honeycomb. *International Journal of Solids and Structures*, *48*(5), 803-816.

Zalameda, J. N., & Parker, F. R. (2014). Nondestructive Evaluation (NDE) for Inspection of Composite Sandwich Structures. *NASA/TM-2014-218545*. Retrieved from https://ntrs.nasa.gov/archive/nasa/casi.ntrs.nasa.gov/20150001252.pdf

Zhang, J., & Ashby, M. F. (1992). The out-of-plane properties of honeycombs. *International journal of mechanical sciences*, *34*(6), 475-489.

Zhou, G., Hill, M., Loughlan, J., & Hookham, N. (2006). Damage characteristics of composite honeycomb sandwich panels in bending under quasi-static loading. *Journal of Sandwich Structures & Materials*, *8*(1), 55-90.

Zinno, A., Prota, A., Di Maio, E., & Bakis, C. E. (2011). Experimental characterization of phenolic-impregnated honeycomb sandwich structures for transportation vehicles. *Composite structures*, *93*(11), 2910-2924.